PROCESSING AND PROPERTIES OF ALIGNED CARBON NANOTUBE/GLASS CERAMIC COMPOSITE

GEOFFREY OTIENO

Lincoln College

A Thesis Submitted for the Degree of Doctor of
Philosophy at the University of Oxford
Hillary Term, 2012

Processing and Properties of Aligned Carbon Nanotube/Glass Ceramic Composite

Geoffrey Otieno Lincoln College

Doctor of Philosophy Hilary Term, 2012

ABSTRACT

Previous attempts to produce carbon nanotube (CNT) ceramic composites have resulted in poorly dispersed, unaligned and non-continuous CNTs in the composites with modest improvements in properties. The research presented in this thesis pertains to the production of dense aluminoborosilicate (ABS) glass matrix composites containing aligned and continuous multi-walled carbon nanotubes (MWCNT) of millimetre lengths. This was achieved by infiltrating CVD grown MWCNT preforms using a precursor sol and sintering which achieved 80 ± 2% dense composites. Focused ion beam milling together with image analysis showed that the composites contained 20 ± 2 vol.% MWCNTs, which are aligned and continuous within the glass matrix. Indentation studies showed greater damage tolerance in the composite compared to unreinforced ABS glass. Under compression, there is no significant change in the compressive strength between the composite and the unreinforced glass. The bend strength of microcantilever beams were 1.4 to 1.3 GPa for the composite and glass respectively. Elastic modulus of 84 GPa and fracture toughness (K_{IC}) of up to 2.4 MPa$\sqrt{m}$ were obtained for the composite. The elastic modulus and fracture toughness results are an improvement of 30 % and 240 % over that of unreinforced ABS glass. Fracture surfaces showed apparent MWCNT pullout lengths of up to ~ 1 µm. Analysis indicates that crack bridging by intact MWCNTs provides the majority of the improvement in fracture toughness. Interlayer sliding of the MWCNTs and "sword in sheath" failure mechanism of the MWCNTs prevented the maximum potential performance, with respect to elastic modulus and fracture toughness, from being achieved. Electrical conductivity in the alignment direction of the CNTs showed improvements by a factor of 10^6 compared to unreinforced ABS glass. Furthermore, improvement of a factor of ~ 10 in the thermal conductivity was obtained for the composite over that of ABS glass.

CONTENTS

List of Figures

List of Tables

List of Abbreviations

CNT(s)	Carbon nanotube(s)
ACNT	Aligned carbon nanotube
GCNT	Glass coated carbon nanotube
MWCNT	Multi-walled carbon nanotube
SWCNT	Single-walled carbon nanotube
ABS	Aluminoborosilicate
CMC	Ceramic matrix composite
PMC	Polymer matrix composite
MMC	Metal matrix composite
CVD	Chemical vapour deposition
PECVD	Plasma enhanced chemical vapour deposition
VLS	Vapour-liquid-solid
AAO	Anodic aluminium oxide
CVI	Chemical vapour infiltration
EPD	Electrophoretic deposition
HIP	Hot-isostatic press
SPS	Spark plasma sintering
K_c	Fracture toughness
K_{IC}	Critical stress intensity factor
G_c	Fracture energy
G_{debond}	Debond fracture energy
$G_{pull-out}$	Pull-out fracture energy
$G_{bridging}$	Bridging fracture energy
SENB	Single edge-V-notch beam
EMI	Electromagnetic interference
FIB	Focused ion beam
TGA	Thermogravimentric analysis
EDX	Energy dispersive X-ray spectroscopy
EELS	Electron energy loss spectroscopy
C_p	Specific heat capacity
DSC	Differential scanning calorimetry
E_{glass}	Elastic modulus of glass
E_{cnt}	Elastic modulus of carbon nanotube
E_{comp}	Elastic modulus of composite
σ_{glass}	Strength of glass
σ_{comp}	Strength of composite
V_{cnt}	Volume fraction of carbon nanotubes
V_{GCNT}	Volume fraction of glass-coated carbon nanotube
I	Second moment of area
l_d	Debond length
l_c	Critical length
C	Flaw size
τ_i	Frictional shear stress
$\tau_{sword-in-sheath}$	Frictional shear stress between graphitic walls
r	Radius
r*	Mean radius
r_{GCNT}	Radius of glass coated carbon nanotube
S_{cnt}	Crack bridging length by carbon nanotube

Declaration

The work presented in this thesis was carried out at the department of Materials, University of Oxford, from October 2008 to December 2011 under the supervision of Prof. Richard I. Todd and Prof. Nicole Grobert. All the work is my own unless stated otherwise and has not been submitted for any other degree at this or any other university.

Parts of this work has been patented, published and reported as follows;

1. G. Otieno, N. Grobert and R.I. Todd, *Composite Materials Containing Aligned Nanotubes and the Production Thereof*, Patent Publication Nos. WO/2011/024000 and GB2010/051411 was published on March 03 2011.
2. G. Otieno, A. Koos, F. Dillon, A. Wallwork, N. Grobert, R.I. Todd. *Aligned carbon nanotubes aluminoborosilicate glass composites by sol gel processing*, Carbon, 2010 (48), 2212 -2217
3. G. Otieno, N. Grobert, R.I. Todd "Micromechanical properties of aligned and continuous multi-walled carbon nanotube/aluminoborosilicate glass composites" The 36th International Conference & Exposition on Advanced Ceramics & Composites(ICACC) in Florida, USA. 27th Jan. 2012. Oral Presentation.
4. G. Otieno, A. Koos, F. Dillon, C. Dancer, G. Hughes, N. Grobert, R.I. Todd, Micromechanical properties of aligned carbon nanotube/aluminoborosilicate glass composite, 12th Conference of the European Ceramic Society (ECers), June 2011, Stockholm, Sweden. Poster Presentation
5. G. Otieno, N. Grobert and R.I. Todd. Novel routes to structure properties investigations of CNT/glass composites' Characterisation Seminar Department of Materials, University of Oxford, and 13th June 2011. Oral Presentation

6. G. Otieno, N. Grobert and R.I. Todd. Micromechanical testing of aligned CNT/glass composites. 1 Day research meeting on Advanced Ceramics (1DRAC), Imperial College London, 13th April 2011. Oral Presentation
7. G. Otieno, N. Grobert, R.I. Todd. Aligned carbon nanotubes/borosilicate glass composite by sol gel processing. NanoteC10, Oxford, UK, 3rd Sept. 2010. Oral presentation.
8. G. Otieno, A. Koos, F. Dillon, A. Wallwork, N. Grobert, R.I. Todd.Processing and properties of aligned multi-walled carbon nanotube / aluminoborosilicate glass composites made by sol gel processing. 11th International Conference on the Science and Application of Nanotubes (NT10), Montreal, Canada 29th and 30th June 2010. Poster Presentation.
9. G. Otieno, A. Koos, F. Dillon, N. Grobert, R.I. Todd. Aligned carbon nanotube/glass composite by sol gel processing, NanoteC09, Brussels, Belgium 26th to 29th Aug. 2009. Poster presentation
10. G. Otieno, A. Koos, F. Dillon, N. Grobert, R.I. Todd. Aligned carbon nanotube/glass composite by sol gel processing. Electron Microscopy of Ceramics, Eskisehir (Turkey), 7th to 13th Oct. 2009.

Acknowledgements

This thesis marks the conclusion of the experience of reading for a DPhil in Materials Science at Oxford. The journey was made fulfilling by the many colleagues, friends and family who supported and/or encouraged me either directly or indirectly.

My greatest gratitude goes to my supervisors Prof. Richard Todd and Prof. Nicole Grobert who have been supportive and encouraging in their respective supervisory areas. Their guidance all through the project has been nothing but immaculate. Individually, I credit Prof. Todd for the wealth of knowledge on ceramics and their mechanical properties that I have gained during my DPhil. I especially value the group meetings contributions and ideas that he provided. Prof. Grobert provided expert advice on carbon nanotubes, and I thank her for giving me the freedom to explore the wonderful world of carbon nanotubes.

Additionally, I would like to thank Dr. Antal Koos for discussions on production of carbon nanotubes and practical assistance in the laboratory, and also for the various discussions about Hungary, Romania and the rest of the world. Also, I would like thank the senior members of the two groups I was involved with; Dr. Frank Dillon, Dr. Zabeda Aslam Dr. Claire Dancer and Dr. Amartya Mukhopadhyay who in one way or another I consulted severally during my work. Other group members, Andrew Searle, Jingyu Sun, Adrian Murdock, Karl Mandel, Fatma Dinc, Madhuri Dutta, Dingyu Shi (Dominick), Noor Yahya, Andrew Norton, Mi Du amongst others who I crossed paths with frequently and in sharing equipment. In particular, Andrew Norton, for helping in proof reading this thesis.

I would like to thank the staff of the department of Materials. Just to mention a few; Dr. Alison Crossley, Richard Turner, Chris Salter, Steve Lett, Laurie Walton, Gabriella Chapman, Dr. Gareth Hughes, Dr Adrian Taylor and Marion Beckett who kindly offered assistance when it was required. I am also indebted to thank the ever joyful, now retired Lyn Richmond, at the reception.

I would also like to thank my housemates for two years (Sept 2009-Sept 2011), Ali, Alex, Teera, Brian and Giani for their humour and keeping the house lively during the time we spent together. Also friends from around Oxford in particular Dr. Christopher Nwankwo, Kingwa Kamecu, Francis Oketch, Thomas Polianitis and Dr. Mujtaba Zaka.

This work would not have been possible without the funding from the Rhodes Trust and more so, fellow scholars, the staff and Wardens, Sir Colin Lucas and Dr. Don Markwell. I appreciate Mary Eaton for her help and Sheila Partridge for her kindness and cakes.

Finally, my deepest gratitude goes to my wife Ruth Otieno who was and is always understanding and supportive. Also to the rest of my family, mother Christine Ongaro, mother-in-law Nancy Thuku, my sister Beryl Adhiambo for their understanding and support during this process.

Geoffrey Otieno,
University of Oxford,
March 2012.

Dedicated to My Family

CHAPTER 1

INTRODUCTION

Since the observation of multi-walled carbon nanotubes (MWCNT) by Iijima in a transmission electron microscope in 1991 [1], there has been tremendous amount of research in the production of composites with CNT as the reinforcing phase in matrices. This is due to the excellent mechanical properties amongst other properties demonstrated by the carbon nanotubes (CNTs). Ceramic matrix composite (CMC) materials are new compared to traditional monolithic ceramics and are being established with several promising applications such as high temperature components in turbines and brake disks. Overall, ceramics exhibit excellent mechanical, thermal stability and chemical properties. However, ceramics are brittle due to low fracture toughness. For this reason, their use is limited to a small number of applications. To improve the fracture toughness of ceramics, reinforcements in the form of particulates or fibres have been used.

To date, studies of the reinforcement of ceramic matrices with CNTs have not produced composites reflecting the full potential of the CNTs in terms of mechanical properties. One reason there is little or no improvement in properties is a consequence of high van der Waals interactions between CNTs. This makes it difficult to produced well dispersed CNTs in ceramic matrices. Agglomerates of CNTs result in reduced strength in the composites. The common fabrication approach of composites with CNTs also affects the composite properties achieved. To date, most studies of

CNT/ceramic composites are mainly based on disorderly/randomly oriented nanotubes in a matrix. This stems from the fact that most CNTs are produced and collected in the form of powders. The CNTs are then incorporated in the ceramic matrices in a randomly oriented manner by first dispersing the CNTs in solutions. Also, the strong van der Waals forces make it difficult to control the alignment and the interfacial properties of CNT/ceramic composites. Interfacial properties between CNT and matrix determine the strength of the composites as it governs the load transfer ability from matrix to CNT during mechanical loading. Several approaches to improve interfacial properties have been attempted mostly involving chemical modification of the CNTs. However, this reduces their effectiveness as reinforcements as defects are introduced on the graphitic walls. It is well understood that alignment of fibres in convectional composites gives high strength to volume ratio. This is particularly important when the forces applied are parallel to the direction of the fibres. Therefore, to fully take advantage of the uniaxial strength of CNTs, it is expected that alignment is key.

The goal of this research is to develop an approach for improving the mechanical properties of nanotube reinforced ceramic composite by effectively aligning and dispersing continuous CNTs in glass as a model ceramic matrix. In particular, this research developed a route to the production of aligned CNT/glass composites without any further processing of the raw CNT material. Comparing the properties of the CNTs, glass and the CNT/glass composite can lead to an understanding of the contribution of the CNTs to the properties of composite. This research concentrates on the properties in the alignment direction of the CNTs in the composites taking advantage not only of the exceptional uniaxial CNT strength but also the excellent electrical and thermal properties in the alignment orientation. The thesis details experiments carried out in order to achieve alignment and the characterisation of the CNTs and composites obtained.

The thesis is organised as follows; Chapter 2 gives a background to CNTs and their composites, in particular CNT ceramic composites, detailing fabrication methods and properties. Chapter 3 details the methods used in this thesis for production of CNTs and composites together with instrumentation for characterisation and measurements. The results of the production of CNTs and composites are presented in Chapter 4, along with a discussion on the interaction of the CNTs and the matrix which provides an idea as to the possible governing mechanisms that can be controlled in order to obtain optimised properties. Chapter 5 details the results of mechanical measurements of the CNTs and the corresponding composites with emphasis on a microcantilever beam testing technique. Chapter 6 briefly looks at the electrical and thermal properties. Finally a summary of the findings and prospects for future work is given in chapter 7.

CHAPTER 2

LITERATURE REVIEW

2.0. Composites

Composites are a class of materials made up of two or more distinct phases, one phase being the reinforcing phase such as particulates, fibres or sheets while the other phase is the matrix material. The matrix materials can be metallic, polymeric or ceramic. The matrix holds the reinforcing phase in place and commonly shares load with it. The reinforcing phase is embedded in the matrix in either a continuous or discontinuous manner and is typically a material with desirable properties such as low density, good electrical and thermal conductivity, high strength or fracture resistance.

Composite materials occur naturally, for example in wood which is made up of cellulose fibres in a matrix of lignin and in bones which is made up of collagen and minerals. Fabricated composites have been used for more than 5000 years with one such documented account found in the Bible Exodus 5:6-7 : ‘And Pharaoh commanded the same day the task masters of the people, and their officers, saying “Ye shall no more give the people straw to make bricks, as heretofore: let them go and gather straw for themselves”’. In recent times, the first widely used manufactured composite is asbestos cement which was developed around 1900 [2].

Composites can be classified on the basis of the matrix material or on the basis of the reinforcing material structure. The latter classification leads to particulate composites or fibrous composites. Classification on the basis of matrix materials gives three classes of composites; polymer, metal, and ceramic composites [3]. The next section discusses these classifications of composites based on the matrix material.

2.0.1. Polymer and Metal Matrix Composite Materials

Polymer matrix composites (PMCs) are the most researched composites due to their relative ease of processing [4]. Reinforcements are added to polymers to alter several properties such as conductivity and strength and also to reduce costs. This enables them to be used in diverse applications unlike the pristine polymers. The most commonly used matrices are thermosetting in nature and they include epoxy, vinyl ester and saturated polyester. Thermosetting polymers are made by cross-linking of liquid monomers into rigid solids and are generally brittle materials. Another class of polymers used is the thermoplastic polymer which is made from high molecular weight monomers. The inherent strength of the monomer provides the strength for the thermoplastic polymers by entanglement of the unit monomers [5]. The most commonly used reinforcement materials for polymers are carbon fibres, glass fibres, ceramic particulates [5] and more recently CNTs. Addition of glass fibres for example is commonly used to improve the strength and stiffness of polymers for impact resistance materials and optical films [5]. The addition of ceramic particulates leads to improved strength in polymers and other desirable properties for applications in dielectric [5] dental [6] and bone replacement [7] materials. In addition to improved strength, the use of metals as reinforcements for polymers results in improved electrical properties. This makes them useful in electronic applications such as actuators [8]. The main disadvantages of PMCs are low thermal resistance and high coefficient of thermal expansion which are inherent in the polymer matrices when compared to metals or ceramic matrix composites.

Metal matrix composites (MMCs) have been studied in the past three decades to develop new materials of better performance than metals in terms of strength or stiffness to density ratio, thermal and chemical resistance *etc*. compared to monolithic metals. MMCs are composed of metal matrices such as aluminium, magnesium and copper, and a dispersed phase of either ceramic or other metals. The ceramic fillers could be silicon carbide, alumina, silicon nitride or boron nitride while metallic reinforcement could be tungsten or beryllium among others [9]. These reinforcements could be in the form of fibres or particulates. The fibre reinforced metals consist of either continuous or discontinuous fibres/whiskers with high aspect ratios. The particulate reinforced ceramics consist of platelets or particles dispersed within the metal. This can be achieved by dispersing particles within the metal matrix during processing or precipitation of different phases of the same material during processing. MMCs find applications in space shuttles and commercial airliners, electronic substrates, golf clubs *etc*. The limiting factor to large scale applications of MMCs is the high cost associated with fabrication [9].

2.1. Ceramic Matrix Composites

Composite materials with a ceramic matrix provide several performance advantages over monolithic ceramics. Structural ceramics have high mechanical strength, excellent temperature stability and chemical resistance properties. However, ceramics have low fracture toughness and their intrinsic brittleness limits their applications. In view of this, fibres and particulates are incorporated into ceramic matrices in order to reinforce and toughen them [10]. In the case of fibre reinforced composites, energy is dissipated during crack growth by the debonding of the matrix from the fibres and bridging of propagating cracks by the fibres, thereby improving fracture toughness of the ceramics. This review looks at the use of CNTs (CNT) as the reinforcing phase in ceramic matrices from the developmental aspects, processing and applications. Ceramic matrix composites (CMCs) have been developed to combine ceramics with other reinforcing phases to create materials with new superior properties [11,12,13,14,15,16,17]. Ceramic matrices used in composite fabrication can be classified as either oxides or non-oxides. The common oxide matrices include alumina (Al_2O_3), silica (SiO_2), mullite ($Al_6Si_2O_{13}$), barium aluminosilicate ($BaAl_2Si_2O_8$) and calcium aluminosilicate ($CaAl_2Si_2O_8$). Of these oxides, alumina and mullite are widely used because of their compatibility with common reinforcements. Some of the common non-oxide ceramics include silicon carbide, silicon nitride, boron carbide and aluminium nitride.

A specialised but commercially important subclass of composites is the carbon/carbon composites. These composites are produced by vapour infiltration of an array of carbon fibres and were originally developed for aerospace applications. They also have low density, high thermal conductivity and excellent mechanical properties at elevated temperatures which make it an ideal material for aircraft brakes and rocket nozzles [18].

2.1.1. Reinforcing Materials for Ceramic Composites

Ceramic reinforcements are available in a variety of forms. Initially, ceramic matrix composites (CMCs) consisted of discontinuous reinforcements which were processed via conventional powder processing techniques. The reinforcements were in the form of whiskers, platelets and particulates in the micron size range. Examples are silicon nitride, silicon carbide, boron carbide and boron nitride. Silicon carbide (SiC) is the most commonly used reinforcement because of its compatibility with several oxide and non-oxide matrices [19]. Currently, of increasing interest are CMCs containing continuous fibres as reinforcements for optimisation of the structural properties of the composites. This class of composites show a pseudo-ductile property by mechanisms such as crack bridging, fibre pull-out or fibre debonding to the otherwise brittle ceramic materials (figure 2-1).

Examples of the continuous fibres used include carbon, glass, SiC, mullite and alumina. Generally, carbon fibres are the most investigated reinforcements in CMCs. They were first reported in the 1960s and have been demonstrated to improve the fracture toughness of glass [20,21,22]. SiC is the most attractive because of its strength, stiffness and thermal stability. The fracture toughness of SiC reinforced glass can reach 17 MPa $\sqrt{m}$ from 0.7 MPa $\sqrt{m}$ with various toughening mechanisms involved such as crack bridging, fibre pull-outs, and fibre/matrix debonding [19]. However, the problems of low fracture toughness and strength, poor resistance to creep, fatigue and thermal shock have not been effectively solved by the micron-size fillers. Therefore, the use of nano-size fillers, especially carbon nanomaterials such as CNTs, has taken root as the possible solution to some of the problems faced.

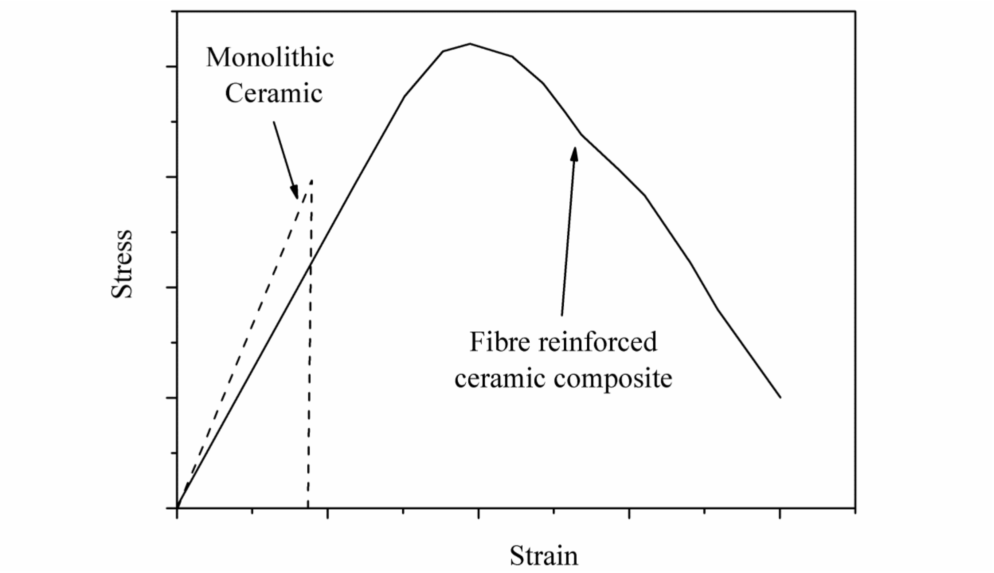

Figure 2-1 Comparison of failure modes for monolithic ceramics and fibre reinforced ceramic.

2.2. Carbon Nanomaterials

Carbon is a remarkable element that exhibits several stable forms ranging from 0D to 3D structures. Examples of the structures include diamond, graphite, carbon nanotubes, graphene and fullerenes. Carbon forms many structures because of its electronic configuration ($1s^2$ $2s^2$ $2p^2$); this configuration gives carbon the ability to form hybrid structures by mixing of the 2s and $2p_x$ $2p_y$ and $2p_z$. This hybridization results in two different hybrid bonds namely sp^2 and sp^3. The sp^3 bonds are typically found in diamond involving $2s^2$ and $2p^2$ orbitals forming four sigma (σ) bonds resulting in a tetrahedral structure. An example of sp^2 bonding is found in graphite which involves formation of three σ bonds from $2s^2$ and one 2p electron; the other 2p electron forms a pi (π) bond. The three σ bonds result in a trigonal planar structure such as in graphite [23]. The different bonding leads to the different structures each showing unique properties.

Graphene can be described as a planar sheet of sp^2 bonded carbon atoms that are packed in a honeycomb crystal lattice of 2-dimensions. It was supposed that these structures could not exist at ambient temperature and pressure. Graphene was, however, produced by Andre K Geim and Kostaya S. Novoselov in 2004 [24]. The van der Waals forces holding the different layers in graphite make it possible to obtain graphene from graphite by mechanical or chemical peeling [25]. Other methods of production involve chemical vapour deposition of carbon atoms to form a layer of graphene [25]. Graphene displays several promising characteristics such as good mechanical properties which are derived from strong sp^2 C-C bonds. The Youngs modulus, E, of graphene was measured by Lee *et al.* [26] to be 1 TPa using an atomic force microscope (AFM) nanoindentation. Graphene has also been shown to have high electron mobility making it a near perfect electronic conductor [27]. This property is due to graphene being a zero gap semiconductor (the conduction band and the valence band overlap) [27], making it a strong candidate for several electronic applications.

Fullerenes, unlike graphene, are large closed cage carbon molecules in a spherical shape. Their discovery is attributed to Kroto, Smalley and Curl in 1985 [16] who observed the C_{60} molecule. Further research on fullerenes was boosted when Kratschmer and Huffman isolated solid C_{60} [28]. C_{60} is the most famous and abundant fullerene. Other fullerenes with more carbon atoms have also been isolated. Addition of rings of hexagonal carbon rings around the fullerene carbon network forms capsules which are higher fullerenes. Conceptually, if more rings are added, and the capsule is elongated, tubular structures with fixed diameters are formed *i.e.* nanotubes which are discussed in the next section.

2.3. Carbon Nanotubes

2.3.1. Introduction to Carbon Nanotubes

The work on fullerene chemistry in the 1980s by Smalley and co-workers at Rice University later led to the observation under a transmission electron microscope and description of CNTs by Iijima and co-workers in the early 1990s [1]. Tubular structures of less than 100 nm in diameter had previously been reported in 1950's and 1970's by Radushkevich *et al*. and Endo *et al*. respectively [29]. A carbon nanotube can be visualised as a graphene sheet rolled into a tube with hemispherical caps at both ends. The graphene sheets (figure 2-2) can be rolled into different structures, *i.e.*, armchair, zigzag and chiral. The nanotube structure can be defined by a chiral vector $\overrightarrow{C_h} = n\,\overrightarrow{a_1} + m\,\overrightarrow{a_2}$ where $\overrightarrow{a_1}$ and $\overrightarrow{a_2}$ are unit vectors in a two dimensional lattice, and n and m are integers. Thus the structure of any nanotube can be expressed in terms of the two integer's n, m and a chiral angle (θ) (figure 2-2).

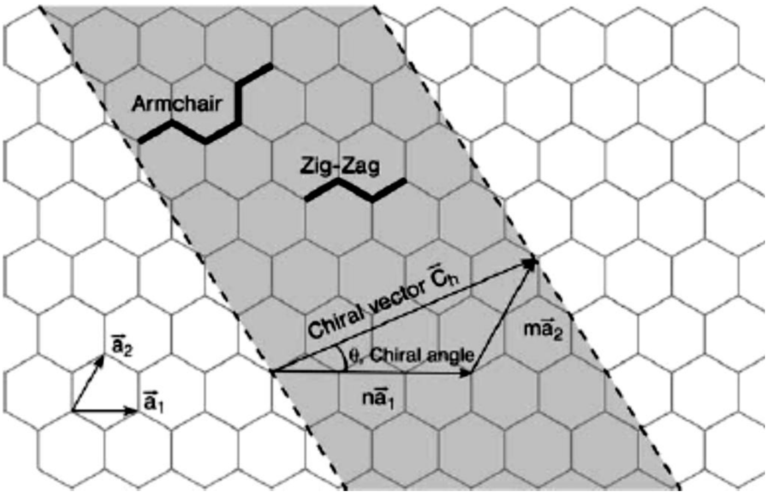

Figure 2-2 Schematic diagram showing the chiral vector and chiral angle in rolled graphite sheet with a periodic hexagonal structure [30].

For example, when n=m and $\theta = 30^o$ an armchair structure is formed (figure 2-3a). Zigzag CNTs are formed when m or n = 0 and $\theta = 0^o$ (figure 2-3b) and chiral nanotubes are formed for other values of n and m with θ between 0^o and 30^o (figure 2-3b). The properties of the tubes depend on the atomic arrangement during rolling, along with the diameter and length of the tube [30].

CNTs can be classified into two categories; single-walled carbon nanotubes (SWCNTs) and multi-walled carbon nanotubes (MWCNTs). MWCNTs consist of two or more concentric cylindrical shells of graphene sheets coaxially arranged around a central hollow core with an interlayer separation similar to that of graphite *i.e.* ca 0.34 nm [30]. The differences in properties between SWCNT and MWCNT are reviewed in section 2.5.

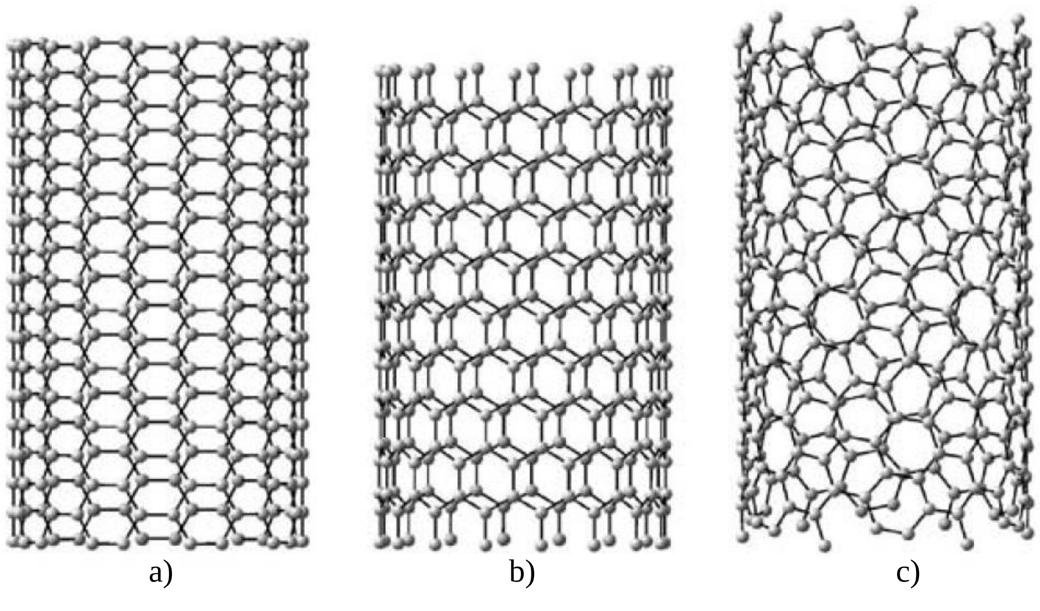
a)
b)
c)

Figure 2-3 Illustration of the atomic structure of (a) an arm chair (b) a zig-zag and (c) a chiral nanotube [31].

2.3.2. Production of Carbon Nanotubes

Bulk synthesis of good quality and high purity CNTs at low cost is essential for use of CNTs in practical applications such as composites. Various synthesis methods have been developed for the bulk production of CNTs. The primary methods of producing CNTs include arc discharge, laser ablation and chemical vapour deposition (CVD) [17]. The electric arc discharge method was used to produce CNTs when they were observed by Iijima in 1991. The arc discharge equipment (figure 2-4) works by applying a potential across two electrodes usually made of carbon rods of few millimetres in diameter separated by a small distance *e.g.* 1 mm in an inert atmosphere like helium. A high current discharge (100 A) passes through the carbon electrodes in plasma resulting in evaporation of carbon atoms from the electrodes. If no catalyst is used, MWCNT are formed while if SWCNT are desired, small amounts of catalyst (iron, cobalt, or nickel) particles are incorporated on the anode. Currently, arc discharge method is predominantly used for synthesis of high quality CNTs [32].

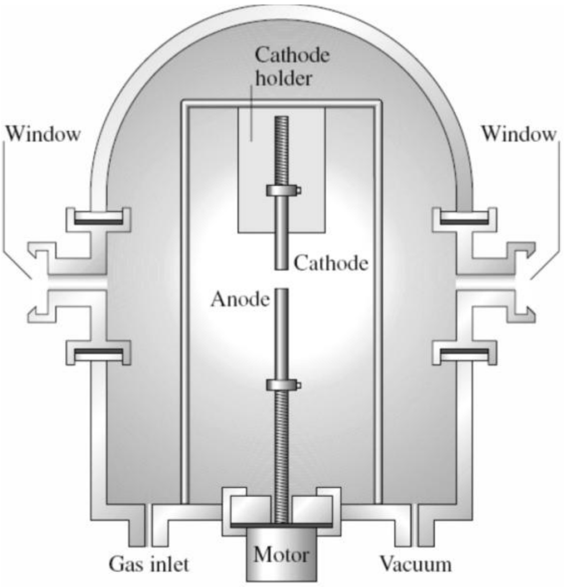

Figure 2-4 Sketch of an electric arc discharge setup [32]

Laser ablation typically uses graphite targets placed within a quartz tube in an inert atmosphere and held at a high temperature *e.g.* 1200 ^{o}C. An intense laser beam incident to the target evaporates carbon atoms from the graphite target. The inert gas carries the evaporated atoms from the hot furnace zone into a cooled copper target where the carbon atoms condense into CNTs (figure 2-5). The production of both MWCNT and SWCNT can be achieved without catalysts [32].

Both the laser ablation and arc discharge techniques are limited in the volume of CNT sample they can produce in comparison to the size of the carbon source. Also the equipment requirements and the large amount of energy consumed by these methods make them mostly suitable for laboratory research [33]. In addition, impurities in the form of amorphous carbon and catalyst particles are also produced. This necessitates a second separation stage to obtain only CNTs. Also, CNTs from arc discharge and laser ablation methods consists of CNTs with no particular alignment. Due to these drawbacks of laser ablation and arc discharge methods, the chemical vapour deposition technique is widely used for large scale production of good quality CNTs. The next section looks at chemical vapour deposition method for production of CNTs.

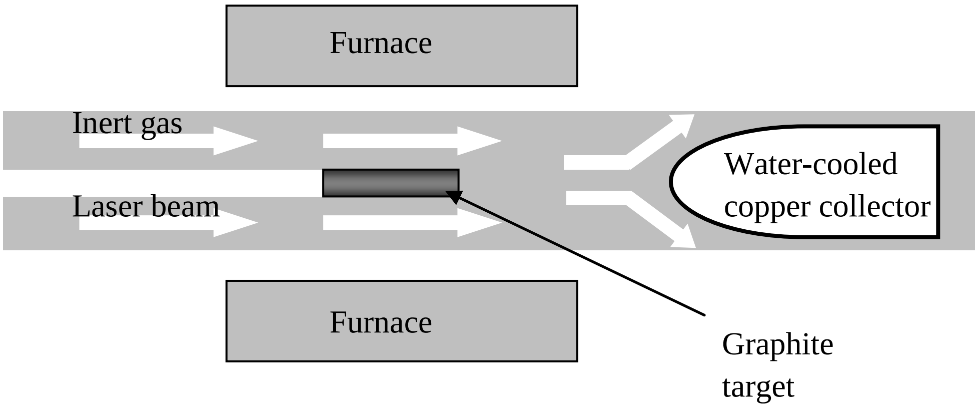

Figure 2-5 Laser ablation method for production of CNTs [32]

2.3.3. Chemical Vapour Deposition

Chemical vapour deposition (CVD) is an irreversible deposition of a solid from a gas or a mixture of gases through a heterogeneous chemical reaction. CVD is a continuous process and is currently the most used technique for high yield and low impurity production of CNTs at moderate temperatures. In addition, CVD has the capability to control the size, shape and alignment of the nanotubes [34]. Broadly, there are two variations of CVD; thermal CVD and plasma enhanced chemical vapour deposition (PECVD). In this thesis, CVD will simply refer to thermal CVD. In PECVD, wherein, a plasma is used to create a glow discharge, CNT growth is achieved at temperatures as low as 120 ^{o}C unlike in CVD where temperatures typically greater than 500 ^{o}C are used. Details of set up and basic operation of PECVD can be found in the literature such as by Meyyapan [23]. Even though lower temperatures are possible with PECVD compared to CVD, this is countered by the expensive experimental set up [23] [35]. Therefore, CVD has taken root as the main method for production of CNTs and is discussed further.

There are broadly two categories of CVD *i.e.* cold wall and hot-wall CVD. In cold-wall CVD, a substrate containing a metal catalyst, *e.g.* Fe, is heated directly on a holder (by resistance or induction) in an inert chamber. At the desired temperature, a carbon source is introduced into the chamber for growth of CNT on the substrate [36]. Cold-wall CVD growth of CNTs is not widely reported compared to the hot-wall CVD, where the whole reactor chamber is heated. This is due to difficulty in setting up large scale area growth of CNTs in cold-wall CVD. Also, instrument demands such as requirement of a vacuum [23] have also made cold wall CVD less popular for CNT production. On the other hand, hot-wall CVD widely described in the literature involves apparatus consisting of a tubular furnace where a quartz tube is inserted and kept at atmospheric pressure. An example of a hot-wall reactor is shown in figure 2-6 where a carbon feedstock is introduced into the quartz tube maintained at temperatures of typically between 600 and 1200 ^{o}C. The CNTs grow on the catalyst in the reactor and are collected after the reactor has cooled to below 300 ^{o}C. Broadly, there are three requirements for production of CNTs by CVD. They include 1) a carbon source, 2) elevated temperatures 3) a catalyst and/or catalyst support. These three requirements are discussed next together with the suggested growth mechanisms of the CNTs.

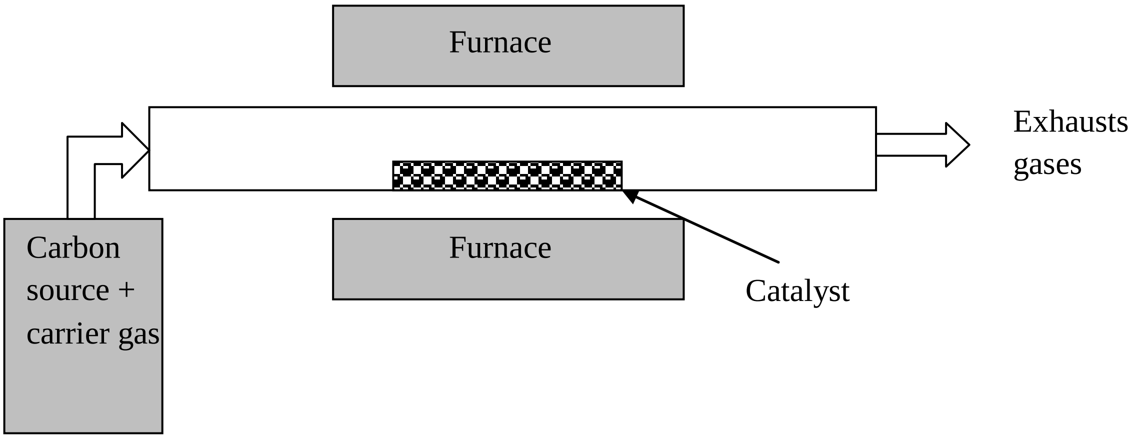

Figure 2-6 A schematic of a hot wall CVD setup.

2.3.3.1. Carbon Precursors for CNT Production

Examples of carbon sources for CVD CNT growth include ethylene, acetylene, toluene, benzene, cyclohexane, ethanol and carbon dioxide [23]. Campbell *et al.* [37] and [38] showed that the molecular structure of the carbon precursor affects the morphology of the CNTs produced. They suggested that linear hydrocarbons decompose to form atomic carbon or linear dimmers and trimers and hence produce straight and hollow CNTs. On the other hand, cyclic hydrocarbons *e.g.* benzene and cyclohexane produce relatively curved CNTs with bridged walls in the case of MWCNTs.

2.3.3.2. Temperature Requirements

From experiments, it has been demonstrated that low temperature CVD (600-900 ^oC) is used to produce MWCNTs while high temperature (900-1200 ^oC) is used for SWCNTs [39]. Experiments have shown that temperature also affects the yield and diameter distribution [40,41]. For example, Kumar and Ando [42] produced CNTs from camphor (a botanical hydrocarbon) as the carbon source, on alumina-silicate impregnated with Fe and Co catalyst, and showed that the yield of CNTs was low at temperatures below 650 ^oC. The yield increased with increasing temperatures of up to 750 ^oC. Between 750 to 850 ^oC, they observed that both the diameter size and diameter distribution increased drastically. The increments were attributed to more decomposition of the carbon source with the increasing temperature. They also observed SWCNT at temperatures above 850 ^oC.

2.3.3.3. Catalyst and Catalyst Support

The catalyst can be introduced in the CVD reactor in two ways; supported on the substrate or introduced as floating particles mixed with the carbon feedstock. For the supported catalyst approach, the commonly used substrates for catalysts include quartz, silicon, silica, silicon carbide, alumina, alumino-silicate and graphite [23]. The same catalyst *e.g.* Fe behaves differently on different supports. Therefore an understanding of the catalyst-substrate interaction is key to production of CNTs by

CVD [43]. Furthermore, the surface morphology of the support has also been shown to affect the yield and quality of the CNTs. For example, studies by Ando [42] and Hernadi [44] showed that alumina-silicate support with nano-pores containing catalysts gave high yield CNTs of narrow diameters. The floating catalyst approach was developed by Endo [45] for production of vapour grown carbon fibre. The method works by introducing pyrolised carbon source *e.g.* benzene, the catalyst (Fe) and carrier gas (H_2) into a vertical furnace reactor; the CNTs are collected at the bottom of the furnace [45]. The CNTs growth occurs while the catalyst floats through the furnace. In the case of a horizontal reactor [46] with a quartz tube, the floating catalyst particles attach on to the quartz tube, at which CNTs grow. The floating catalyst approach is the most amenable to scale up [23].

The most commonly used catalysts are the transition metals such Fe, Co and Ni. This is due to the high carbon solubility and diffusion rate in these metals [47]. Other metals used for CNT production include Cu, Au, Ag, Pt and Pd [48]. Orgaonometallocenes such as ferrocene, cobaltocene and nickelocene have also been used in CVD growth as catalyst sources [23]. At elevated temperatures in the reactor, the metallocenes decompose to form a metal which in turn catalyzes the growth of CNTs. Overall, the catalyst size determines the diameter of the CNTs produced [38]. Pre-patterned substrates with controlled catalyst size have been used to produce CNTs with controlled diameters [49]. Thin films of metals have also been successfully used to grow CNTs [50]. It is important to note that besides the type of catalyst material, the concentration of the catalyst has also been shown to affect the yield and diameter of CNTs with the optimum concentration dependent on the type of catalyst [42].

2.3.3.4. Carbon Nanotube Growth Mechanisms in Thermal CVD

The growth mechanism for CNTs during CVD is still debatable. However, the most accepted mechanism is the vapour-liquid-solid (VLS) mechanism described for whisker growth [51]. Briefly, the hydrocarbon source in gas state impinges on a metallic particle which catalyses the decomposition of the gas. The carbon saturates the bulk or surface of the catalyst and is precipitated as a CNT. From observations of the produced CNTs, two models of growth mechanisms are described; tip growth and base growth.

Tip growth occurs when the catalyst interacts weakly with the substrate hence the precipitation of carbon occurs at the bottom of the metal. This pushes the whole metal particle off the substrate (figure 2-7a). The growth of the CNT is maintained if the surface of the metal catalyst is exposed for more hydrocarbon decomposition [42]. The growth stops when the catalyst particle is covered with excess carbonaceous material as depicted in figure 2-7a [42]. For base growth, the interaction between the metal and the substrate is strong resulting in the precipitation of carbon from above the metal particle (figure 2-7b) [42]. However, it is still not clear whether the catalyst is in liquid or solid state during the precipitation of the CNTs, also, whether the diffusion process occurs in bulk or just on the surface of the catalyst. It is important to note that even though the catalyst particles have melting points of ~1500 ^{o}C, the reduced size of the particles (*ca.* 10nm) have been shown to melt at temperatures of 600-900 ^{o}C [48], thus it is possible that the catalyst particles are in liquid state. Helveg *et al.* [52] demonstrated that both bulk and surface diffusion occurs during precipitation. They decomposed methane on Ni catalyst and observed that the Ni remained faceted during growth of MWCNT [52]. They reported that the CNT growth was due to surface dynamic interaction between surface atoms and the Ni catalyst. Simulations to show surface diffusion in growth of CNTs have also been reported [53]. Banhart *et al.* [54] observed continued growth of MWCNTs which had a metal encapsulated in its inner core within a transmission electron microscope and concluded it was bulk diffusion. The experiments were performed at 600 ^{o}C under an electron beam (300 KeV) for 90 minutes. Carbon atoms from the MWCNT dissolved into the catalyst particle and were re-deposited in the form of SWCNT or MWCNTs of smaller diameters. Therefore, it is plausible that both surface diffusion and bulk diffusion occur in the growth of CNTs and the overriding factors are the type of catalyst and growth conditions. This area will need further investigations to provide a clear distinction of the type catalyst together with conditions that result in each specific growth mechanism.

Overall, production of CNTs by CVD has shown good control of different CNT properties such as diameter, yield and alignment. There are a variety of parameters that could be altered to obtain CNTs of interest *i.e.*, SWCNT or MWCNTs. Even though the growth mechanism is still debatable, experiments have shown that both surface diffusion and bulk precipitation are possible and should largely depend on the catalyst and/or the substrate in use.

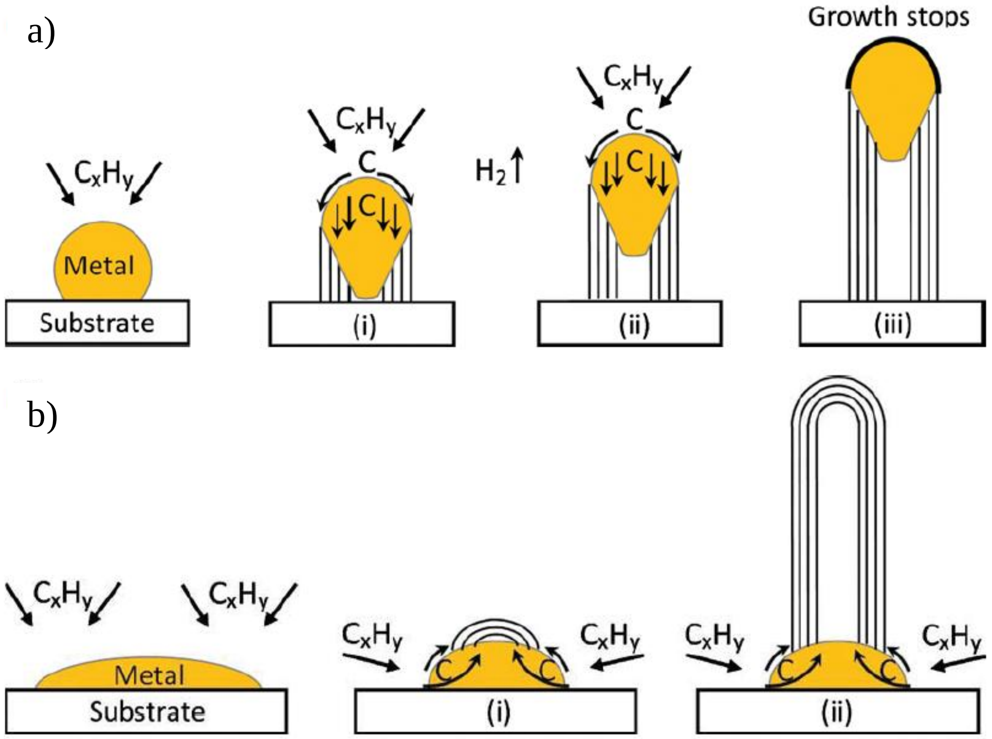

Figure 2-7 Schematic of CNT growth a) tip growth and b) base growth [42]

2.4. Properties of Carbon Nanotubes

It was previously discussed that three of the four valence electrons of carbon form sp^2 hybrid orbital which forms a trigonal planar σ bonds. The sigma orbitals form strong covalent bonds. The 4th valence electron of carbon is the $2P_z$ which is perpendicular to the plane of the σ orbitals; this forms a weaker π bond with the $2P_z$ orbitals of neighbouring carbon atoms. The π bonds define the Fermi surface hence they are responsible for the transport properties of CNTs. In this section, the mechanical properties and the transport properties will be discussed.

2.4.1. Mechanical Properties of Carbon Nanotubes

Testing and calculation of the mechanical properties of CNTs has been difficult. This is demonstrated by the numerous studies (table 2-1) that show results of 1 order difference on the same group of CNTs, *e.g.*, for SWCNT reported results for Young's modulus range from 0.3 – 1.2 TPa. This large spread in data is mainly attributed to the testing methods and the variability in different nanotubes as a consequence of synthesis method, purification, and also a tremendous limitation on the specimen size [55]. Therefore, it has been difficult to reproduce test results. The elastic modulus of CNTs has been obtained by different techniques including atomic force microscopy, measuring thermal vibrations in a transmission electron microscope and mathematical modelling techniques.

Table 2-1 Reported Young's modulus from the literature for different CNTs.

CNT	**Youngs Modulus**	**Technique**	**Group**
SWCNT	1.06 TPa	Approximation from graphite.	Ruoff *et al.* [56]
	0.32-1.47 TPa	AFM	Yu *et al.* [57]
	1.3±0.06 TPa	TEM – thermal vibrations	Krishnan *et al.* [58]
	1.24 TPa	Modelling	Goze *et al.* [59]
MWCNT	0.27-0.95 TPa	AFM	Yu *et al.* [57]
	1.28±0.59 TPa	AFM	Wong *et al.* [60]
	1.8±0.9 TPa	TEM – thermal vibrations	Tracey *et al.* [61]

Experimentally, CNTs have been shown to have an elastic modulus of around 1 TPa (table 2-1), hence, this is the number generally quoted for the CNTs elastic modulus for both SWCNT and MWCNTs. This is an order of magnitude higher than the best carbon fibres [62].

Quantum mechanics calculations have been used to predict that the strength of SWCNTs is greater than 100 GPa [63,64]. Table 2-2 shows some selected experimental results of the strength of CNTs. It is difficult to draw any conclusions from the few experimental studies done on the strength of CNTs. The table shows a large variation in the strengths. The strength of CNTs depends on the amount of defects such as atomic vacancies on the CNT walls [65]. For applications where strength is of importance, reducing the amount of defects is desirable.

Table 2-2 Selected strength results reported in the literature for different CNTs.

Tensile Strength (GPa)	**Carbon Nanotube type**	**Test Method**	**CNT synthesis method**	**Group**
30	SWCNT	Tension in SEM	Laser ablation	Yu *et al.* [66]
11-63	MWCNT	Tension in SEM	Arc discharge	Yu *et al.* [57]
150	MWCNT	Tension in TEM	Arc discharge	Demczyk *et al.* [67]
3.6	MWCNT	Tension in SEM	CVD	Xie *et al.* [65]

2.4.2. Electrical and Thermal Properties of Carbon Nanotubes

CNTs have experimentally been shown to have high current carrying capacity in the order of 10^9 Acm^{-2} [68] which is 3 orders of magnitude greater than copper and is attributed to ballistic electron transport in the CNTs [68]. The measured room temperature electrical resistivities are of the order 10^{-6} - 10^{-4} Ωcm [69].

Thermal conductivities of up to 6600 $Wm^{-1}K^{-1}$ have been predicted by molecular dynamic simulations for individual perfect SWCNTs [70] which are higher than those of diamond and basal graphite (2000 $Wm^{-1}K^{-1}$) [23]. Hone *et al.* [71] measured the thermal conductivity of a mat of SWCNT from arc discharge and obtained a thermal conductivity of 35 $Wm^{-1}K^{-1}$. For MWCNTs, Kim *et al.* [72] measured the thermal conductivity of a single MWCNT on micro-fabricated device and obtained a thermal conductivity of 3000 $Wm^{-1}K^{-1}$ at room temperature. This is three orders higher compared to previous estimates from bulk mat specimens [73]. It is clear that individual CNTs have extremely high thermal conductivity unlike bulk CNTs. The lower thermal conductivity in bulk CNTs is attributed to inter-tube interactions [73].

The π bonds in CNTs are also reasons for strong aggregation between CNTs in solid state and solutions. Another significant property of CNTs that is relevant to composite fabrication is the high aspect ratio (length to diameter) which is thought to be good for load transfer between the CNT and matrix [74].

Stemming from these properties, applications in diverse areas such as tissue scaffolds [75], super capacitor electrodes, atomic force microscope tips and field emission guns have been suggested [76]. Many investigators have also endeavoured to fabricate advanced CNT composites which exhibit one or more of these CNT properties. A large number of studies on CNT composites has been on CNT-polymer matrix with comparatively few investigations on inorganic matrix-CNT composites [77,78,79,80]. Of the studies on CNT-ceramic composite, some have focused on the potential of toughening that CNTs can provide [81,82,83,84]. As analogues to micron-size fibre reinforced composites, incorporating CNTs as nano-fibres in ceramics aims to enhance strength coupled with other properties of the CNTs such as thermal conductivity. An example of such a ceramic nanocomposite is being investigated by NASA (USA) by using CNTs to make ceramic composites for use in their spacecraft [11]. The next section looks into previous research in regards to developing composites based on CNTs and ceramic matrices and the results of these attempts.

2.5. Carbon Nanotube Ceramic Composites

Nanocomposites consist of either inorganic or organic phases dispersed in either an inorganic or organic phase with at least one phase being of the nanometre size [5]. The multifunctional properties of the combinations are often more than any of the individual properties [85,86], *i.e.*, composite materials combine a broad spectrum of desired properties such as stiffness and strength coupled with good thermal conductivity, chemical resistance or low weight properties amongst others. In 1991 Niihara proposed the concept of structural ceramic nanocomposites as an improvement to microstructural fabrication of composites [87]. Currently, several researchers are working on the production of high performance ceramic nanocomposites for applications in areas requiring a combination of properties that are not offered by traditional monolithic ceramics. The last decade has seen an increase in the research of CNTs as structural and functional material in polymers, ceramics and metal matrices [88]. However there are several key challenges to overcome in order to produce composites which manifest the individual CNTs properties such as tensile strength. The challenges include the mass production of good CNTs in terms of the properties of interest, for example, defect free CNTs would be ideal for toughening applications in ceramic composite. During processing, problems of uniform dispersion of CNTs in the matrix should be addressed. Also a degree of control of the interface between the CNT and the ceramic matrix would be ideal for example in load transfer applications. For ceramic matrices, a further challenge is that sintering is often carried out at temperatures that would damage CNTs. The next section will discuss the issues encountered while processing CNT-ceramic composites.

2.5.1. Challenges of Processing CNT/Ceramic composites

Achieving good dispersions of CNTs has long been a challenge that stems from the high van der Waals attractions that exist between the CNTs, which is compounded by high surface areas and aspect ratios. This renders them difficult to disperse in a solvent which is usually a first step in the production of conventional ceramic composite. Without a good dispersion, agglomerates will often occur in a composite (figure 2-8a). These agglomerates can act as defect sites and regions of stress concentration leading to composite failure in structural applications. However, when a good dispersion is achieved (figure 2-8b) whereby there is a uniform distribution of individual CNTs within the matrix, the contribution of the each CNT, for example in mechanical properties is maximised [89,90]. Agglomeration is worsened with increasing CNTs loading in a matrix due to the large surface areas involved [91]. In this case, the CNTs are more often in contact and the matrix may not wet the entire surface area of the CNTs [89]. For ceramic composites agglomeration occurs at low CNT loadings. Cha and co-workers [92] observed that agglomeration occurred at loadings of 1.8 vol.% in alumina prepared by molecular level mixing and ultrasonication. Improved mechanical properties are common for low loadings but high loading results in degradation of the mechanical properties of the composites (figure 2-9) [92,93].

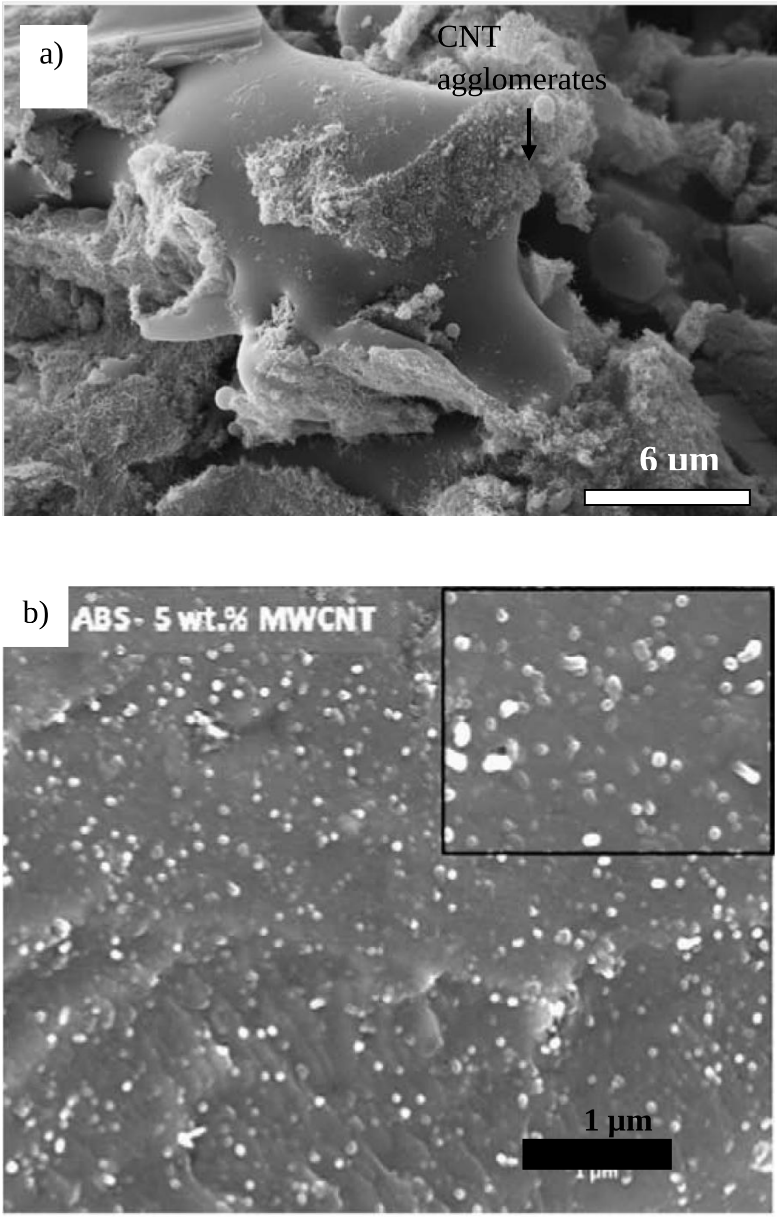

Figure 2-8 SEM image of a fracture surface of (a) a poorly dispersed CNT composite in borosilicate glass and [94] (b) homogeneously dispersed CNT in borosilicate glass matrix with some individual CNT pull-outs visible [91].

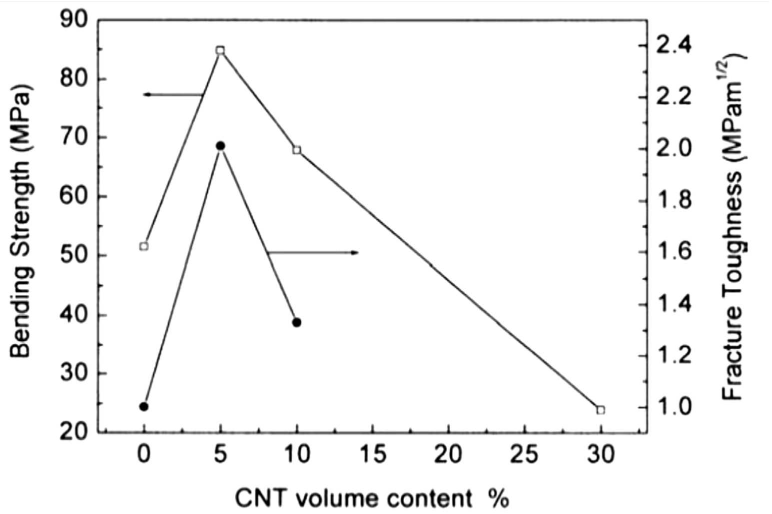

Figure 2-9 Variation of bending strength and fracture toughness with CNT content for SiO_2/MWCNT nanocomposites [93].

In the case of electrical and thermal properties, the percolation threshold for electrical and thermal conductivity is more likely to be reached at well dispersed higher CNT loading [95,96]. There are reports of lower percolation threshold (< 1 wt.%) in crystalline ceramics CNT composites compared [95,96] to glass ceramics CNT composites (>2.5 wt.%) [97], this is attributed to concentration of the CNTs at the grain boundaries in the crystalline ceramic composites which provide the conducting path.

Different processing methods have been employed in an attempt obtain good dispersions in CNT ceramic composites. They include conventional powder processing [98,99], colloidal processing [82,100,101] and sol gel processing [102,103]. Purification and modification of the CNT walls is also carried out to improve the dispersion of CNTs primarily in solvents or solution based processes. Several CNT modification chemistry routes on the CNT walls have been developed. The most widely used is the refluxing of the CNTs in acids to introduce functional groups on the CNT walls which improves dispersion of CNTs in ceramic matrices [104,105]. Also, good dispersions have been achieved by use of organic surfactants [106,107,108,109].

Other than the mixing methods, alternative methods of producing CNT ceramic composites have been investigated. For instance, Peigney and co-workers [110] produced CNTs on alumina powders containing Fe catalyst as precursor for CNT/oxide composite. The resulting powders were hot pressed to form the final CNT/Al_2O_3 composite. The fracture toughness of the composites was higher than that of monolithic alumina. Other non-conventional methods used for producing CNT ceramic composites include electrophoretic deposition [111] of a solution containing both CNTs and ceramic powders, and chemical vapour deposition of a ceramic on the CNT surfaces [112], both methods were shown to produce well dispersed CNTs in the matrices. In view of these methods, it is clear that obtaining a good dispersion is a crucial step in obtaining CNTs / ceramic composites.

CNT/Ceramic interfacial behaviour is another key factor affecting the mechanical and physical properties of the CNT nanocomposites. Compatibility and wettability between CNTs and ceramics is often poor and results in a weak interfacial strength [113]. However, we previously demonstrated an intimate bonding of borosilicate glass on individual CNTs [114]. Seeger *et al.* [102] showed SiO_2 intimately bonded to a CNT after sol gel processing. From conventional fibre reinforced ceramics theory, the fibre/matrix interface is a major consideration in producing the composites. It follows that CNT/ceramic interface will play a crucial role in determining the effect of CNTs in the composites. Even though intimate CNT/ceramic interfaces have been observed, it is noteworthy that there are no reports of direct measurements of interfacial strength of CNTs in ceramic systems. Therefore, further research is required in order to understanding the effect of the interface in *e.g.* the mechanical properties of the CNT/ceramic composites. The next section reviews the different composite synthesis methods which are mainly aimed at tackling one or more of the issues encountered when fabricating CNT-ceramic composites.

2.5.2. Processing Methods for Carbon Nanotubes Ceramic Composites

2.5.2.1. Powder Processing

Powder processing has been the most prevalent method of producing ceramics since the early stages of research on CNT-ceramic nanocomposites. The processing is usually done by mixing CNTs with ceramic powders in the micron size range, followed by ball milling or sonication in a solvent to disperse the powders and CNTs with or without surfactants. The powders are then dried, sieved and densified. Several reports [81,83,93,98,99] have used this method to produce CNT-ceramic composites with varying success. Figure 2-10a shows a good dispersion of CNTs when a surfactant is used during powder processing while figure 2-10b shows agglomerated CNTs within the matrix when no surfactant is used in processing [83]. Generally, by minimizing the size of the ceramic particles, a large surface of the CNT is expected to be in contact with the powders hence improved dispersion in the final composite. Large ceramic powder particles also lead to geometric agglomeration [105].

Peigney *et al.* [115] successfully used superplastic forming with mixtures of sub micron powders to perform a high temperature extrusion processing (figure 2-11). This method produced composites containing some aligned CNTs (figure 2-12a and b). Another attempt at powder processing was performed by Ma *et al.* [116], who fabricated nano-SiC/CNT composites by mixing 10 wt.% CNT with nano-SiC powders and hot pressing at 2273 ^{o}C. The fracture toughness and bend strength of the composites were reported to be around 10% better than monolithic SiC.

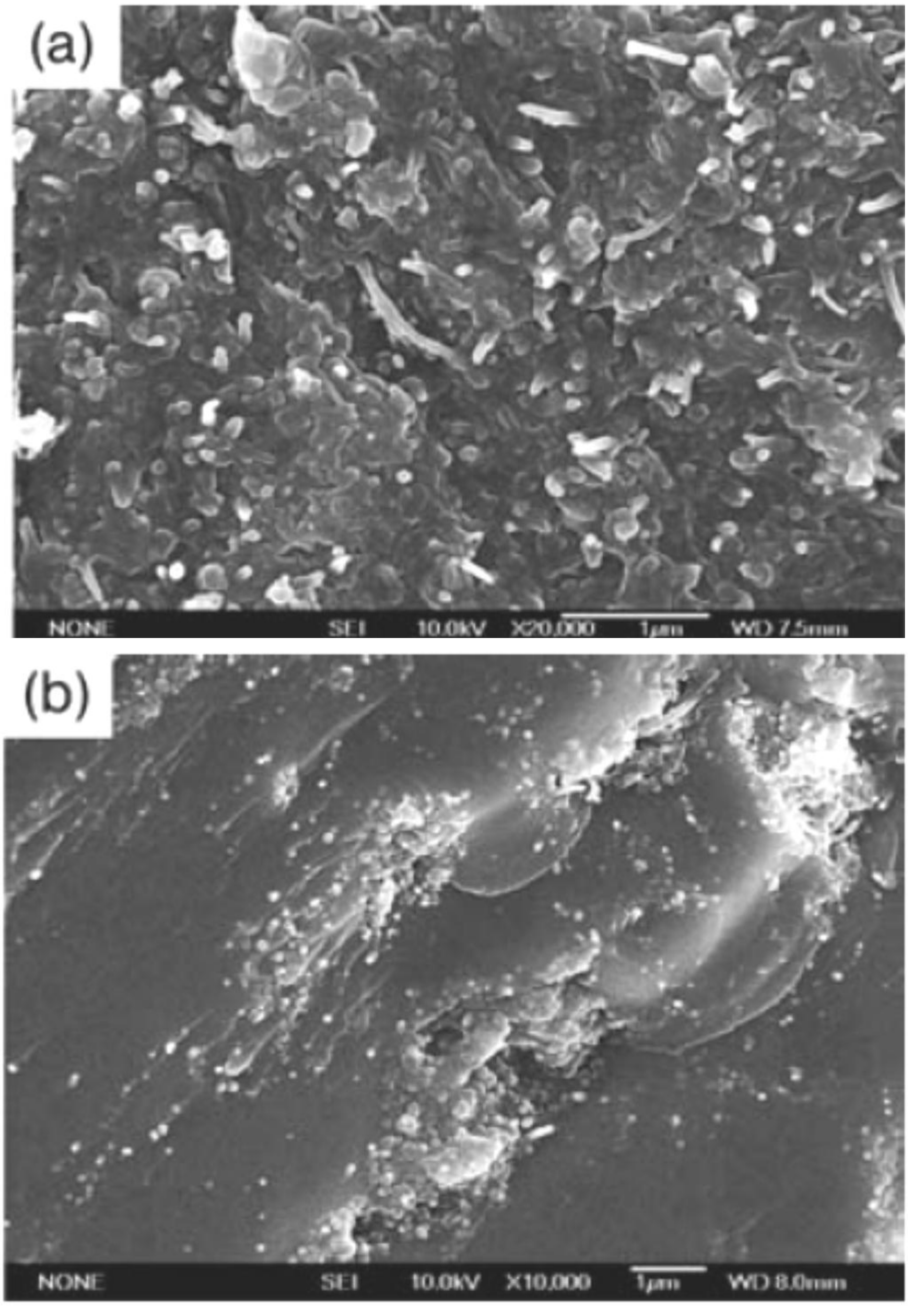

Figure 2-10 SEM fractographs of powder processed SiO_2/5 vol.% MWCNT composite (a) with surfactant (b) without surfactant [83].

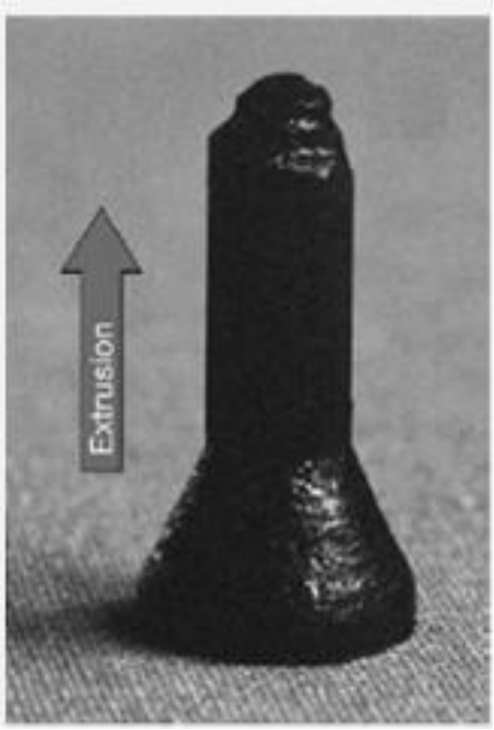

Figure 2-11 Photograph of Fe-Al_2O_3/CNT nanocomposite produced by high temperature extrusion process [115].

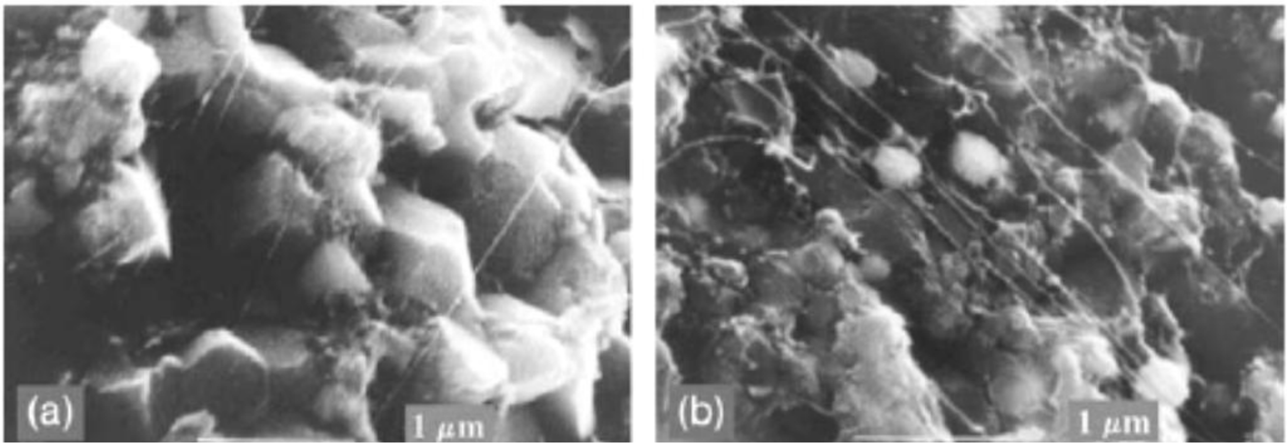

Figure 2-12 SEM images of the fracture surfaces of extruded Fe-Al_2O_3/CNT and FeCo-$MgAl_2O_4$/CNT nanocomposites [115].

2.5.2.2. Sol Gel and Colloidal Processing

Sol gel processing is a route to fabricating CNT ceramic composites where an initial mixture of CNTs in a liquid suspension is mixed with a liquid ceramic precursor. A condensation reaction generates the ceramic precursor gel with CNTs incorporated within the matrix. The powder (dried gel containing CNTs) is subsequently calcined and sintered to give a CNT-ceramic matrix composite. Research on sol gel processing has concentrated on CNT-silica matrix largely because the sol gel processing of silicate systems is well established [117,118]. Seeger *et al.* [102,103] pioneered the use of sol gel processing for CNT-ceramic nanocomposite processing. They mixed MWCNTs with tetraethyl orthosilicate (TEOS, silicate precursor) and acidified water (catalyst) to generate a silica gel containing CNTs. The dried gel obtained was sintered at 1150 ^{o}C in argon producing well dispersed CNTs in the SiO_2 matrix.

Agglomeration is not entirely circumvented in sol gel processing, and other steps such as modification of the CNTs and use of surfactants have been explored prior to mixing CNTs with the liquid ceramic precursors. A further step has been to modify the CNTs with silica based organics (organosilanes) [119], which aims to improve the dispersion of CNTs in silicate based precursors. Chu *et al.* [105] also used sonication to aid the gelling process and at the same time take advantage of the mixing force of ultrasound. This resulted in a homogeneous dispersion of CNTs in the resultant ceramic matrix (figure 2-13) [105]. Sol gel has also been used to coat individual CNTs (figure 2-14) with the aim to improve dispersibility during further processing *i.e.* mixing with other powders prior to sintering. Examples of CNT coating with sol gel ceramic precursors include silica [120] [109], titania [121] and alumina [122]. The composite rods were used as reinforcing fibres in composites. Boccaccini *et al.* [123] used such rods to improve the dispersion of CNTs in borosilicate glass powders. The coated CNTs showed high thermal oxidation resistance of up to 1200 ^{o}C in air [123].

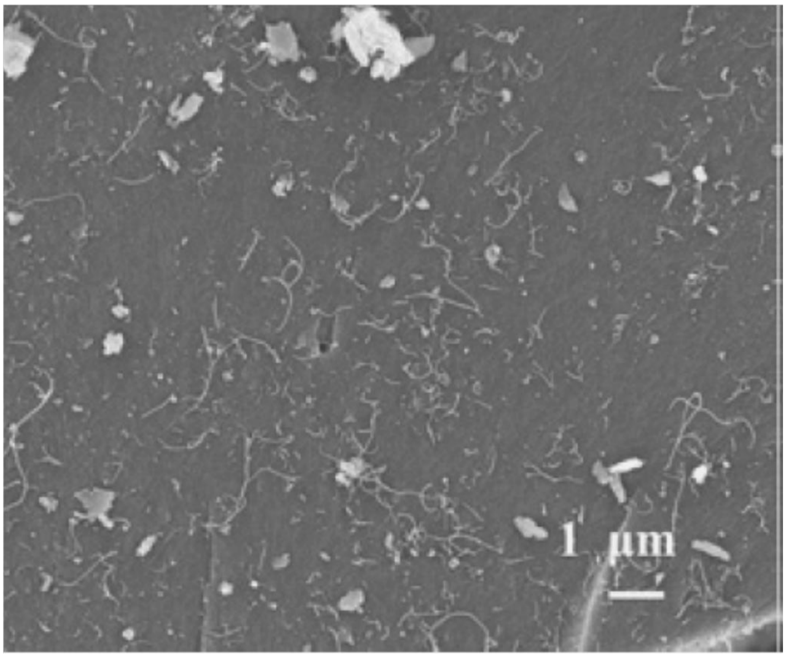

Figure 2-13 SEM image of fracture surface of a MWCNT/borosilicate glass composite produced by sol gel technique [105].

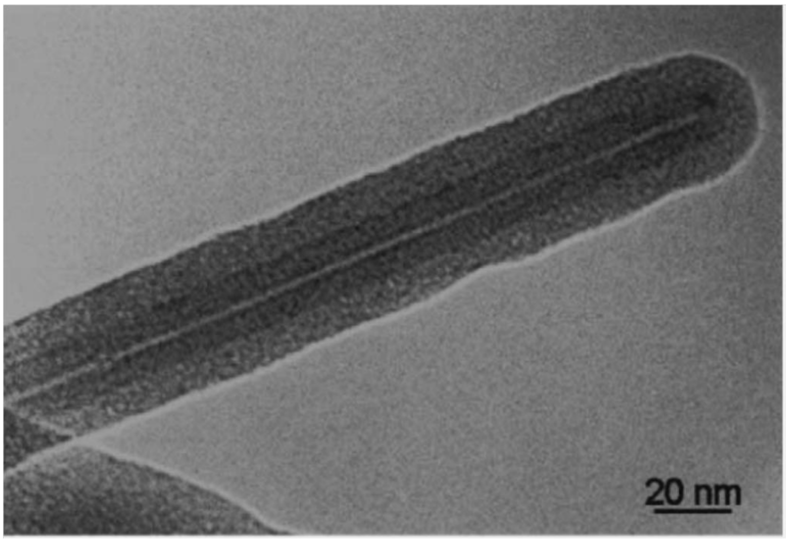

Figure 2-14 TEM image of silica coated CNT [102] by sol gel.

The justification for using colloidal chemistry for dispersion of CNTs is based on the fact that the ceramic particles in a suspension can be encouraged to coat the CNTs by altering the surface properties of both the CNTs and the ceramic particles. Using opposite surface charge for the CNTs and particles, the particles can coat the CNTs through heterocoagulation process. This requires chemical functionalisation of the CNTs which do not contain any surface charge in pristine form. Acid functionalisation is normally used whereby the acid attacks defect sites and CNT end caps reducing their lengths and introducing carboxyl groups on the CNT walls. These groups electrostatically stabilise CNTs in polar liquids by developing a negative surface charge. The coated CNTs are thus prevented from agglomerating due to reduced van der Waals forces [124,125,126]. The dispersion is either dried and sintered or incorporated in other matrices and sintered. An example of heterocoagulation was carried out by Fan *et al.* [84] who prepared Al_2O_3/0.5 wt.% SWCNT and Al_2O_3/1 wt.% SWCNT nanocomposites by colloidal dispersion of powders and hot pressing (1600 ^oC in argon at 20 MPa for 1 hour). The composites showed good CNT dispersion. CNT functionalisation can also be achieved by gas phase treatment process [127,128]. Surfactants and dispersants are often used to form stable colloidal suspensions containing both CNTs and ceramic particles. Examples of heterocoagulated CNT/ceramic powder are shown in figure 2-15a and b. Other ceramic particles that have been used in synthesis of composites via the surfactant route include Si_3N_4 and SiO_2. Figure 2.16 shows a fracture surface of a composite produced by heterocoagulation process of Al_2O_3 and 0.1% MWCNTs. The image exhibits homogeneously dispersed CNTs within the matrix hence demonstrating the success of such a process in producing CNT/ceramic composites.

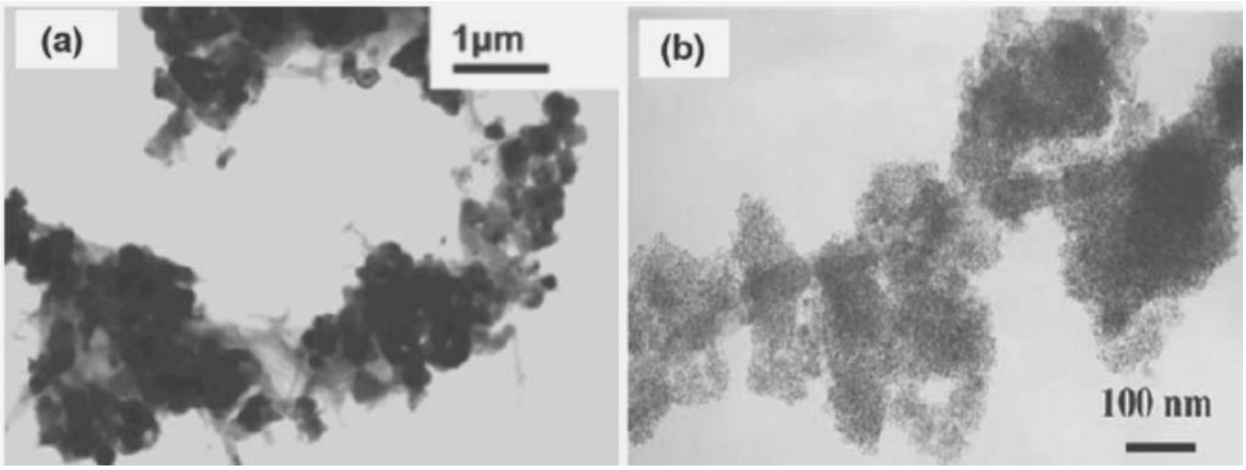

Figure 2-15 TEM images showing adsorption of (a) Al_2O_3 [82] and (b) TiO_2 [121] during heterocoagulation.

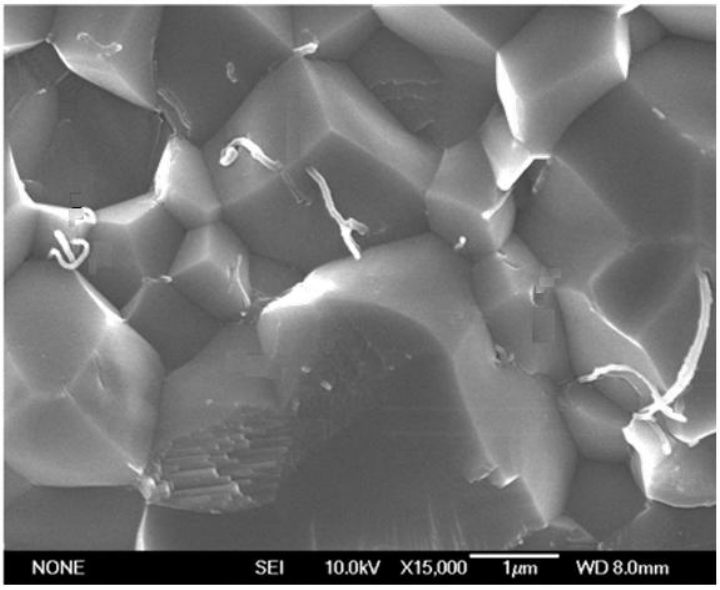

Figure 2-16 SEM of a fracture surface of sintered bulk made from Al_2O_3/0.1 wt.% CNT powder produced by heterocoagulation showing well dispersed CNTs [82].

2.5.2.3. *In-situ* Growth of CNTs in Ceramic Powders and Templates

Growth of CNTs in ceramic powders (Al_2O_3, MgO) impregnated with catalysts (Fe, Co) was first reported by Peigney and co-workers [129]. A CVD setup used for the production of CNTs was employed. The CNTs are grown within the ceramic powders which can be consolidated using the various techniques such as hot pressing, spark plasma sintering and high temperature extrusion [115]. The problem of agglomeration is still encountered with this type of *in-situ* growth of CNTs which results in undesired composite properties *e.g.* reduced fracture toughness when compared to parent matrices [130]. An *et al.* [131] also used this method to produce CNT ceramic nanocomposites and they observed modest improvement in the wear and mechanical properties of the nanocomposites.

Another method of obtaining CNTs within ceramic matrices *in-situ* is by spray pyrolysis during CVD growth of CNTs. Kamalakaran *et al.* [132] used a mixture of liquid carbon source (xylene) and catalyst (ferrocene) with alumina nanoparticles sprayed into a furnace at 1000^oC under argon atmosphere. The method has also been attempted with SiC powders [132]. This technique still results in agglomeration of CNTs leading to undesirable mechanical properties [132].

Using templates such as anodic aluminium oxide (AAO) for growing aligned CNTs within the regularly arrayed nano-channels of uniform length and diameter of the AAO was demonstrated by Xia *et al.* [133]. The anodised alumina containing arrays of parallel pores of 30-40 nm provided a template for CNT growth and thereafter acts as the matrix (figure 2-17). Xia *et al.* [133,134] used this method to grow CNTs of up to 20 μm in length which corresponded to the height of the anodised AAO. The catalyst nanoparticles were deposited in the pores of the AAO for CVD growth of CNTs within the nano-pores. They obtained aligned MWCNT/alumina composites which they used to demonstrate the toughening mechanisms observed in conventional micron size reinforced composites.

The *in-situ* methods are very attractive in that they involve relatively fewer processing steps, can be used for a variety of matrices and the process is scalable. The process has been used for other matrices such as TiN [135,136] and $BaTiO_3$ [137]. However there are several drawbacks to the processes which include i) the catalyst particles are inevitably included in the composites, ii) CVD process often results in some amorphous carbon that will not be removed from the composite; these two phases in the final composites can be undesirable during sintering and, iii) apart from the AAO templating technique, the other *in-situ* techniques mentioned do not result in homogeneously distributed CNTs in the composites.

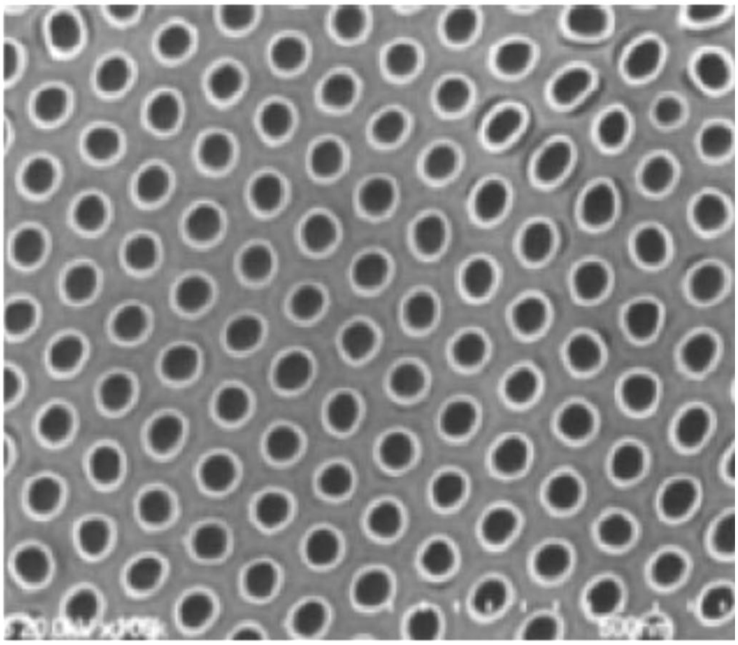

Figure 2-17 SEM image of a CNT/Al_2O_3 composite made by a template of anodised alumina [133].

2.5.2.4. Chemical Vapour Infiltration of a CNT Preform

Chemical vapour infiltration (CVI) is a method that is used to deposit material within a porous body usually made up of continuous fibres. Reactant gases diffuse into the preform and a deposit of matrix is obtained as a result of a chemical reaction occurring with the fibres. The infiltration is either by diffusion or exerted pressure. Using CVI, Chandrashekar [112] infiltrated a CNT preform that was obtained by CVD. Silane and dichloromethane were used as the matrix source resulting in polysilane and silicon nitride. The composite showed that, although the matrix coated the CNTs, there was no complete filling of the interstitial spaces and the composite appeared extremely porous (figure 2-18). This contributed to a reduced hardness for the composite compared to the matrix demonstrating that CVI technique is not suitable for infiltration of CNT preforms to obtain dense CNT/ceramic matrix composite.

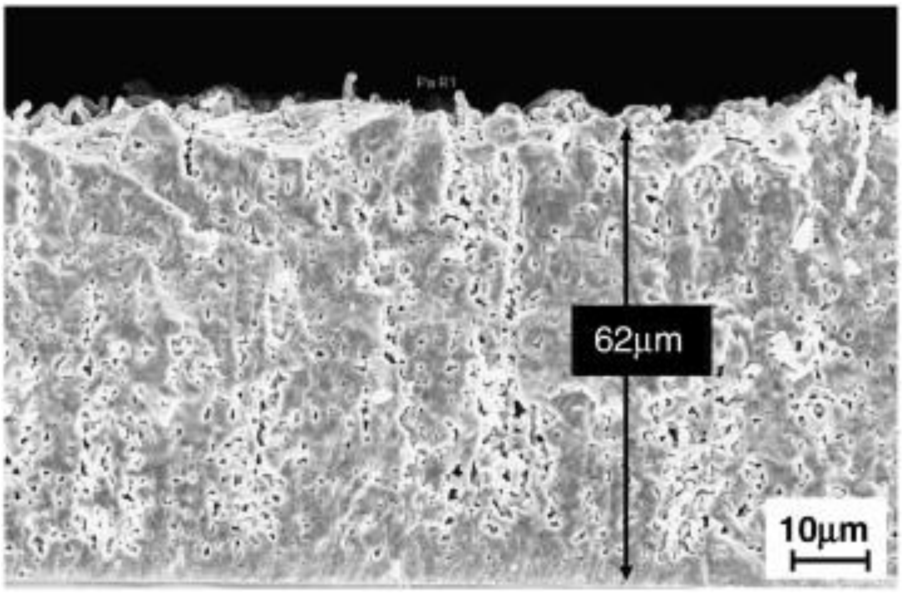

Figure 2-18 SEM image of a CNT carpet (62 µm CNT length) filled with poly-Si by chemical vapour infiltration [112].

2.5.2.5. Electrophoretic Deposition

Electrophoretic deposition (EPD) is a commonly used method in processing of ceramic coatings and composite materials [98]. EPD is achieved through movement of charged particles dispersed in a solvent under applied electric field. The motion of charged particles to an electrode results in a homogeneous rigid deposit. The technique can be applied to particulate solids of size < 30 μm and to colloidal suspensions [138]. The charge of the suspended solids can be modified by chemical reactions, adsorption of ions or by surfactants. Boccaccini *et al.* [139] have comprehensively reviewed the process of EPD of CNTs with ceramic matrices. The process of co-deposition of CNTs and ceramic nanoparticles is presented schematically in figure 2-19. Cho *et al.* [140] and Chicatun *et al.* [111] used EPD for co-deposition of CNTs with TiO_2 and SiO_2 nanoparticles for possible biomedical applications. In both cases [111,140], appropriate surface modifications were used to obtain CNT/ceramic nanoparticle suspensions for EPD. The composites showed homogeneously dispersed CNTs but were extremely porous. The authors did not sinter the composites, and did not measure any properties of the composite. EPD has also been used to produce hydroxyapatite/CNT composites [141,142] and CNT/Fe_3O_4 nanocrystal films for electronic device applications [143]. Overall, EPD is suitable for production of porous CNT/ceramic composites which is not desirable for applications where good mechanical properties are desirable.

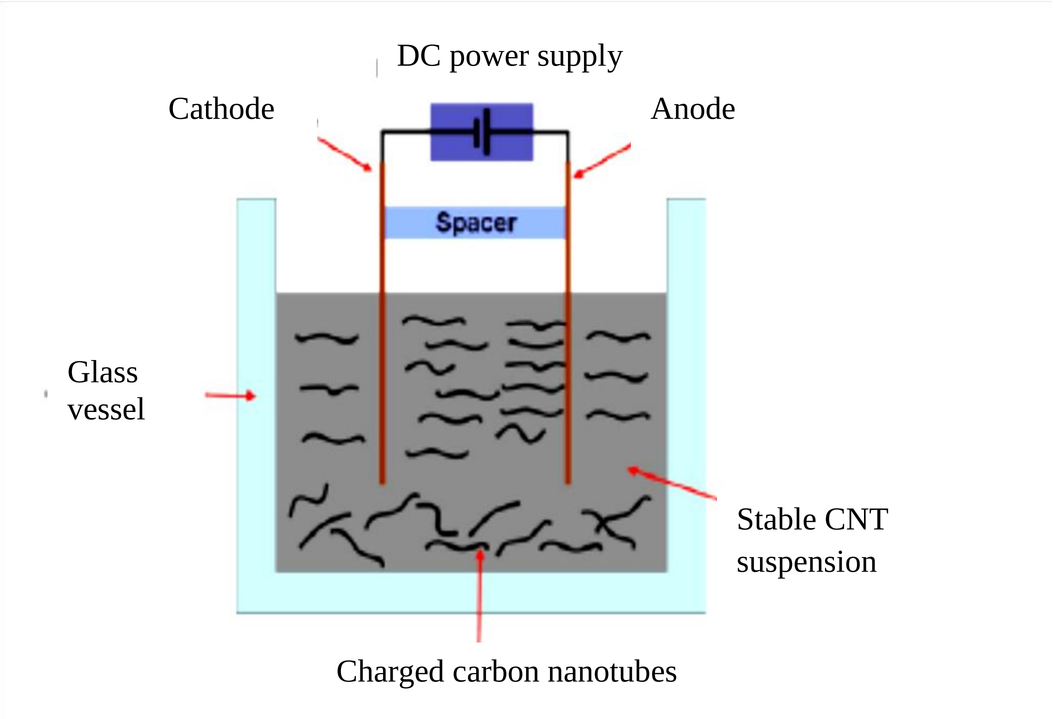

Figure 2-19 Schematic diagram of the electrophoretic deposition of CNTs [139].

2.5.3. Carbon Nanotube/Ceramic Composite Sintering Techniques

Conventional sintering methods for ceramics involve temperatures above 600 ^{o}C at which CNTs will oxidise if performed in air. Pressureless sintering, and hot isostatic pressing (HIP) of matrices containing CNTs have been shown to result in degraded CNTs [115,130]. Peigney *et al.* [115] found that most nanotubes were damaged during the preparation of the CNT-oxide composites by extruding at 1550 °C. Sintering in inert atmosphere of Ar and N_2 has been used widely to prevent degradation of CNTs in both pressureless and HIP processes. However, it is difficult to completely remove impurities and oxygen that will react with the CNTs during the consolidation process. Other than pressureless sintering and HIP, spark plasma sintering (SPS) is gaining favour with researchers due to the premise that shortened consolidation times allows less time for any reactions between impurities in the matrix and CNTs [144]. The process is touted to be more cost effective and offers higher productivity due to the shortened sintering times. A comparison of SPS and HIP [145] consolidation methods of CNT/Si_3N_4 is shown in figure 2-20. Improved density when SPS is used translates to improved mechanical properties *i.e.* hardness and fracture toughness.

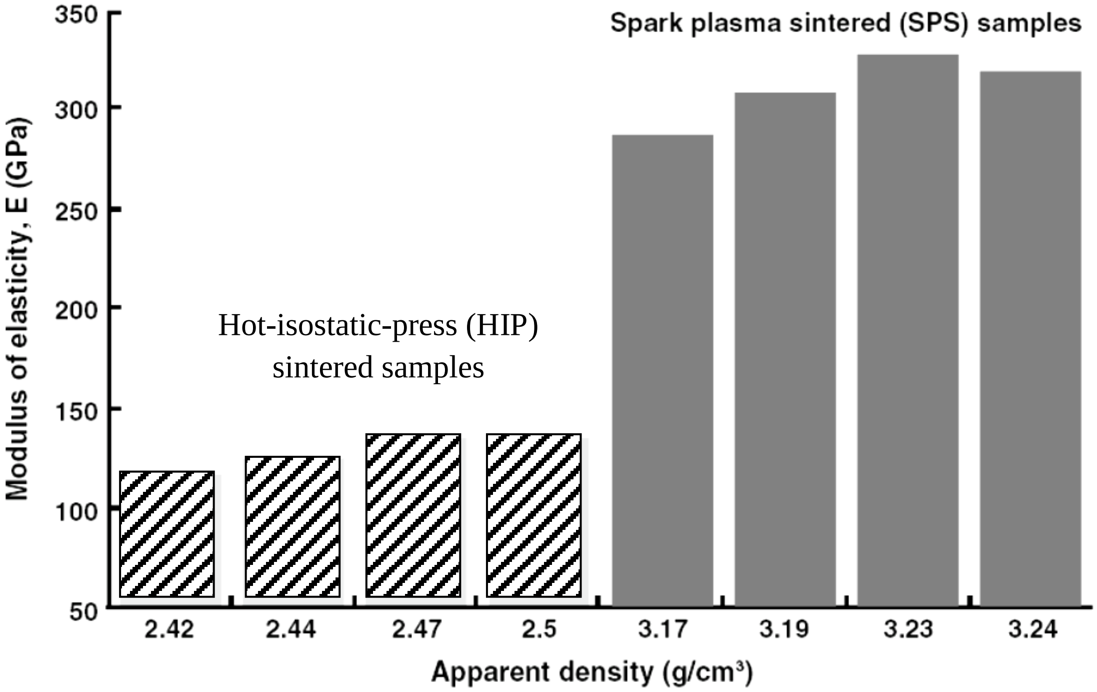

Figure 2-20 Modulus of elasticity of composites as a function of apparent density for 6wt.% MWCNT/Si_3N_4 produced by HIP and SPS. SPS results in 100% increase in modulus of elasticity compared to HIP [145].

2.6. Mechanical Properties of CNT/Ceramic composites

2.6.1. Quantitative Mechanical Properties

The most studied application for CNT/ceramic composites is the possibility of their use as structural materials with excellent toughness. Toughening in fibre reinforced composites is typically achieved by an interface that is weak enough to allow debonding of the matrix from the fibre and yet strong enough to allow load transfer from the matrix to the reinforcing phase [146]. Crack bridging (traction force on the cracks propagating around the fibre) and fibre pull-out (work needed to pull broken fibres against residual friction force at the fibre matrix interface) contribute to the fracture toughness of fibre/ceramic composites. A significant amount of research into quantitative determination of toughening in CNT/ceramic nanocomposites has focused on the measurement using indentation/crack length method. Two examples of groups that have used indentation/crack method are Zhan *et al.* [81] and Wang *et al.* [147]. Zhan *et al.* measured the fracture toughness in 10 wt.% SWCNTs/Al_2O_3 composites using the Vickers indentation technique and obtained fracture toughness of 9.7 MPa $m^{1/2}$ which is three times higher than pristine Al_2O_3. Wang *et al.* on the other hand questioned the validity of the results and performed comparative experiments and obtained no improvement in the fracture toughness [147]. They pointed out that shear deformation under the indenter because of CNTs may limit the cracking around the indenter resulting in artificially high fracture toughness values [147]. Berguiga *et al.* [148] reported 54 % and 69 % improvement in toughness for 0.025 and 0.05 wt.% CNT loading in Al_2O_3. The micro-hardness method used by Zhan [81], Wang [147] and Berguiga [148] for measuring fracture toughness (K_{IC}) is based on the concept that crack length at the applied load relates to the toughness (tougher materials will have shorter cracks). The relations are presented by the equation $K_{IC} = \alpha \left(\frac{E}{H}\right)^{1/2} . \left(\frac{P}{C^{3/2}}\right)$

where, E is the Young's modulus, H is the hardness, P is the applied load, C is the radial crack length and α is a constant depending on the geometry of the indenter. However, Wang *et al.* reported that the indentation crack length technique is not valid for CNT/ceramic composites [147]. They fabricated CNT-alumina composites using the procedure by Zhan *et al.* [81] and used the single-edge V-notched beam test (SENB) to obtain K_{IC}. The results obtained showed no improvement in K_{IC}. Wang *et al.* further carried out indentation tests on graphite alumina composites and observed that indentation behaviour is similar in the two materials, which they considered to bear out their hypothesis, thus demonstrating that addition of carbon allows shear deformation under the indenter [149]. They pointed out that the cracking is suppressed by the accommodation of the deformation around the indentation so that the apparent toughness is high.

Recently, a review of the Vickers indentation method has detailed its limitations in measuring fracture toughness [149]. The review concludes that Vickers indentations should not be used to obtain absolute K_{IC} because what Vickers indentation fracture toughness measures cannot be readily defined. Consequently, there has been an increasing number of publications [91,150,151,152] in the literature using edge notch beam test to measure the K_{IC} of CNT/ceramic composites. SENB however, is a more laborious process compared to indentation techniques. Several recent SENB results show improvement in fracture toughness but not as much as Zhan reported in [81]. An overall improvement in mechanical properties is observed with an increase in the CNT loading [83,91,147,153]. Yamamoto *et al.* [150] also compared the indentation and SENB results and obtained a significant difference between the two methods *i.e.* 6.64 and 5.90 MPa $m^{1/2}$ for indentation and SENB respectively for 0.9 vol.% CNT/alumina composites. Some selected CNT/ceramic composite mechanical properties together with the processing techniques is presented in table 2-3.

Since the microstructure and processing conditions affects the mechanical properties of ceramic matrices, comparison of only a few studies does not allow an evaluation to be made on the effect of different processing methods. It is difficult to separate the contribution of CNTs in the composite from processing induced property improvement which could be related to changes in microstructure induced by the CNTs. This problem highlights the difficulty of separating the intrinsic effects of the presence of CNTs from the processing related changes in matrix microstructure that they induce.

Table 2-3 shows several investigations on the effects of CNTs on the mechanical properties of Al_2O_3-based nanocomposites. However, there is little comparison between results since the test methods, processing techniques, CNT volume fraction and type of CNTs used are different. Overall, the Al_2O_3-based composites show modest improvements in the mechanical properties. For crystalline ceramics, CNTs have been shown to form networks at the grain boundaries. This often results in heterogeneous distribution of CNTs at grain boundaries, which in turn can strongly influence the mechanical properties [81]. In view of this, CNT glass matrices are of particular interest since there is no consideration of changes in microstructure such as grain sizes and boundaries. Several reports on CNT glass composites are available [83,93,123,148,154,155]. A good example is the report by Ning *et al.* [93] who provided images showing agglomerated CNT in the matrix but still observed an increase in the mechanical properties of the composite. This can be attributed to the crystallisation of the glass matrix [74]. Evidence of such crystallisation was observed by Guo *et al.* [154] who used colloidal processing method and SPS for consolidation at temperatures of 950-1050 ^{o}C hence lowering the sintering times but still observed cristobalite (crystalline SiO_2). The presence of cristobalite makes it difficult to interpret the Young's modulus and fracture toughness of 60.51 GPa and 2.74 MPa $m^{1/2}$ obtained. To avoid the occurrence of cristobalite, Chu *et al.* [105] produced 5 wt.% CNT/ aluminoborosilicate glass composites and obtained improvement in hardness of *ca.* 1 GPa over that of their pristine aluminoborosilicate glass (7.3 GPa). Mukhopadhyay *et al.* [91] studies on aluminoborosilicate glass provide good trends to summarise the properties improvement by CNTs on borosilicate glass. Both bending strength and fracture toughness increased to a maximum 10 wt.% CNT after which the properties deteriorated (figure 2-21a and b). This was attributed to agglomeration of CNTs at loadings above 10 wt.% [91]. Of course, it is expected that different systems (carbon nanotube and processing methods) will show improvement in mechanical properties after which there will be a decrease due to agglomeration effects. Other studies on borosilicate glass were carried out by Boccaccini and co-workers, who produced an 85 % dense composite of 10 wt.% MWCNT/borosilicate glass by hot pressing [94]. They observed agglomeration of CNTs on the fracture surface. The low densification coupled with agglomeration resulted in poor mechanical properties compared to unreinforced borosilicate glass.

Table 2-3 Overview of mechanical properties of CNT/ceramic matrix nanocomposites reported in the literature.

Matrix material	**CNT content**	**Processing routes**	**Investigated properties (%) indicates property improvement compared to monolith**	**Year**
Al_2O_3	SWCNT 10 vol.%	Powder processing	Fracture toughness (VI): 9.7 MPa $m^{1/2}$ (200%)	2002 [81]
Al_2O_3	SWCNT 10 vol.%	Powder processing	Fracture toughness (SENB): 3.33 MPa $m^{1/2}$ (3%)	2002 [147]
Al_2O_3	MWCNT 4 vol.%	Powder processing	Friction coefficient: 0.45 (-10%), Wear loss: 2 MPa $m^{1/2}$ (-45%)	2003 [131]
Al_2O_3	MWCNT 7 vol.%	Powder processing	Fracture toughness (SENB): 6.8 MPa $m^{1/2}$ (117%),	2008 [156]
Al_2O_3	MWNT 1 wt.%	Colloidal processing	Bending strength: (10%)	2005 [101]
Al_2O_3	MWCNT 12 vol.%	Colloidal processing	Fracture toughness (SENB): 5.55 MPa $m^{1/2}$ (80%)	2006 [120]
Al_2O_3	MWCNT 0.9 vol.%	Colloidal processing	Fracture toughness (SENB): 5.9 MPa $m^{1/2}$ (25%),6.64 MPa (41%), Bending strength: 689.6 MPa (27%) Bending strength: 490 MPa (44%)	2008 [150]

Al_2O_3	MWCNT 0.5 wt.%	*In-situ* CVD	Fracture toughness (VI): 4.62 MPa $m^{1/2}$ (12%), Hardness: 905.9VH (12%)	2008 [157]
Al_2O_3	MWCNT 10 vol.%	*In-situ* CVD	Frictional coefficient: 0.073 (-50%)	2008 [158]
Al_2O_3	MWCNT 1.5–3.3 vol.%	Sol-gel	Fracture toughness (VI): 1.1 MPa $m^{1/2}$ (10%)	2005 [159]
SiC	MWCNT 1–5 vol.%	Sol-gel method	Fracture toughness (VI): 5.4 MPa $m^{1/2}$ (12.5%), Hardness: 30.6 GPa (20%) with 5 vol.%	2007 [107]
Si_3N_4	MWCNT 1 wt.%	Powder processing	Bending strength: (37%)	2003 [121]
Si_3N_4	MWNT 1–5 vol.%	Colloidal processing	Decrease in both modulus and strength	2006 [145]
SiO_2	MWCNT 5–30 vol.%	Powder processing	Fracture toughness (VI): 2 MPa $m^{1/2}$ (100%), Bending strength: 85 MPa (65%) with 5 vol.%	2003 [93]
SiO_2	MWCNT 5 vol.%	Colloidal processing	Fracture toughness (VI): 2.46 MPa $m^{1/2}$ (146%), Bending strength: 97 MPa (88%)	2004 [83]

SiO_2	MWNT 10 vol.%	Colloidal processing	Fracture toughness (VI): 2.74 MPa $m^{1/2}$ (158%), Young's modulus: 43.89 MPa (38%)	2007 [154]
SiO_2	MWNT 5 vol.%	Colloidal processing	Work of fracture: 0.32 MPa $m^{1/2}$ (53%), Compressive strength: 6.1 MPa (33%)	2008 [155]
SiO_2	SWNT 0.05 wt.%	Sol-gel method	Fracture toughness (VI): 1.05 MPa $m^{1/2}$ (69%)	2008 [160]
SiO_2/ Al_2O_3/B_2O_3	MWCNT 2.5-15 wt.%	Sol-gel	Fracture toughness: 0 wt.% - 0.7 MPa $m^{1/2}$ (SEVNB) 10wt.%- 1.6 MPa $m^{1/2}$ 15 wt.%- 1.4 MPa $m^{1/2}$ Bending strength: 0 wt.% - 50 MPa (4 point bending) 10 wt.%- 96 MPa 15 wt.%- 70 MPa	2010 [91]
SiO_2	MWNT 6 wt.%	Sol-gel method	Hardness: 350Hv (100%)	2001 [109]

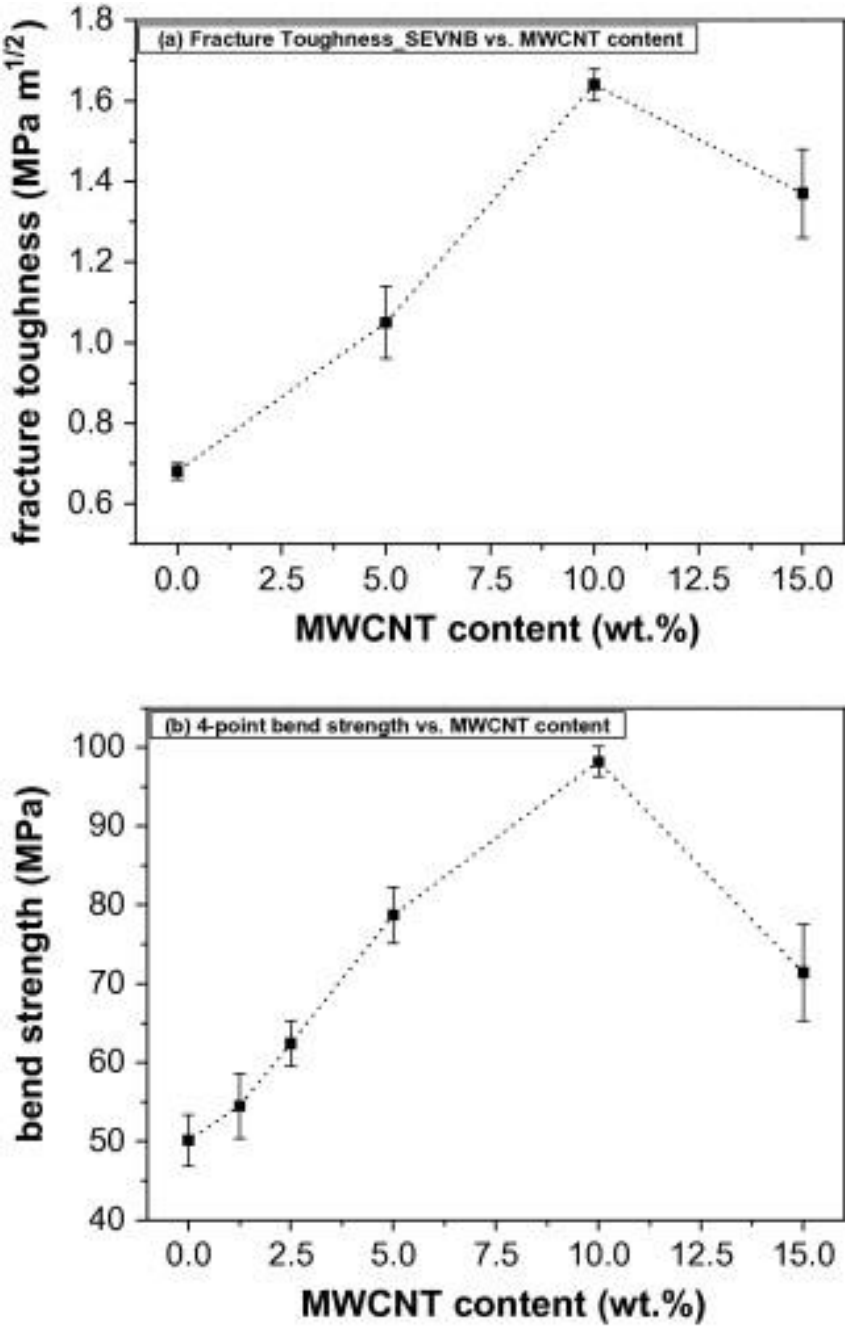

Figure 2-21 Variations of (a) fracture toughness (SEVNB) and (b) flexural strength (four-point bending) with MWCNT content in aluminoborosilicate glass [91]

The other aspect of interest is the tribological behaviour of the CNT ceramic composites. An *et al.* [131] used a silicon nitride sliding ball with 1 µm diamond slurry to measure wear resistance, and they observed that with increasing CNT content of up to 4 wt.% in alumina there was reduced wear loss, but the property deteriorated for higher CNT content. The same observation was obtained by Lim *et al.* [161] (figure 2-22) for hot pressed alumina/CNT composites. This was attributed to agglomeration of the CNTs at higher loading *i.e.*, the inability of the matrix to cover the CNTs' high surface area at such high CNT loading. At lower loadings, improvement in the wear properties was attributed to decrease in friction coefficient. This is due to the lubricating properties of CNTs which stem from the graphitic layers. As a result, there is possible rolling of CNTs between the composite interface and the counter-body. Other tribological studies using hydroxyapatite for biomedical applications were carried out by Balani *et al.* [162] and Chen *et al.* [163]. They observed an improvement in the wear resistance and a lower friction coefficient with increasing loading of CNT up to 20 wt.%. Xia *et al.* [158] carried out tribological tests on aligned CNTs/alumina composites and observed that larger diameter CNTs were more resistant to buckling in the axis direction and explained that the frictional coefficient of the composite was dependent on the buckling behaviour. Therefore, it follows that like graphite, introduction of CNTs in ceramic matrices improves the tribological properties by providing lubrication.

Zapata *et al.* [164] conducted creep tests on SWCNT/alumina composites in uniaxial compression and observed an improvement of two orders in creep resistance of the composite compared to pure alumina of the same grain size. In alumina, grain sliding is the dominant mechanism leading to creep deformation and in the composite SWCNT is thought to block the grain boundary sliding hence an improvement in the creep properties.

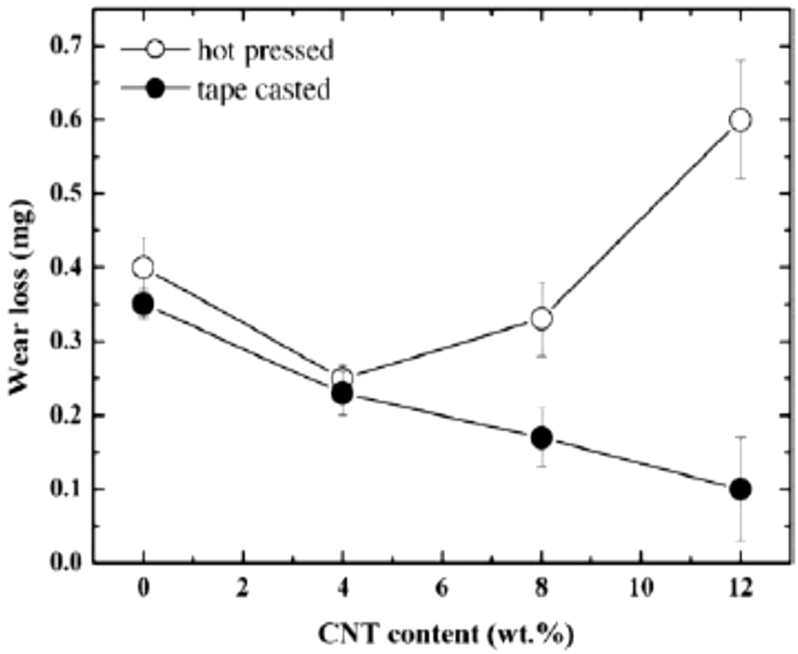

Figure 2-22 Variations of weight loss with CNT content for Al_2O_3/MWCNT nanocomposites [161].

2.6.2. Toughening Mechanisms in CNT/ Ceramic Composites

Quantitative determination of mechanical properties of CNT ceramic composites has not provided clear results. Several issues such as measuring methods and standards to be resolved are further complicated by the minimal results available in the field of CNT/ceramic composites. Moreover the results of improvement in mechanical properties do not directly link these improvements to the observed mechanisms involved. Toughening is often associated with crack bridging, crack deflection and fibre pull-out mechanisms that dissipate energy. Xia *et al.* [133] summarised these three processes known to micron-size fibre reinforced composites and provided an additional mechanism (shear deformation) that might be responsible for dissipating energy resulting in improved mechanical properties (figure 2-23). Xia *et* *al.* demonstrated CNT shear deformation (figure 2-24) and explained that this would also lead to improved toughness. However, their studies did not go as far as producing any quantitative results due to sample size limitations.

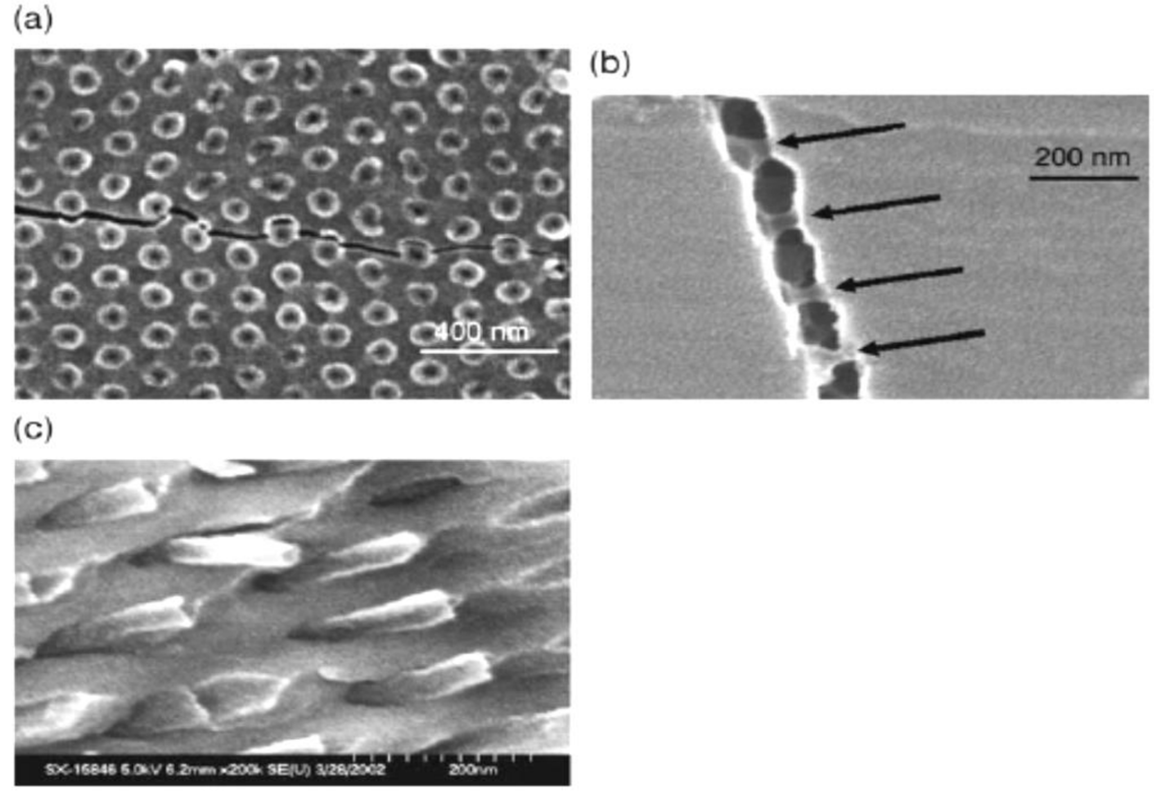

Figure 2-23 Scanning electron micrograph showing (a) crack intersection with successive alumina/MWCNT interfaces and deflection around the CNT along the interface; (b) CNT bridging the gap between crack surfaces and (c) apparent CNT pull-out [133].

Crack bridging by the CNTs provides traction that restrains the crack from opening thus reducing the driving force for crack propagation [91,133,165]. Energy is consumed in form of elastic strain energy due to fibre stretching caused by continued crack opening [91,165]. A significant development into the understanding of the toughening mechanisms of CNTs was done by Mukhopadhyay *et al.* [91]. They showed that in glass matrices, CNT crack bridging was the prominent mechanism leading to fracture toughness. They observed that CNTs bridged cracks of up to 100 nm and debonding of the matrix from the CNTs did not occur at the actual CNT/glass interface, but away in the matrix. The same study also showed that debonding of the fibres did not occur at the actual CNT/borosilicate glass interface but away from the interface. The contribution to pull-out was shown to be minimal due to the short pulled out CNTs (*ca.* 100 nm) observed on fracture surfaces. Cho *et al.* [166] later carried out a similar study on a similar composite system to Mukhopadhyay *et al.* [91] and obtained an improvement in toughness which they attributed to pull-out and debonding. The pull-outs observed on the fracture surfaces in both studies are in the nanometre range and any frictional forces will only be effective over these short lengths. Therefore, it is less likely that contribution from pull-out will be significant as observed by Mukhopadhyay *et al.* [91].

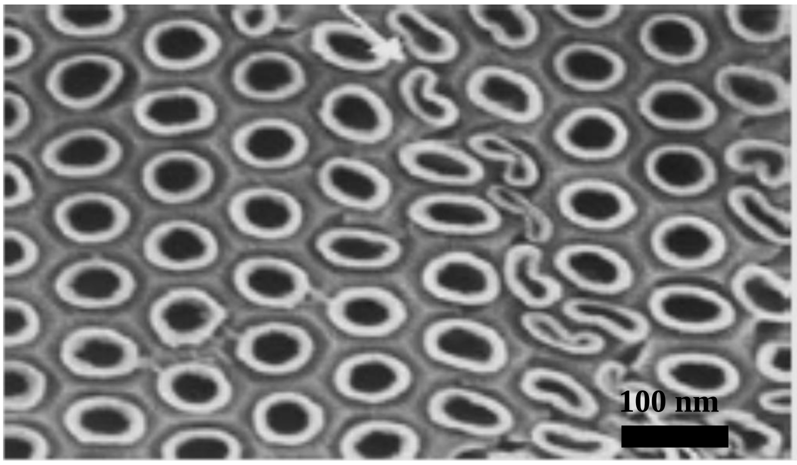

Figure 2-24 SEM micrograph showing collapse of CNTs into shear bands (indicated by arrows) [133].

Another possible toughening mechanism unique to MWCNTs is the sword-in-sheath failure mechanism. Each concentric graphitic wall making the MWCNT fails at a length away from the previous concentric graphitic wall along the length of the

MWCNT, *i.e.*, in a sword-in-sheath manner, thus sometimes termed ‘sword-in-sheath toughening mechanism’. We have previously showed that aligned CNTs/glass composite show significant pull-outs and sword-in-sheath of up to 1 µm in length [114]. Even though sword-in-sheath mechanism has previously been observed [57], its possible contribution to toughening composites has not been investigated. It worth noting that Mukhopadhyay [91] and Cho [166] did not report any sword-in-sheath failure mechanism unlike in our study [114], which suggests that aligning CNTs in a composite activates sword-in-sheath toughening mechanism.

2.7. Electrical, Dielectric and Thermal Properties

2.7.1. Electrical and Dielectric Properties

Since CNTs have been shown to have very high electrical and thermal conductivities, there have been several investigations towards fabricating functional CNT/ceramic nanocomposites in order to take advantage of these properties. Studies have shown that the electrical conductivity of CNT/ceramic composites depends greatly on the processing route. Flahaut *et al.* [130] used catalytic CVD to fabricate Fe-Al_2O_3/CNT composite powders. The powders were hot pressed at 1500 ^oC and 43 MPa for 15 minutes. The electrical conductivities for 8.5 vol.% and 10 vol.% CNT nanocomposites were 40-80 and 280-400 Sm^{-1} respectively. The resulting composite was 88.7% dense and the elevated hot pressing temperatures caused structural damage to the CNTs thereby yielding lower electrical conductivity results. Mukherjee *et al.* [81] prepared 5.7, 10 and 15 vol.% CNT/Al_2O_3 composites by ball milling the SWCNTs with alumina nanopowders and consolidation using SPS at 1150-1200 ^oC for three minutes. They observed that addition of 5.7 vol.% SWNT improved the electrical conductivity from ~10-12 Sm^{-1} to 1050 Sm^{-1} and they obtained 3345 Sm^{-1} for 15 vol.%. The sudden increase in the electrical conductivities was attributed to the retention of the structural integrity of the CNTs at lower sintering temperatures by SPS. Yamamoto *et al.* [150] prepared 0.9, 1.9 and 3.7 vol.% MWCNT/Al_2O_3 by ultrasonic dispersion of acid treated CNTs in ethanol. This was followed by addition of aluminium hydroxide to the solution with continued sonication. The resulting powder was consolidated using SPS at 1500 ^oC and 20 MPa pressure for ten minutes. The composite was fully dense but the electrical conductivities obtained (0.0013, 1.3 and 65.3 S m^{-1} respectively) were low due to the high sintering temperatures which damaged the CNTs. Contrary to reports on improvement in electrical properties, a study by Huang and Gao showed that the electrical conductivity of MWCNT/$BaTiO_3$ composite decreased up to MWCNT content of 3 wt.% [137]. This observation was attributed to formation of Schottky barrier at the CNT/matrix interface [137]. Overall, these reports suggest that processing methods, together with the type of matrix greatly affects the electrical properties of the composites.

The measured percolation threshold for electrical conductivity in CNT/ceramic composites ranges from 0.64 - 4.7 vol.%. This depends on the type of ceramic matrix and the processing route employed [82,83]. Peigney *et al.* investigated the percolation behaviour of $MgAl_2O_3$/CNT composites containing 0.2-25 vol.% CNT [95]. The composites were prepared by catalytic chemical vapour deposition and the consolidation of the powders was done by hot pressing at 1300 ^oC. They obtained a percolation threshold of 0.64 vol.% (0.31 wt.%) where the electrical conductivity increased by over seven orders of magnitude. Another similar study on percolation properties was carried out by Shi and Liang [167] on 3Y-TZP (3 mol.% yttria-stabilised tetragonal polycrystalline zirconia)/MWCNT composites. They fabricated the composites by ball milling 3Y-TZP with MWCNT and consolidated the powders SPS at 1250 ^oC and 60 MPa and obtained a percolation threshold of 4.7 vol.% (1.7 wt.%). Shi and Liang [167] also observed that the dielectric constant also increased by about two orders of magnitude near the percolation threshold which they attributed to polarisation effect of CNT clusters resulting in increased electric charge storage, hence an improvement in the dielectric constant [168]. Note worthy also is the study by Ahmad *et al.* who studied the electrical and dielectric properties of Al_2O_3/MWCNT prepared by SPS at 1350 ^oC [96]. A percolation threshold of 0.79 vol.% was obtained. They further observed that the dielectric constant reached 5000 in low frequency region by addition of 1.74 vol.% MWCNTs. Mukhopadhyay *et al.* [97] recently studied the percolation threshold of randomly orientated MWCNTs dispersed in borosilicate glass matrix, where the powders were obtained by sol-gel processing and consolidation was done by hot pressing at 950 ^oC and 25 MPa. Electrical percolation was achieved with 2.5 MWCNT wt.% with the electrical conductivity of up to 2.1 Sm^{-1} for a 15 wt.% CNT content (figure 2-25) [97]. From these observations, it appears that the percolation in ceramic depends on the matrix material and as previously discussed, on the processing method of the composite.

The electromagnetic shielding properties of CNTs stem from their good electrical conductivity. The introduction of CNTs to ceramic matrices is an easy way of improving their electromagnetic interference (EMI) properties. Several studies report on the EMI shielding properties of CNT/polymer composites [169,170], however, there is very little work reported on EMI properties of CNT ceramic composites. Xiang *et al.* fabricated MWCNT/SiO_2 by hot pressing and studied their EMI shielding properties [171]. They observed that the EMI shielding effectiveness (SE) of the composites improved with increasing CNT content. They obtained the highest SE of 66 dB at 34

GHz with 10 vol.% MWCNT/SiO_2 composite. The observed improvement in the SE is primarily attributed to the increase in the electrical conductivity of the composites. Xiang *et al.* [171] compared the CNT composites with carbon black (CB) and obtained that at 10 vol.% CB/SiO_2 and 34 GHz, the SE was only 10 dB. In conclusion, the EMI properties of ceramics can be altered by addition of CNTs which have good EM absorption characteristics.

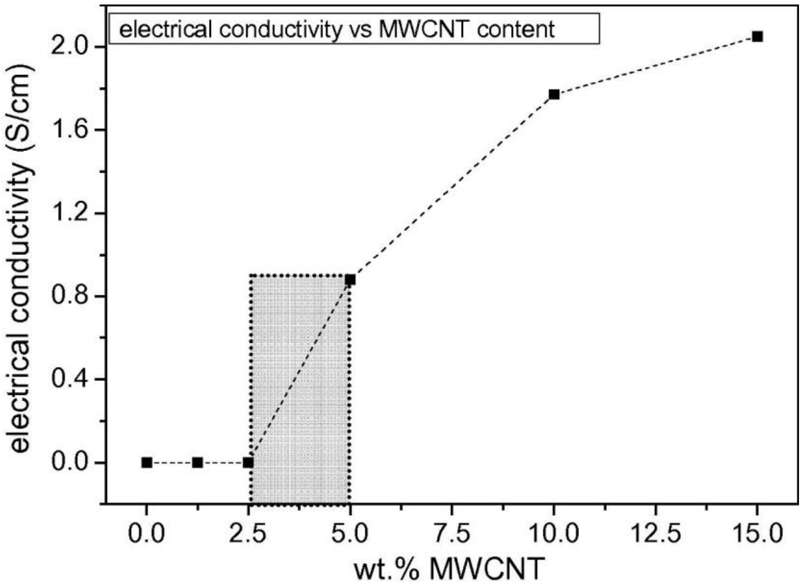

Figure 2-25 Variation of dc conductivity with different CNT loading in the MWCNT/borosilicate glass composite [97].

2.7.2. Thermal Properties

Since CNTs have very high thermal conductivity along the axis because phonons propagate easily along the tube with very little scattering, they have been investigated for improving ceramic matrix thermal properties. Just like in electrical conductivity, a thermal percolation network is expected to enhance heat flow within a CNT/ceramic composite. However, the measured thermal conductivity for such composites is much lower than the predicted values from the volume fractions and available thermal conductivity of CNTs. The enhancement of the thermal properties is considerably lower than that of electrical properties [172,173]. It is well understood that the interface between the CNT and matrix plays an important role in thermal conduction. The formation of Kapitza contact resistance at the CNT-ceramic matrix interface [174,175] explains the low thermal conductivity properties obtained. In a percolating network, the resistance at the nanotube-ceramic and nanotube-nanotube contact points act as blocking and scattering sites of phonons. Huxtable *et al.* [176] used molecular dynamics simulations to demonstrate that thermal transport in CNT composites is restricted by a small interface thermal conductance hence the thermal conductivity of the composite is lower than estimated or expected values. Table 2-3 shows the modest improvement in the thermal conductivity obtained from MWCNTs/SiO_2 composites prepared by ball milling and SPS at 950-1050 ^{o}C for 5 and ten minutes [172]. The highest room temperature thermal conductivity of 4.08 $Wm^{-1}K^{-1}$ was obtained for 10 vol.% MWCNT/SiO_2, which is a 65% improvement compared to pure SiO_2.

Table 2-4 SPS processing conditions of SiO_2/MWCNT nanocomposites and their relative densities, grain sizes and thermal conductivities measured at room temperature [172].

Materials	**Processing conditions (°C/MPa/min)**	**Relative density (%)**	**Grain size (nm)**	**Thermal conductivity ($Wm^{-1}K^{-1}$)**
Pure SiO_2	950/50/5	100	–	2.42 ± 0.16
Pure SiO_2	1050/50/5	100	–	2.47 ± 0.05
5 vol.% MWCNT/SiO_2	950/50/5	100	21.08	3.36 ± 0.02
5 vol.% MWCNT/SiO_2	950/50/10	100	21.08	3.41 ± 0.02
5 vol.% MWCNT/SiO_2	1050/50/5	100	21.92	3.45 ± 0.01
5 vol.% MWCNT/SiO_2	1050/50/10	100	21.92	3.48 ± 0.01
10 vol.% MWCNT/SiO_2	950/50/5	100	21.08	3.67 ± 0.02
10 vol.% MWCNT/SiO_2	950/50/10	100	18.78	3.62 ± 0.05
10 vol.% MWCNT/SiO_2	1050/50/5	100	21.08	3.97 ± 0.04
10 vol.% MWCNT/SiO_2	1050/50/10	100	22.12	4.08 ± 0.01

Table 2-4 summarises a trend that increasing the CNT content in the matrix results in increasing thermal conductivity, approximately doubling that of pure silica matrix at 10 vol.% CNT content. Mukhopadhyay *et al.* [97] also carried out similar studies on MWCNT/aluminoborosilicate glass composite and obtained improvement of up to 70 % in thermal conductivity with 15 wt.% CNT content compared to 1.3 $Wm^{-1}K^{-1}$ obtained for pristine aluminoborosilicate glass. The study by Mukhopadhyay *et al.* [97] also showed that the thermal diffusivity and conductivity increased with increasing CNT content especially above 5 wt.% MWCNT content. It is difficult to obtain an objective comparison between the relatively few studies in the literature on improvements in thermal properties by CNTs in ceramic matrices. Improvements observed are still very modest compared to the individual measured thermal conductivity of CNTs (3000 $Wm^{-1}K^{-1}$) [70,71] and those of CNT mats, 35 $Wm^{-1}K^{-1}$ [72]. However, like in electrical properties, it is highly likely that for randomly orientated CNTs in ceramic matrices, interfacial resistance, type of CNTs (including defect density and length), the type of matrix (which also contributes to thermal conductivity) and processing methods will affect the thermal properties of a CNT/ceramic composite.

2.8. Alignment of Carbon Nanotubes in Ceramic Matrices

The alignment of CNTs in a matrix is of great importance especially when load is borne parallel to the CNTs. From this review, it is evident that randomly orientated CNTs embedded in ceramics only show improvements that are a fraction compared to the full potential of properties that CNTs exhibit. CNTs are extremely strong in bending and like carbon fibres could be very useful when arranged in a uniaxial direction [5]. Also, from this review, it is observed that there has been very little research in aligning CNTs in ceramic matrices. This is because of processing limitations when dealing with ceramics unlike *e.g.* polymers where alignment can be achieved by various methods including, microtoming, filtering, using magnets, extrusion, flow orientation and even mechanical stretching. Most of these methods are not available when processing ceramics. For those available to ceramics, the complexity of material processing makes them difficult to use. The methods for alignment of CNTs in ceramics include extrusion [115], electrophoretic deposition [112], low vapour pressure infiltration (CVI) [112] of CNT preforms and growth of CNTs in templates. Other than *in-situ* growth of CNTs in template and CVI infiltration of CNT templates [135,136,137], the extrusion and electrophoretic deposition methods lead to discontinuous CNTs in a matrix. This is because the processing involves dispersion of CNTs which also further limits the weight fraction to low percentages. To obtain continuous CNTs within a matrix, templating using anodic alumina as previously described was used. This method is limited by the thickness of the template which determines the length of the CNT composite achievable. Therefore, the CNTs are continuous but relatively limited in length, typically hundreds of micrometers [133]. The infiltration technique offers the best route to obtaining long continuous CNTs in a ceramic matrix. The CNTs are produced as aligned preforms and are infiltrated with the desired ceramic matrix by several available routes. As ceramics have relatively high melting points, melt infiltration is difficult to achieve and there are no reports of this. Another infiltration technique is chemical vapour infiltration that was first used on CNTs by Chandrasekhar [112]. The drawback to this method is that it produces porous and non-uniformly infiltrated preform [112].

Other than these two attempts, there has been no progress in making continuous aligned CNTs in ceramic matrices. Furthermore, these studies only looked into the hardness of the composites due to sample size limitations. The data generated was mainly qualitative thus not giving any insight into the possible property improvements achievable by incorporating aligned CNTs in ceramic matrices. The next section introduces a novel technique for producing aligned CNTs in ceramics in a simple, repeatable and consistent manner.

2.9. Conclusion and Scope

This work has reviewed several methods of production of CNT/ceramic composites with mixed results in the performance of the composites. Ongoing research on the processing techniques will provide better understanding to the methods and lead to improved fabrication techniques. The general challenges that need addressing include the following;

a) obtaining good dispersions at high CNT loading that might lead to improved properties. This is however coupled with the likelihood of difficulty in obtaining fully dense composites at such loadings.

b) the lack of control and understanding of the interface between the CNT and the ceramic matrices. The experience of micron-size reinforced ceramics shows that the interface will be crucial in understanding the mechanical behaviour of CNT/ceramic composites. However, in CNT/ceramic nanocomposites, the interface behaviour is expected to be significantly different from conventional carbon fibre ceramic composites due to the unique chemical structure of the CNTs.

c) an effective technique in production of aligned CNT/ceramic composite that is scalable in order to take advantage of the axial properties of the CNTs in load bearing and transport applications.

CNTs offer tremendous opportunity for development of advanced functional materials, but until such bottle necks are cleared, their applications will remain limited. Several researchers have reported improvements in CNT-based composite systems properties. On application of the CNT/ceramic composites, there are several areas which could be explored. One possibility of critical importance is heat dissipation in electronic devices such as mobile phones which limits the reliability of the devices. Such commercial products require composite materials with multifunctional properties. CNT/ceramic nanocomposites produced also have potential applications in thermal management areas such as thermal interface materials for electronic devices. In high power situations, inorganic matrices may offer improved stability compared with current systems. For optical applications, sol-gel techniques have been employed to produce transparent and structural composites containing low volume fractions of fibres. To date, there are several commercial applications on the market although they are still limited in view of the potential CNTs offer. This is partly due to the low production yield of CNTs and the cost of CNTs leaving much to be done through technological innovations. For commercialisation of CNT/ceramic composites, the fabrication and consolidation methods will have to be cost effective.

2.10. Novel Approach to Aligned CNT/Glass Composite via Sol Gel Processing

Fabrication of aligned CNT/ceramic composites using sol gel processing employs infiltration of the interstices between aligned CNTs preforms with a pre-ceramic sol. This approach eliminates issues of dispersion and the final composite consists of aligned CNTs in a ceramic matrix. The approach taken in the present study was to first produce CNTs several millimetres in length using chemical vapour deposition techniques. CVD was chosen as it is the only method that gives aligned as-produced CNTs. These macroscopic structures are easy to handle and provide structures that can be tested mechanically by conventional methods. The production of CNT preforms was based on previous research [46] which was optimised to generate long continuous CNTs on substrates. The need to obtain well aligned, clean CNTs that required no further processing was achieved by controlling various growth parameters. An infiltration technique using sol gel was used to fill the interstices of the CNT preforms. Aluminoborosilicate glass which can be processed via sol gel was investigated as a model matrix material. The borosilicate sol that gave the matrix used was based on previous research and was selected because of its low sintering temperature [117]. These methods allowed for less complicated set up and quick infiltration procedures while preserving the alignment of the CNTs in the matrix. CNT walls functionalisation is circumvented in such a process. This processing method eliminates dispersion steps commonly encountered with other processing methods. Consolidation of the composite was by hot pressing leading to a well densified material.

The composites produced are expected to have electrical and thermal properties close to those of the CNTs in the direction of alignment. This eliminates problems of percolation for electrical conductivity and Kapitza contact resistance in thermal conductivity encountered in randomly orientated composites. Due to alignment and continuity, the electrical and thermal properties of individual CNTs are expected to be maximised in the composites. At the same time, in the direction of CNT alignment in the composite, the CNTs will be expected to show good load carrying ability due to their excellent mechanical properties.

CHAPTER 3

Materials and Materials Characterization

3.0. Overview

This chapter will describe the methods used to produce aligned carbon nanotube (ACNT) preforms, aluminoborosilicate (ABS) sol and the ACNT/ABS glass composite and the characterisation techniques employed at different stages. Section 3.1 discusses the production of materials while 3.2 describes the different imaging and chemical characterisation techniques. Section 3.3 explores the mechanical property testing methods. Finally section 3.4 looks into the details of measuring transport properties of the composite, ABS and ACNT preforms.

3.1. Materials

3.1.1. Production of Aligned Carbon Nanotube Preforms

Aligned CNTs (ACNTs) were grown on quartz substrates by a floating catalyst aerosol CVD setup schematically shown in figure 3-1 adopted from A. Koos and N. Grobert [46,177]. The set up is made up of four sections as follows;

i) the aerosol generator unit which consists of a piezoelectric ceramic that produces an aerosol/mist.
ii) the furnace section where the aerosol is decomposed and the CNTs grow
iii) gas flow control unit that monitors the flow of the aerosol into the furnace

iv) an exhaust section at the end of the setup is used to stop any particulates and gases escaping into the air/atmosphere.

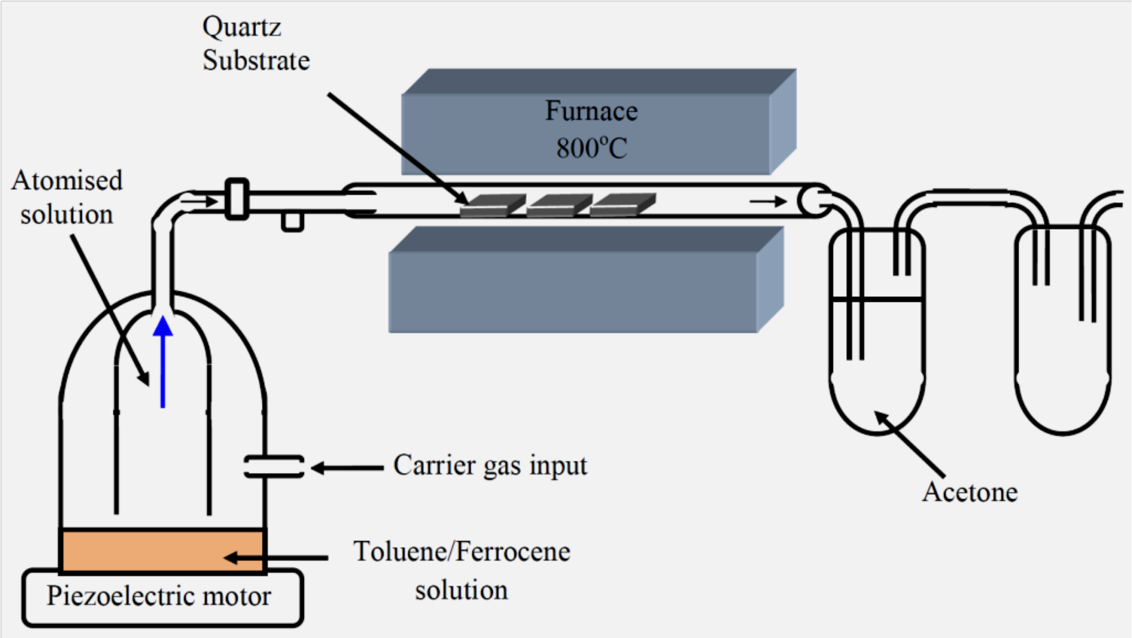

Figure 3-1 A schematic of the aerosol assisted CVD setup used.

A typical experiment is done using a quartz tube of 2.2 cm inner diameter inside a 50 cm long horizontal tube furnace. The quartz tube is loaded with rectangular quartz substrates of 20x10 mm. A solution of 5 wt% ferrocene (Fe $[C_5H_5]_2$, Aldrich 98%, the iron catalyst precursor) in toluene ($[C_6H_5CH_3]$, Aldrich, the carbon source) was put in the aerosol generator unit. One end of the quartz tube was connected to the aerosol generator and the exhaust pipe connected at the opposite end. The unit was purged with argon gas for 5 minutes before the furnace was turned on. The experiments were carried out at 800 °C with Ar as the carrier gas for the aerosol into the quartz tube. The Ar flow rate was 1000 standard cubic centimetres per minute (sccm) for varying durations of 1 hour to 12 hours. At the end of the experiment, the flow rate was reduced to 100 sccm while the furnace was left to cool to 200 ^{o}C. The quartz substrates were then collected for CNT preform harvesting.

To remove the CNT preforms from the substrates, two approaches were employed; i) mechanical lift-out and ii) acid assisted ACNT preform lift-off. Mechanical lift out involves a thin wire wedged at one end of the preform/quartz substrate interface which is forced through to separate the CNT preform from the quartz substrate. For acid assisted lift-off, the ability of hydrofluoric acid (HF) to dissolve quartz was employed. The quartz substrates with attached CNTs were dipped in concentrated HF and left for 30seconds. The preforms were collected and washed with distilled water repeatedly until the water was neutral when tested with a litmus paper. The aligned nanotube preforms were dried in a furnace at 200 ^{o}C for 12 hours.

3.1.2. Sol Gel Precursor Materials

The ABS sol was prepared by a modification of the method by Chiou and Thomas [117]. An initial solution was prepared by mixing 4.7 ml tetraethyl orthosilicate ($Si[OC_2H_5]_2$) with 2.25 ml of 4 M aluminium trisecbutoxide ($Al[OCH(CH_3)C_2H_5]_3$) forming a clear solution. A second solution was prepared by mixing 4.7 ml ethanol with 1 ml of 2 M sodium acetate (NaO_2CH_3), 0.7 ml of trimethyl borate ($B[OCH_3]_3$), 0.5 ml 67% nitric acid (catalyst) and 0.5 ml of distilled water resulting in a clear solution. Subsequently, the first solution was slowly added to the second solution with stirring. The sol is expected to yield aluminoborosilicate glass with 63 wt.% SiO_2, 24 wt% Al_2O_3, 10 wt% B_2O_3 and 3 wt% Na_2O.

3.1.3. Infiltration and Drying

Infiltration of the sol into the ACNTs preforms was achieved by placing them in a shallow sol bath with *ca.* 1/5th of the preform height immersed. To speed the infiltration, the setup was placed in a flask and evacuated to create a vacuum. The sol was left to gel and dry within the interstices of the ACNT at room temperature for 12 h. The gel infiltrated ACNT was further dried at 350 °C in air for 3 h to remove the organics. Multiple infiltrations were applied in order to increase the amount of matrix introduced in the interstices.

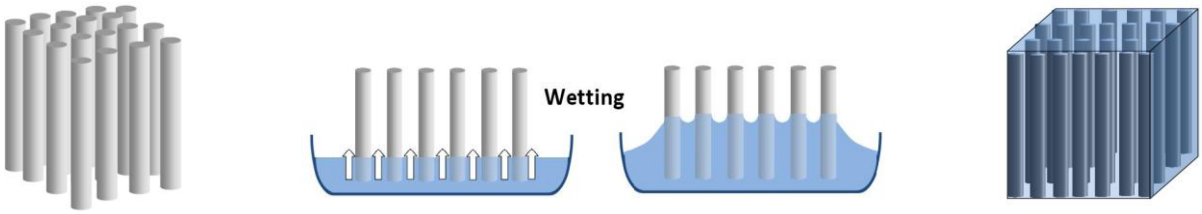

Figure 3-2 Schematic of the sol infiltration process

3.1.4. Sintering

Pressureless sintering was performed on sol infiltrated preforms in a tube furnace with flowing argon at temperatures of 1100 ^{o}C. Hot pressing was also used to consolidate the dried sol infiltrated preforms. The process provides both heat and pressure simultaneously to sinter and mold the dried gel infiltrated ACNT preforms. The hot press used is shown schematically in figure 3-3. It is made up of an induction heating coil around a graphite die. The die is surrounded by fiber insulation and a steel covering enclosure which is water-cooled. There are gas inlets and outlets to feed in argon gas to prevent oxidation of the insulation, graphite die and the sample. A hydraulic press is used to apply the pressure typically of 25 MPa. An alternating current is supplied to the induction heating coil inducing a current in the die. This leads to a temperature increase which is measured using a thermocouple touching the graphite die. The temperature used for sintering was 1100 °C and a holding time of 10 minutes. A typical experiment would involve loading several sol infiltrated ACNT preforms separated by glass matrix in the graphite die with the alignment of the nanotubes perpendicular to the direction of applied pressure. Several samples could be hot pressed at the same time using separating graphite spacers within the same die. With each hot press, an ABS glass sample (blank) was also produced from a powder made from dried sol for comparison.

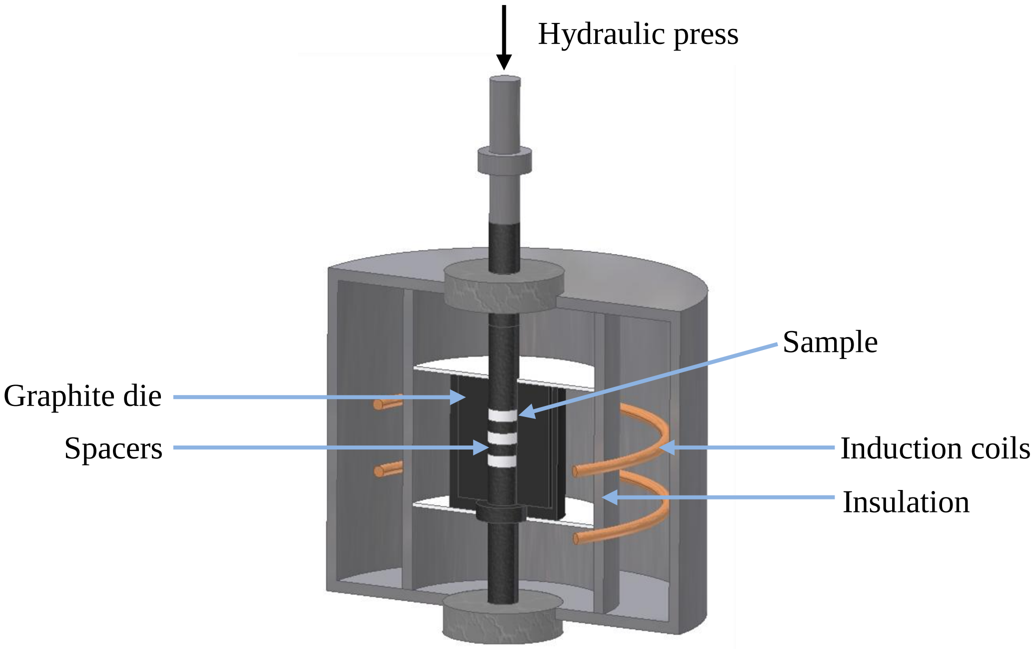

Figure 3-3 Schematic of the hot press machine used [178]

3.1.5. Polishing and Platinum Coating

For testing and analysis of the hot pressed materials, sample size reduction and polishing was necessary. Cutting of the samples was done using a slow saw fitted with diamond cutting blade. The slow saw ensured little chipping and clean cuts on the surface and edges. Grinding was done on steel plates with 25 μm diamond paste purchased from Kemet (UK) Ltd. Polishing was carried out sequentially with 9 μm, 6 μm, 3 μm and 1 μm diamond polishing pastes on cloth purchased from Kemet Ltd. In order to avoid charging of samples such as glass when viewed under a scanning electron microscope (SEM), a 3 nm layer of platinum was sputtered onto the surface of interest. Charging results in regions of very high brightness obscuring the features on the sample.

3.1.6. Focused Ion Beam Milling and Polishing

Other than polishing using diamond pastes, a different method of removing material is focused ion beam milling (FIB). This method is commonly used to prepare polished samples for SEM and electron transparent membranes for transmission electron microscopy (TEM).

The focused ion beam instruments used are based on Gallium ions form impinging on a sample knocking off atoms on the surface. The Gallium source is liquid Ga in a reservoir which flow to a needle tip. A large negative bias between the tip and extractor electrodes causes field emission of the Ga^+. The ions form a cone of ca. 5 nm at the tip with ca. 2 μA current. The Ga^+ beam then passes through apertures to further define the exact current to be used for milling. Objective lenses are used to obtain a focused beam on the sample. Scanning coils are used to move the beam on the surface of the sample and thus provide images by detecting ions or secondary electrons from the sample. The knocking off of atoms *i.e.* milling, can be used to generate predefined features on a sample. This occurs when the Ga^+ ions interact with the sample in an elastic manner causing atoms to be ejected from the sample. In this research, ACNT/ABS composite and ABS glass were milled to produce samples for mechanical testing and microstructural investigation using electron microscopes. Two different FIB systems were used. The FEI FIB200, which was operated at 30 kV with beam currents of 1pA to 20 nA. The resolution of the beam is 10 nm. The FEI FIB200 was used to produce polished cross sections for microstructural investigations and production of cantilever beams for bend tests. The Zeiss NVision 40 FIB instrument which has both an SEM and a FIB column tilted by 54^o to each other, and a resolution of 4nm was used for transmission electron microscopy sample preparation. This FIB instrument is also equipped with a gas injection system for deposition of materials e.g. platinum. Sample preparation on the Zeiss NVision instrument was carried out by Dr. Gareth Hughes at Department of Materials, University of Oxford.

3.2. Microstructural and Chemical Characterisation

3.2.1. Scanning Electron Microscopy

As SEM is a standard microscopy technique, details of the operations will not be given here and can be found in several texts e.g. Physical principles of electron microscopy by Egerton R.F. [179]. Two scanning electron microscopes were used in all the work presented in this thesis namely JEOL 840F and JEOL 6500 both with field emission guns for electron sources. Secondary electron imaging mode was used during standard image acquisition. The microscopes were operated at either 5 keV or 10 keV. For the ACNT preforms, as produced material was placed on aluminium stub and imaged. For the composites, polished samples or fractured surfaces were stuck onto an aluminium stub using an electrically conducting double sided tape. ABS glass samples were coated with a 3 nm Pt coating while the CNT preforms and the composites did not require Pt coating.

3.2.2. Transmission Electron Microscopy

TEM was used to obtain the diameters of the nanotubes and probe into the finer details of the microstructure of the nanotubes and the composites. Features such as iron inclusions in the inner core of a nanotube and the graphitic walls of the nanotubes making up the preform can be obtained. The basic working of a TEM involves an electron beam transmitted through a sample that is typically less than 100 nm in thickness within a vacuum system. The transmitted electrons produce a projection of the sample. Two proprietary transmission electron microscopes namely a JEOL 2000FX and a JEOL 4000 were used to obtain TEM images at typical electron accelerating voltages of 200 keV and 400 keV respectively. The TEM sample preparation for the nanotubes involved breaking the preform by sonicating in ethanol before dropping the solution containing CNTs onto a carbon grid for imaging. For the composite, a sample was crushed using a mortar and pestle and the powder put on a TEM grid for imaging. This method is quick and easy to perform but it is damaging to the samples.

Another TEM sample preparation involved using focused ion beam (FIB) milling on polished samples. This technique enables site specific selection for TEM sample preparation. Furthermore, the method allows for choice in the direction of milling with reference to the alignment of the nanotubes in the composite *i.e.* either transverse or axial direction. The samples were prepared using the Zeiss NVision 40 FIB. Briefly, the TEM sample preparation was performed as follows; a region of interest was selected and coated by 1 µm platinum to protect it from ion milling. This was followed by milling trenches on either side of the platinum coated region to a depth of 5 μm leaving approximately a 3 μm thin membrane in the bulk material. The stage was then tilted to 45° to allow an undercut of the milled membrane leaving a suspended membrane. These milling steps were typically done at 7000 pA at 30 keV acceleration voltage. The suspended membrane was cut off from one end and welded using platinum on to a micromanipulator. The opposite end of the membrane was cut loose and the membrane was now fully attached to the micromanipulator. The membrane was then transferred to a TEM grid by welding the free end and cutting off the end fixed to the micromanipulator. Further thinning using currents of 300 pA to 100 pA was carried out leaving a membrane of less than 100 nm on the grid for TEM imaging. TEM studies on JEOL 4000 were carried out by Dr. Antal Koos of the Department of Materials at University of Oxford.

3.2.3. Raman Microspectroscopy

Raman microspectroscopy is the most widely used and generally the first tool for characterising CNTs. It relies on the inelastic scattering of light by molecules and provides information about the vibrational and rotational nature of the molecules causing the scattering. The four main peaks or groups of peaks in a Raman spectrum shown in figure 3-4 are used to evaluate CNTs. These include, the radial breathing modes (RBM), the defect induced D-band, the tangential graphitic band (G-band) and the G'-band that is an overtone of the D-band [180]. The RBM are observed between 150-350 cm^{-1} and the frequency of the RBM is related inversely to the diameter of the nanotubes. These modes are usually not observed for MWCNTs. The G peak appears at 1600 cm^{-1} and is generally used in conjunction with the D peak to give the relative defect density of the nanotubes produced as a ratio D/G. The larger the ratio the more the defects present in the nanotube. The G peak has also been used for determination of alignment of the nanotubes with the peak being highest when the CNTs are parallel to the incident beam and lower when CNTs are perpendicular to the incident beam [181]. A distinction between metallic and semiconducting CNTs can also be made using the G-peak [182]. The D band appears between 1250 cm^{-1} and 1450 cm^{-1} and is a result of defects in the CNTs. A corresponding overtone of this peak is appears between 2500 cm^{-1} and 2900 cm^{-1} (G' band). These four bands are characteristic for CNTs and make Raman spectroscopy an indispensible first characterisation tool for determining the quality and nature of CNTs. The Raman spectra presented in this thesis were taken using a JY Horiba Labram 300 Aramis imaging Raman microscope. The samples were cut off sections of ACNT's or fractured composite placed on a glass slide. A helium/neon laser (632 nm) was used to record at least three spectra for each sample.

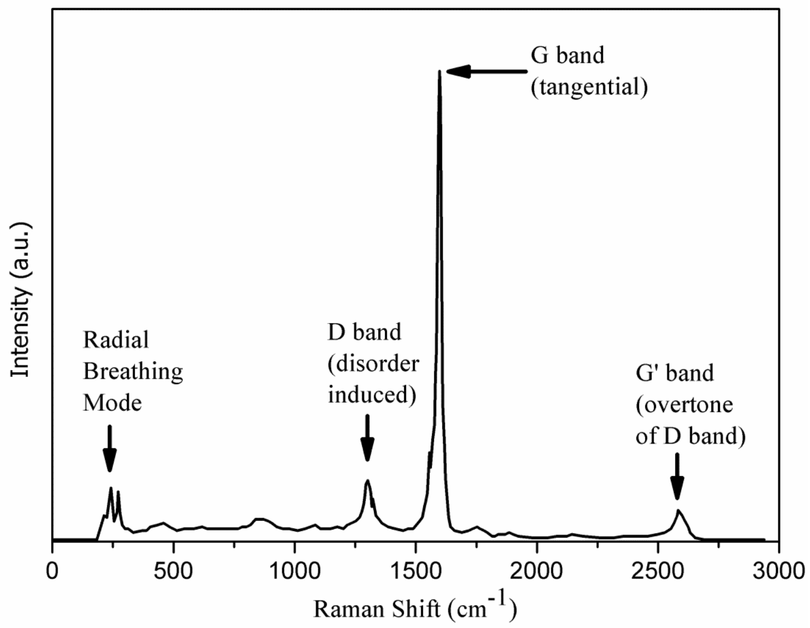

Figure 3-4 An idealised Raman spectrum of a carbon nanotube

3.2.4. Thermogravimetric Analysis

Thermogravimetric analysis (TGA) is a technique that allows weighing of a sample as function of temperature and/or time during heating process. In TGA a sample is heated to a target temperature using a desired heating rate while recording the masses at specific temperatures. The experiments can also be carried out in inert gas atmospheres. TGA experiments were performed on a Perkin Elmer Pyris 7.0 instrument (U. K.). The runs consisted of a ramp at a steady rate of 50 °C/min, from 50 to 850 °C under air. In this thesis, TGA was used to determine the amount of non-carbonaceous material present in the ACNT preforms produced, which are classified as impurities. The oxidation resistance of the nanotubes (the highest temperature the CNTs can withstand prior to burn out) was also determined using TGA.

3.2.5. Energy Dispersive X-ray Spectroscopy

Energy dispersive X-ray spectroscopy (EDX) is a chemical microanalysis technique used in conjunction with SEM and TEM. The technique works as follows; during imaging, the electron beam bombarding a sample ejects electrons from the atoms that make up the sample leaving holes. The holes are filled by electrons from higher energy states of the atoms. In the process x-rays are emitted to balance the energy between the two quantised electronic states. Each x-ray photon is therefore characteristic of the element from which it was emitted. The x-rays are collected by a detector and analysed for the energies and count leading to an elemental composition of the sample by comparison with known characteristic energy values. The EDX system used was an Oxford Instruments Inca Energy system. In this thesis, the elemental composition of the bulk composite was confirmed using EDX.

3.2.6. Electron Energy Loss Spectroscopy

Electron energy loss spectroscopy (EELS) is another elemental analysis technique that works by measuring the loss in kinetic energy of electrons after interacting with a sample. This technique in conjunction with TEM provides local (atomic) information about the structure along with the chemical composition of a solid sample. The details of the operation of EELS are given by RF Egerton [183]. In this study, EELS was used to study chemical composition at the interface between CNTs and the matrix after sintering process. The system used in the experiments is composed of a Gatan image filter that is capable of chemical analysis using EELS within a JEOL JEM-3000F TEM instrument. All the EELS experiments were carried out by Dr. Rebecca Nicholls of the Department of Materials, University of Oxford.

3.3. Mechanical Property Characterization

This section describes three different methods used to measure the mechanical response of the ACNT, ABS glass and the ACNT/glass composites. Indentation studies are described in section 3.3.1, compression testing described in section 3.3.2 and finally a bend test method using microcantilevers is described in section 3.3.3.

3.3.1. Indentation studies

An indentation study quantifies a material’s resistance to plastic deformation when placed under a load. Measuring mechanical properties by imprinting an indenter describes the hardness of the material. The indentation hardness test can be divided into two categories: microindentation and nanoindentation synonymous with the size of the indent imprinted which is a consequence of the size of the load used.

3.3.1.1. Microindentation

Microindentation hardness testing measures the hardness of a material on a microscopic scale with the size of the indentations produced by a dead load typically between 1 N to 10 N. The length of the impression produced is usually measured with a microscope. The load and the impression lengths are then used to calculate the hardness of the material under test. The indentations were made using a square based pyramid indenter (AVK-C1/C2, Mitutoyo) on polished samples and loads applied were 10 N for 5 seconds.

3.3.1.2. Nanoindentation

A nanoindenter, unlike the microindentation test, applies and measures the load and displacement into the test material continuously during the test. One advantage of using a nanoindenter is that by using a depth sensing indenter and known indenter geometry, no microscope imaging is required for calculation of hardness and stiffness of the test sample. An example of the load-displacement graph from a nanoindenter is shown in figure 3-5.

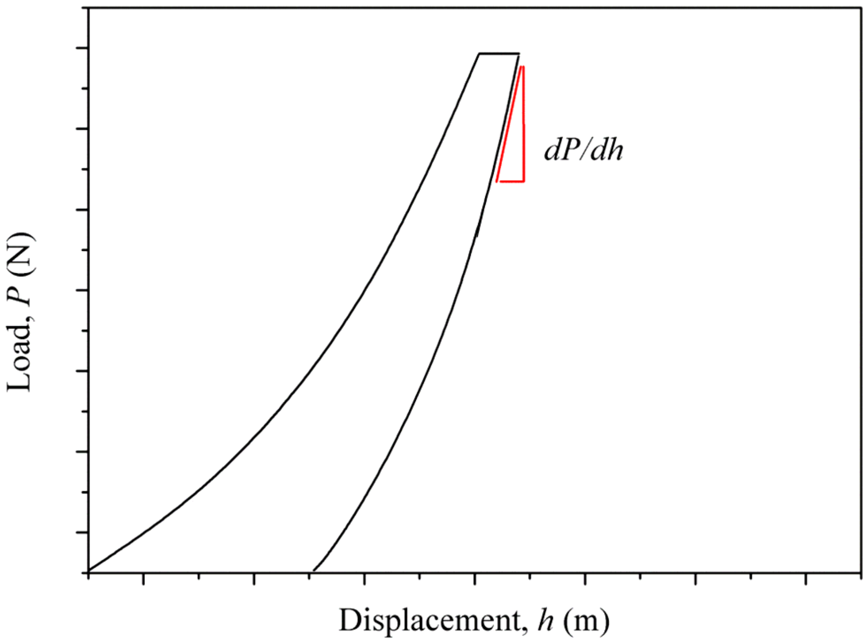

Figure 3-5 A typical load-displacement graph obtained from a nanoindentation test.

There are two different types of results reported by nanoindenter: 1) The hardness and modulus over a defined range is based on continuous stiffness and hardness readings and are not covered in this thesis, and 2) the hardness and modulus from unload which is based on the unloading stiffness and are calculated based on equations by Oliver-Pharr [184].

$$S = \frac{dP}{dH} = \frac{2E_r\sqrt{A\beta}}{\sqrt{\pi}} \qquad \text{Equation 3.1}$$

Where:

S = measured stiffness of the upper portion of the unloading curve

A = projected contact area at a given indenter depth

E_r = reduced modulus

β = correction factor which is 1.034 for Berkovich indenter

The indenter contact area was calculated using $A = 24.5h_{\max}^2$ for a perfect Berkovich indenter.

The Hardness from unloading is calculated using the following equation [185]:

$$H = \frac{P_{\max}}{A} \qquad \text{Equation 3.2}$$

where H, P_{max} and A are hardness, maximum load and the area of the indent.

This hardness definition is different from conventional hardness definition. In the nanoindentation analysis the hardness is calculated utilizing the contact area at maximum load whereas in conventional tests the area of the residual indent after unloading is used.

Nanoindentations experiments were performed using a depth sensing Berkovich indenter instrument (XP MTS NanoInstruments) at room temperature to;

a. obtain the Young's modulus and hardness for ABS glass and ACNT/ABS composites in two different CNT orientations *i.e.* indenter parallel to and perpendicular to the CNT alignment in the composite.
b. perform bend test on cantilever beams which are discussed in section 3.3.3 and 5.3. The nanoindenter was used to apply a constant loading rate on cantilever beams while the load was measured leading a load-displacement curve.

3.3.2. Compression Testing

Compression testing is a technique used to determine the behaviour of materials under compressive loading. The tests are performed on a universal mechanical testing instrument whereby the specimen is loaded between two plates. A force is then applied to the sample by moving the crossheads together. The force is recorded against deformation and this is used to obtain a compressive yield stress and compressive modulus of elasticity. The stress, σ, is obtained by dividing the applied force, *F* by the cross sectional area, *A*. The strain, ε, is the change in length of the sample Δl divided by the length of the sample, *l*.

$$\sigma = \frac{F}{A} \text{ and } \varepsilon = \frac{\Delta l}{l} \qquad \text{Equation 3.3}$$

The samples in this research were tested using a universal testing machine (Mains U.K.) with a 3 kN load cell. The samples were cuboids, with dimension of *ca.* 2 mm. The glass and composite samples were cut using a precision diamond saw and polished on all 6 faces. The ACNT compression samples were produced from 2 mm long ACNT preforms which were cut to shape and size using a razor blade. The testing for the CNT/ABS composite and the CNTs were done with the force applied parallel to the alignment direction of the nanotubes as shown in figure 3-6.

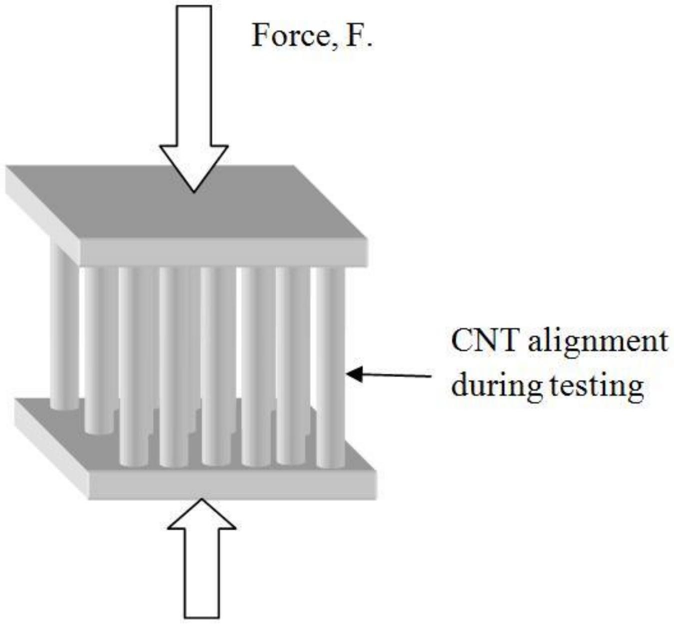

Figure 3-6 Schematic of compression testing with respect to the orientation of the carbon nanotube alignment

3.3.3. Cantilever Beams

A beam can be defined as a structure which is loaded with forces acting transversely to the length. The loads can either be point loads or uniformly distributed along the beam. Loading in the transverse direction leads to stresses in the beams from the bending action of the loads. Since this thesis is concerned with cantilever beams *i.e.* a beam fixed at one end and free at the other end (figure 3-7a), examples and formulations will be demonstrated with such beams. On loading a cantilever beam, one section of the beam will experience tension while the other compression as schematically represented in figure 3-7b. Cantilever beams will normally bend to form a curve when a force F is applied causing a bending moment M. The bending moment at any point along the beam is calculated as

$$M = F(L-x) \qquad \text{Equation 3.4}$$

where L is the length of the cantilever beam and x is the distance between the fixed end and the point being considered.

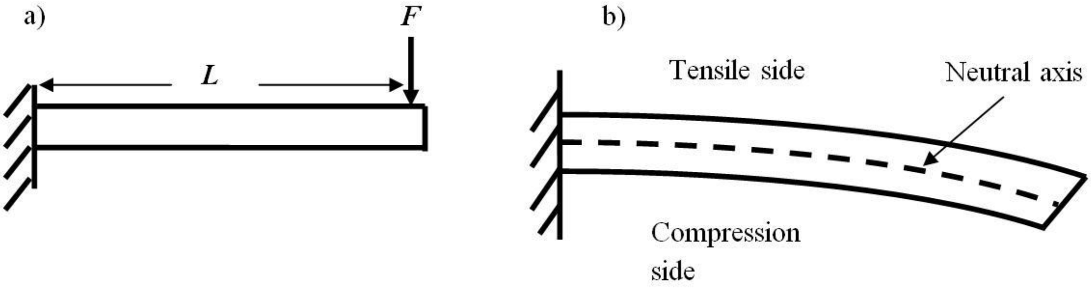

Figure 3-7 Sketches of cantilever beams showing a) an unloaded cantilever beam and b) loaded beam with a curvature and tensile and compression sides.

The general formula that describes bending of beams is given below and can be found in several books such as Roaks Formulas for Stress and Strain [186].

$$\frac{M}{I} = \frac{\sigma}{\delta} = \frac{E}{R} \qquad \text{Equation 3.5}$$

Where M is the moment, R is the radius of curvature, I is the second moment of area, E is the elastic modulus, σ is the stress and $\boldsymbol{\delta}$ is the distance from the neutral axis measured normal to the length of beam. The stress distributions have the maximum tensile stress on the top and maximum compressive stress on the bottom and the stress is zero at the neutral axis. In this research, the beams used were of triangular cross sections (figure 3-8) of height, *h,* and width, *w,* milled out of bulk composite or glass material using FIB. The triangular geometry was selected over those of square or rectangular cross-sections due to the complexity involved in FIB milling of microcantilever beams of these geometries *i.e.* square and rectangular cross-section. Due to the triangular shape, the neutral axis is at 2/3 the height (*h*) from the apex [187] of the cantilever beam shown in figure 3-8.

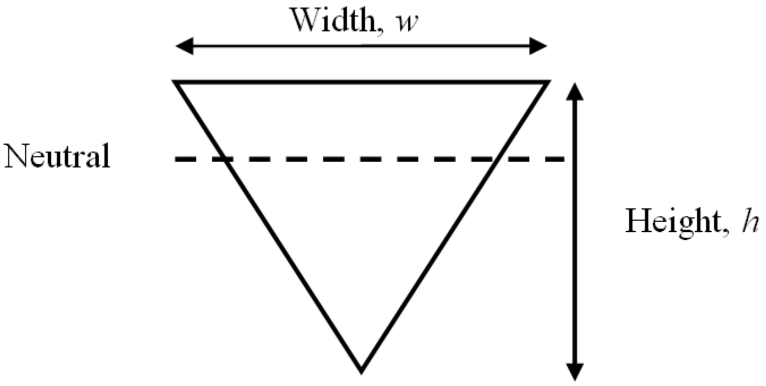

Figure 3-8 Cross section of cantilever beams fabricated for bend tests.

On loading the cantilever beam, the beam curvature, R, is approximately equal to the second derivative of the neutral axis *i.e.* $R = \frac{dx^2}{d^2y}$ (*y* is the beam deflection).

Equation 3.5 can be rearranged to $\frac{1}{R}=\frac{M}{EI}$. Replacing $\frac{1}{R}$ with $\frac{d^2y}{dx^2}$ the rearranged equation 3.5 gives

$$M = EI\,\frac{d^2y}{dx^2} \qquad \text{Equation 3.6}$$

Equating equations 3.4 and 3.6 gives equation 3.7 which is a second order differential equation.

$$F(L-x) = EI\,\frac{d^2y}{dx^2} \qquad \text{Equation 3.7}$$

Using appropriate boundary conditions, equation 3.7 is integrated twice to obtain the deflection of the beam at different points along its length as follows;

$$EI\,\frac{dy}{dx} = FLx - \frac{Fx^2}{2} + A \qquad \text{Equation 3.8}$$

Applying the boundary condition that the gradient is horizontal, $\frac{dy}{dx}=0$ at *x=0,* gives *A=0.*

$$EIy = \frac{FLx^2}{2} - \frac{Fx^3}{6} + B \qquad \text{Equation 3.9}$$

Applying boundary condition such as, when there is no deflection at *y=0,* x= *0,* gives *B=0.*

Equation 3.9 can be rearranged to

$$y = \frac{Fx^2}{6EI}(3L-x) \qquad \text{Equation 3.10}$$

Deflection at free end, y_o, when *x=L* is given by

$$y_o = \frac{FL^3}{3EI} \qquad \text{Equation 3.11}$$

Inserting I (the second moment of area for a triangular shape = $\frac{wh^3}{36}$) into equation 3.11 gives

$$y_o = F \times \frac{12L^3}{Ewh^3} \qquad \text{Equation 3.12}$$

Rearranged to give

$$E = \frac{F}{y_o} \times \frac{12L^3}{wh^3} \qquad \text{Equation 3.13}$$

This equation relates elastic modulus to measurable quantities such as load, *F*, displacement, *y*, and beam dimensions *L*, *w* and *h*.

From equation 3.5

$$\sigma = \frac{My}{I} \qquad \text{Equation 3.14}$$

The maximum compressive stress occurs at $y = -\frac{2}{3}h$, while the maximum tensile stress occurs at $y = +\frac{1}{3}h$. Since the compressive stress is twice that of the tensile, the tensile stress is labelled σ_{min}. The σ_{min} on a cantilever beam failing on the tensile side (figure 3-7b) is obtained by replacing *M with FL*, *I with* $\frac{wh^3}{36}$, and $y = +\frac{1}{3}h$, giving;

$$\sigma_{\min} = \frac{36FL}{wh^3}\left(\frac{1}{3}h\right) = \frac{12FL}{wh^2} \qquad \text{Equation 3.15}$$

If a load is applied near the free end of the cantilever beam until failure while recording load and the displacement, equations 3.13 and 3.15 can be used to obtain elastic modulus and the minimum stress in the beam. The minimum stress is obtained at failure load (maximum load) and the length between the point of load application and failure of the beam (*L*).

3.3.3.1. Fabrication of Microcantilever Beams

The microcantilevers were produced using a FEI FIB200. A triangular cross section beam was milled out of a bulk ACNT/ABS composite or ABS glass sample. This was done by first milling a ‘U’ shaped trench using high beam currents typically 5000 pA. The trench was then undercut by tilting to 45^o with beam currents of typically 5000 pA. The milling angle resulted in beams of equilateral triangle cross section. The front face of the cantilever was cleaned first before the undercut faces were cleaned with low beam currents of 1000 pA. The beam lengths were kept close to 24±5 μm and width between 3-6 μm and height of 3-4 μm. All the beams were milled parallel to the direction of the MWCNT nanotubes in composite. Prior to testing, the cantilever beams were imaged using JEOL 6500 SEM or JEOL 840F to determine the length, width and height of the beam. To study fracture toughness, a sharp notch was made near the fixed end of the beam using a beam current of 50 pA. The notch depth was determined using SEM images of the fracture surface.

3.3.3.2. Testing of Microcantilever Beams

Bend tests and fracture toughness tests of the microcantilevers were done using a nanoindenter (MTS nano XP). A Berkovich diamond indenter was used for loading the beams. The nanoindenter is fitted with a piezoelectric stage from MTS Nano Vision. An optical microscope is used as an aid for loading and finding the microcantilevers on the bulk sample. The MTS Nano Vision stage is used to obtain a topographical image of the microcantilever beams in a similar manner as an AFM scan using the indenter tip. The topographical image enables the precise location of the indenter tip on the microcantilever beam during the loading. The beams were loaded near the free end until fracture at constant displacement rate of 10 nm s^{-1} with a target displacement of 3.5 μm to ensure that fracture occurred. During testing, the load and displacement were recorded. The cantilevers were imaged using SEM after testing to confirm failure.

3.4. Thermal Properties

To obtain the thermal conductivity (κ) of the CNTs, ABS and CNT/ABS composite, it was necessary to carry out experiments to determine the specific heat capacity (*Cp*) of the composites and the thermal diffusivity (*α*). The relationship between thermal conductivity and thermal diffusivity and specific heat capacity is given by

$$\kappa = \alpha \rho C_p \quad \text{Equation 3.16}$$

where *ρ* is the density of the material under investigation. The densities of the composites and glass were measured using the Archimedes method while that of the CNT preforms was obtained from the dimensions and mass. The *α* and *Cp* were obtained using laser flash and calorimetry.

3.4.1.1. Differential Scanning Calorimetry (DSC)

Differential scanning calorimetry (DSC) is a thermal analysis technique that can be used to obtain specific heat capacity of materials by comparing with sapphire as a standard. A DSC has a reference pan (empty) and a sample pan. Thermocouples are used to monitor the temperature of the two pans which are mounted on separate heating blocks. The temperature is continually measured with the aim of maintaining the same temperature in both pans. The amount of energy required to maintain the equilibrium in temperature alludes to the thermal events within the sample. This difference in energy required to maintain balance in temperature is related to the specific heat capacity of the sample. Using sapphire as a standard, the relationship in equation 3.17 was used to calculate the *Cp* of ACNT preforms, ABS and CNT/ABS composites.

$$C_{p(s)} = \frac{E_s}{E_r} \times \frac{M_r}{M_s} \times C_{p(r)} \qquad \text{Equation 3.17}$$

Where C_p(s) : Cp of sample (unknown)

C_p(r): Cp of the reference (sapphire)

E_s : Heat flow to the sample (corrected for by the empty pan)

E_r : Heat flow to the reference, sapphire, (corrected for by the empty pan)

M_s : Mass of sample

M_r : Mass of reference

In this research, a Perkin Elmer Hyper DSC was used for determining the Cp of the samples at heating rates of 5 ^{o}C / minute from room temperature to 100 ^{o}C. The masses of the samples used in the experiments were 4-5 mg.

3.4.1.2. Thermal Diffusivity by Laser Flash Technique

Thermal diffusivity is the property that determines the speed at which heat propagates by conduction within a material. In this study, thermal diffusivity was obtained using the laser flash technique. Figure 3-9 shows a schematic of the flash method. A sample is held at a desired temperature before it is subjected to a pulse of energy (laser) on one face and the increase in temperature on the opposite face is measured as a function of time. The thermal diffusivity is then obtained from the thermogram. The samples used were discs of 10 mm diameter and *ca.* 1.5 mm thickness. The CNT samples were tested with the CNTs aligned parallel to the direction of the measured heat flow. The laser used was a 100J Nd-glass laser. The radiation from the rear of the sample was collected via a lens and mirror system and focused on an infrared detector which was analysed to give the thermal diffusivity. Details of the operation of the laser flash technique can be found in reference [188]. The laser flash experiments were carried out by Mr. Andrew Wallwork at Manchester University.

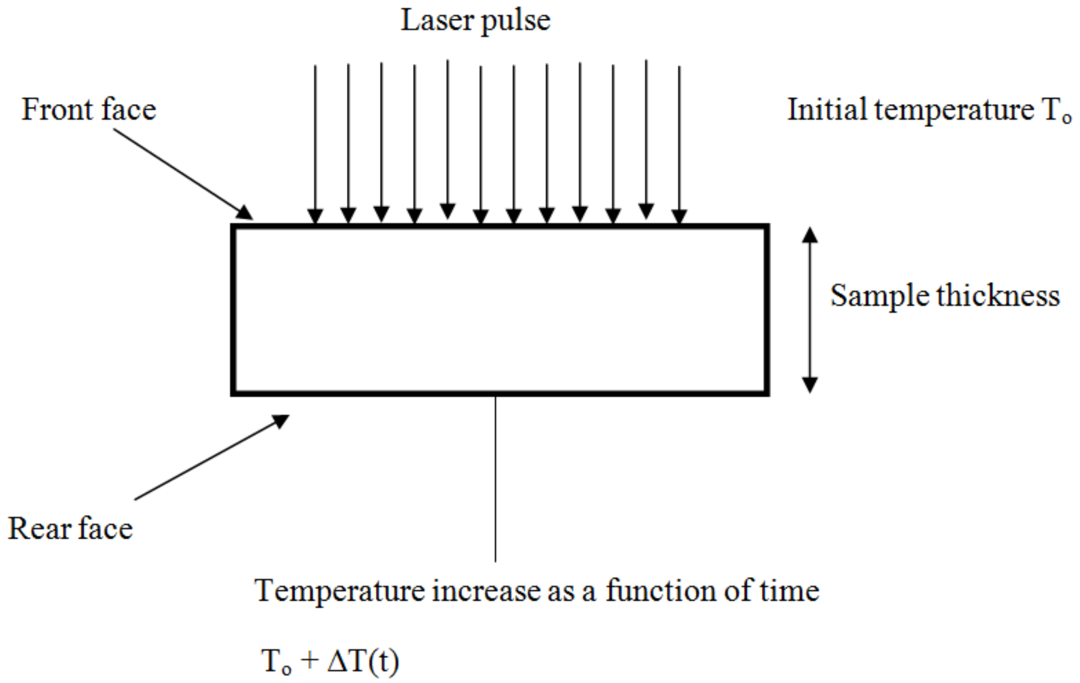

Figure 3-9 Schematic of the laser flash method for measuring thermal diffusivity.

3.4.2. Testing of Electrical Properties

The through thickness electrical properties were measured using an ohmmeter. The CNT/ABS composites were first polished on opposite faces using diamond slurries from 25 µm to 1 µm finish. Gold was sputtered on these faces and the resistance across them was measured. Measurements were carried out on 2 mm thick specimen in the axial direction of the ACNT.

CHAPTER 4

Microstructural and Chemical Analysis of ACNT Preforms and ACNT/ABS Composite

4.0. Overview

In this chapter, results of the properties of aligned multi-walled carbon nanotube preforms and the corresponding glass composites studied by SEM, TEM and several chemical analysis methods are reported. The studies were carried out to elucidate the microstructure and the chemical properties in both bulk materials and on individual nanotubes making up the composite. Section 4.1 looks at the results of properties and quality characterisation of the ACNT preforms while section 4.2 details the results of sol gel infiltration and properties of the composites. Section 4.3 is a discussion of the results. Section 4.4 summarises the findings in this chapter.

4.1. Aligned Multi-walled Nanotube Preforms

Figure 4-1 shows the range of lengths achieved for different durations of experiment at one litre per minute flow rate. The maximum height of the ACNT preform attained was 7.1 mm for the CVD reactor used in this study. Figure 4-2a) and b) show photographs of CVD carbon nanotube preforms obtained for six hour and four hour experiments respectively on different geometries of the substrate. The growth of CNTs preforms is not uniform for whole length of the quartz tube. The most rapid growth was observed close to the centre of the 500 cm long tube furnace where the temperature is ~800 ^oC. This is the optimum growth temperature of the MWCNTs in the reactor used. The length of the preforms decreases towards the ultrasonic unit nozzle end from the middle following the decreasing temperature profile pattern of the furnace. CNT growth beyond the centre of the reactor is poor in terms of alignment and graphitic quality.

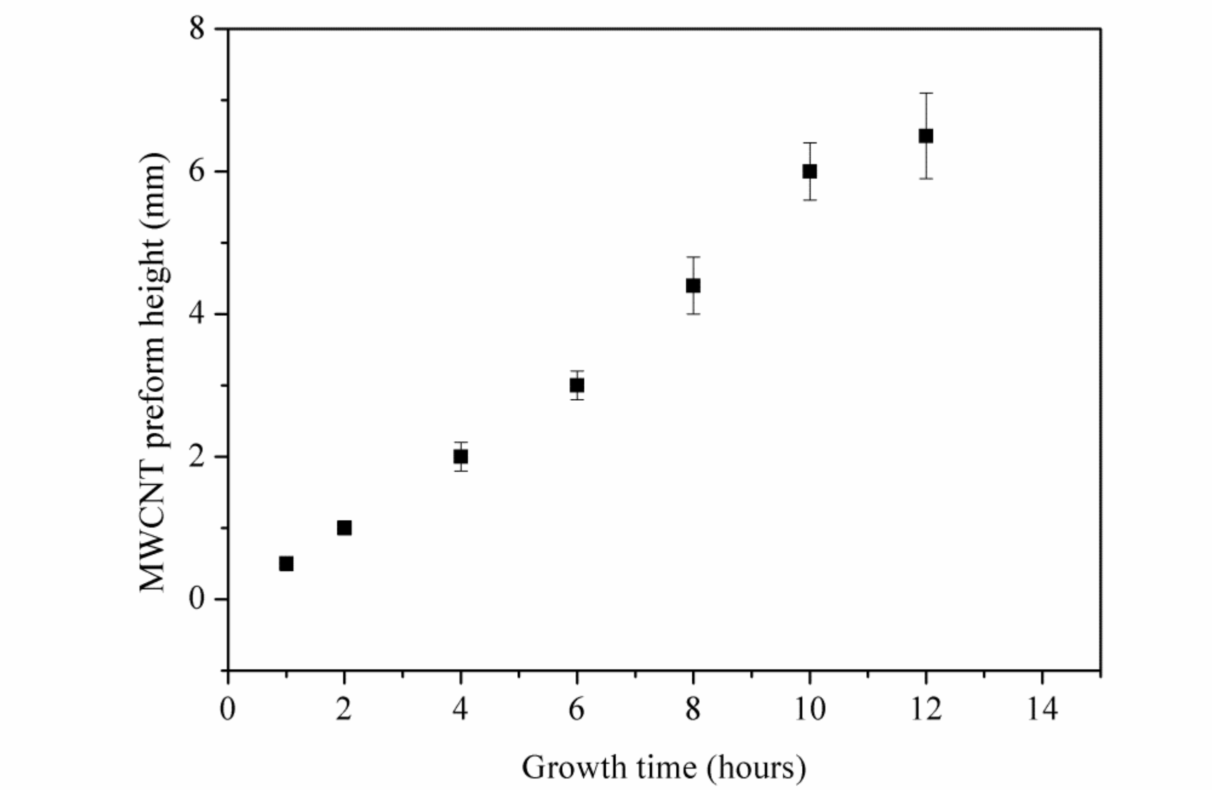

Figure 4-1 A comparison of growth time with the length of the MWCNT preforms produced.

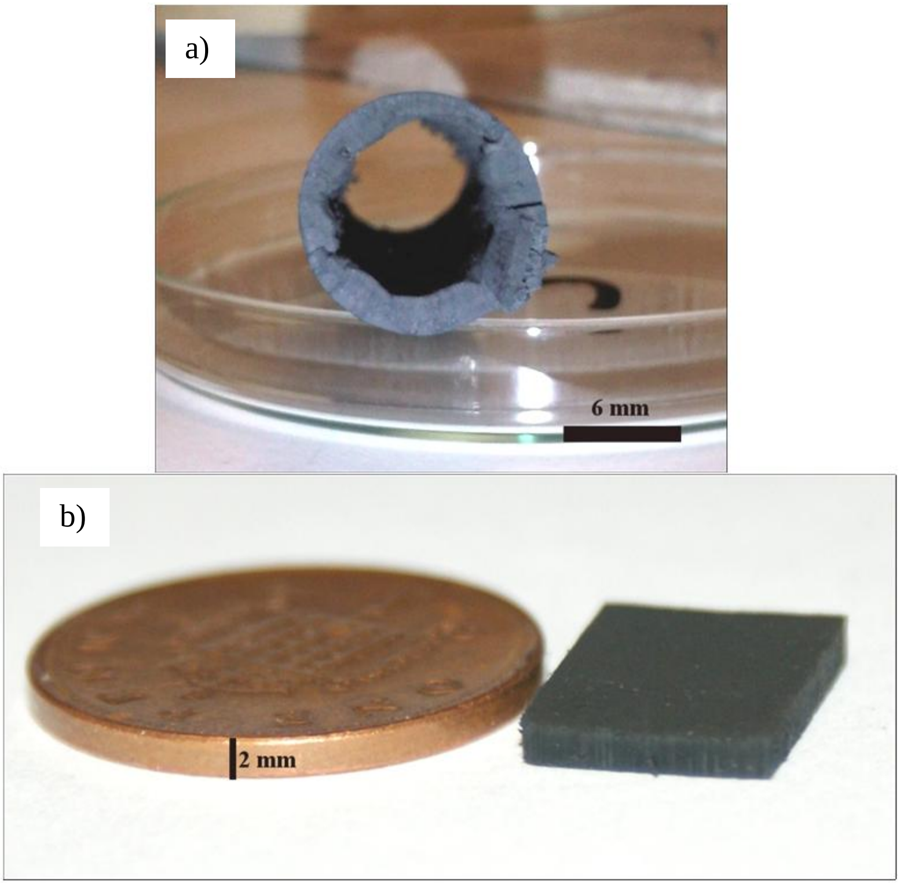

Figure 4-2 Photographs of multi-walled carbon nanotube preforms for a) cylindrical substrate such as the quartz tube and b) flat quartz substrate ACNT preform compared to a British one penny coin.

4.1.1. Structural Investigation of ACNT Preforms and CNTs by SEM and TEM

Since CNT morphology is a key aspect influencing the properties of the final composite at macroscopic level, the properties of the CNTs such as diameter, cross section and presence of flaws were investigated using both SEM and TEM. SEM studies revealed that the CNTs grow perpendicular to the quartz substrate or the quartz tube. The individual CNTs form a parallel structure within the preform as in schematic 4-3a and figure 4-3b. The preforms are also shown to be clean with no amorphous carbon deposits in the interstitial spaces as in figure 4-4a and b. Analysis of SEM images of the preforms revealed the average volume fraction of the MWCNTs in the preform as 10 ± 2%.

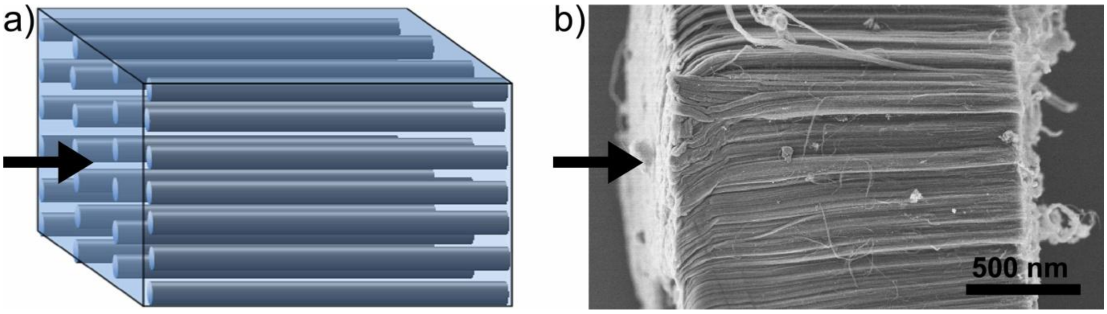

Figure 4-3 Schematic a) shows the alignment of the CNTs within the preforms and b) an SEM image of a corresponding preform produced from a flat quartz substrate. The arrows show the axial alignment direction.

TEM studies showed that the CNTs making up the preform are multi-walled in nature (figure 4.5a and b). The inter-wall separation between the concentric graphitic walls was determined from a high-resolution TEM (HRTEM) image (figure 4.5 b). Figure 4.5c shows lattice fringes obtained from a line profile on figure 4.5b. The 11 lattice fringes in figure 4.5c span a length of 3.7 nm, hence 0.336 nm for each fringe which corresponds to graphite inter-wall separation of 0.34 nm [189]. Also, from TEM images such as figure 4.5a, stacking faults appearing as folds are visible on the MWCNT. Catalyst particles (Fe) inclusions in the inner core of the nanotubes are also visible in figure 4-5a.

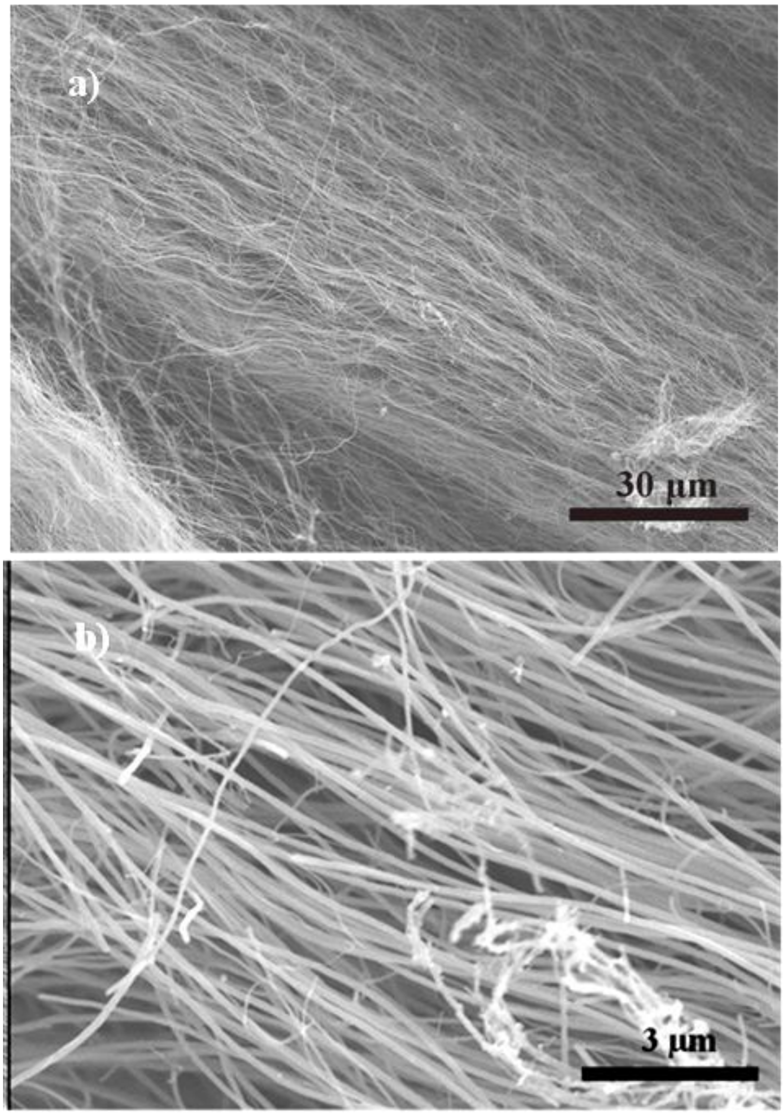

Figure 4-4 SEM images showing a) CNTs making up a preform and b) at higher magnification showing interstitial spaces are free of amorphous carbon deposits.

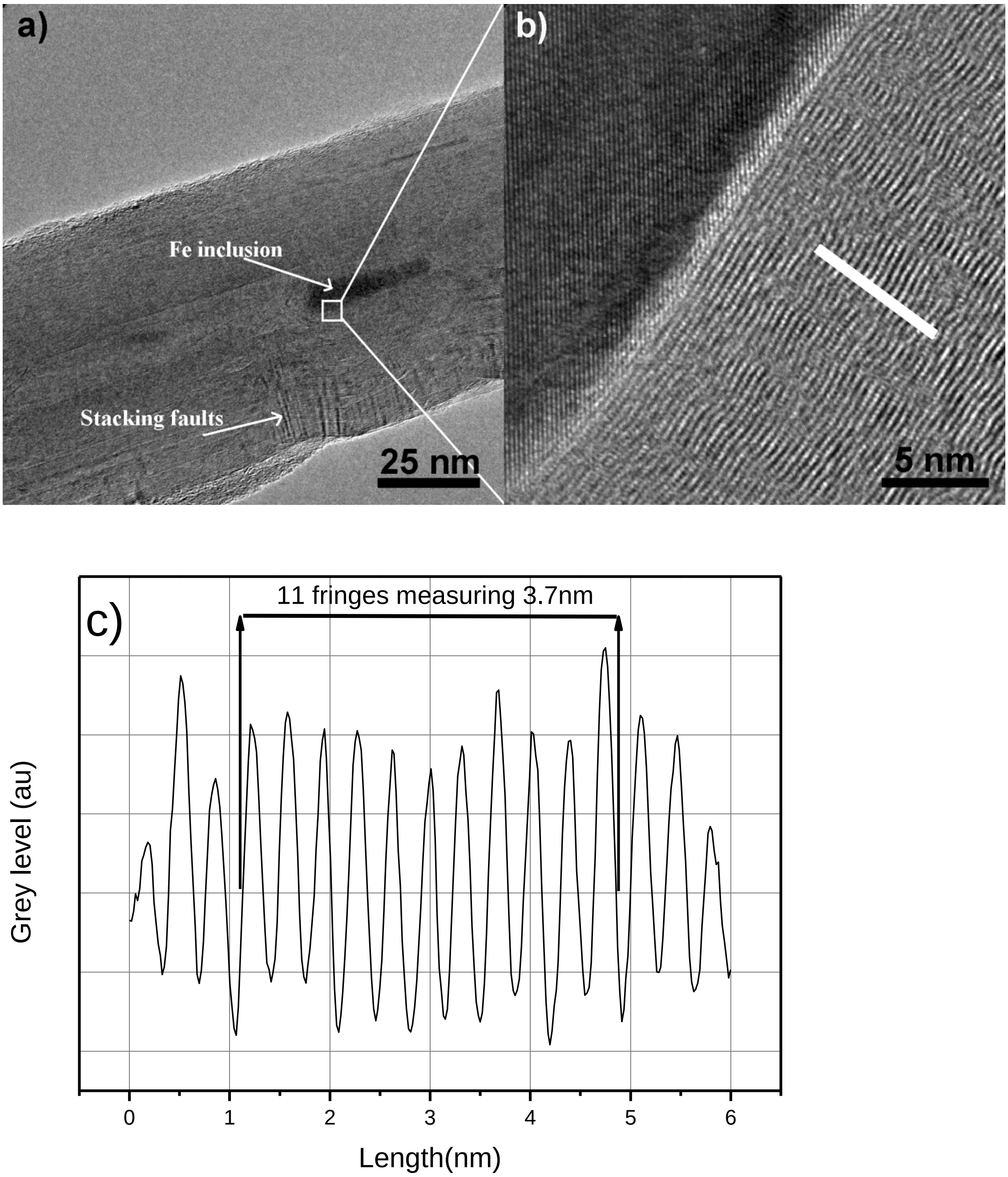

Figure 4-5 TEM images a) and b) showing iron inclusions and folds on the CNTs. Plot c is obtained from the white line on TEM image b) The line profile measurements were done using Image J software.

Using several TEM images such as in figure 4-6a, the diameters of the CNTs were determined by measuring the mean line profiles across individual CNTs as shown in figure 4-6b. The diameters ranged between 10 nm to 140 nm with a mean of 80 nm. 80 %

of the CNTs had diameters below 100 nm as summarised on the bar graph in figure 4-7. The preform densities were found to be 0.15 ± 0.04 gcm^{-3} by measuring the dimensions and weighing the preforms.

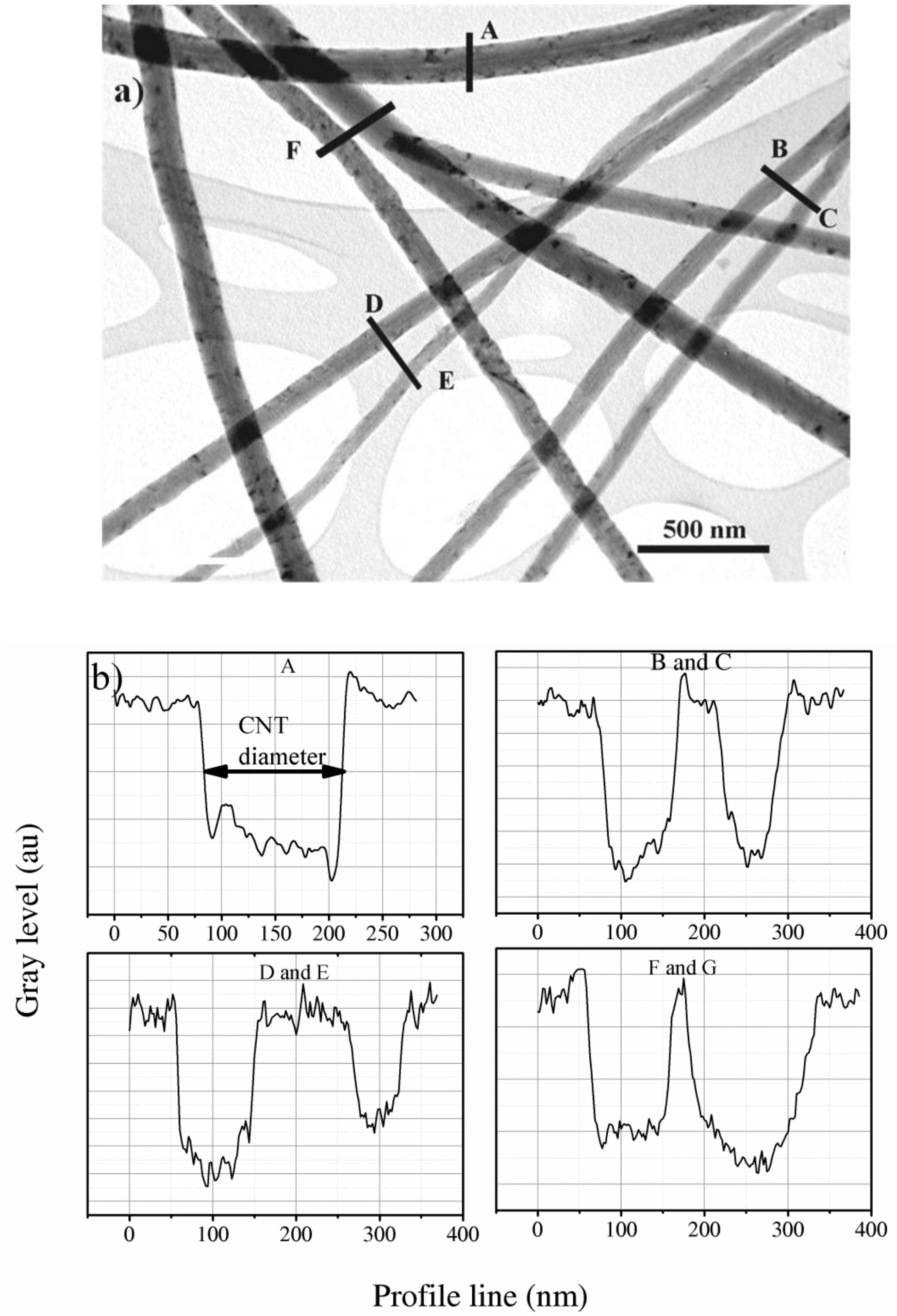

Figure 4-6 An example of a TEM image of CNTs used to measure diameters and b) the corresponding mean profile of the intensity levels of the selected nanotubes used to obtain the diameters.

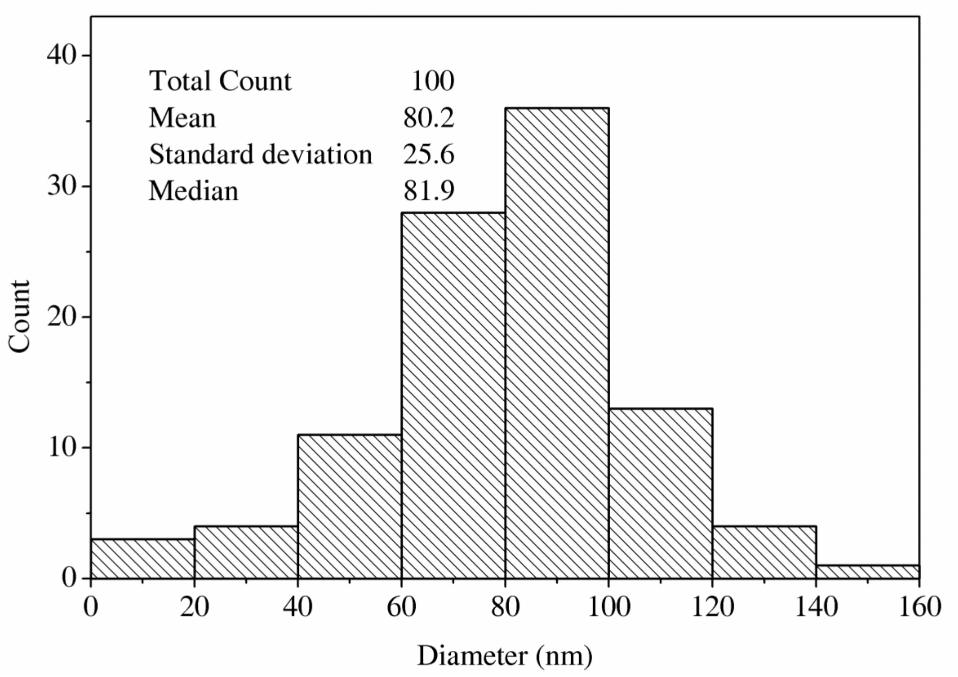

Figure 4-7 Distribution of CNTs produced in a 4 hour experiment.

4.1.2. Quality of ACNT Preforms

The quality of the preforms was studied by looking at the amount of impurities such as catalyst particles within the bulk materials. Also, the disorder in the graphitic structure of the MWCNTs making up the preforms was investigated. The quality of the preform affects both the mechanical and transport properties of the composites fabricated. This section will look at the results of the quality of preforms used in fabrication of the composites by TGA and Raman spectroscopy.

4.1.2.1. Thermogravimetric Analysis

TGA results obtained after burning preforms weighing 3-4 mg in air are presented in figure 4-8. After the experiment a red powder was collected in the TGA pan. This was attributed to iron oxide since iron was used as the catalyst in production of CNT preforms. The results show that the residual mass after burning a preform in air up to 850 °C is less than 1 wt%. This fact implies that the CNT preform had a carbon purity more than 99 wt%. Therefore, in terms of carbon content, the preforms are considered to be of high quality. Secondly, the TGA results show that the CNT preform oxidation onset is 550 ± 10 °C. The oxidation continues over a range of 100 °C ending at 650 ± 10 °C.

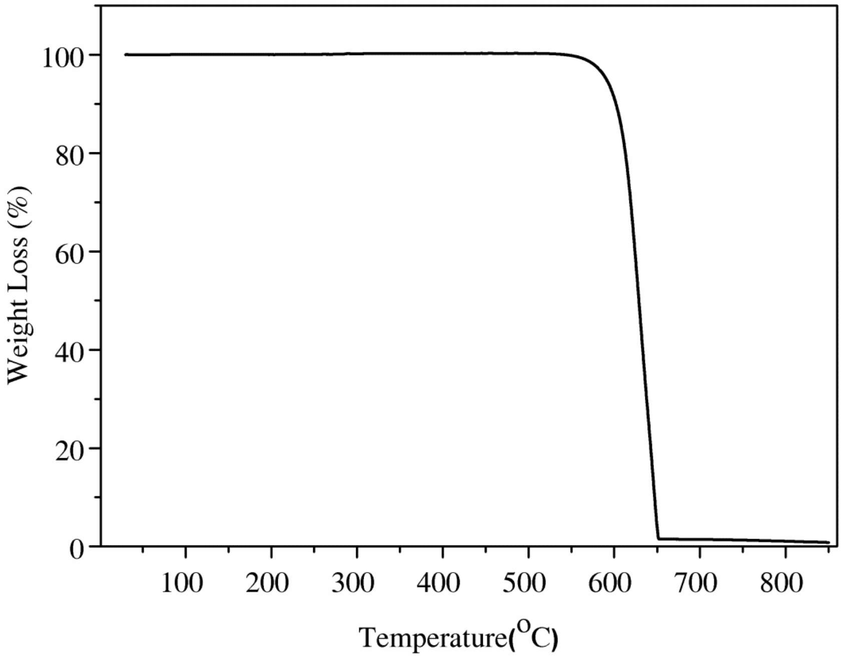

Figure 4-8 Thermogram of a CNT preform tested in air from 25°C to 850°C.

4.1.2.2. Raman Studies of the CNT Preforms

The Raman spectrum is used to qualitatively investigate the relative defect density on the CNTs constituting the preform. The characteristic feature of the graphitic layers is the G peak appearing at 1574 cm^{-1} and the D peak which appears at 1341 cm^{-1} shown in figure 4.9. The D/G intensity ratio obtained from the preform is between 0.35 – 0.40. The G' peak is an overtone of the D peak.

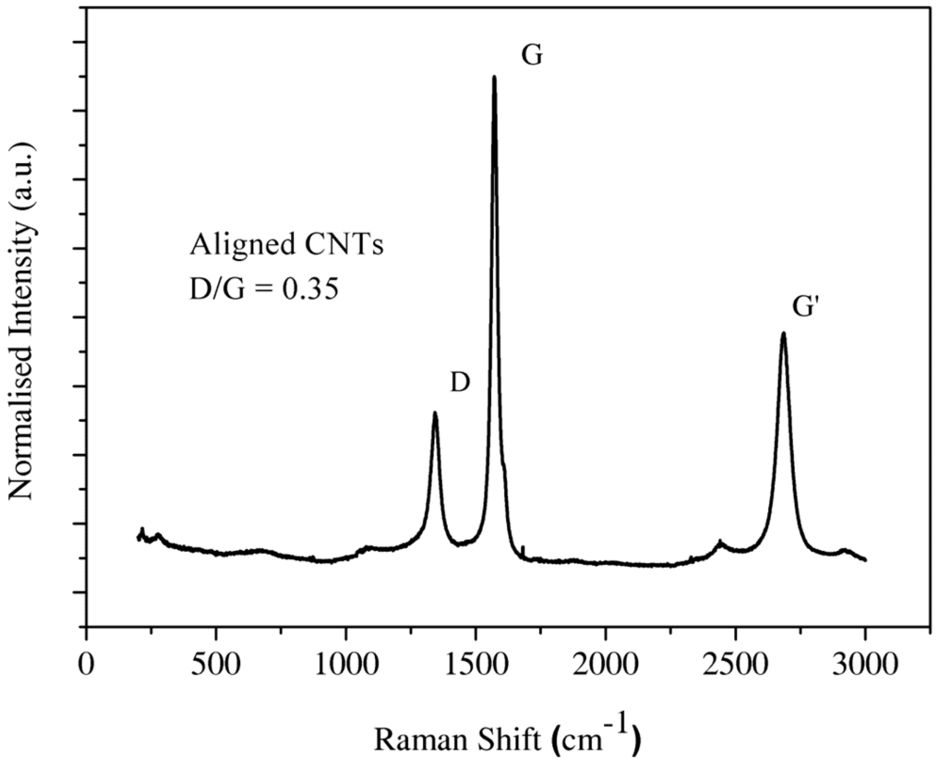

Figure 4-9 A representative Raman spectrum of a CNT preform.

4.2. Infiltration of MWCNT Preforms with ABS sol and Hot Pressing

The experimental results of the effect of the number of infiltrations for different heights of preforms are presented in figure 4-10. The weights were measured after a 450 °C heat treatment in air to remove any unreacted matrix precursor materials such as tetraethylorthosilicate (Si precursor). This process reduced the apparent weight gain owing to the sol infiltrate. The step is necessary as it improves the overall efficiency of sol infiltration during successive infiltration processes. Infiltrations were repeated until there was little or no increase in the percentage weight change in two consecutive infiltrations. This appears after 4-5 infiltrations at which the graphs plateau as shown in figure 4-10.

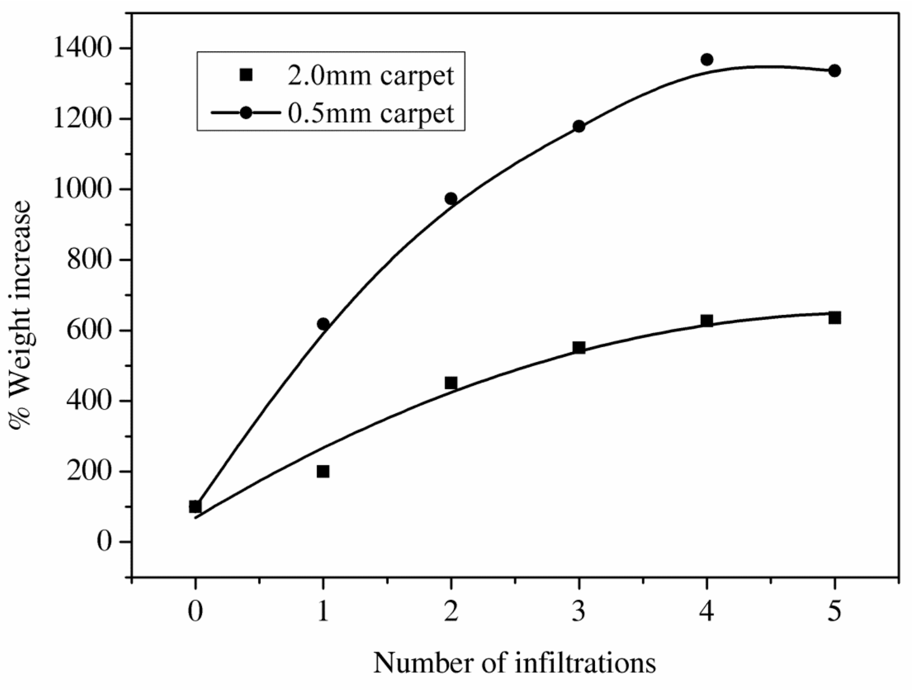

Figure 4-10 Percentage weight increase with different number of capillary assisted infiltrations.

SEM images were used to investigate the wetting of the CNTs by the ABS sol. Comparing figure 4.11a (an un-infiltrated ACNT preform) with figure 4-11b, it is evident that the MWCNT preforms were effectively wetted and infiltrated by the borosilicate glass sol. Further investigation also revealed a variation in the infiltration on different regions within the same preform (figure 4-11c). Such variations were not observed after multiple infiltrations. A TEM image of a section of a dried gel infiltrated ACNT preform (figure 4-11d) shows that the MWCNTs are effectively embedded in the matrix. Investigation of the effect of layering preforms (figure 4-12) during hot pressing did not reveal any weaving effect between two adjacent preforms.

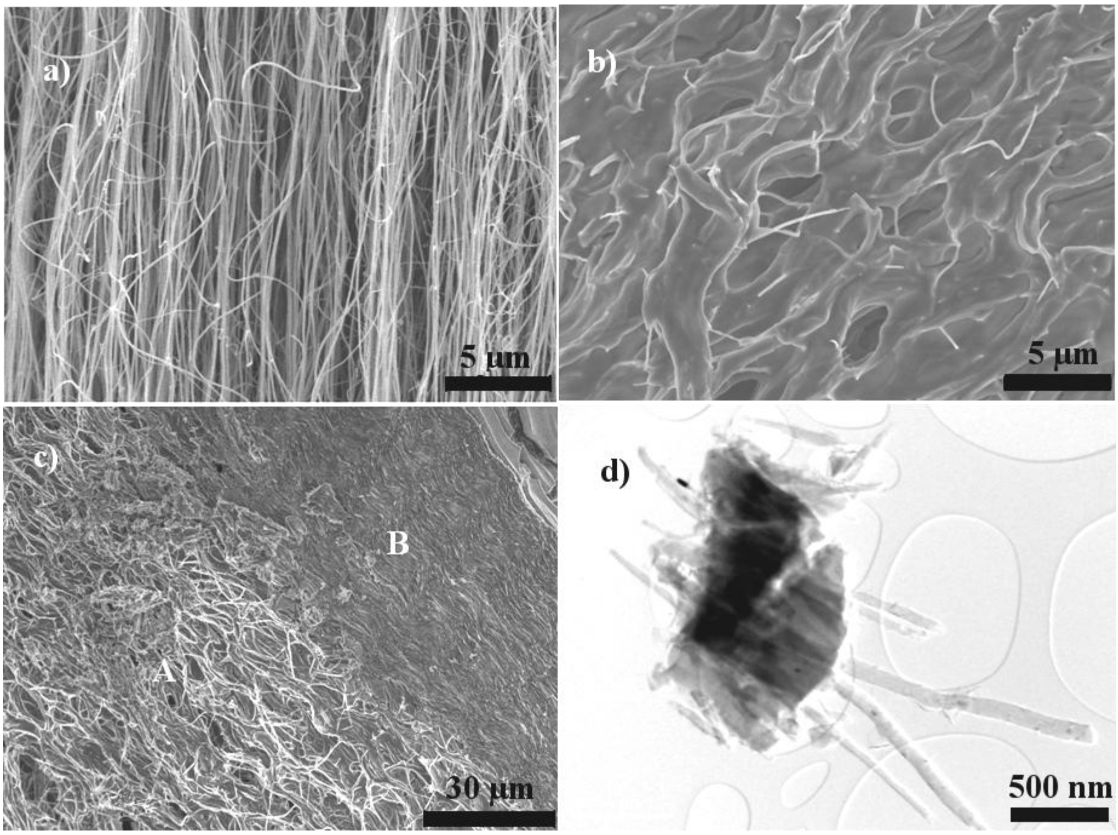

Figure 4-11 (a) SEM image of an ACNT preform; (b) SEM micrograph of a sol-infiltrated ACNT preform with the fracture normal to the plane of the preform; (c) SEM of a heat treated (450 ^{o}C) sol infiltrated ACNT preform showing local variations in the level of infiltration *i.e.* regions A and B; (d) TEM image of dried section of the sol infiltrated preform showing CNTs embedded in the matrix and showing good alignment.

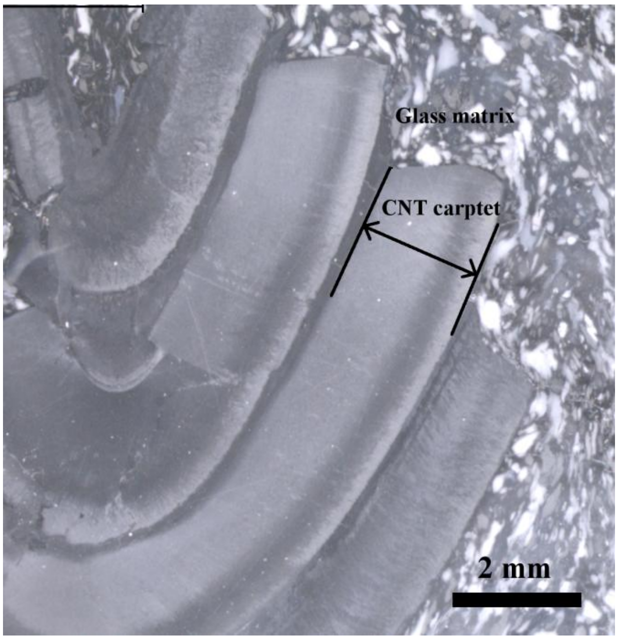

Figure 4-12 An optical image of four preforms (carpet) layered up during hot pressing with the interface between the preform containing the glass matrix.

4.2.1. Chemical Analysis of the Composite

To confirm that the CNTs had survived the high temperature (1100 ^{o}C, holding time of 10 minutes) and pressure (25 MPa) during hot-pressing, a Raman spectrum (figure 4-13a – composite plot) was taken from the bulk composite sample. The characteristic Raman peaks for a CNT were observed suggesting the presence of graphitic material. To determine whether the processing increased the amount of defects on the CNTs, the D/G peak of the hot pressed composite was compared to that of the ACNT preform (figure 4-13a). An average change in the D/G ratio from 0.35 in the ACNT preform to 0.40 in the composite was obtained.

The chemical composition of the glass is expected to be 63 wt% SiO_2, 24 wt% Al_2O_3, 10 wt% B_2O_3 and 3 wt% Na_2O. This was calculated from the mole ratios of the precursors used in preparing the glass. Figure 4-13b shows an EDX spectrum taken from a fracture surface of the composite. Analysis of the EDX spectrum shows the composition of the high concentration elements (Al and Si) in the composite and a Carbon peak from the CNTs.

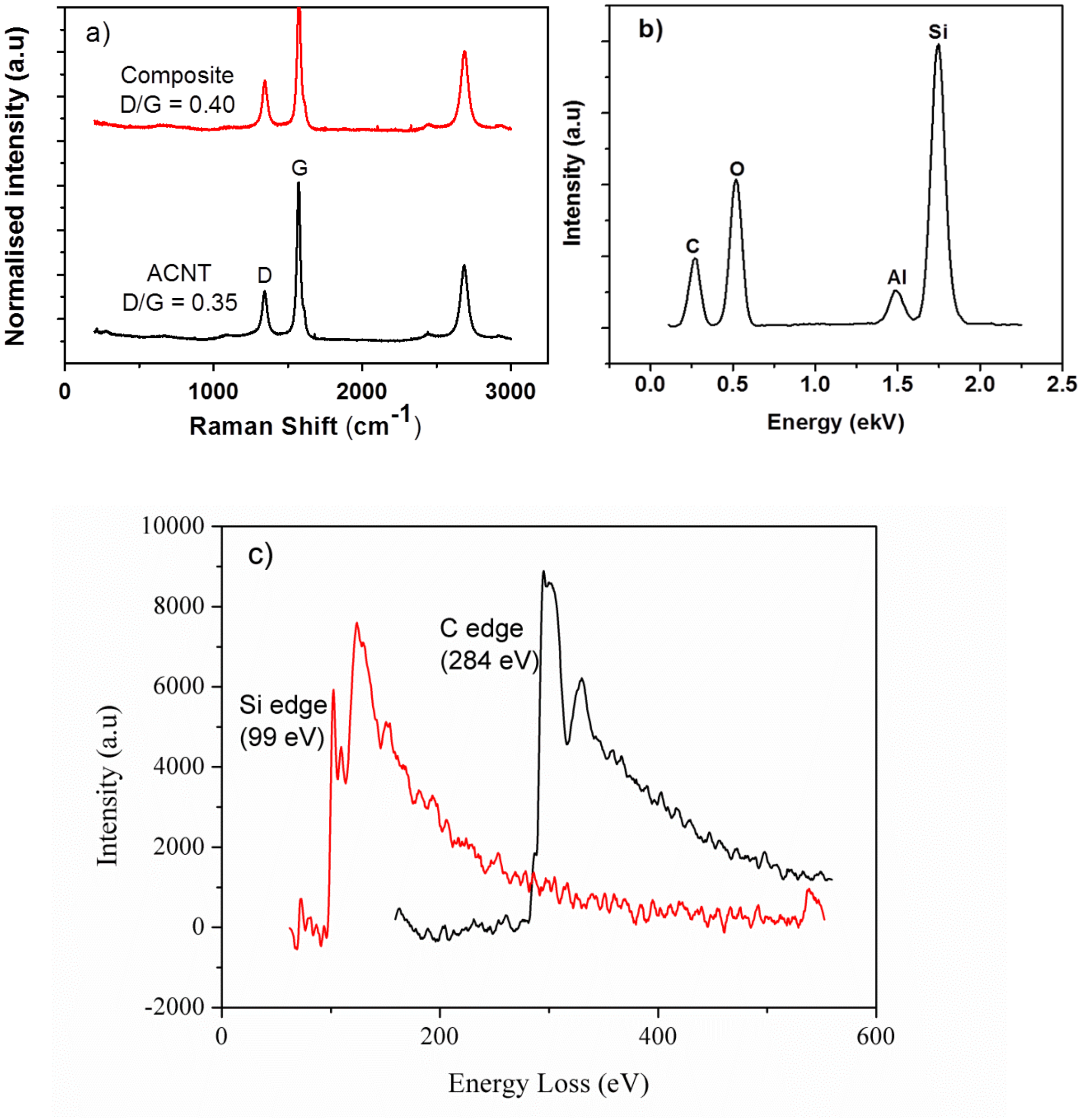

Figure 4-13 Spectra of composite (a) Raman of the composite compared to ACNT preform (b) EDX spectra and c) EELS spectra of both a carbon and silicon edge.

EDX did not detect boron due to limitation of the EDX instrument used coupled with the low atomic number of boron. Sodium was not detected in the EDX spectrum due to the small percentage in the glass composition. EELS analysis (figure 4-13c) of the composite shows the presence of Si and carbon however, a boron edge was not detected due to the small amount of boron in the composite (10%). Also, since EELS is a very local probing technique (nm areas), possible boron segregation during processing could make it difficult to detect by EELS.

4.2.2. Microstructural Characterisation of the Composites

The average of five measured densities for hot pressed composites is presented in table 4-2 and is compared to those of ABS glass and the CNT preforms. The extent of densification as a percentage is obtained from the rule of mixtures. The residual porosity in the composites' microstructure is 8-12%. To observe such porosity and the arrangement of the nanotubes within the composite, SEM and TEM imaging was performed and are discussed next.

Table 4-2 Densities of ACNT/ABS composite, ABS and ACNT preform.

	ACNT/ABS composite	**ABS glass**	**CNT preform**
Measured density, ρ, (g/cm^3)	2.1±0.3	2.3±0.1	0.15±0.04
% Dense	90±2	98±1	10±2

4.2.3. Observation of Polished and Fractured Surfaces

After sequential mechanical polishing of the composite using diamond slurry of particle sizes from 25 µm to 1 µm, distinguishable regions of the CNT preform and those of glass were observed under an optical microscope (figure 4-12). SEM images (figure 4-14a and c) show polished surfaces devoid of any cracks. At higher magnification, SEM images (figures 4-14b and d) reveal CNT pull-outs in both longitudinal and transverse orientations of the polished surfaces. The pull-outs correspond to the spatial arrangement of the CNTs *i.e.* parallel aligned nanotubes are visible in figure 4-14b while tips of broken off nanotubes and holes in the matrix are present in figure 4-14d.

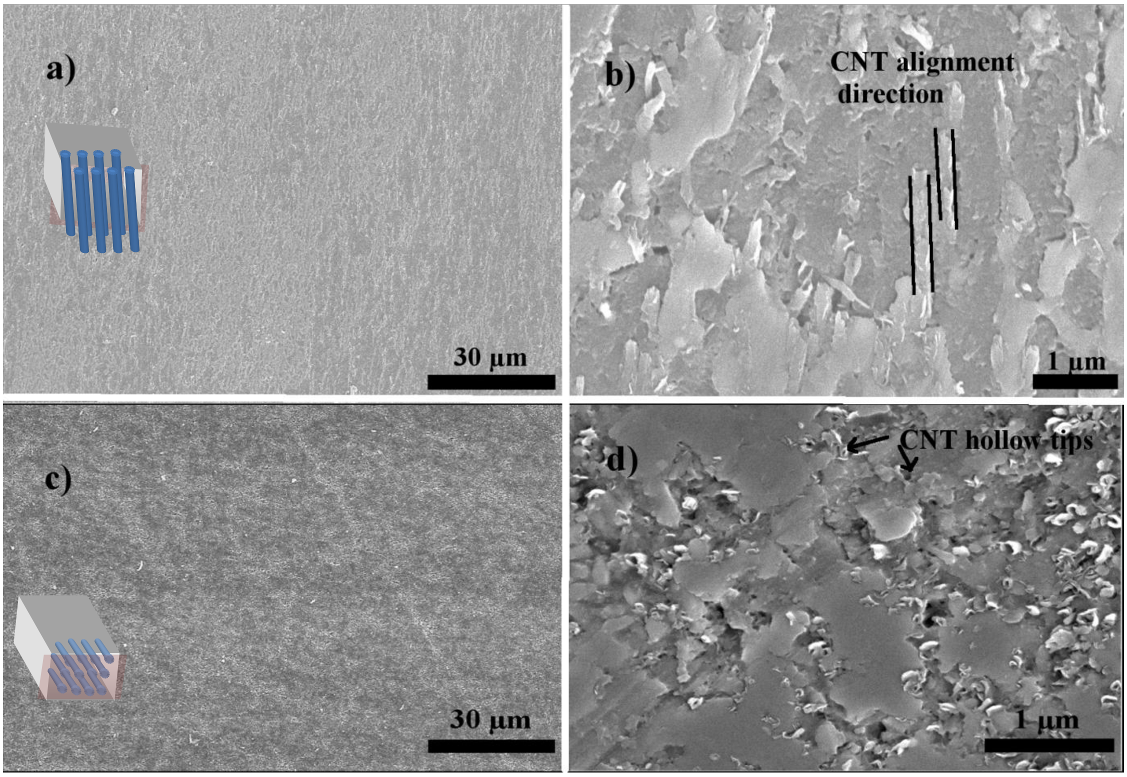

Figure 4-14 SEM images showing polished composites a) and b) along the CNT alignment surface and c) and d) perpendicular to the CNT alignment direction.

To further demonstrate the alignment of MWCNTs in the composite, SEM images of a sample subjected to fracture perpendicular to the alignment direction of the CNTs are shown in figures 4-15a and b. Copious amounts of pulled-out CNTs and sword-in-sheath failed CNTs of 1μm or less in length are observed with corresponding holes on the matrix. The fracture induced was not under controlled load or displacement.

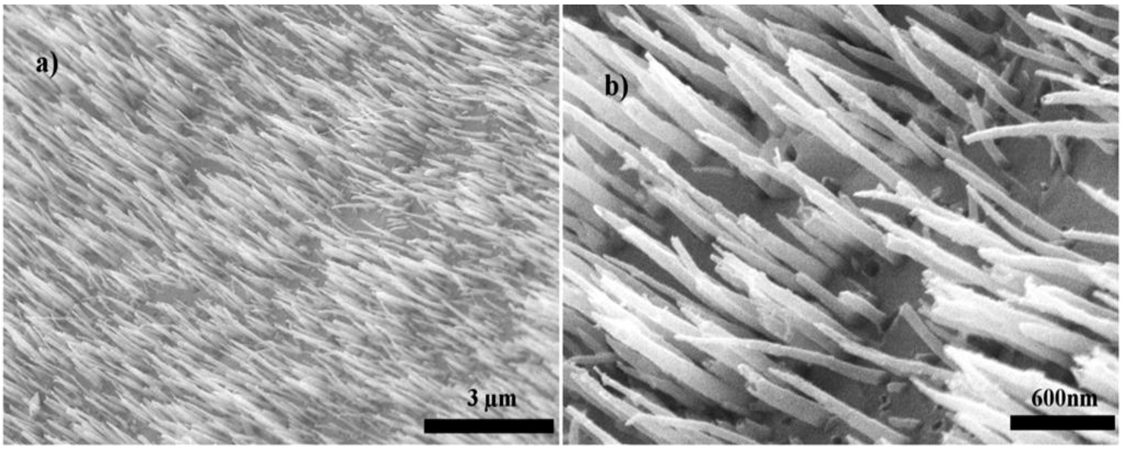

Figure 4-15 SEM images of a fracture surface perpendicular to the alignment direction of the CNTs in the composite.

Polishing using focused ion beam (FIB) milling into the bulk of the composite in conjunction with SEM studies confirms that the CNTs are highly aligned. Figure 4-16 shows bright rounded/oval shaped boundaries of CNTs while the grey region is the glass matrix. Milling through the composite also revealed some sub-micrometer pores as shown by the arrows in figure 4-16. The good dispersion of the CNTs is also revealed in figure 4-16. The area and volume fraction of the CNTs after sintering was obtained from image analysis of the FIB milled SEM images. The area fraction of the CNTs was 20 ± 2% of the composite. The FIB SEM imaging technique was further utilized to probe into the bulk of the composite by doing a sequential FIB and imaging. Either a few or many CNTs could be reconstructed through the matrix as shown in figure 4-17.

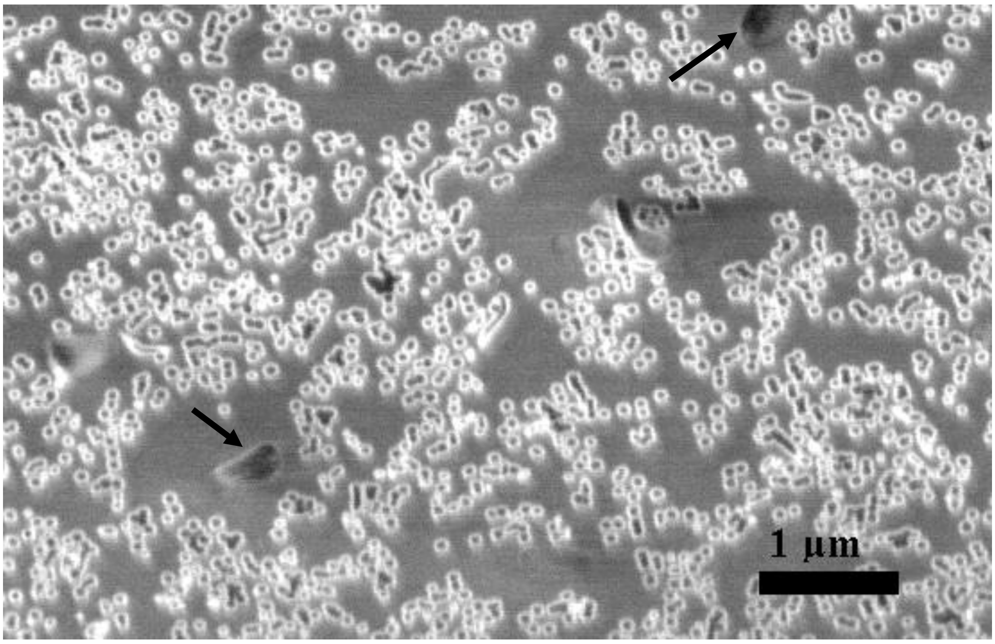

Figure 4-16 SEM images of a FIB slice into the composite with the milling done perpendicular to the direction of alignment.

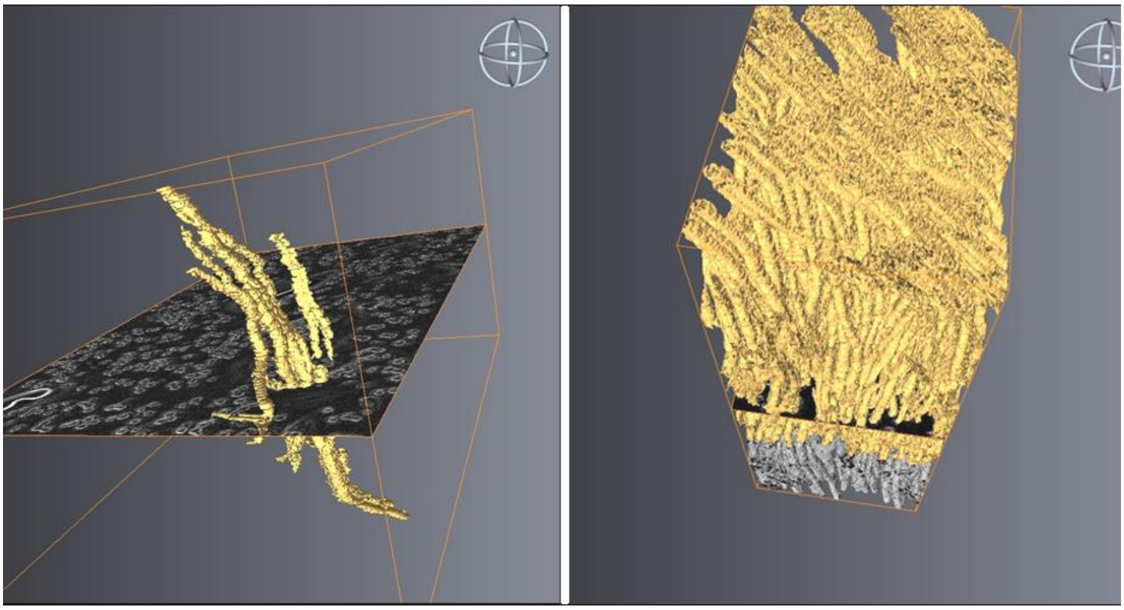

Figure 4-17 3D tomographs from SEM images of FIB slices reconstructed into a representation of the bulk composite. The reconstruction was done using Avizo software.

4.2.4. Observation of the ABS/CNT Interfaces by TEM

Figure 4-18a shows a TEM image where the sample was prepared by crushing the composite using a mortar and pestle. The matrix is observed to be intimately bonded on to the CNT. This demonstrated the good wetting of the MWCNTs by the sol without any processing of the CNTs. Figure 4-18b shows a TEM image from a lift-out specimen prepared using the FIB. The CNTs are observed end-on and can be distinguished from the rest of the glass matrix. A higher magnification TEM image (figure 4-18c) of one of the CNTs shows a bright centre due to the hollow inner core of the MWCNT. Neither cracks nor spaces are observed between the CNT and the matrix. A higher magnification of the interface (figure 4.18d) reveals no clear transition between the CNT and the matrix. The CNT graphitic walls are visible in figure 4.18d.

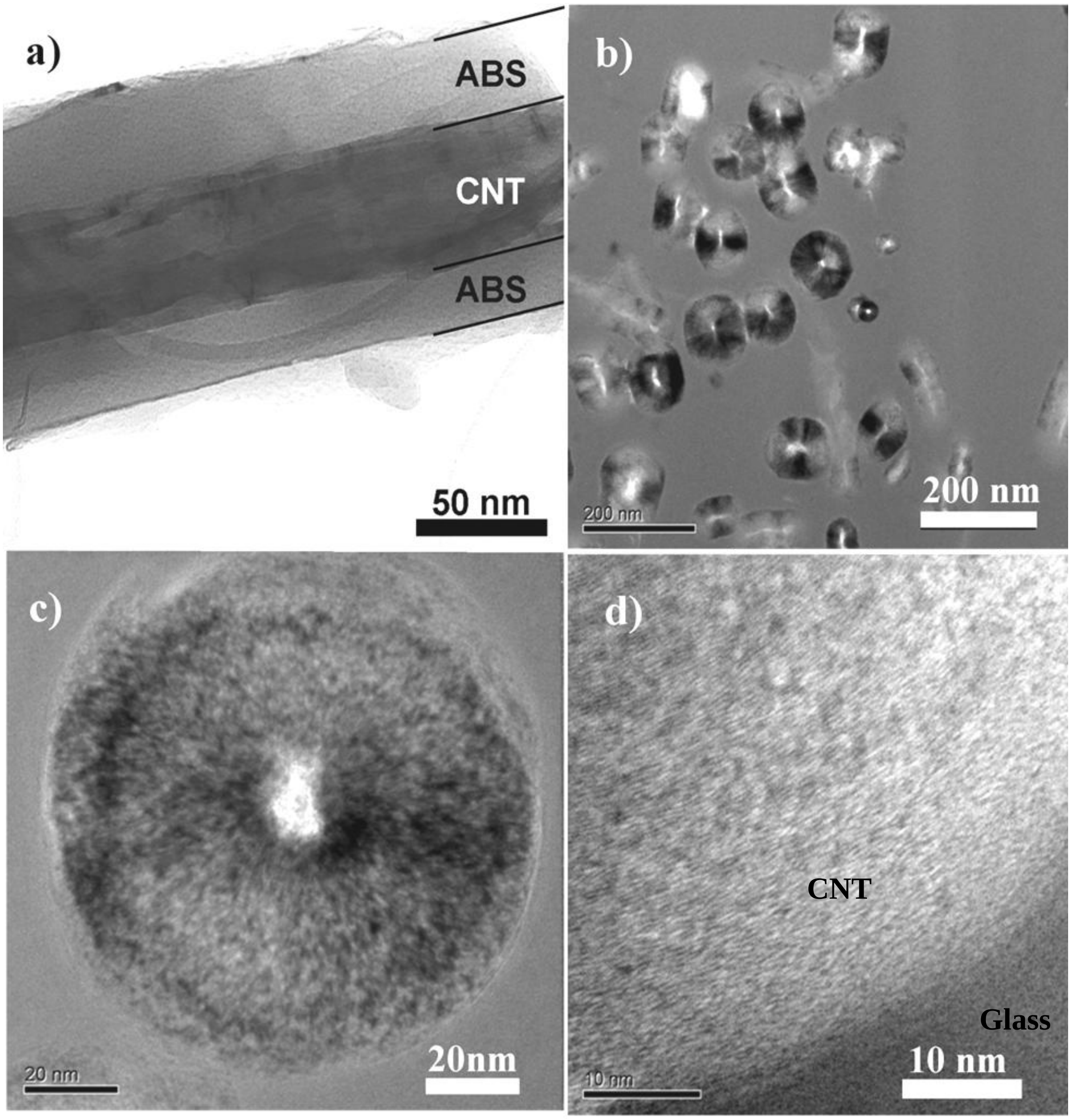

Figure 4-18 TEM images of a) a crushed composite b & c) FIB fabricated TEM sample showing intimate contact between CNT and ABS matrix. Image d) is a higher magnification of the interface with no observable cracks or voids at the interface and no clear transition between the MWCNT and the matrix.

4.3. Discussion

The results of the lengths of CNT preforms show for the first time that aerosol CVD with floating catalyst produced MWCNTs of 7 mm in length with average diameters of 80 ± 25 nm. The observed tapered growth on a substrate is schematically shown in figure 4-19, following the temperature profile of the furnace. This is because the optimum CNT growth condition of the reactor used is 800°C, which is attained at around the centre of the tube furnace. For the same reason, the CNT growth is rapid near the centre of the furnace. Poor growth and quality of CNTs beyond the centre is due to most of the Fe catalysts being used at the initial half of the CVD reactor to facilitate growth. There is a limit in the length achievable with the reactor under the conditions used. This is evident in the decreased growth rate of CNTs as shown in the plot of growth time vs. preform height in figure 4-1. The limit is attributed to catalyst poisoning by amorphous carbon that blocks active sites on the Fe nanoparticles [42].

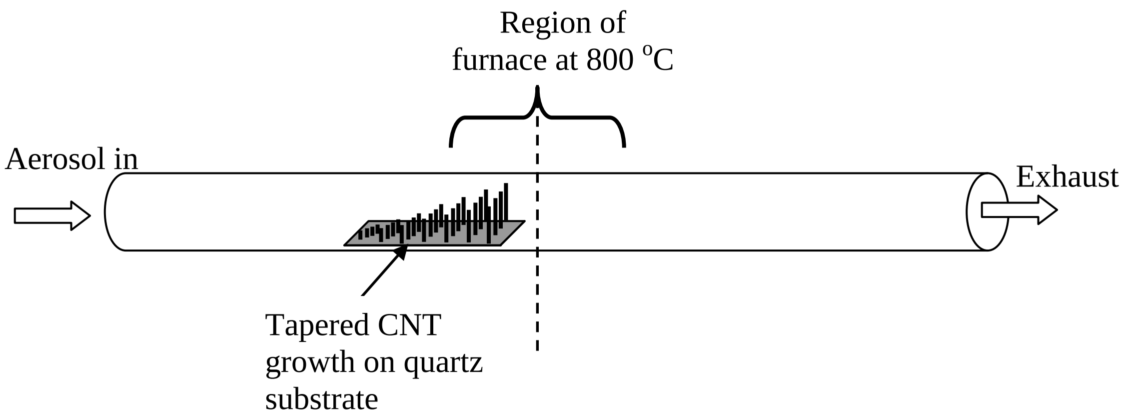

Figure 4-19 Schematic of the position and skewed growth of CNTs preforms in the reactor.

Preforms of greater than 2 mm in height are easy to handle for composite fabrication and allow macroscopic tests such as compression and indentation in the bulk. Crucially, for composite fabrication, flat substrates were preferred due to ease of sol infiltration. SEM observation of the CNT preforms reveal that they are clean which circumvented the need for further purifications. SEM observation of the preforms revealed that the nanotubes are aligned (figure 4-3) and continuous. Since the aim of the study was to obtain aligned CNTs within a glass ceramic matrix, the production of preforms with already aligned CNTs is important so as to avoid any alignment processing during composite fabrication. The alignment was maintained in the composite, which was demonstrated by a) fracture surfaces showing pull-outs and sword-in-sheath failed CNTs (figure 4-15), b) FIB cross sections observed by SEM (figure 4-16) and TEM (figure 4-18b), and c) 3D FIB tomography of bulk composite (figure 4-17). Importantly, the present processing route results in a well dispersed CNT composite with no regions of agglomeration. Also, the maintained alignment and continuity of the CNTs in the composite is important for electrical and thermal conductivity in the longitudinal direction of the composite or mechanical loading transverse to the CNTs.

The volume fraction of the ACNT preform of 10 ± 2% obtained by image analysis was confirmed by infiltrating a preform with the ABS sol followed by slow drying ensuring no lateral shrinkage occurred. A fracture was induced perpendicular to the alignment of nanotubes in a well infiltrated region as shown in figure 4-20. The area fraction was obtained by counting pulled-out CNTs and ‘holes’ from pulled-out CNTs in an imaged area such as in figure 4-20. Using an average diameter of 80 nm, the area fraction of the MWCNT was obtained as 10 ± 2 % which is equivalent to the volume fraction and corresponds to the preform image analysis results. Furthermore, the rule of mixtures was also used to approximate the volume fraction of the CNT preforms produced by using the equation $\rho_{preform} = \rho_{cnt} V_{f-cnt} + \rho_{air}(1 - V_{f-cnt})$, where V_{f-}

$_{cnt}$, ρ_{cnt}, ρ_{air} are the volume fraction of CNTs, density of CNTs and density of air respectively. For example, a rectangular cuboid of an ACNT preform measuring 2.8x2.9x1.7 mm (length, width and height) had a mass of 2.26 mg. The measured preform density is 0.165 g cm^{-3} and commonly reported density of MWCNTs is 2 g cm^{-3} [190]. Using the density of air at 25 ^{o}C of 1.2 x 10^{-3} g cm^{-3} gives a V_{cnt} of *ca.*8 %.

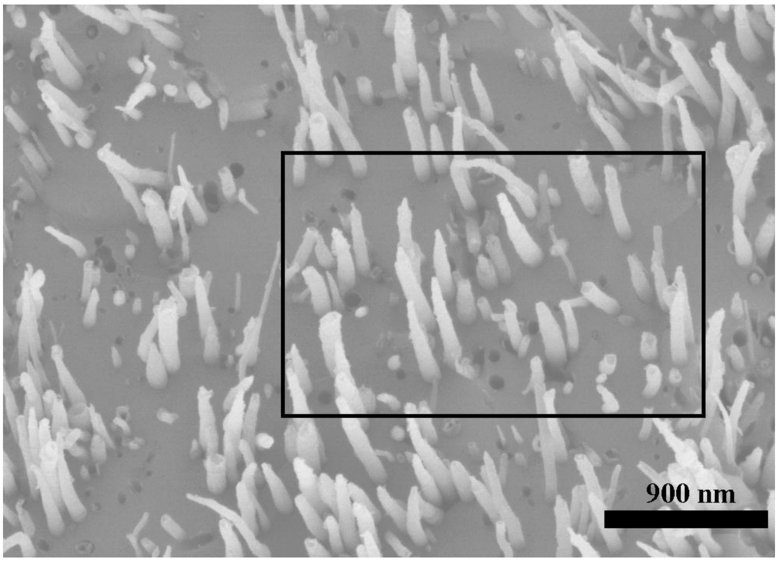

Figure 4-20 SEM image of a dried sol infiltrated sample. The Rectangular area measures 2340 x 2030 nm (y length of the box corrected for 45^{o} tilt). The number of CNTs counted in the box is 83 giving an area fraction of 9 %.

The volume fraction of the CNTs in the composites is 20 ± 2 % which is a 10% increase compared to the preform. This is because the hot pressing of the sol infiltrated ACNT preforms resulted in shrinkage in the in-plane direction. Attempts to disperse more than 10% CNTs in ceramic matrices by conventional methods have resulted in agglomeration which severely compromises the mechanical properties of composites [74] [91].

The CNTs produced are of high carbon purity (99% carbon) and low defect density. The folds and Fe inclusion in the inner core of the CNT (figure 4-5a) are common to CVD grown CNTs [191]. Evidence of such defective graphitic structures [192] appear in the Raman spectra (D-peak). A comparison of the G and the D peak is an indicator of the quality of the CNTs [192]. The D/G ratio of 0.3 - 0.4 suggests that the CNTs have low defect density. A smaller ratio would be desirable however the aerosol CVD method is known to produce CNTs with the folds previously mentioned. High temperature treatments (3000 ^{o}C) have been shown increased graphitisation of CNTs [193] thus reducing the D/G ratio. The costs associated with this process are great thus it is not ideal as a processing route. Raman analysis of CNTs within the hot pressed CNT/ABS glass composite showed a small increase in the average D/G ratio from 0.35 to 0.4 suggesting that processing of the composite introduced some defects on the CNTs. This is attributed to the 1100 ^{o}C consolidation temperature in the presence of metal oxides making up the matrix, which would react with the CNT graphitic walls at such elevated temperatures. The onset of oxidation of 550^{o}C is indication of good quality nanotubes as defective nanotubes oxidise at temperatures lower than 550 ^{o}C [46]. The high oxidation resistance (550 ^{o}C) obtained from TGA results is also important in the sintering process of the composite. As high temperatures are involved and the presence of oxygen would destroy the CNTs, the high oxidation onset is desirable.

TEM studies into the nature of the interface revealed that the ABS glass matrix effectively wetted the MWCNTs with no voids or cracks around the interface. This demonstrated the good adhesion of the glass onto the CNT. Higher magnification TEM images of the interface such as in figure 4.18d showed no clear transition between the CNT and the matrix suggesting a reaction bonding might have occurred during processing.

4.4. Summary

A bulk aligned multi-walled carbon nanotube/aluminoborosilicate glass composite was successfully fabricated from CVD grown aligned CNT preforms. The preforms are clean and consist of CNTs with average diameter of 80nm. The composites were 90 ± 2% dense.

Sol gel processing generally resulted in porous structures thus pressure and heat was used for consolidation. This processing method resulted in increased volume fraction of the CNTs from 10 ± 2% in the preform to 20 ± 2% in the composite.

Raman studies and TEM images showed that processing of the composites (infiltration and hot pressing) drastically alter the CNTs. Raman studies showed a small increase in the D/G ratio from 0.35 to 0.40 after hot pressing of the sol infiltrated preforms suggesting the processing induced some defects on the CNTs.

Alignment of the MWCNT in the composite was maintained and demonstrated by fracture surfaces showing pull-outs and sword-in-sheath failed MWCNT (figure 4-15). Additionally, FIB cross sections observed by SEM (figure 4-16) and TEM (figure 4-18b) revealed aligned arrangement of the CNTs in the composite. Importantly, the present processing route results in a well dispersed CNT composite with no regions of agglomeration. 3D tomography by FIB and SEM (figure 4-17) confirmed that the CNTs are continuous within the composite.

TEM studies on the nature of the interface shows that the ABS glass matrix effectively wetted and bonded to the MWCNTs. For mechanical properties, the interface between the CNTs and the matrix plays an important role. In particular, effective load transfer to the CNTs from the matrix during loading is expected to result in improved strength in the composite. The next chapter looks into the mechanical properties of the composites produced in which the interface properties will be discussed further.

CHAPTER 5

Investigation of Mechanical Properties

5.0. Overview

This chapter looks at the performance of the aligned MWCNTs/borosilicate glass composites under different loading conditions. Section 5.1 looks at the results of hardness and elastic modulus of the composite by microindentation and nanoindentation. Section 5.2 reports the compressive strength of the composites, ACNT preforms, and borosilicate glass. Section 5.3 describes the bend strength results of the composites and glass using microcantilever beams. In section 5.4, results of fracture toughness from notched microcantilever beams are reported. Finally, section 5.5 discusses and summarizes the mechanical properties of the composites in relation to ACNTs and borosilicate glass.

5.1. Indentation Results

Figure 5-1a shows the load-displacement graph obtained from nanoindentation of the composite in which the indenter tip was perpendicular and parallel to the alignment of the CNTs (transverse and axial direction). For comparison, a result from an indentation in the ABS glass is also presented. The initial sections of the load-displacement graphs are not smooth possibly due to asperities on the contact surface.

The nanoindenter imprint for a transverse indentation is shown in figure 5-1b with a contact area of µm in dimensions, implying several CNTs were under load during the test.

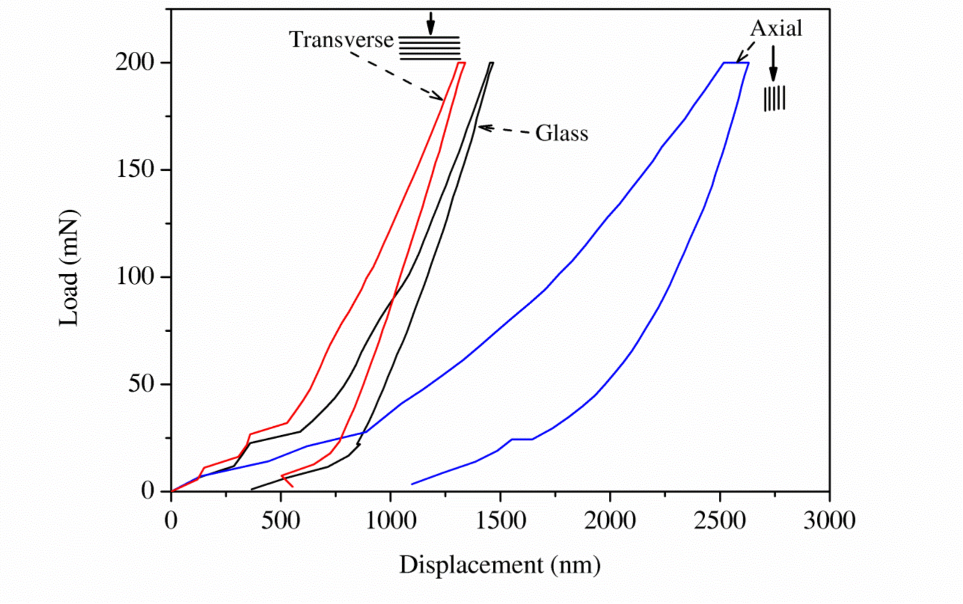

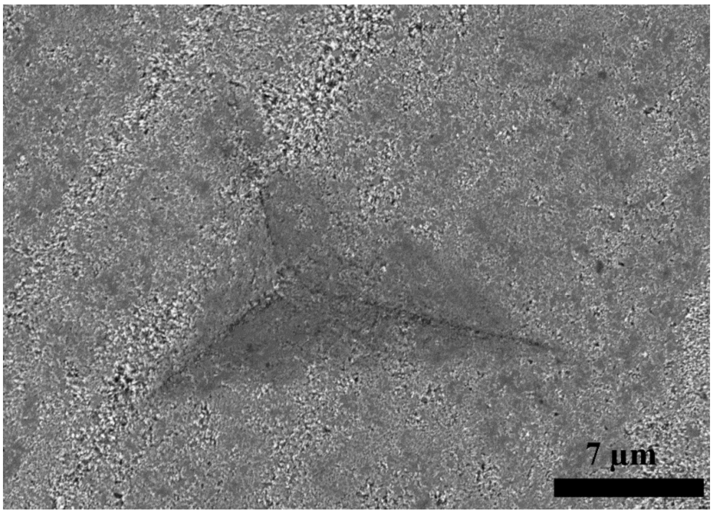

Figure 5-1 a) A representative load-displacement graph for nanoindentations on the composite in different orientations and ABS glass matrix and b) an SEM image of a representative Berkovich indenter imprint on a transverse nanoindentation test.

Table 5-1 summarises the results from nanoindentation results for both the ABS and composites in the different orientations. The hardness and reduced elastic modulus E_r were obtained as outlined in chapter 3 section 3.3.1.2. Nanoindentation in the transverse direction showed an improvement of 10% and 28% in stiffness and hardness respectively compared to the ABS glass matrix. Additionally, indentation in the transverse direction shows improvements of *ca.* 170% and 430% in elastic modulus and hardness respectively compared to axial indentation. The glass hardness and stiffness results are typical for the borosilicate glass tested with similar hardness result having been reported for a similar composition of glass [105]. In this study, a modest improvement in both stiffness and hardness in the transverse indentation direction is obtained. However, a reduction in the stiffness and hardness in the axial direction is observed.

Table 5-1 Summary of the nanoindentation results for glass and both the axial and transverse directions for composite.

	ACNT/ABS composite		**ABS glass**
	Tip parallel to CNTs (Axial) 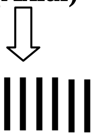	**Tip perpendicular to CNTs (Transverse)** 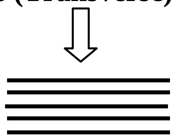	
Elastic Modulus (GPa)	26.4±0.8	70.6±3.3	62.9±2.9
Hardness (GPa)	1.8±0.1	9.6±0.5	7.4±1.3

Using Vickers indentations, higher loads of up to 10 N applied for 10 seconds resulted in cracks in the composite and glass. Typical residual indentations on glass and composites in two orientations are shown in figures 5-2a-f. Indentation in the transverse direction (figure 5-2a) resulted in suppressed cracking unlike in the axial direction (figure 5-2b) where extensive radial cracking are observed. The radial cracks appear to originate from the corners (figure 5-2c). Also, in the transverse test orientation, CNTs are observed to bridge cracks (figure 5-2b) while in the axial test, cracks are deflected around the CNTs as shown in figure 5-2d. In glass, both the radial and lateral cracks are more pronounced and extensive damage is demonstrated by a chip being removed from the indentation volume as shown in figure 5-2e & f. This is because the ABS glass is an anomalous glass hence it densfies under the indenter. This phenomenon is however completely suppressed in the composites under the same load. This is a clear indication that CNTs in the composite improved the damage tolerance of glass.

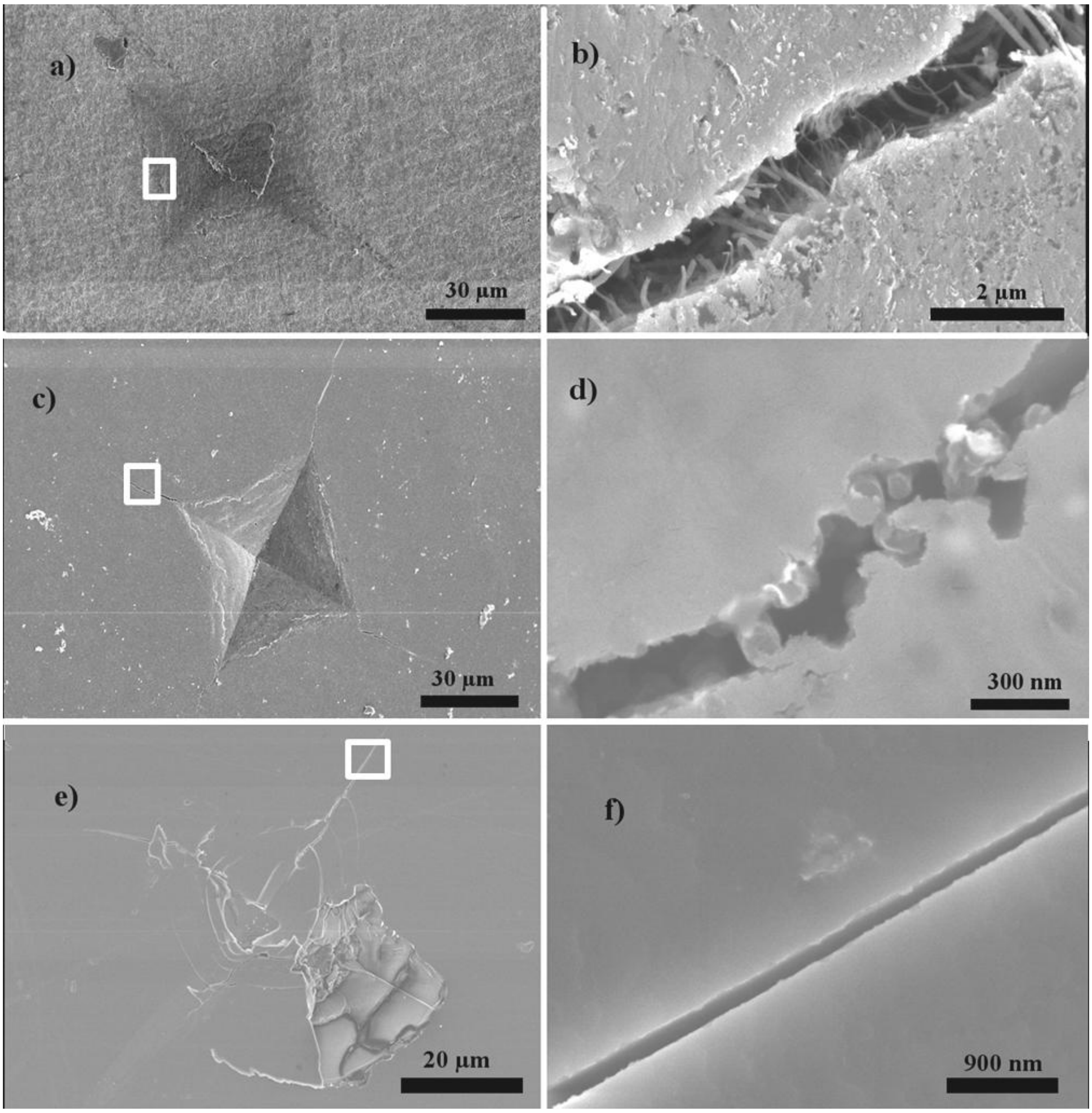

Figure 5-2 SEM images of Vickers indentation imprints of transverse (a) and axial (c) composites and glass (e) using 10 N load. b, d & f are the corresponding zoomed in sections highlighted in white on images a,c, and e respectively.

5.2. Compression Test Results

This section reports the results of the measurements of compression properties of the composites. It must be mentioned that the strain measurements are obtained from the displacement of the instrument which is also compliant therefore overestimates the strains in the specimens.

There are two regions of slope in the compression test plots (figure 5-3a-c). The low slope region in the compression tests represents the bedding in region which is attributed to difficulty in obtaining absolute flat contact surface between the compression platens and the sample. The high slope region can be used (in principle) to obtain the compressive elastic modulus of the samples.

The glass compression graph (figure 5-3b) shows several cracking events typically at strains of < 1%. Pieces were observed to break off before final failure of the glass. The compressive strength (σ_f) of the ABS glass is 66 ± 9 MPa. Previous reports show that borosilicate glass of percentage composition of 81 wt%-SiO_2, 13 wt%-B_2O_3, 4 wt%-Na_2O and 2 wt%-Al_2O_3 has a compressive strength of 160 MPa [194]. The bend strength of macroscopic specimens of the same composition as the ABS glass used in the present study is 50 MPa [91].

For the composites (figure 5-3c), matrix cracking was observed at strains ranging between 2–5 %. Also, ‘graceful failure’ was observed in the composites unlike in glass where there is a sudden drop in load beyond σ_f of glass. The compressive failure stresses and strains for the different sets of materials (ACNT, ABS and ACNT/ABS composite) are reported in table 5-2.

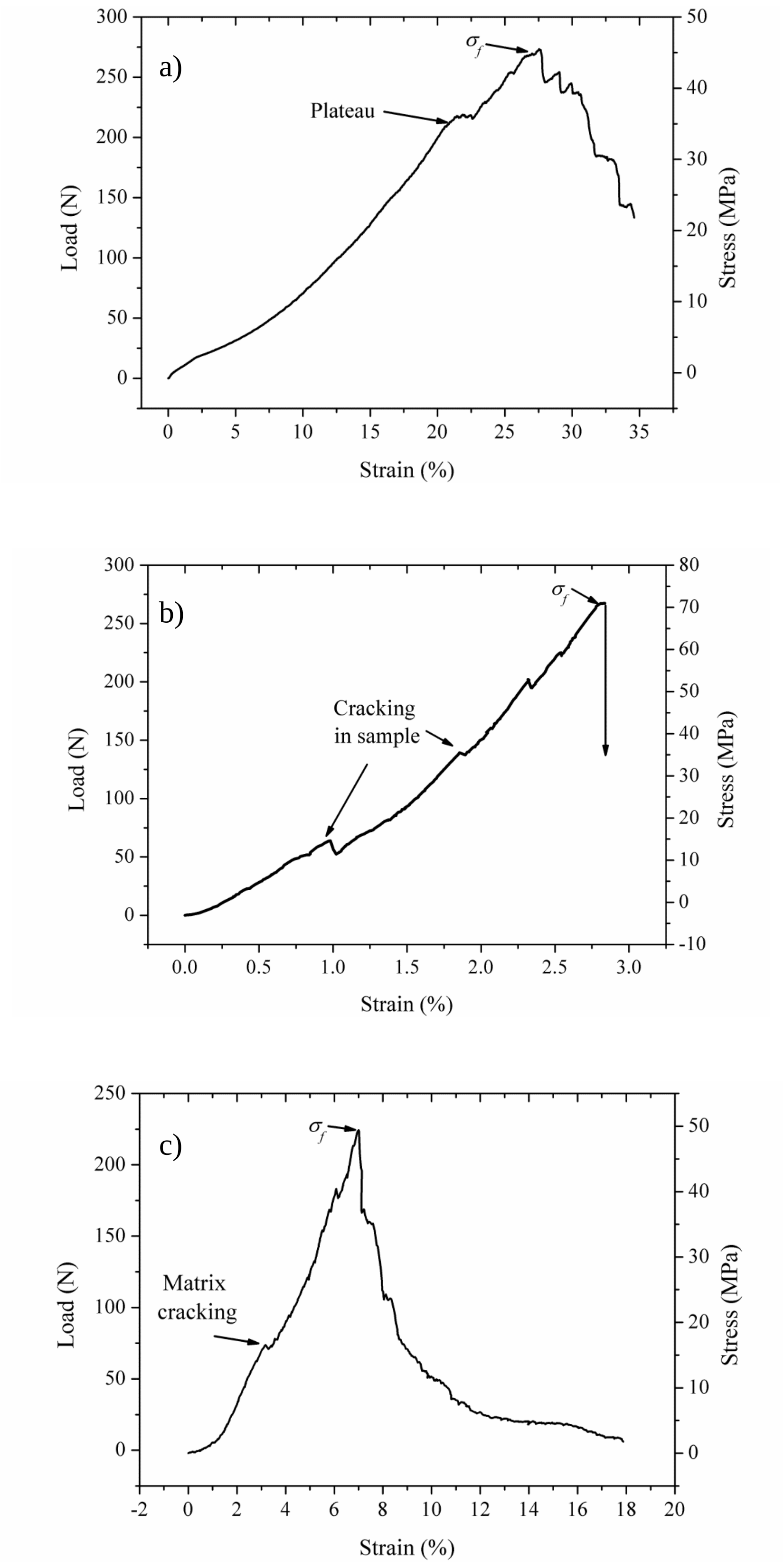

Figure 5-3 Representative stress strain curves for a) ACNT preform b) ABS glass and c) ACNT/ABS composite

Table 5-2 Average compressive properties for ACNT preforms (six measurements), ABS (four measurements) and ACNT/ABS composite (four measurements)

Sample	**Failure Strength σ_f (MPa)**
MWCNT Preform	40 ± 6
ABS glass	66 ± 9
MWCNT/ABS Composite	64 ± 9

SEM images of a preform after compression are shown in figure 5-4a and b. CNT buckling in the preform is clearly evident. SEM images of the ACNT/ABS composite after compression tests show regions with MWCNT pull-outs and crushed debris (figure 5-5a). There is no evidence of buckling of the MWCNTs in the composite. The glass fracture surface is smooth and features such as ridges commonly referred to as hackles are observed (figure 5-5b).

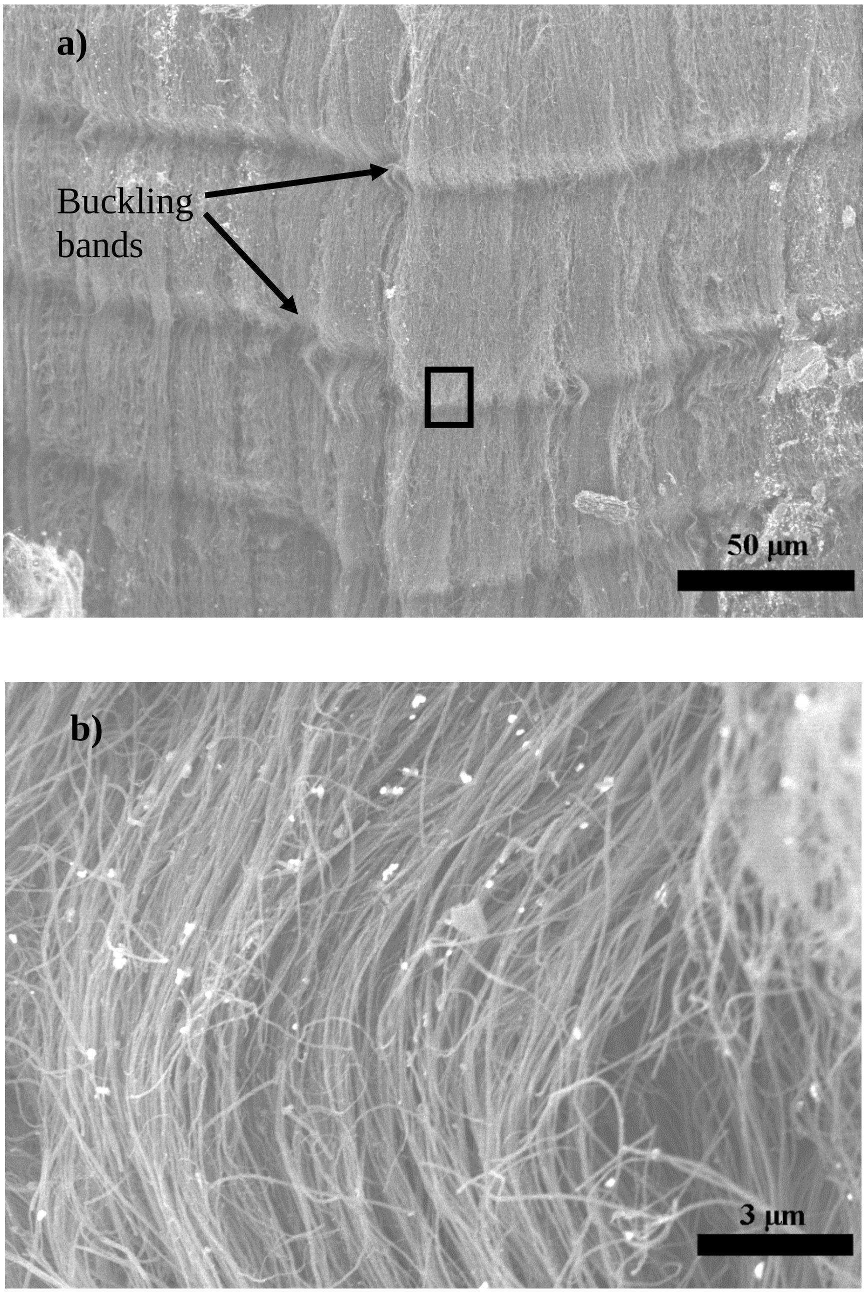

Figure 5-4 SEM images showing a) buckled bands in the ACNT preform after compression testing and b) a close-up image of the box (□) in figure 5-4a showing buckled MWCNTs.

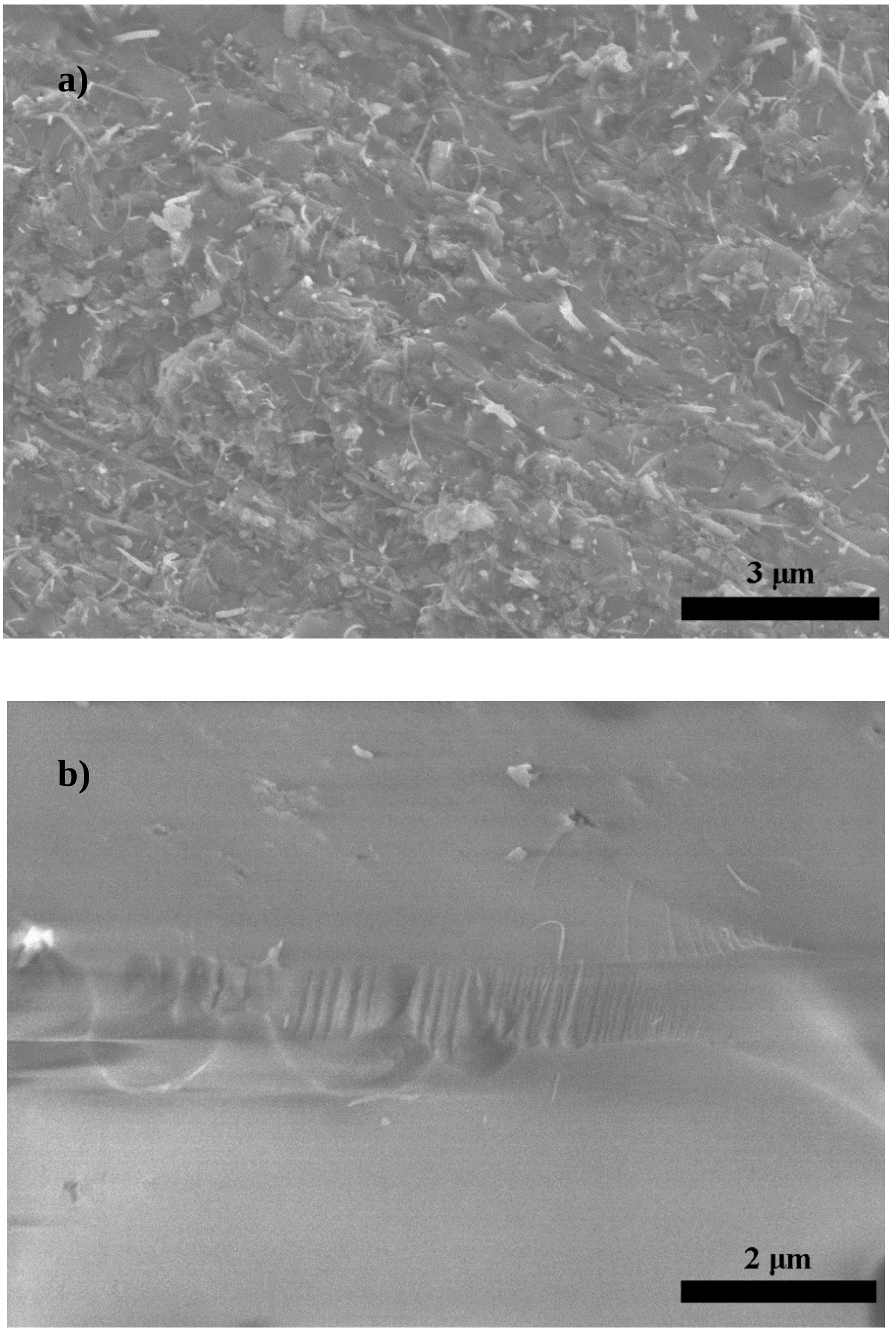

Figure 5-5 SEM image of a) composite fracture surface showing MWCNT pull-outs after compression testing and b) of ABS glass showing smooth surface with hackles.

5.3. Microcantilever Beams Tests

In this section, the results of the fabrication of the cantilever beams in terms of the lengths and shape of the beams, and the bend test results are provided.

5.3.1. Microcantilever Beams Fabrication and Geometry

A schematic diagram of the microcantilever beams produced is shown in figure 5-6a and the corresponding beams in a composite are shown in figure 5-6b. Figures 5-7a-d shows the different stages of fabrication of the microcantilever beams. Figure 5-7a shows FIB milled set of trenches of depth 10 µm which leaves a cantilever section measuring *ca.* 30 x 10 µm (length by width). The length of this section is parallel to the alignment direction of the CNTs and the section is not suspended at this stage. The second milling stage involved undercutting the cantilever section to produce a suspended cantilever beam. Figures 5-7b shows the sample tilted at 45° prior to undercutting which is shown in figure 5-7c.

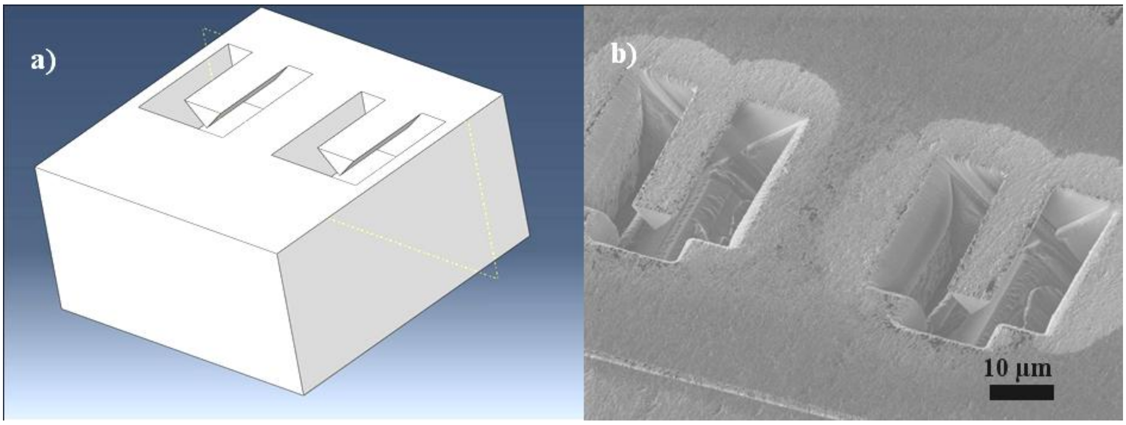

Figure 5-6 Microcantilever beams a) schematic and b) in CNT/ABS composite.

After one side of the section was undercut, a 180° rotation was performed and the opposite length was undercut. This resulted in a beam of triangular cross section with sufficient clearance beneath as shown in figures 5-7c (side view) and 5-7d (plan view). Cleaning using low beam currents was performed to remove re-deposited material (shown in figure 5-8b) on the beam.

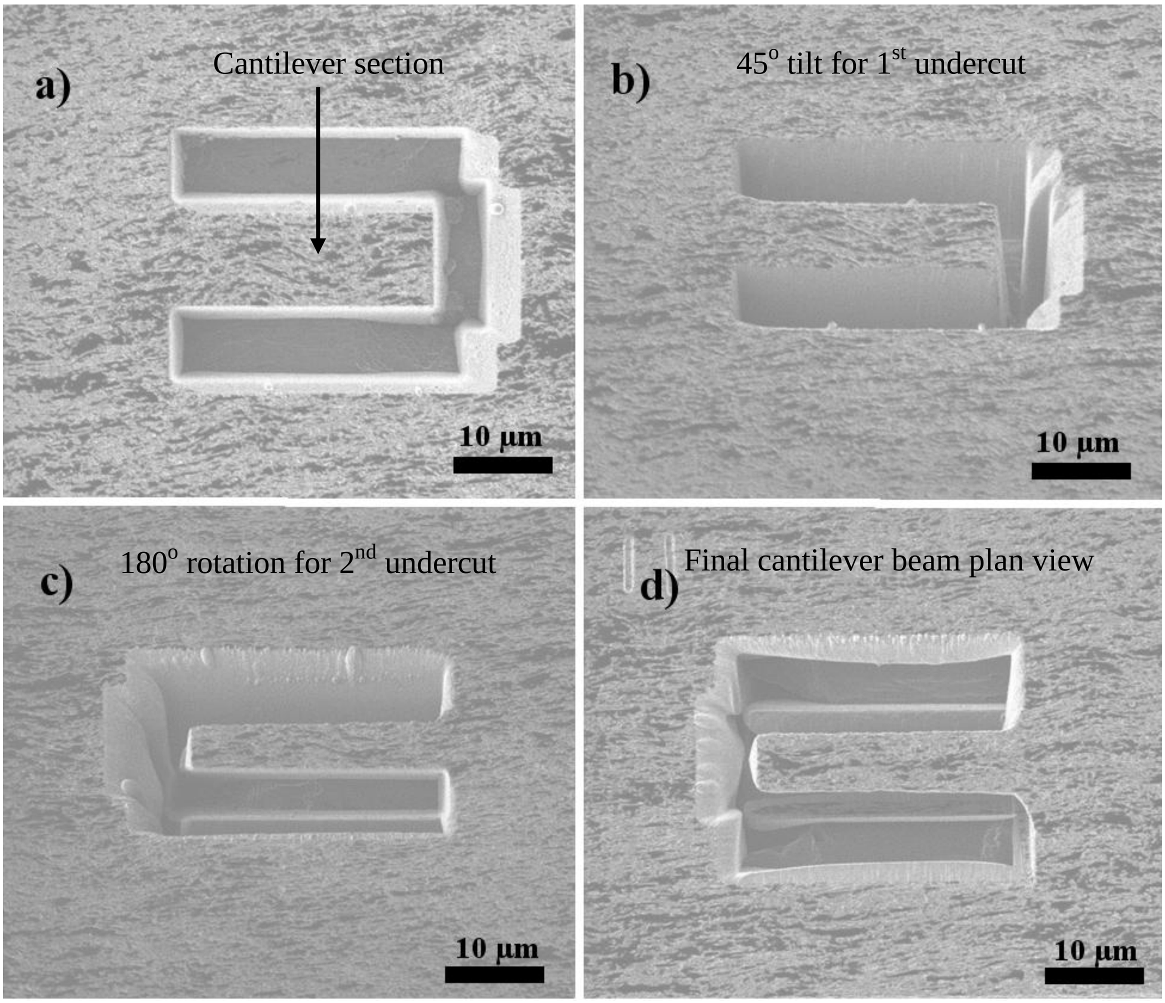

Figure 5-7 SEM images showing the stages in the fabrication of a microcantilever beam.

The cantilever beams produced had lengths, widths and heights (defined in figure 5-8 a & b as *l*, *w*, and *h*) typically between 20 – 28 µm, 4 – 7 µm and 2 – 5 µm respectively. The variation in the dimensions was due to the cleaning process to remove re-deposited material. The width and the length were measured from different points along the beam and an average value was obtained. The beam heights were determined from a measurement taken from a 45° tilted SEM image such as figure 5-8b. The measured height was corrected for the 45^o projection. A summary of the dimensions of a typical beam is presented in table 5-3. Figure 5-8b also confirms that the beams are isosceles with the apex having an angle of 90 ± 10^o. Free ends of the cantilever beams were clean with little or no re-deposited materials.

Table 5-3 A summary of a microcantilever beam dimensions.

Dimension	**Width**	**Length**	**Height**
Average	5.6	26.1	3.3
Standard deviation	0.1	0.2	-

To obtain the area fraction of the CNTs in the beam, image processing (using Image J software) of SEM images (such as in figure 5-8b) was used. The free end reveals features of nanotubes in spherical & elliptical shapes. For a given area of the cross section of the cantilever beam, the matrix is subtracted leaving only the area occupied by the CNTs. Figure 5-9 shows a result of one such image processing and the corresponding CNT volume fraction. The average area fraction of nanotubes from five such processed images is 20 ± 2 %.

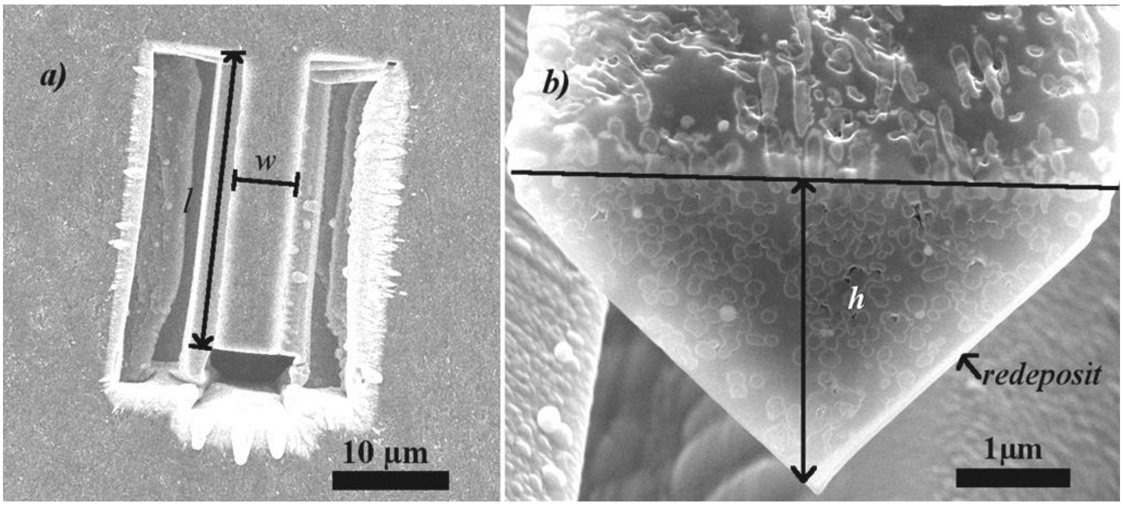

Figure 5-8 a) SEM images showing the length *l*, width *w* and height *h* of a cantilever beam. b) The re-deposited material which was removed prior to testing.

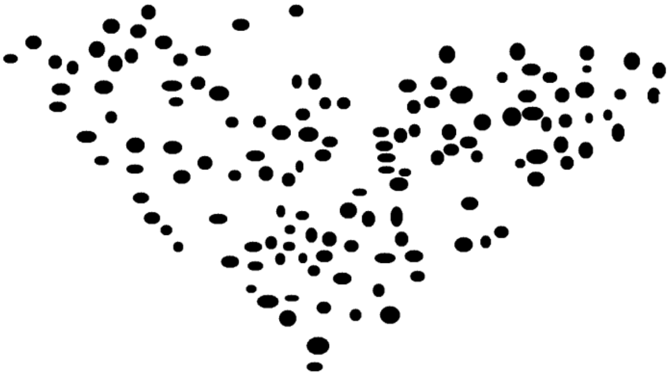

Area	**9.2 µm^2**
MWCNT Area	**1.7 µm^2**
Number of CNTs	**166**
Volume fraction	**18%**

Figure 5-9 An example of image processing result showing the regions covered by the nanotube and the corresponding nanotube area properties.

5.3.2. Microcantilever Bend Test Results

The bend tests of the microcantilever beams involved two processes. First, a high resolution scan of the cantilever beam to be tested was obtained by atomic force microscopy (AFM) using an MTS nanoindenter instrument (fitted with NanoVision stage capable of producing AFM images). This is important for the placement of the nanoindenter tip on the microcantilever beam in the second step. An example of an AFM image obtained is shown in figure 5-10. In order to create the scan, an optical image was initially used to locate the beams. The second step involved applying a load on the microcantilever beam with the nanoindenter at a location near the free end (see figure 5-10). This was done while monitoring the load and displacement. The load-displacement results are presented next.

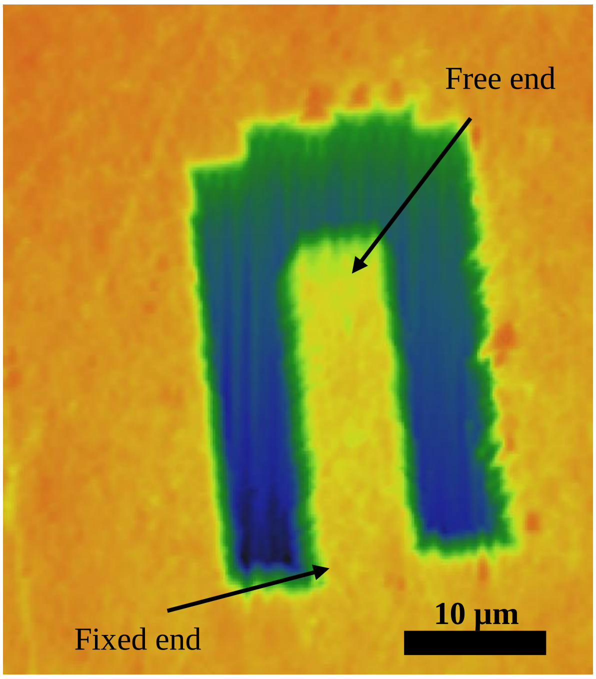

Figure 5-10 An AFM scan of a cantilever beam used to locate the free end and accurately position the indenter tip prior to loading using the nanoindenter.

5.3.2.1. Results for the ABS Glass Bend Tests

Figure 5-11a shows a typical load-displacement graph for a ABS glass beam loaded to failure. The ABS glass shows linear elastic behaviour (load and displacement increased in a linear relationship, hence no plasticity occurred) obeying Hooke’s law followed by brittle fracture. There was no evidence of sub-critical crack growth as the plot remains linear through the test. The fracture surface of the glass tested beams appears smooth as shown in figure 5-11b.

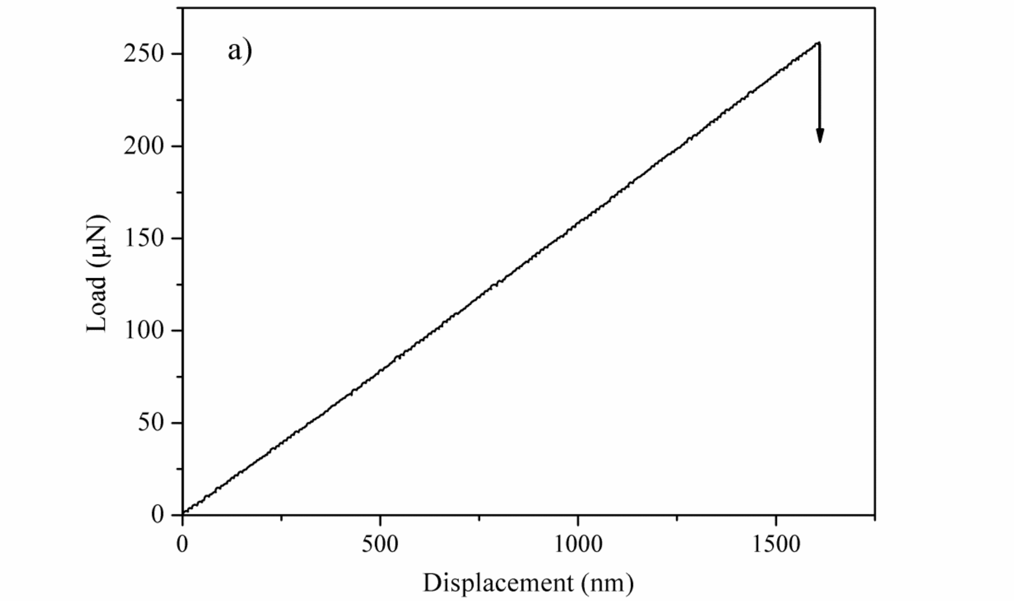

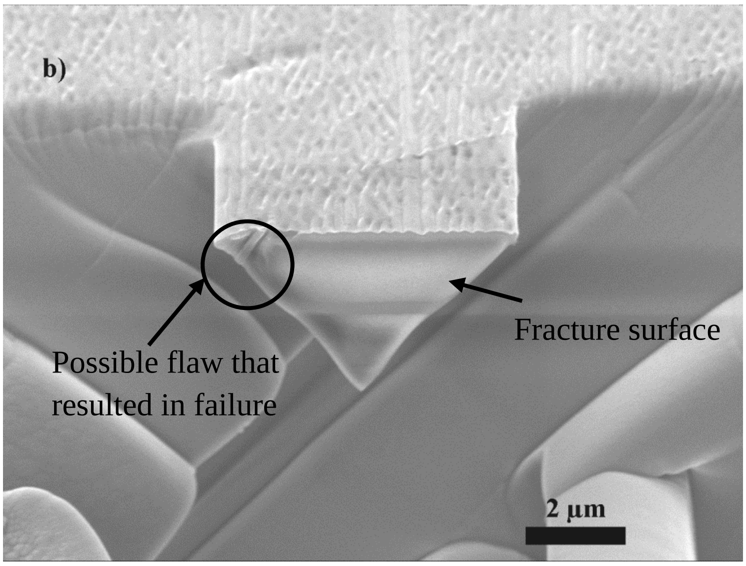

Figure 5-11 Representative a) load-displacement plot for a glass microcantilever beam loaded to failure. b) Fracture surface of a test glass beam.

Applying the load-displacement data and beam dimensions to equation 3.13 and 3.15, a maximum tensile stress vs. strain graph (figure 5-12) is obtained. The effective beam length was not the entire beam as the indenter tip was placed a small distance (2-3 µm) from the free end of the beam.

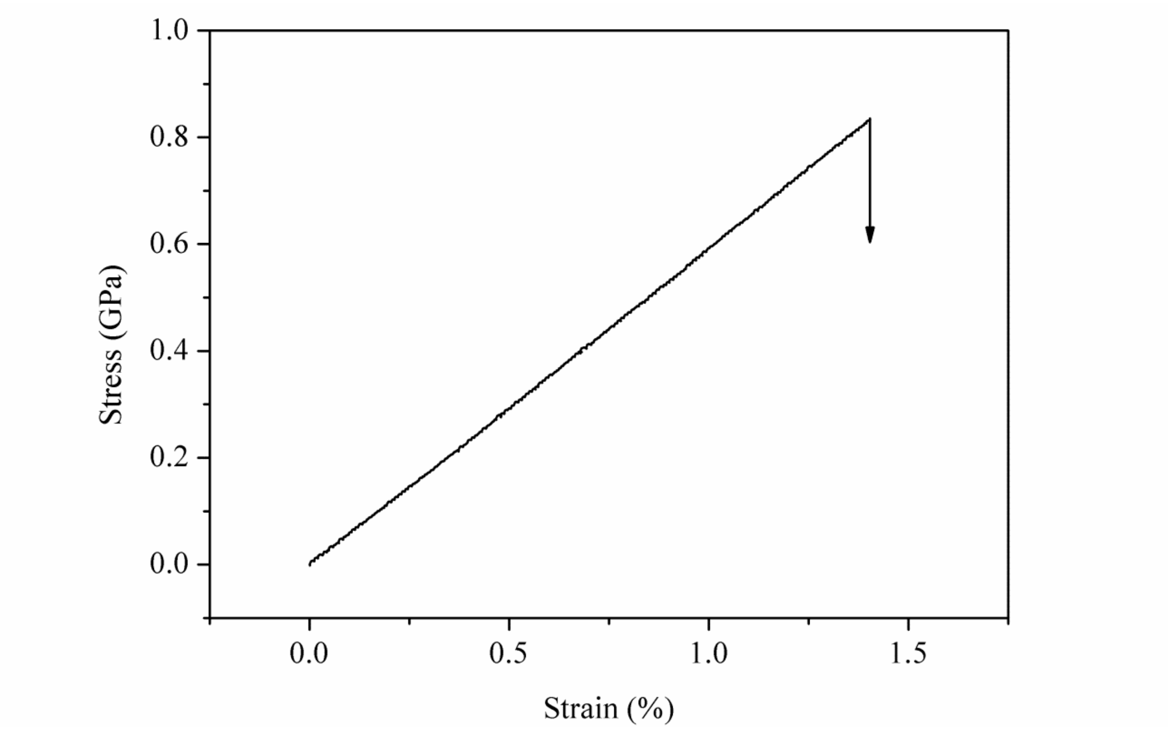

Figure 5-12 Representative stress-strain graphs for ABS glass.

The bend strength of glass (σ_{glass}) is defined as the maximum tensile stress before failure. The results are presented in table 5-4 with the corresponding strains at failure. Elastic moduli of the glass (E_{glass}) cantilever beams were obtained from the gradient of the stress-strain graph. The E_{glass} results for 5 ABS glass microcantilever beams are presented in table 5-4. The results agree well with reported values for bulk borosilicate glass [195].

Table 5-4 Properties of ABS glass microcantilever beams

Beams	Bend Strength (GPa)	Maximum Strain (%)	Elastic Modulus (GPa)
a	1.4	2.1	67.1
b	1.9	2.5	65.5
c	0.9	1.4	60.5
d	0.4	0.5	62.4
e	1.7	2.5	66.8
Average	1.3	2.5	64.5
Standard Error	0.3	1.4	1.5

5.3.2.2. Results for the ACNT/ABS Composite Bend Tests

An example of a load-displacement graph obtained from loading a composite microcantilever beam is shown in figure 5-13a. The loading region of the curve does not show a linear elastic behaviour as was observed in ABS glass. A profile with a curvature beginning at the onset of loading with different gradients at the beginning (A) and prior to maximum load (B) is observed. Figure 5-13b shows loading and unloading of a microcantilever beam to successive higher displacements until failure. The composite shows a residual displacement after each cycle yet there are no obvious steps in the load-displacement curve.

The initial elastic moduli of the composites, E_{comp}, were obtained from the tangent at the origin of a stress strain curve such as shown in figure 5-14. The average initial elastic modulus for the composite was 84 ± 4.6 GPa for 5 samples (table 5-5). This is an improvement by *ca.* 30% to that of ABS glass. From table 5-5, the elastic moduli immediately prior to failure (figure 5-14) for the 5 microcantilever beams tested are on average 37% lower than the composite elastic modulus.

The bend strength of the composite, σ_{comp} is the maximum stress attained in the stress-strain graphs. There is no significant difference in the bend strength of the composite over that of glass. There was a small amount of stable crack growth prior to the load dropping abruptly at ultimate strength (figure 5-14).

Figure 5-15a and b shows SEM images of a beam tested to failure and a higher magnification image of the fracture respectively, which alludes to fracture toughening mechanisms such as pull-outs whose contributions are investigated further in section 5.4.

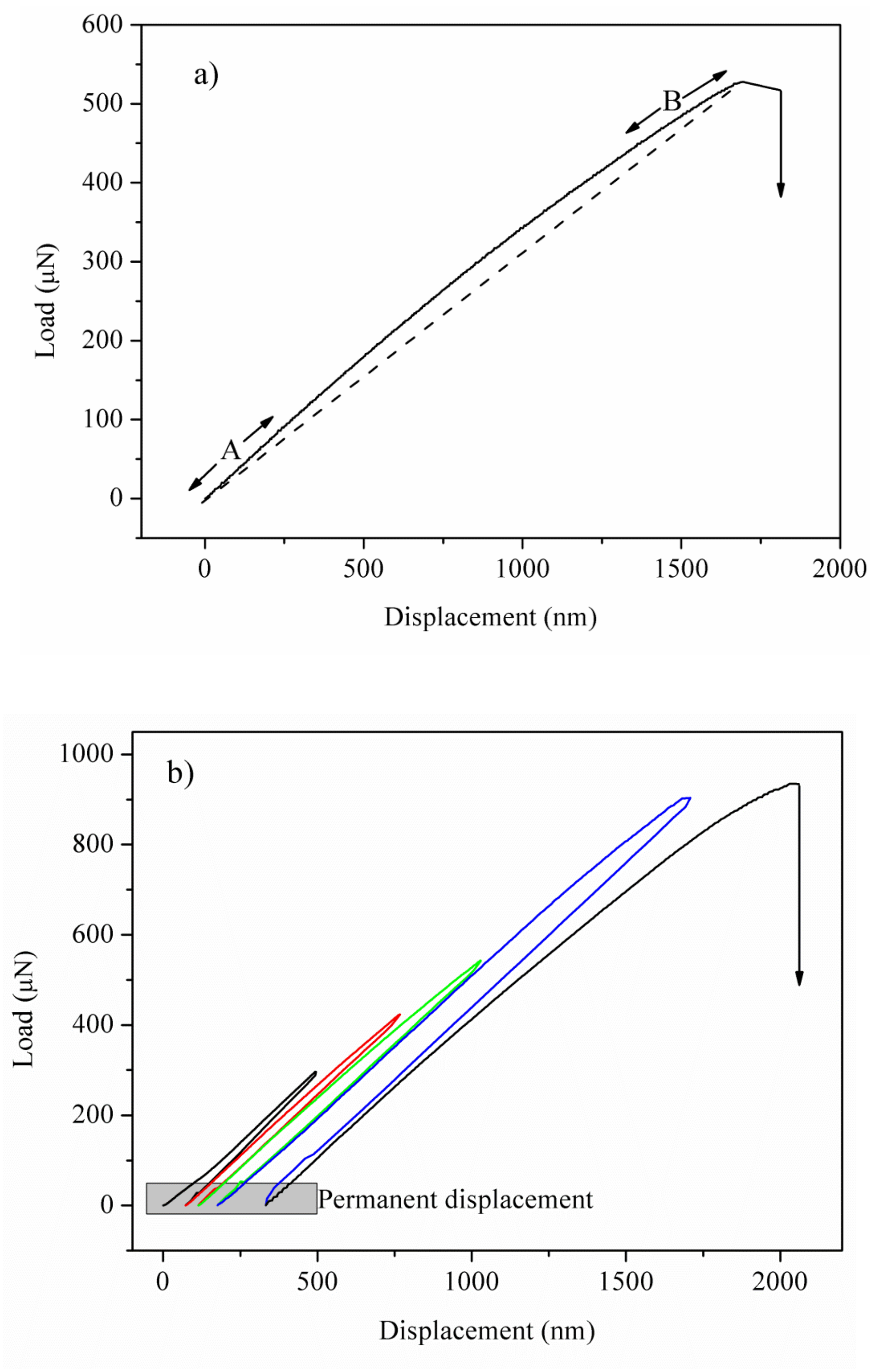

Figure 5-13 a) A typical load-displacement graph of CNT/ABS glass composite (dotted line added to show bowing). b) loading-unloading curve on the composite until failure.

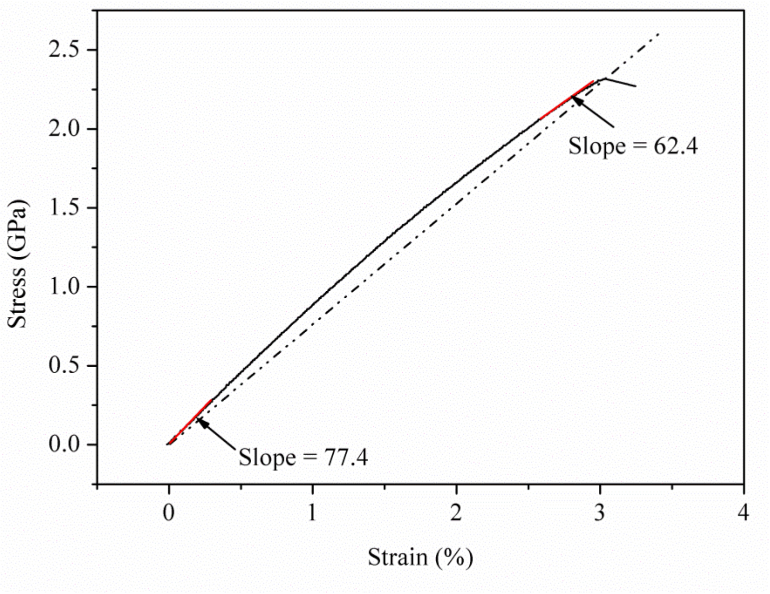

Figure 5-14 Stress-strain plot of a representative composite tested to failure showing changing in gradient in the profile.

Table 5-5 Properties of ACNT/ABS glass composite microcantilever beams

Beams	**Bend Strength (GPa)**	**Maximum Strain (%)**	**Initial Elastic Modulus (GPa)**	**Modulus Prior to Failure (GPa)**
a	1.4	4.0	77.4	62.4
b	2.0	5.3	79.4	67.8
c	1.2	3.0	89.7	61.1
d	1.0	2.5	88.5	64.4
e	1.4	3.7	86.3	52.3
Average	**1.4**	**3.7**	**84.3**	**61.6**
Standard Error	**0.2**	**0.5**	**2.5**	**2.6**

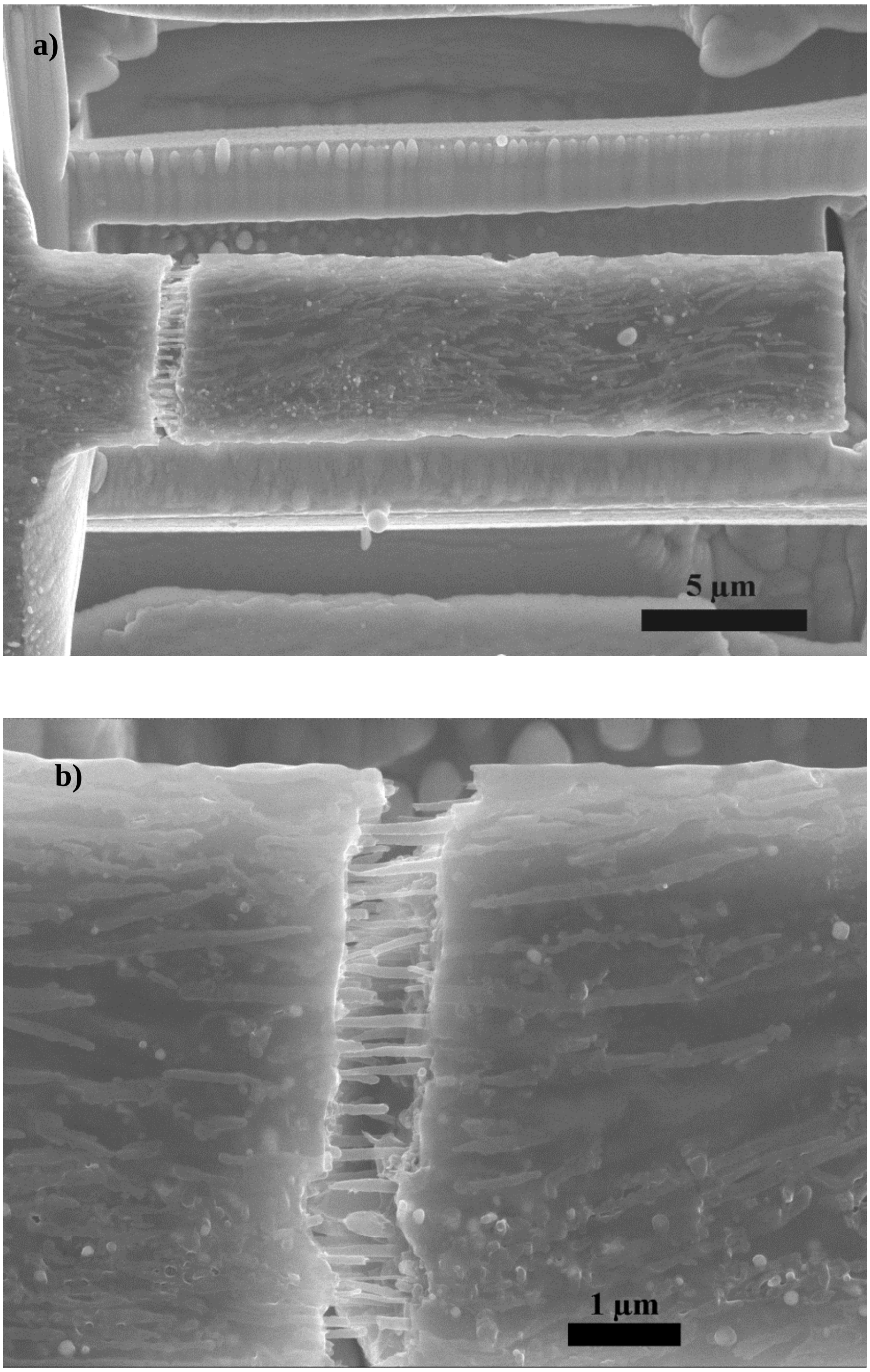

Figure 5-15 SEM images of a) a tested microcantilever beam and b) higher magnification of a fracture surface showing broken CNTs which suggest they were bridging the crack opening prior to being pulled out and failing.

5.3.3. Microcantilever Fracture Toughness Test Results

This section presents the results from testing microcantilever beams to measure fracture toughness. The microcantilever beams had been notched near the fixed end.

5.3.3.1. Notch Results

Figure 5-16 shows the beam geometry obtained for fracture toughness with the effective length L (indenter tip to fixed end) and Ln (indenter tip to notch). The beam width *w* and height *h* are obtained from SEM as with the bend strength tests (see figure 5-8). It is important to note that the notch depths were found to vary. This difference is due to the alignment of FIB and the different milling rates of the materials *i.e.* glass and composite. Using similar settings in the FIB for milling, significantly different notch depths were obtained *e.g.* in milling with 50 pA beam current at an inputted notch depth of 900 nm resulted in a notch depth of 800 – 900 nm in the composite while on the glass only *ca.* 500 nm was obtained. To mitigate this, different milling times were used.

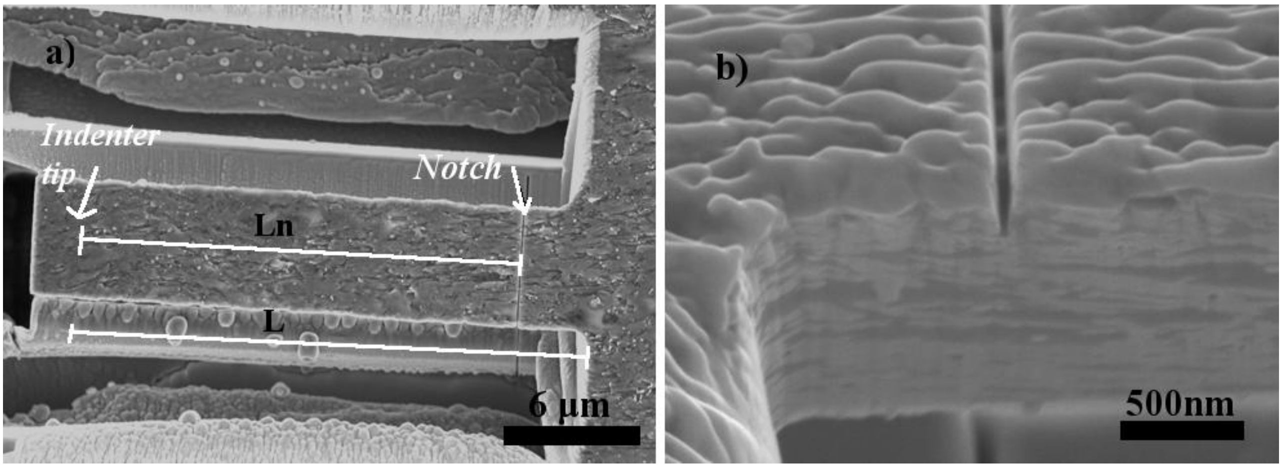

Figure 5-16 SEM images of a fracture toughness cantilever beam a) showing position of the notch near the fixed end b) side view of the notch.

5.3.3.2. Fracture Toughness of ABS Glass.

A typical load-displacement graph of a tested notched ABS glass microcantilever beam is shown in figure 5-17. An unstable crack growth is evidenced by a sudden drop in load at maximum strength. The loading experiments took *ca.* 5 minutes. The specimens fractured at the FIB milled notch which was confirmed by SEM (figure 5-17b). Also, similar images to figure 5-17b were used to confirm the notch depths.

The measured parameters from the nanoindenter were Load, *L* and displacement, δ. For a straight through edge crack under uniform tensile stress the fracture stress is related to maximum flaw depth (notch depth) *c* and the fracture toughness (the critical stress intensity factor K_{IC}) by the equation 5.1 [196]

$$\sigma_f = 1.12 \times \frac{K_{IC}}{\sqrt{\pi c}} \qquad \text{Equation 5.1}$$

It must be noted that 1) the equation is not strictly valid for triangular cross section beam as stress varies over crack length, and there is no previous equation in the literature for triangular cross-section beam, 2) an approach of load factor resulted in similar results as using equation 5.1. For this reasons it was important to compare specimens with similar crack lengths such that the relative results are consistent within themselves.

Using equation 3.15 and 5.1, failure stresses and fracture toughnesses for three tested glass microcantilever beams were calculated and are presented in table 5-6. The average fracture toughness of 0.7 MPa √m agrees well with previous reports of this composition of borosilicate glass [91] using macroscopic specimens tested by the single edge V-notched beam method.

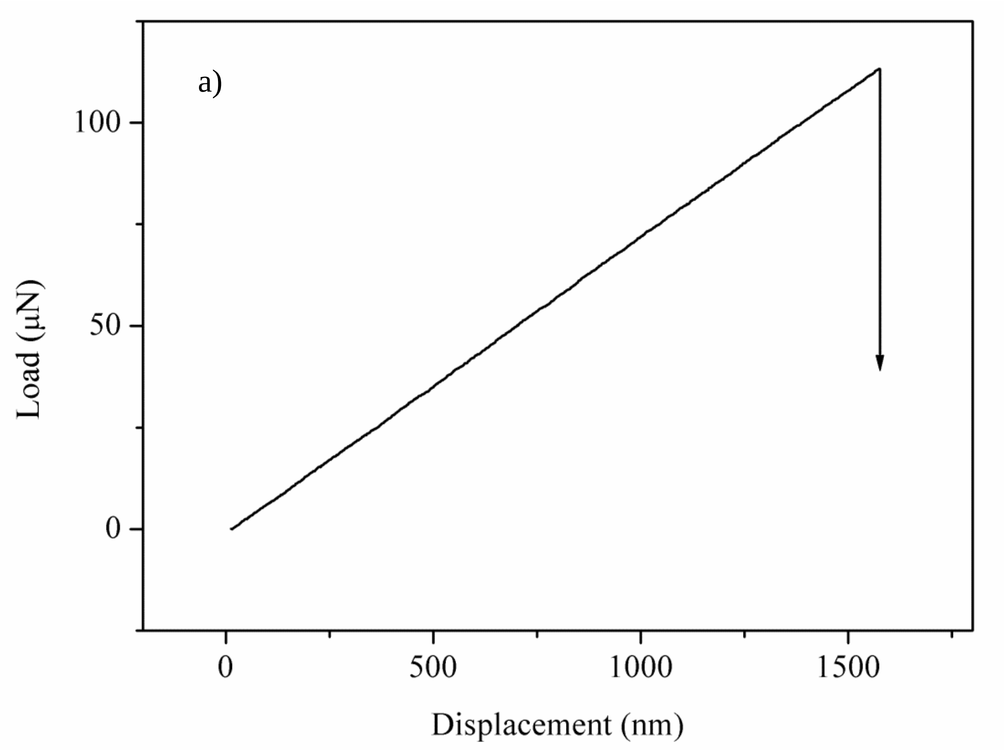

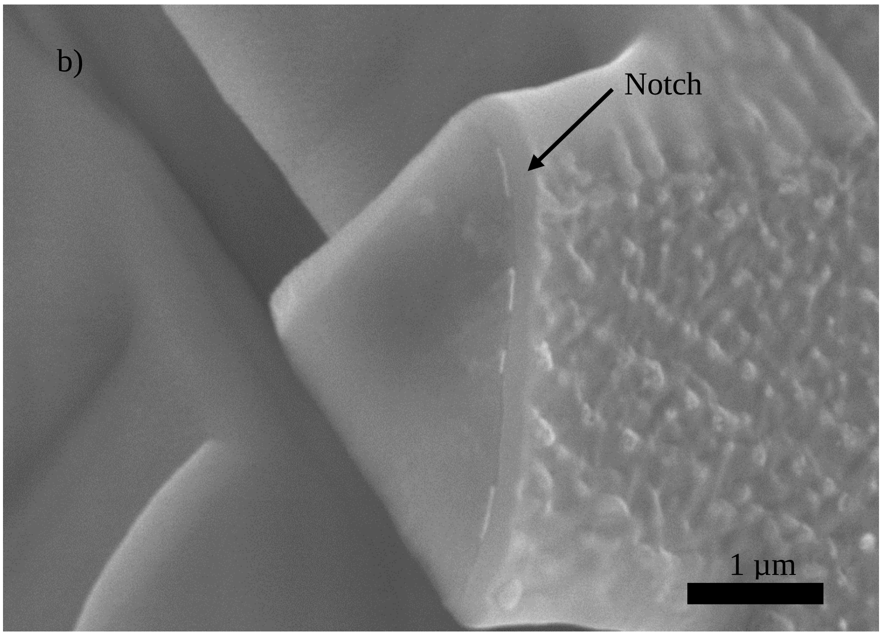

Figure 5-17 a) Load displacement graph of a fracture toughness test on glass and b) SEM image (tilt 45^o) shows that the failure occurred at the FIB notch.

Table 5-6 Fracture properties for ABS glass

Cantilever Beam	**Notch/Height ratio**	**Fracture Stress** σ_f **GPa**	**Fracture Toughness** K_c $MPa\sqrt{m}$
a	0.16	0.58	0.77
b	0.12	0.67	0.75
c	0.19	0.41	0.61
Mean		**0.55**	**0.71**
Standard error		**0.08**	**0.05**

5.3.3.3. Fracture Toughness of the Composite

Figure 5-18a and b show examples of load-displacement graphs of the CNT/ABS composite. The profile has several features not present in the ABS glass. Of significance is the region (B-C) in figure 5-18a over which the load plateaus or decreases (figure 5-18b) prior to a region of increasing load. This is followed by a region of stable reduction in load before failure. The extent of this region varied considerably (see figure 5-18 a and b).

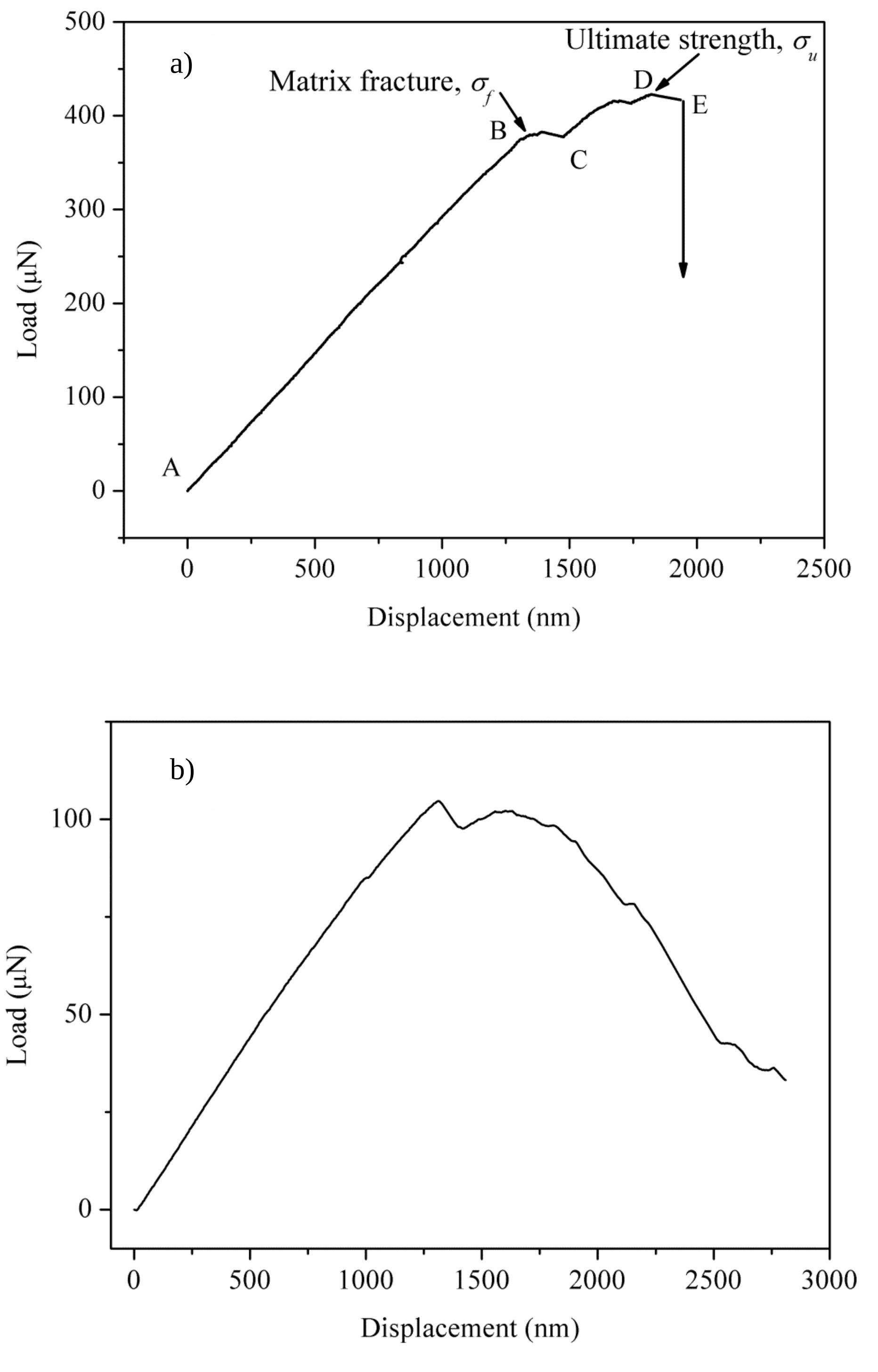

Figure 5-18 Typical load-displacement graphs of composites a) shows a small region of stable crack growth (D-E) while b) shows a greater region of stable crack growth.

Figure 5-19 shows an SEM image of a notched microcantilever beam loaded to just beyond point B shown in figure 5-18a. A crack extending (indicated by arrows on figure 5-19) nearly to the bottom of the beam is observed. It was difficult to determine with certainty if the cracks had traversed to the bottom of the beams. This is because the apex of the beam at the fixed end is largely shadowed from the electron beam in the SEM, which necessitated large tilt angles. Nevertheless, the image clearly demonstrates that there was no catastrophic failure of the matrix, and point B is the onset of matrix failure and is followed by a region of stable crack growth.

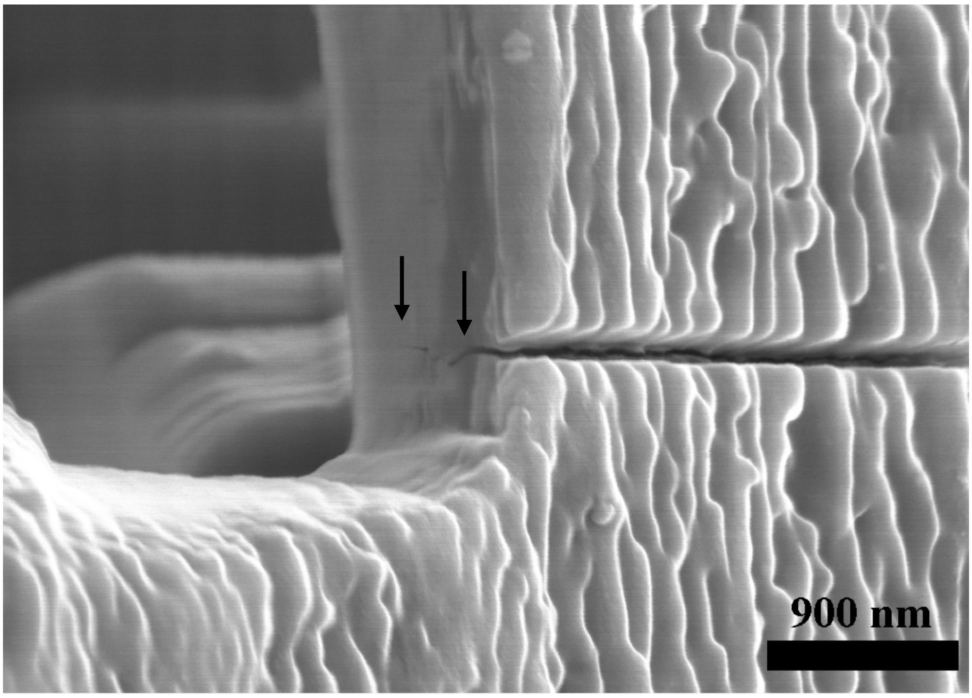

Figure 5-19 SEM image of a microcantilever beam loaded to the onset of matrix failure.

Using equation 5.1, the fracture toughnesses for composite microcantilever beams were obtained at point B and the results are presented in table 5-7. An average toughness of 1.4 MPa √m is obtained which is 100% improvement over the 0.7 MPa √m of glass. If the calculated K_c results were on an R-curve, the results would represent K_c near the beginning of the R-curve.

Table 5-7 Fracture properties of CNT/ABS glass composite

Sample	Notch/Height ratio	Fracture Toughness K_c $MPa\sqrt{m}$
a	0.23	1.71
b	0.23	1.73
c	0.26	1.57
d	0.33	1.34
e	0.24	1.21
f	0.36	1.40
g	0.29	1.33
h	0.29	1.34
i	0.31	1.30
Mean	**0.29**	**1.44**
Standard Error	**0.02**	**0.06**

The area under the load-displacement graph for a beam that showed significant stable crack growth after the maximum load (figure 5-18b) was used to estimate the fracture energy (identified here with the plateau of G_c of an R-curve) as 71 $\mathrm{Jm^{-2}}$. This result is an approximation as the graph does not return to zero. The G_c corresponds to a critical stress intensity factor, K_c of 2.4 MPa √m using equation 5.2 [196] (the E used is the average onset E from table 5-5). The amount of extra fracture energy required to improve the toughness of the ABS glass from 0.7 to 2.4 MPa √m is 63 $\mathrm{Jm^{-2}}$.

$$G_c = \frac{K_c^{\ 2}}{E} \qquad \text{Equation 5.2}$$

5.3.3.4. Observation of Fracture Surfaces

SEM images of the fracture surfaces are shown in figure 5-20 a and b. ‘Matrix pull-outs’ are observed as stubs of matrix at the embedded ends of the CNTs (labelled ‘x’) in figure 5-20a and b. The diameters of the ‘matrix pull-outs’ (~120 nm) are on average higher than those of the starting CNT diameters (~80 nm). This implies that the ‘matrix pull-outs’ are occurring in the glass. These pull-outs are CNTs coated with glass as was previously observed in TEM images (figure 4-18a), and will be referred to as glass-coated CNTs (GCNTs) in this thesis. It is noted that debonding of the GCNTs must have occurred for the pull-outs to be observed. The length of the GCNT (marked II) in figure 5-20a is *ca.* 100 nm. Also, the presence of a fracture ring around the embedded end of GCNTs in figure 5-20a (I) and figure 5-20b (Y), shows that debonding occurred in matrix. Using FIB slicing and imaging, the debond lengths obtained were *ca.* 200 nm implying that the fracture ring does not extend significantly into the matrix. Also, the tapering of the CNTs shows that sword-in-sheath failure occurred (figure 5-20a and b). This failure mechanism has been shown to occur in MWCNT [57]. A feature of the failure of CNTs whereby the sword is within the matrix is shown in figure 5-20b, labelled A.

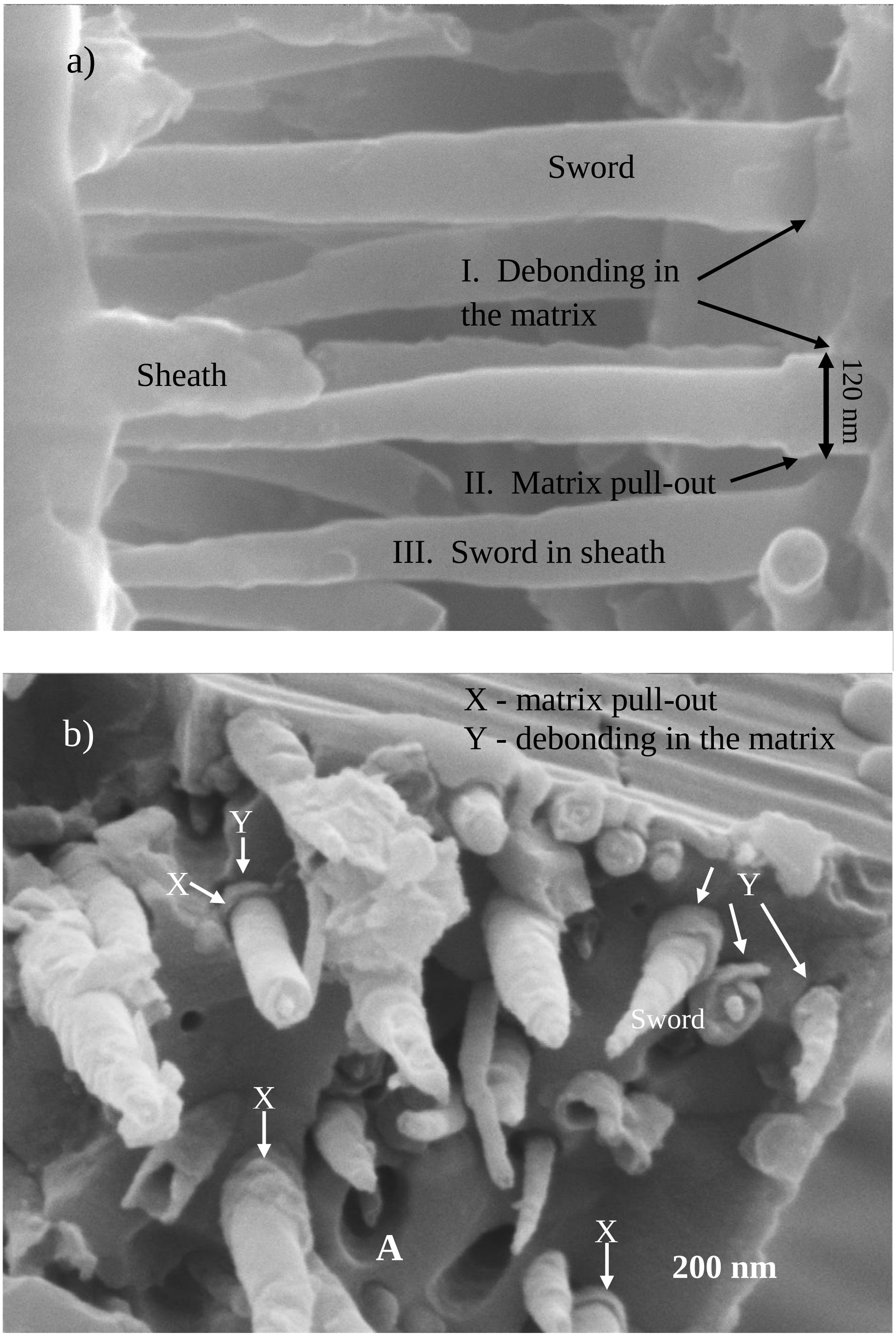

Figure 5-20 SEM images of a) side view and b) top view of fracture surfaces of the composite. Both images show debonding in the matrix, matrix pull-out and sword in sheath failure of CNTs on a fracture surface of composite.

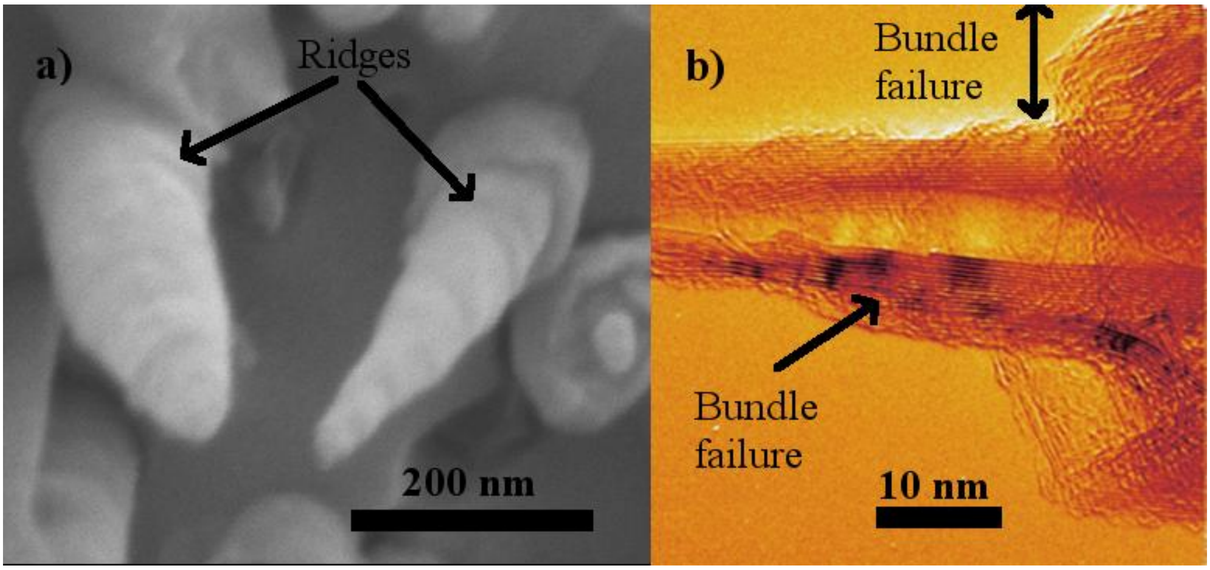

Figure 5-21 SEM image (a) showing ridges and TEM image (b) showing the several graphitic walls failure (bundle failure).

Figures 5-21a and b are SEM and TEM images of CNTs that had failed by a sword in sheath mechanism. The images show evidence of bundle graphitic walls failure. These are observed as ridges on the surface of the CNTs in figure 5-21a. TEM images also affirm the bundle failure behaviour as shown in figure 5-21b.

5.4. Discussion

The MWCNTs used in the present study consist of concentric walls which are held together by weak van der Waals forces. In the absence of any corrugation, the CNT walls are inherently prone to sliding (similar graphite). Loading and unloading graph of a composite beam to successive higher displacements until failure (figure 5-13b) alludes to interwall sliding. The successive loading resulted in permanent deformation as was shown in figure 5-13b. The permanent displacement is attributed to frictional forces which arise during sliding from van der Waals bonding between the CNT walls which contributes to inherent friction. Another reason for the permanent displacement is the presence of surface asperities in the concentric graphitic walls of the CNTs which were observed in the TEM images as folds (figure 4-5a). The interwall sliding is also thought to be the reason of the bowing in load-displacement graphs of the composite under bend tests. The sliding phenomenon compromises the strength of the composite by reducing load transfer from the matrix to the MWCNTs.

5.4.1. Elastic Modulus and Hardness

The elastic modulus of the CNTs, E_{cnt}, can be estimated from the linear elastic region of the composite stress-strain graphs from the microcantilever bend tests using the rule of mixtures (equation 5-6).

$$E_{cnt} = \frac{E_{comp} - (1 - V_{cnt})E_{glass}}{V_{cnt}} \qquad \text{Equation 5.5}$$

where E_{cnt}, is the elastic modulus of the CNTs, E_{comp} are the elastic moduli of beams a-e given in table 5-5, and E_{glass} is the elastic modulus of glass (64.5 GPa). The average volume fraction of CNTs in the composite, V_{cnt} is 20%. This gives an average

E_{cnt} value of 164 ± 28 GPa. The E_{cnt} obtained from the rule of mixtures is an under estimate of the true E_{cnt} because of 1) CNT interwall sliding and 2) residual porosity in the composite which were observed in FIB polished surfaces (figure 4-16). Nevertheless, the results are within reported values of CNTs produced by CVD [197]. A previous report showed that E_{cnt} of xylene/ferrocene solution derived MWCNTs was *ca.* 100 GPa [197] and tertramethylamine/ferrocene solution derived MWCNTs were 300 GPa [197]. Also, tests on individual MWCNTs grown by CVD have also shown elastic modulus below 100 GPa [198]. This spread in E_{cnt} data is attributed to different testing and production methods of the MWCNT (see table 2-1). In any case, the present study approximation of E_{cnt} of 164 GPa for MWCNTs produced from toluene/ferrocene solutions is well within the range of previous reports of CVD grown MWCNTs. Even with the uncertainties, it is evident that the E_{cnt} is higher than E_{glass}.

Nanoindentation in the transverse orientation showed improvements of 10% and 28% in elastic modulus and hardness respectively compared to glass. This suggests that load bearing by the CNTs is better in this loading orientation. The ability of CNTs to bend or stretch under loading (see schematic 5-22, transverse) is also alluded to in compression testing of preforms in which CNTs are seen to buckle as shown in figure 5-4a, and is discussed in section 5.4.2. The improvement in the E of the ACNT/ABS composite system in the transverse direction of indentation by ~10%, and in bend tests by ~30% compared to the ABS glass is attributed to the contribution of the E_{cnt} to the composite.

Indentation in the axial direction of the composite showed reduced hardness and elastic modulus compared to the ABS glass. This is attributed to poor load transfer to the inner graphitic walls of the CNTs (see schematic 5-22, axial). Also, in this test orientation the glass matrix properties dominate the composite properties thus most of the load is borne by the glass. The load bearing by the glass is alluded to in SEM image figure 5-2d, in which a crack approaching CNTs was deflected around the CNTs. The deflection of the crack occurs in the matrix and not at the actual CNT/ABS interface which was shown in 1) TEM image from crushed samples (figure 4-18a) and 2) SEM images of ‘matrix pull-outs’ on fracture toughness tests (figure 5-20a and b). This suggests that the actual CNT/ABS glass interface is of a different property and is stronger than the glass.

In summary, the load transfer to the CNTs is better in the transverse indentation orientation which shows improved hardness and elastic modulus. In axial indentation, there is poor load transfer to the inner concentric CNT walls. In bending, interwall sliding is thought to reduce the efficiency of load transfer from the matrix to the MWCNTs.

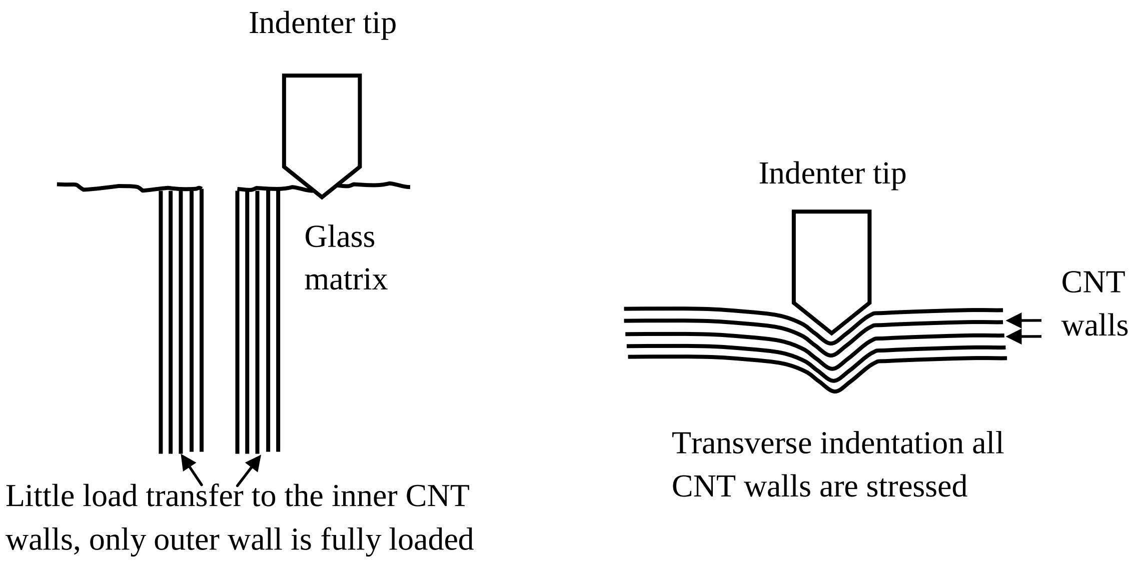

Figure 5-22 Schematic of indentation in a) axial and b) transverse direction.

5.4.2. Compressive and Bend Strength

The compression strength of the ACNT preform is less than that of glass and composite. To evaluate this, preform compressive strength is used to approximate the compressive strength of the individual CNTs (σ_{cnt}) using equation 5-6. The area of the ACNT preform ($A_{preform}$) used in the compression test in figure 5-3a was 3.2 mm^2, volume fraction of 10% and the maximum load attained was 275 N which gives 430 MPa for σ_{cnt}.

$$\sigma_{CNT} = \frac{P}{A_{preform} \times V_{cnt}}$$ Equation 5.6

This is an order of magnitude lower than the reported tensile measurement performed on CVD grown MWCNTs (3.6 GPa) [199]. The reduced compressive strength is attributed to the high susceptibility of MWCNTs to buckle under compression. In the preforms, buckling is favoured because of the high aspect ratio (length/diameter) of the MWCNTs of 25,000 and the presence of free volume. From Euler's buckling theory, the load at which buckling would occur on an unconfined two mm long MWCNT making up the preform can be calculated using equation 5-7 [200].

$$P = \frac{\pi^2 EI}{l^2}$$ Equation 5-7

where P is the critical buckling load, l is the effective length (2 mm), E is the elastic modulus of MWCNTs, I is the second moment of area of a MWCNT. I is approximated as a solid tube of diameter 80 nm using $\pi d^4 / 64$. Even with an ambitious elastic modulus for MWCNT of 1 TPa [57], the P required for buckling of MWCNT to occur is only 5 pN. This gives a stress of 1 kPa on each individual CNT of 80 nm in diameter. The estimation from Euler's theory is a factor of six lower than the experimental value (430 MPa). This is because in the ACNT preform, there is significant cross linking of MWCNTs which holds the preform together; hence Euler theory is insufficient and does not capture the complex behaviour of interaction between the MWCNTs. This cross linking will cause MWCNT pinning which would increase the load required for buckling. Local and coordinational buckling in the preforms was confirmed by SEM images (figure 5-4a and b). The length *l*, which would explain the strength of CNTs in the preform under compression in the experiment, is obtained from equation 5-7 using the load on an individual CNT (2.2 µN). This is calculated as 3.0 µm. This corresponds well to the width of the bands (not spaces between the bands) in figure 5-4b, which are also in the micrometer range. In the composite, the MWCNTs are confined within the matrix which restricts the extent of buckling (lateral stabilisation) due to lack of free volume. Even though the glass initially fails in the composite, it will still largely constrain the CNTs against buckling.

The lack of improvement in the compression strength of the composite compared to the ABS glass is attributed to the presence of flaws in the composite. The low compressive strength of ABS glass in this study compared to other studies [194] is attributed to 1) the glass not being fully dense (98%) and 2) the glass test specimens were not confined in compression tests, therefore pieces broke off from the specimens beyond the matrix cracking (figure 5-3b).

In summary, buckling of CNTs is not effective in the composite during compression due to lateral stabilisation of the CNTs by the glass matrix. Therefore, the CNTs do not effectively contribute the compression strength of the composite. Nevertheless, there is significant stable fracture region shown by the composite (figure

5-3c) unlike glass (figure 5-3b) suggesting damage tolerance of glass is improved by incorporation of CNTs as previously observed in indentation studies.

Average bend strengths of 1.3 and 1.4 GPa were obtained for glass and composites respectively. The bend strength for glass is unusually high. Bulk ABS glass of similar composition and processing conditions used in the present study was shown to have a bend strength of *ca.* 50 MPa [91]. The high bend strength results in both glass and composites in the present study are attributed to the small flaw sizes that concentrate stresses less than the large flaws that are present in macroscopic samples. This is given in Griffith's equation; failure stress is inversely proportional to the square root of crack size, $\sigma_f \, \alpha \, C^{-1/2}$ [201]. Using equation 5-8

$$K_c = 1.12 \times \frac{2}{\sqrt{\pi}} \times \sigma_f \sqrt{C} \qquad \text{Equation 5-8}$$

where K_c is the fracture toughness of glass (0.7 MPa $\sqrt{\text{m}}$), σ_f is the failure strength of glass (1.3 GPa) and C is a half-penny surface crack. The average flaw size (C) that resulted in failure for the glass beams is *ca.* 200 nm. This size is similar to the surface asperities seen in the SEM image (figure 5-11 and 5-19).

The fact that the bend strength in the composite microcantilever beams are similar to ABS glass is attributed to a trade off between increased toughness in the composite due to the presence of CNTs and increased flaw size *vis a vis* the more dense ABS glass. The presence of the CNTs in ABS glass inhibits full densification of the composite as reported in chapter 4 [91,93]. Another possible reason for lack of improvement in bend strength in the composite is MWCNT interwall sliding as the load is redistributed possibly from the matrix to the CNTs.

5.4.3. Contributions to Improvement in Fracture Toughness in the Composite

The four (4) general regions of classifications of the load-displacement curve of the notched microcantilever beams for the composites are identified and described using figure 5.23a and b as follows

Region AB: The region from A-B shows the non linear loading behaviour of the CNT/ABS composite system. The end of this region, point B, was investigated by loading a beam to just beyond it (point B) and the cantilever beam observed using SEM. This showed no evidence of catastrophic failure in the specimen and therefore point B corresponded to the onset of matrix crack growth. Therefore, point B was used to obtain the fracture toughness of the composite at this point (B), *i.e.* toughness at onset of fracture.

Region BC: In this region, there is displacement with no load increase and is attributed to propagation of the crack to the bottom of the microcantilever beam, debonding of GCNTs and interwall sliding within the MWCNTs. The average crack opening in this region is 126 nm (see table 5-8). The MWCNTs are assumed to be intact. From previous work with the same glass matrix and randomly orientated MWCNTs, the CNTs were shown to be intact at crack openings of up to 100 nm [91]. The CNTs in the study in reference [91] were observed to fracture at the interface due to bending across the crack. This is not the case in the present study for which CNTs are expected to bridge larger crack openings due to alignment and stress distribution along the CNT length.

Region CD: This region is attributed to CNTs bearing load evidenced by the fact that the load continues to rise after matrix fracture in section BC. Therefore, the predominant mechanism that leads to increase in load with displacement is attributed to intact CNTs bridging the crack. The region peaks at the ultimate strength of the composite (D). This section thus identifies the contribution of intact CNTs bridging the crack and GCNTs pull-out to the toughening of the composites.

Region DE: This region shows a decrease in load with displacement (figure 5-18a and b). The stable crack growth observed is indicative of some progressive toughening mechanism such progressive failure of the most stretched CNTs across the crack opening.

Incorporation of aligned CNTs in ABS glass results in improvement in fracture toughness of the composite by 240% (0.7 to 2.4 MPa $\sqrt{\mathrm{m}}$) when the total fracture energy beyond point B is considered. This is attributed to several toughening mechanisms shown figure 5-23a and b, which show schematics corresponding to the observed fracture surfaces in figure 5-20a and b. The schematics summarise three of the four toughening mechanisms that could have led to improvement in toughness of the composite compared to glass. They are I) debonding of the GCNTs, II) matrix pull-out (GCNT pull-out), and III) sword in sheath failure of the MWCNTs. The fourth mechanism is CNT bridging. The bridging of the crack by intact CNTs will occur as soon as the crack begins to open. The contributions of the four mechanisms to improvement in fracture toughness are evaluated next.

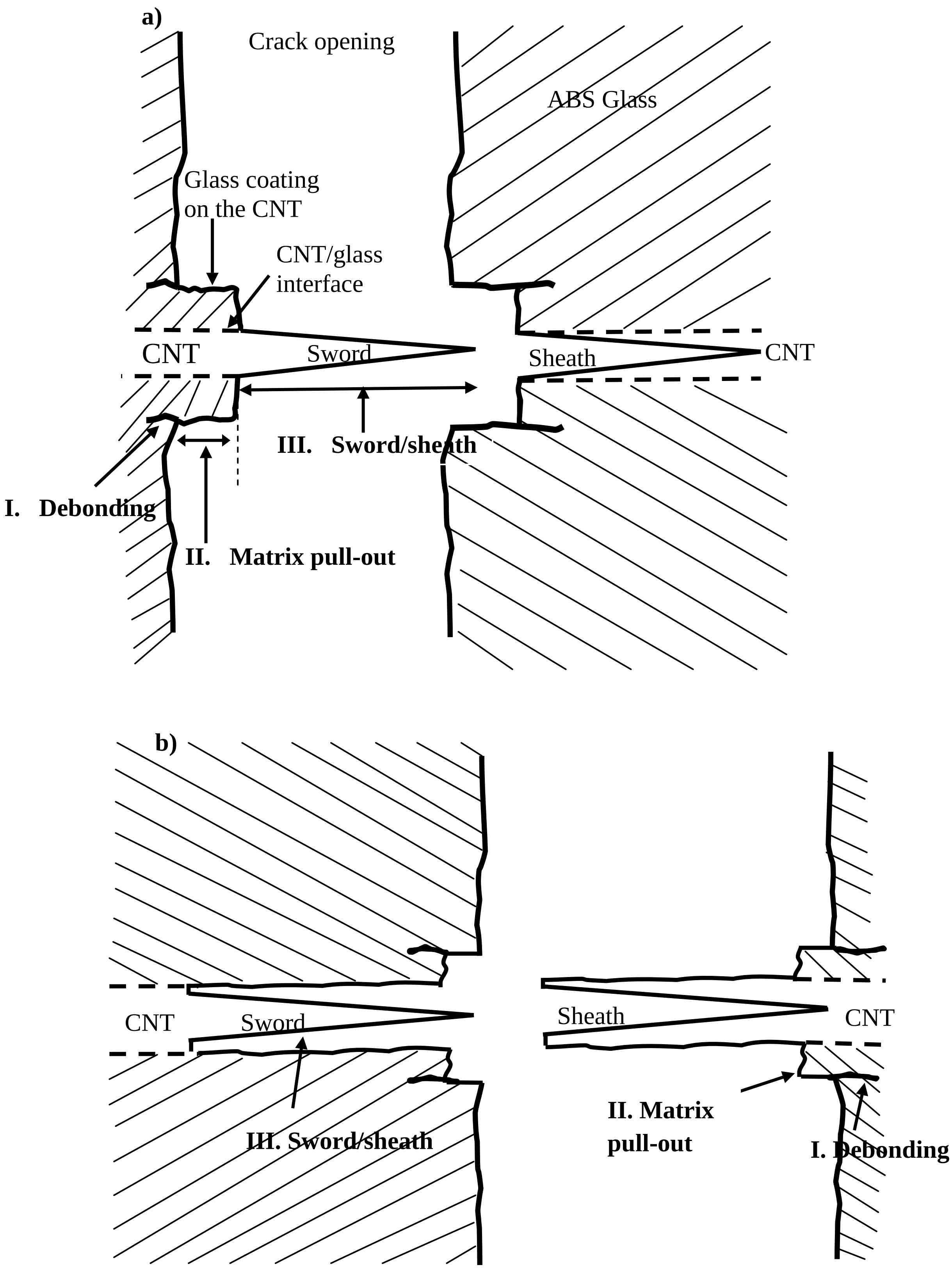

Figure 5-23 Schematic of the two modes of pull-out a) where the sword is external to the fracture surface b) the sword is within the fracture surface.

5.4.3.1. Contribution of Debonding in the Matrix

Debonding is a major requirement for other toughening mechanisms such as pull-out to occur. SEM images (figure 5-20a and b) of the fracture surfaces show that debonding occurs away from the actual CNT/ABS interface *i.e.* in the glass (schematically shown in figure 5-23a and b). The presence of these GCNTs also implies that debonding had occurred. The length of debonding, l_d, of *ca.* 200nm is used to approximate the work of fracture in the debonding process using equation 5.10.

$$W_{debond} = 2\pi r l_d G_c \times N \qquad \text{Equation 5.10}$$

where, r is the radius of the debonded GCNT (*ca.* 60nm); G_c is the energy required to create new surface in ABS glass (debonding occurs in the matrix), this is obtained 7.5 $\mathrm{Jm^{-2}}$ (using equation 5.2 and K_c of 0.7 $\mathrm{MPa}\sqrt{\mathrm{m}}$ and E of 65 GPa). The number of GCNTs per unit cross-sectional area, N, is related to the GCNT volume fraction (V_{GCNT} = 45 vol.% due to increased radius from 40 nm to 60 nm), and the GCNT radius, r (60 nm) by $N = V_{GCNT} / \pi r^2$. Therefore, the total contribution if all the GCNT debonded to fracture energy (G_{debond}) is given by

$$G_{debond} = \frac{2V_{GCNT} l_d G_c}{r} \qquad \text{Equation 5.11}$$

The work of fracture (energy dissipated in fracture) during debonding is calculated to be *ca.* 11 $\mathrm{Jm^{-2}}$ for the 50% of CNTs that show GCNT pull-out. The contributions due to friction and GCNT bridging during the debonding process are small (see appendix A1). Also, the contribution from the fracture in the cross-sectional area is also small and contributes is *ca.* 1 $\mathrm{Jm^{-2}}$ (see appendix A2)

5.4.3.2 Contribution of GCNT Pull-out to Toughening

After the matrix failure, the load applied to the cantilever beams goes into opening the crack. The opening of the crack results in pull-out of the debonded GCNTs (labelled II in schematic 5-23a and b). The frictional forces resisting GCNT pull-outs occur at the glass/glass interface and not the actual CNT/ABS glass interface. The action of pulling out GCNT sections results in dissipation of energy (due to friction) that would have otherwise gone into propagating the crack. Pull-outs occur due to the variability of the strength of the GCNTs which originates from random defects along the GCNTs. If we consider a GCNT with a remaining embedded length of *l* being pulled out by an increment of distance *dl* (figure 5-24), the work done in pulling out the GCNT is the product of the force acting on the GCNT and the distance moved in the direction of the force. This can be represented in equation 5.12.

$$\Delta W_{pullout} = 2\pi r l \tau_i dl \qquad \text{Equation 5.12}$$

where *l* and *r* are the remaining pull-out length and radius. $2\pi r l$ is the surface area over which the frictional force is acting and τ_i is the frictional force (shear stress at the interface). The work done in pulling the GCNT out completely is therefore given by

$$\Delta W_{GCNT} = \int_0^{l_0} 2\pi r l \tau_i dl = \pi r l_0^2 \tau_i \qquad \text{Equation 5.13}$$

The number of GCNTs per unit cross-sectional area, *N*, is related to the CNT volume fraction, V_{GCNT}, and the GCNT radius, r_{GCNT}, by $N = V_{GCNT} / \pi r_{GCNT}^2$.Therefore the pull-out work of fracture can be obtained by

$$G_{pullout} = \frac{V_{GCNT} {l_0}^2 \tau_i}{r_{GCNT}} \qquad \text{Equation 5.14}$$

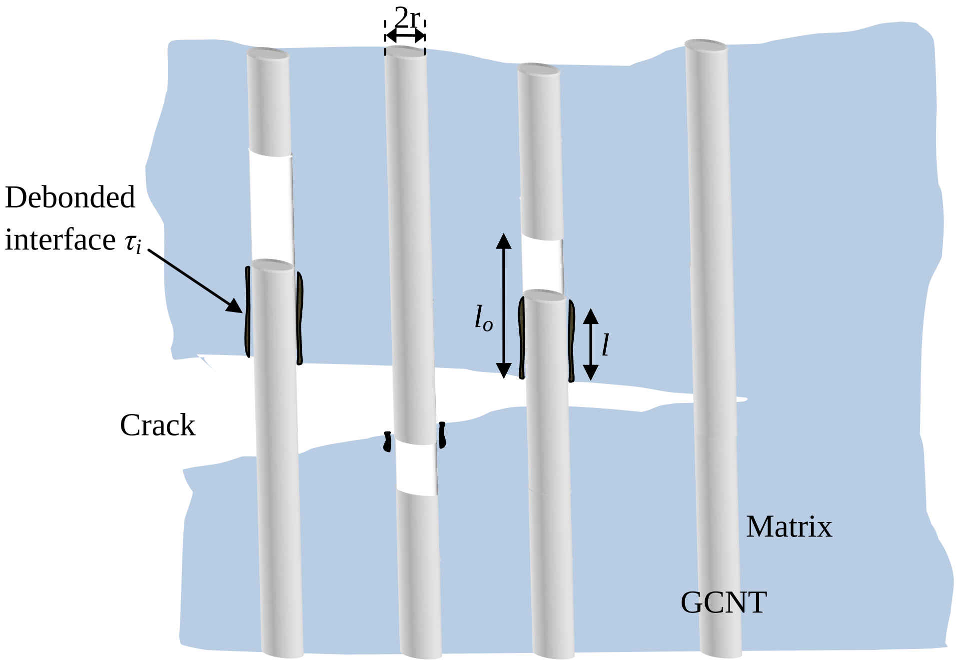

Figure 5-24 Illustration of a crack opening showing pull-out and nanotube bridging of the crack providing traction to slow down the crack.

The interfacial shear strength τ_i is estimated using equation 5.15 [202]

$$\tau_i = \frac{\sigma_{glass} r_{GCNT}}{2l_d} \qquad \text{Equation 5.15}$$

Using l_d (debond length) of 200 nm (figure 5-20a and b), r_{GCNT} of 60 nm σ_{glass} of similar glass composition used of 50 MPa [91], τ_i of 8 MPa is obtained. Therefore, taking l_o (pull-out length) of 100 nm (figure 5-20a and b), V_{GCNT} of 45 % and radius of pull-outs of 60 nm, the estimate of contribution of $G_{pull\text{-}out}$ is 1 Jm^{-2}. This value is an overestimate as only about 50% of the CNTs show pull-outs on the fracture surface *e.g.* in figure 5-20a and b. The overall contribution of pull-outs is about 0.5 Jm^{-2}. The small contribution to toughness by pull-outs in the present study is attributed to short lengths of the pull-outs (~100 nm) as the frictional force providing crack closing traction are only effective over these short lengths.

5.4.3.3. Contribution of CNT Bridging

As soon as the crack begins to open, the CNTs bridging the crack start stretching. Therefore, as the matrix fails, CNT bridging is already in effect providing crack closing traction. According to classical composite theory, the stress is distributed along the length of a CNT bridging a crack from a maximum at the crack reducing to a minimum away from the crack plane. An estimate of the strain energy absorbed by bridging CNTs ($G_{bridging}$), which is subsequently released on fracture of the CNTs, is obtained from calculating the work done in extending the CNTs over a critical *'debonded'* length, l_c using equations 5.16 and 5.18 (the debond length in this case is the required length for CNTs to stretch for an observed bridging across a crack and will be referred to as sliding length). In this case the outer layer is assumed to fracture as the matrix crack passes since it is bonded strongly to the matrix. This activates sliding of the broken outer layer relative to the rest of the CNT. Equation 5.17 accounts for the work done against interfacial friction and the elastic energy stored in the CNTs when they begin to fail. An approach of estimating the l_c required for a CNT to bridge a crack opening of length S nm was developed using a hinged beam model as shown in figure 5-25. At the ultimate strength of the composite, where the most stretched CNTs begin to fail, the maximum length required for a CNT to bridge the crack opening is calculated using the model. The angle θ in figure 5-25 is obtained from the length of the indenter tip to the notch, x, and the displacement from matrix fracture to maximum load, y, as $\theta = \tan^{-1} y/x$. The length of the bridging CNT is then obtained from the beam height (corrected for the presence of the notch). The results are shown in table 5-8. The strain on the CNTs at failure can be obtained using equation 5.16 [91]

$$\overline{\varepsilon_{cnt}} = \frac{\overline{\sigma}}{E} = \frac{\sigma^{*}_{cnt}}{2E_{cnt}} = \frac{S_{cnt}}{l_c} \qquad \text{Equation 5.16}$$

where $\overline{\varepsilon_{cnt}}$ is the mean strain on the CNTs, S_{cnt}, are the calculated bridging CNT lengths shown in table 5-8 and is the critical length, l_c, of the CNTs required for a bridging of S nm to occur. The σ_{cnt} and E_{cnt} are the strength (10 GPa [102]) and elastic modulus (164 GPa from section 5.4.1) of the CNTs. Using these parameters, the critical length, l_c is obtained as 1.9 µm (table 5-9). The results imply that on average a sliding length *ca.* 1.0 µm of CNTs on either sides of the fracture surface is required for the observed bridging S to occur. Since the E_{cnt} is an underestimate, the calculated l_c values also underestimate the actual sliding length. These observations strongly indicated that in ACNT/ABS composite system, the shortest length over which there is interwall sliding is *ca.* 2 µm.

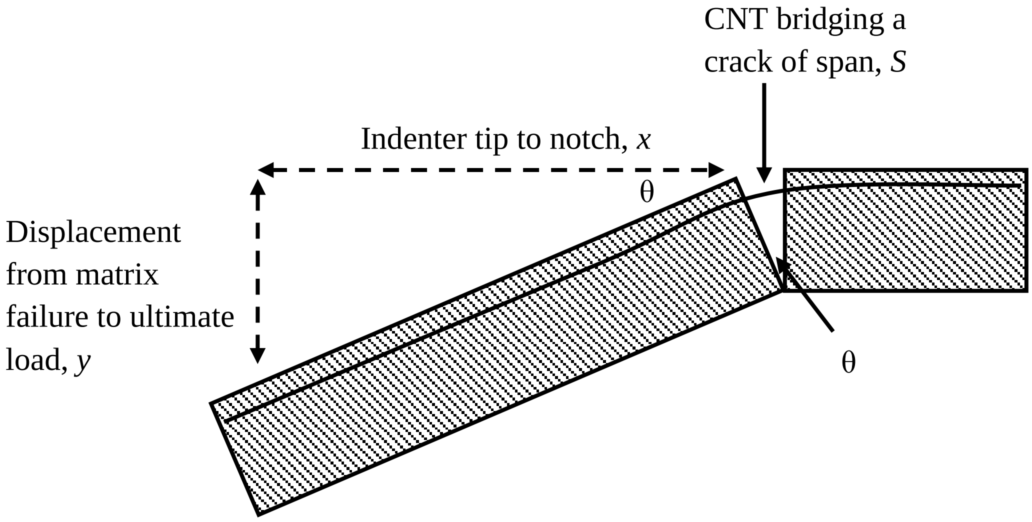

Figure 5-25 Schematic of a cantilever beam prior to ultimate strength showing bridging CNT prior to failure.

An estimate of for the strain energy absorbed by the bridging CNTs is made by calculating the work done in extending the CNTs during crack opening using equation 5.17 [91,202]

$$G_{bridging} = \frac{\sigma_{cnt}^{2} V_{cnt} l_c}{3E_{cnt}} \qquad \text{Equation 5.17}$$

replacing l_c with $2SE_{cnt}/\sigma_{cnt}$ from equation 5.15 gives

$$G_{bridging} = \frac{2\sigma_{cnt} V_{cnt} S}{3} \qquad \text{Equation 5.18}$$

Using a modest CNT tensile strength of 10 GPa [57], and S of 57 nm from table 5-8, the contribution from bridging is obtained as 76 Jm^{-2}. The amount of energy required to increase the toughness of the composite from 0.7 to 2.4 MPa $\sqrt{\text{m}}$ is 67 Jm^{-2}. The bridging is therefore able to account for all the observed toughening.

Table 5-8 Bridging and debond length of the CNTs.

Sample	**Length of plateau region (nm)**	**Plateau onset to ultimate strength (displacement) (nm)**	**Calculated Bridging Length, *S* (nm)**	**Critical Length, l_c (μm)**
a	114	487	78	2.6
b	158	341	46	1.5
c	97	560	53	1.7
d	143	344	55	1.8
e	95	506	48	1.6
f	146	741	60	2.0
Mean	**126**	**497**	**57**	**1.9**
Standard Error	**11**	**61**	**5**	**0.2**

5.4.3.4. Contribution of sword-in-sheath Failure Mechanism

Sword-in-sheath failure mechanism are shown in figure 4-5a&b and figure 5-20a&b. By considering each slip event of the concentric CNT walls as a pull-out, an approximation of the contribution from the infinitesimal increment in the failure of CNTs leading to the sword-in-sheath failure was made. The work done by sliding of one concentric tube relative to another (W_s) is calculated using a similar approach to that in section 5.4.4.2.

$$W_s = \pi r^* l^2 \tau_{sword-in-sheath} \qquad \text{Equation 5.19}$$

where r^* is the mean radius of a CNT that has failed in a sword-in-sheath manner, $l_{sword\text{-}in\text{-}sheath}$ is the length of one slip section and $\tau_{sword\text{-}in\text{-}sheath}$ is the shear strength between two graphitic layers. A CNT of diameter 80 nm has *ca.* 120 concentric graphitic walls. The mean radius after the full sword-in-sheath failure has occurred is 20 nm. An average slip length of 8.3 nm for one section (slip event) is obtained by assuming an equidistant slip length for 120 concentric graphitic layers over a length of 1 µm (see figures 5-15b and 5-20a). Therefore, taking r^*, $l_{sword\text{-}in\text{-}sheath}$ and $\tau_{sword\text{-}in\text{-}sheath}$ of 20 nm, 8.3 nm and 5 MPa (for a perfect graphite) [57], the work done for an individual slip event is 2.6 x 10^{-15} J. For N CNTs ($N = V_{cnt} / \pi r^2$, r in this case is the radius of the CNTs 40 nm), the total contribution from sword-in-sheath failure is *ca.* 0.1 Jm^{-2}. Similar argument shows that reducing the number of slip events results in increased contribution of sword-in-sheath failure. SEM observations (figure 5-21) showed that several sheets fail at once rather than one CNT graphitic sheet after another. Consequently the potential for improvement in toughness by sword-in-sheath mechanism could be higher in the present study, however, it is still going to be negligible. From observations of copious amounts of sword in sheath failure of CNTs (figure 4-15), it is concluded that this mechanism is a limiting factor to achieving optimum toughening.

5.4.3.5. Concluding Remarks on Fracture Toughness

The improvement in the toughness of the ACNT/ABS composites originates almost entirely from the action of intact CNTs bridging the crack during fracture. The experimental results show an improvement in toughness from 0.7 MPa$\sqrt{\text{m}}$ for unreinforced ABS glass to 2.4 MPa$\sqrt{m}$ for 20 % ACNT/ABS composite. This improvement would require fracture energy of *ca.* 67 Jm^{-2} (which was an underestimate). From investigation of the different possible contributions to toughness, the improvement from bridging is by far the most important toughening mechanism contributing a potential 76 Jm^{-2} to the fracture toughness in the present study. A recent report shows [91] that bridging is the main contribution to toughening in a similar CNT/ABS composite consisting of randomly orientated CNTs. It is important to note that the level of densification was 88-92% in the present composite and the improvement in the composite fracture toughness on denser samples should be higher.

The matrix debonding contribution is limited because it occurs over short distances and in the matrix rather than on the actual CNT/ABS interface. Reports on Si sols adhering strongly and uniformly coating CNTs are present in the literature [105,102]. Therefore, in the present composite system it is likely that the ABS sol structure at the interface is of a different structure [102]. Since there are no reports on toughness of aligned CNT/glass ceramic matrices, a comparison with randomly oriented MWCNT/aluminosilicate glass will be made. A recent study of 15 wt% MWCNT in aluminosilicate glass stated [166] that failure occurred at the actual CNT/ABS interface, clearly, this is unlikely to have been the case as shown in figure 5-21 and 5-22 and also as reported by Mukhopadhyay et al. [91]. Even though there were no high resolution SEM images to prove this phenomenon of failure at the actual interface, the study used similar diameter (70 nm) MWCNTs. Most importantly, the average lengths of the CNTs were only *ca.* 4 µm. From the present study, it has been shown that the length required for bridging by CNTs of radius 40 nm is *ca.* 2 µm, as a consequence, in the study by Cho *et al*. [166] the probability of an intact CNT of length 2 µm bridging a crack is limited. Instead the inner CNT walls would pull-out from the outer walls at a lower force than could be enacted by an intact tube. Therefore, pull-outs will readily occur without significant CNT bridging contribution contrary to observations by Mukhopadhyay *et al.* [91]. For this reason the improvement in toughness measured by chevron notch beam method by Cho *et al* [166] peaked at *ca.* 1.3 MPa $\sqrt{\mathrm{m}}$ for 15 wt.% CNT. Whereas, Mukhopadhyay *et al.* with much longer CNTs (>10 µm) obtained 1.6 MPa $\sqrt{\mathrm{m}}$ with only 10 wt.% CNTs. Toughening by pull-out mechanism which was attributed to improvement in toughness by Cho *et al.* [166] is also of limited contribution in ACNT/ABS glass composite system in the present study. The GCNT fail near the fracture plane resulting in short pull-out lengths providing a contribution of only 0.5 J m^{-2} to toughness.

The perceived pull-outs (sword-in-sheath failure) is evidently easy and occurs over lengths of up to 1 µm and results in little contribution to toughening. Therefore, compared to randomly orientated CNT glass composites where sword-in-sheath was not observed [91,166], alignment appears to activate this mechanism. The sword-in-sheath contribution to toughening is limited to less than 0.1 Jm^{-2} in the present study. Therefore, any attempts to suppress this mechanism by stitching the graphitic walls together in MWCNTs will require a proper understanding of this failure mechanism if improved toughness is to be obtained. From this analysis, it is concluded that the bridging of the crack by intact CNTs has a greater contribution to toughening than the pull-outs (CNT self pull-out *i.e.* sword-in-sheath, and pull-out in the matrix *i.e.* GCNT) and debonding mechanisms.

CHAPTER 6

Electrical and Thermal Properties of ACNT Preforms and ACNT/ABS Composite

6.0. Overview

In this chapter, results of the transport properties of aligned carbon nanotube preforms and the corresponding glass composites are presented. The through thickness electrical measurements of the ACNT preforms are compared to those of the composite. The thermal diffusivity together with specific heat capacity results of ABS glass, CNT, and ACNT/ABS glass are reported and discussed. The studies were carried out to elucidate the effect of alignment of CNTs on bulk transport properties of ABS glass. Section 6.1 looks at the electrical properties of the ACNT preforms composite system while section 6.2 details the thermal properties of the composites. A discussion and summary of the chapter is given in section 6.3.

6.1. Electrical Conductivity Results

The through thickness electrical resistivity results obtained from measuring resistance of *ca.* 2 mm long CNT preforms are presented in table 6-1. The resistivity was obtained by the equation 6.1 [203].

$$\rho = R\frac{A}{l}$$ Equation 6.1

where ρ is the electrical resistivity, R, A and l are the measured electrical resistance, cross sectional surface area and through thickness length (~ 2 mm). To obtain the electrical conductivity, σ, the reciprocal of ρ was taken [203].

From table 6.1, the ACNT preform has the lowest resistivity of *ca.* 10^{-4} Ωm. Since the preforms are 10 Vol.% dense, the effective electrical conductivity of the MWCNTs is obtained by using the actual contact surface area of the CNTs other than the preform surface area. Therefore, in the preforms tested, the effective resistivity of CNTs is a factor of ten less *i.e.* 10^{-5} Ω m. The electrical resistivity of glass is 16 orders higher than that of the composite system. It is well known that glass is an electrical insulator. Aligning CNTs in ABS glass lowers the resistivity to ~ 10^{-3} Ωm. Considering the semi conductor resistivity generally ranges from 10^{-4} to 10^{6} Ωm [203,204] the composite resistivity of ~ 10^{-3} Ωm lies close to the metallic conductor threshold of ~ 10^{-4} Ωm. It is noteworthy that the composite resistivity is one order higher than the resistivity of the pristine CNT preform.

Table 6-1 Electrical properties of the ACNT/ABS composite compared to ACNT preforms and borosilicate glass [203].

	ACNT/ABS composite	**ACNT preform**	**ABS glass** [203] **(fully dense)**
Electrical resistivity ρ (Ωm)	$1.3\text{x}10^{-3}$- $2\text{x}10^{-3}$	$1.8\text{x}10^{-4}$ - $2.0\text{x}10^{-4}$	10^{13}
Electrical conductivity (Sm^{-1})	500 - 800	5000 - 5500	10^{-13}

6.2. Thermal Conductivity Results

Thermal properties measured in this study are presented in table 6-2. The thermal diffusivity measurements which were obtained from laser flash technique show the axial thermal diffusivity of the composite system at 25 ^{o}C to be 2 orders higher than ABS glass. The ACNT preform has the highest thermal diffusivity thus the improvement in the diffusivity in the composite is attributed to the CNTs. From table 6.2, the measured C_p of ACNT preform and the composite system are more than double that of glass. Thermal conductivities of the materials were calculated from the thermal diffusivity, heat capacity measurements and measured densities on table 4-2 using equation 6.2 [205].

$$\kappa = \alpha \rho C_p \qquad \text{Equation 6.2}$$

where α is the thermal diffusivity, ρ is the density and C_p is the specific heat capacity. The axial thermal conductivity of the composite of 15.8 Wm^{-1}K^{-1} is an improvement of 80 % and 1190 % to those of ACNT and ABS glass respectively.

Table 6-2 Thermal Properties of the ACNT/ABS composite compared to ACNT preforms and borosilicate glass.

	ACNT/ABS composite	**ACNT preform**	**ABS glass (fully dense)**
Thermal diffusivity α (cm^2 s^{-1})	0.13 ± 0.01	0.44 ± 0.01	0.0065 ± 0.0012
Specific heat capacity C_p (Jg^{-1}K^{-1})	1.9 ± 0.1	1.8 ± 0.1	0.8 ± 0.06
Thermal conductivity κ (Wm^{-1}K^{-1})	15.8 ± 0.2	8.7 ± 0.1	1.2 ± 0.1

6.3. Discussion of the Electrical and Thermal Properties

The difference in the electrical resistivity of the composite and that of the CNT preforms is attributed to poor contact between the sputtered gold electrodes with the CNTs. From chapter 4, figure 4-14 d, the surface of diamond slurry polished composite in the axial direction showed fractured CNTs. The fractured CNTs on the surface may have led to poor connectivity with the embedded CNTs in the bulk reducing the electrical conductivity. Recently, we measured the electrical conductivity of a 15 wt. % [97] MWCNT in a similar ABS glass to be 2.1 Sm^{-1}. The 15 wt% corresponds to *ca.* 17 vol.% (density of CNT is taken as 2 gcm^{-3} [190]). Due to agglomeration of CNTs during processing, there are no reports on 20 vol.% randomly oriented CNT ceramic composites. The aligned CNT composites do not rely on percolation threshold as with randomly orientated composites. The randomly orientated CNT composites have contact resistance between interconnecting CNTs reducing the effective bulk electrical conductivity. In aligned composite, such problems are circumvented. Nevertheless, the conductivity of the ACNT/ABS composite are two orders higher than the 17 vol.% composites we previously reported [97] and in the literature [123] for aluminosilicate glass composite with randomly oriented MWCNTs. Therefore, aligning of CNTs is thought to be better for electrical conductivity. For applications where electrical conductivity is of relevance, aligning CNTs in the direction of transport would be of benefit than randomly dispersing CNTs in matrices.

The reduction in thermal diffusivity in the ACNT/ABS composite when compared to that of ACNT carpet is due to the extra heat capacity of the ABS matrix. The thermal conductivity of the composite is higher than the rule of mixtures would suggest which is possibly due to some coupling between CNTs and the ABS glass.

Also, though less likely due to 1100 °C temperature used, graphitisation of the CNTs during sintering might have improved the properties of the CNTs [114] reducing the number of defects. Compared to a metal such as copper with a thermal diffusivity of 1.2 $cm^2\,s^{-1}$, the CNT preforms show lower thermal conductivity. The lower thermal conductivity results obtained for ACNT preforms and ACNT/ABS composites compared to the measured 3000 $Wm^{-1}K^{-1}$ [206] for individual CNTs is presumed to be due to structural defects in the individual CNTs. The defects act as scattering sites for phonons due to the interrupted π conjugation system [206]. HRTEM reveals such defects in the form of embedded Fe catalyst particles and folds/kinks in the walls of the CNTs (figure 4-5b). A survey of the literature shows a good agreement of the results obtained in this study with other studies. Borca-Tasciuc et al used a photothermoelectric technique to measure the thermal diffusivity along a MWCNT array. They obtained a value of *ca.* 0.52 $cm^2\,s^{-1}$ at room temperature [207]. Hou et al. used a photothermal–resistance technique and measured three samples and obtained thermal diffusivity values of 0.30, 0.44 and 0.66 $cm^2\,s^{-1}$, respectively [208]. However, studies have shown that the reduction in length from mm to micrometers results in improved thermal diffusivity by Huangqi et al. [209]. Huangqi showed that 20 µm CNT arrays showed a thermal diffusivity of up to 4.6 $cm^2\,s^{-1}$. The increased thermal diffusivity compared to the CNT arrays attributed to reduced degree of alignment in longer arrays and possible presence of contacts between CNTs as the length is increased resulting in phonon scattering. Therefore, reducing the intertwining observed in the preforms should ideally improve the thermal conductivity. Furthermore, graphitisation treatment should also reduce the amount of structural defects on the CNTs which provides further potential for improvement in the transport properties of the CNT preforms and the composites.

CHAPTER 7

Summary and Suggestions for Further Work

7.0. Conclusions

The present study produced aligned CNT/glass ceramic composites by a novel route which did not require post production dispersion or alignment of the CNTs. The mechanical and transport properties of the CNT preform starting material and the composite were tested. The materials were compared to unreinforced glass and the following conclusions were reached:

a. Preforms containing CNTs of up to 7 mm in length were produced by CVD. The preforms contained MWCNTs with 10 ± 2 vol.%, density of 0.15 g cm^{-3} and were stable in temperatures of up to 550 ± 10 ^{o}C in air (see chapter 4). Also, the preforms were clean, devoid of amorphous carbon in the interstices and did not require any further processing for composite fabrication. The CNTs had an average diameter of 80 nm and carbon purity of more than 99%.

b. The ACNT preforms were infiltrated using a borosilicate sol without further processing. The glass matrix was obtained by gelling and drying of the sol within the interstices of the ACNT preforms. To improve the efficiency of infiltration, multiple infiltrations were performed. Consolidation by hot pressing resulted in composites containing aligned CNTs in the glass ceramic matrix. The composites were 90 ± 2% dense with a volume fraction of 20 ± 2% (see chapter 4).

c. Addition of CNTs to the ABS glass ceramic improved the damage tolerance of the glass under Vickers indentation in which the composites showed suppressed cracking. This is attributed to improved toughness in the composite compared to glass. This is due to CNTs acting as bridges across cracks and deflecting propagating cracks in the composite, unlike in glass where cracks growth is unstable. Also, the stiffness of the CNTs may also prevent densification under the indenter.

d. Addition of CNTs to glass improved the hardness and elastic modulus (in the transverse direction) in indentation testing by 10 and 28% respectively. The improvement is due to all the CNT walls being under load when indented in this orientation. The modest improvement can be explained by the composite not being fully dense. In the axial direction of testing showed a decrease in modulus due to the load being transferred to the outer CNT wall only. The properties of glass dominated the composite in the axial direction.

e. Under compression, the composite showed graceful failure compared to the ABS matrix which is evidence of progressive toughening. The composite did not show any improvement in strength compared to the glass under compression. This is due to the low compressive strength of the CNT preforms compared to glass. The CNTs in the preform are susceptible to buckling even though intertwining constrained the buckling. In the composite the CNTs are constrained from buckling by the matrix.

f. The load-displacement profiles of the microcantilever beams were not linear elastic with lower elastic modulus before failure compared to the initial loading section. In the case of ABS glass, the profile was linear through the loading region with elastic modulus similar to that of bulk ABS glass (65 GPa). The elastic modulus of the composite was ~30% better than unreinforced ABS glass and within 14% of those measured by indentation tests. The bowing profile and the modest improvement in elastic modulus were attributed to sliding within the MWCNTs walls which was confirmed by observation of permanent displacement during a loading-unloading cycling experiment. There was a little stable crack growth in some microcantilever beams suggesting some progressive toughening unlike ABS glass in which unstable fracture occurred at the maximum load. No significant difference in the bend strength of glass (1.3 ± 0.3 GPa) and the composite (1.4 ± 0.2 GPa) was observed which was attributed to the small flaw size in the cantilever beams (~200 nm) that concentrate stresses less unlike in macroscopic specimens.

g. Fracture energy measurements implied a fracture toughness (on notched microcantilever specimens) of 2.4 MPa$\sqrt{m}$ for the composite, which is *ca.* 240% improvement over that of unreinforced ABS glass (0.7 MPa$\sqrt{m}$). The fracture toughness of ABS glass corresponds to that of ABS glass measured by macroscopic methods. Notched beams load-displacement profiles for the composite had a plateau region followed by subsequent increase in load. The onset of the plateau does not represent catastrophic failure of the beams and is attributed to matrix growth leaving behind intact MWCNTs.

h. Further analysis determined that crack bridging mechanism by intact CNTs in the composite compared to glass can account for all the improvement in toughening by consuming an extra 67 Jm^{-2} during fracture. Other toughening mechanisms included debonding in the matrix, matrix pull-out, and sword in sheath failure of MWCNTs which contributed 11, 0.5 and 0.1 Jm^{-2} respectively.

i. Pull-outs occurred in the ABS glass and not at the actual ACNT/ABS interface and were of the order of 100 nm, hence the minimal contribution to toughness by this mechanism. The calculated minimum length required for CNTs of 80 nm in diameter to bridge a crack is ~2 µm, without which the inner walls will pull out from the outer wall which is bonded to the matrix.
j. The alignment of CNTs in ABS glass decreased the electrical resistivity of the glass to the order 10^{-3} Ωm from being an insulator. The thermal conductivity in the direction of alignment of the composite improved by 1190% over that of glass from 1.2 to 15.8 W $m^{-1}K^{-1}$.

7.1. Suggestions for Further Work

a. Improvement in the processing method to obtain fully dense composites could be explored. An example would be to use advanced sintering methods such as spark plasma sintering. This might improve the densification and influence the mechanical properties by altering the ACNT/ABS interface.
b. Bend tests on macroscopic samples could be explored to understand the effect of alignment of CNTs on ABS glass ceramic at a macroscopic level. This would require production of longer CNT preforms. Specific to the present study, the production of arrays of CNTs in large areas could be achieved by use of box furnace, and possibly use of plasma to assist in synthesis.
c. As interwall sliding has been identified as a possible limiting mechanism to improvement in elastic modulus and fracture toughness, joining the CNT walls to suppress the sliding could be explored. In principle this should improve the elastic modulus. This can be achieved by using other CNTs such as nitrogen doped CNTs

which have corrugated internal structures that could suppress sliding and sword in sheath failure. Also, chemical treatment to stitch the CNT walls together could be explored.

d. Further analysis to determine the chemical structure of the ABS/CNT interface could be explored. This would enable controlled engineering of the interface properties, for example, a weaker interface would activate more pull-outs which could improve the fracture toughness of the composite.

e. The present study explored sol gel infiltration of CNT preforms with a model glass ceramic matrix. In view of this, other ceramics that can be processed through sol gel, such as alumina, could be attempted.

f. For applications, the CNT preforms could be infiltrated with suitable sols such as alumina (for improved wear resistance compared to glass) to produce friction braking components. The CNTs would act as heat dissipating channels mediating in improving thermal shock properties of the ceramic. The challenges to overcome in such a case would be to produce 100% dense composite for improved strength and large area production over tens of centimetres in dimensions would also be required. For applications, such as thermal interface materials in electronics, infiltration with sols to provide structural rigidity and providing extra heat dissipation could be attempted. The thermal conductivity of the CNTs could be improved by graphitisation at high temperatures prior to use in composite fabrication.

REFERENCES

1 Iijima S. Helical microtubules of graphitic carbon. 1991;354:56-58.

2 Bentur A, Mindess S. Fibre reinforced cementious composite. London: Elsevier; 1990.

3 Kumar CK. Ceramic Matrix Composite. 2nd ed. Springer; 2003.

4 Desai AV, Haque MA. Mechanics of the interface for carbon nanotube–polymer composites. Thin-Walled Structures. 2005;43(11):1787-1803.

5 Hull D. Introduction to Composite Materials. Cambridge University Press; 1981.

6 Souza JA, Goutianos S, Sovgaard M, Sorensen BF. Fracture resistance curves and toughening mechanisms in polymer based dentalcomposites. Journal of the Mechanical Behavior of Biomedical Materials. 2011;4(4):558-571.

7 Ramakrishna S, Mayer J, Wintermantel E, Leong KW. Biomedical applications of polymer-composite materials: a review. Composite Science and Technology. 2001;61(9):1189-1224.

8 Shahinpoora M, Kim KJ. Novel ionic polymer–metal composites equipped with physically loaded particulate electrodes as biomimetic sensors, actuators and artificial muscles. Sensors and Actuators A: Physical. 2002;96(2-3):125-132.

9 Clyne B, Withers PJ. An Introduction to Metal Matrix Composites. Cambridge University Press; 1993.

10 Mallick PK. Fibre reinforced composites: Materials, manufacturing and design. New York: Marcel Dekker Inc.; 1993.

11 Miyoshi K, Vander L, Sayir A, Tomasek A, Farmer S. Nasa projects LEP, VSP and AFFT.

12 Liu Y, Cheng L, Zhang L, Hua Y, Yang W. Microstructure and properties of particle reinforced silicon carbide and silicon nitride ceramic matrix composites prepared by chemical vapor infiltration. Materials Science and Engineering: A. 2008;475(1-2):217-223.

13 Hua Y, Zhang L, Cheng L, Wang J. Silicon carbide whisker reinforced silicon carbide composites by chemical vapor infiltration. Materials Science and Engineering. 2006;428(1-2):346-350.

14 Park K, Vasilos T. Interface and thermal shock resistance of SiC fiber/SiC composites. Scripta Materialia. 1998;39(11):1593-1598.

15 Zhu S, Mizuno M, Kagawa Y, Mutoh Y. Monotonic tension, fatigue and creep behavior of SiC-fiber-reinforced SiC-matrix composites: a review. Composites Science and Technology. 1999;59(6):833-851.

16 Kroto H, Heath J, O'Brien S, Curl R, Smalley R. C60: Buckminsterfullerene. Nature. 1985;318:162-163.

17 Dervishi E, Li Z, Xu Y, Saini V, Biris AR, Lupu D, Biris AS. Carbon Nanotubes: Synthesis, Properties, and Applications. Particulate Science and Technology: An International Journal. 2009;27(2):107-125.

18 Windhorst T, Blount G. Carbon-carbon composites: a summary of recent developments and applications. Mateials and Design. 1997;18(1):11-15.

19 Evans AG, Zok FW. The physics and mechanics of fibre-reinforced brittle matrix composites. Journal of Materials Science. 1994;29(15):3857-3896.

20 Marshall DB, Evans AG. Failure Mechanisms in Ceramic-Fiber/Ceramic-Matrix Composites. Journal of the American Ceramic Society. 1985;68(5):225-231.

21 Brennan JJ, Prewo KM. Silicon carbide fibre reinforced glass-ceramic matrix composites exhibiting high strength and toughness. Journal of Materials Science. 1982;17(8):2371-2383.

22 Beyerle DS, Spearing SM, Evans AG. Damage Mechanisms and the Mechanical Properties of a Laminated 0/90 Ceramic/Matrix Composite. Journal of the American Ceramic Society. 1992;75(12):3321-3330.

23 Meyyappan M. Carbon Nanotubes. Science and Applications. CRC; 2005.

24 Novoselov KS, Geim AK, Morozov SV, Jiang D, Zhang Y, Dubonos SV, Grigorieva IV, Firsov AA. Electric Field Effect in Atomically Thin Carbon Films. 2004;306(5696):666-669.

25 Choi W, Lahiri I, Seelaboyina R, Kang YK. Synthesis of graphene and its applications: a review. Critical reviews in solid state and materials science. 2010;35:52-71.

26 Lee C, Wei X, Kysar JW, Hone J. Measurement of the Elastic Properties and Intrinsic Strength of Monolayer Graphene. Science. 2008;321(5887):385-388.

27 Harris PJF. Carbon Nanotubes and Related Structures. Cambridge University Press; 1999.

28 Krätschmer W, Fostiropoulos K, Huffman DR. The infrared and ultraviolet absorption spectra of laboratory-produced carbon dust: evidence for the presence of the C60 molecule. Chemical Physics Letters. 1990;170(2-3):167-170.

29 Grobert N. Carbon nanotubes - becoming clean. Materials Today. 2006;10(1-2):28-35.

30 Thostenson ET, Ren Z, Chou TW. Advances in the science and technology of carbon nanotubes and their composites: a review. Composites Science and Technology. 2001;61(13):1899-1912.

31 Popov VN. Carbon nanotubes:properties and application. Materials Science and Engineering. 2004;43:61-102.

32 Bhushan B, editor. Springer handbook of nanotechnology. New York: Spinger-Verlag Berlin Heidelberg; 2003.

33 Kingston CT, Simard B. Fabrication of Carbon Nanotubes. Analytical Letters. 2003;36(15):3119-3145.

34 Endo M, Hayashi T, Kim YA, Muramatsu H. Development and Application of Carbon Nanotubes. Japanese Journal of Applied Physics. 2006;45(6A):4883-4892.

35 Atthipalli G, Epur R, Kumta PN, Gray JL. Ferrocene and Inconel assisted growth of dense carbon nanotube forests. Journal of Vacuum Science and Technology. 2011;29(4):04D102, 1-5.

36 Murayama S, Kojima R, Miyauchi Y, Chiashi S, Kohno M. Low-temperature synthesis of high-purity single-walled carbon nanotubes from alcohol. Chemical Physics Letters. 2002;360(3-4):229-234.

37 Nerushev OA, Dittmar S, Morjan RE, F R, Campbell EB. Particle size dependence and model for iron-catalyzed growth of carbon nanotubes by thermal chemical vapor deposition. Journal of Applied Physics. 2003;93(7):1559433, 1-6.

38 Morjan RE, Nerushev OA, Sveningsson M, Rohmund F, Falk LKL, Campbell EEB. Growth of carbon nanotubes from C60. Applied Physics A. 2004;78:253-261.

39 Seo JW, Forro L. Carbon nanotubes: quantum cylinders of graphene. Elsevier; 2008. p. 135-138.

40 Lee CJ, Park J, Huh Y, Lee JY. Temperature effect on the growth of carbon nanotubes using thermal chemical vapor deposition. Chemical Physics Letters. 2001;343(1-2):33-38.

41 Kaatz FH, Siegal MP, Overmyer DL, Provencio PP, Jackson JL. Diameter control and emission properties of carbon nanotubes grown. Materials Science and Engineering C. 2003;23:141-146.

42 Kumar M, Ando Y. Controlling the diameter distribution of carbon nanotubes grown from camphor on a zeolite support. Carbon. 2005;43(3):533-540.

43 Kumar M, Ando Y. Chemical Vapor Deposition of Carbon Nanotubes. Journal of Nanoscience and Nanotechnology. 2010;10:3739-3758.

44 Hernadi K, Fonseca A, Nagy JB, Bemaerts D, Fudala A, Lucas AA. Catalytic synthesis of carbon nanotubes using zeolite support. Zeolites. 1996;17(5-6):416-423.

45 Endo M. Grow carbon fibers in the vapor phase. Chemtech. 1988 568-576.

46 Koos AA, Dowling M, Jurkschat K, Crossley A, Grobert N. Effect of the experimental parameters on the structure of nitrogen-doped carbon nanotubes produced by aerosol chemical vapour deposition. Carbon. 2009;47(1):30-37.

47 Ding F, Larson P, Larson JA, Ahuja R, Duan H, Rosen A, Bolton K. The Importance of Strong Carbon−Metal Adhesion for Catalytic Nucleation of Single-Walled Carbon Nanotubes. Nanoletters. 2008;8(2):463-468.

48 Moisala A, Nasibulin AG, Kauppinen EI. The role of metal nanoparticles in the catalytic production of single-walled carbon nanotubes—a review. Journal of Physics. 2003;15:S3011–S3035.

49 Ago H, Komatsu T, Ohshima S, Kuriki Y, Yumura M. Dispersion of metal nanoparticles for aligned carbon nanotube arrays. Applied Physics Letters. 2000;77(79):126833, 1-3.

50 Fan S, Chapline MG, Franklin NR, Tombler TW, Cassell AM, Dai H. Self-Oriented Regular Arrays of Carbon Nanotubes and Their Field Emission Properties. Science. 1999;283(5401):512-514.

51 Wagner RS, Ellis WC. Vapor-Liquid-Solid Mechanism of Single Crystal Growth. Applied Physics Letters. 1964;4(5):89-90.

52 Helveg S, Lopez-Cartes C, Sehested J, Hansen PL, Bjerne SC, Rostrup-Nielsen JR, Abid-Pedersen F, Norskov JK. Atomic-scale imaging of carbon nanofibre growth. Nature. 2004;427:426-429.

53 Raty JY, Gygi F, Galli G. Growth of Carbon Nanotubes on Metal Nanoparticles: A Microscopic Mechanism from Ab Initio Molecular Dynamics Simulations. Physical Review Letters. 2005;95(9):096103, 1-4.

54 Rodriguez-Manzo JA, Terrones M, Terrones H, Kroto HW, Sun L, Banhart F. In situ nucleation of carbon nanotubes by the injection of carbon atoms into metal particles. Nature Nanotechnology. 2007;2:307-311.

55 Yuan SJ, Kong Y, Li FS. Mechanical properties of single-walled (5,5) carbon nanotubes with vacancy defects. Chinese Physics Letters. 2007;24(7):2036-2039.

56 Ruoff RS, Lorents DC. Mechanical and thermal properties of carbon nanotubes. Carbon. 1995;33(7):925-930.

57 Yu MF, Lourie O, Dyer MJ, Moloni K, Kelly TF, Ruoff RS. Strength and Breaking Mechanism of Multiwalled Carbon Nanotubes Under Tensile Load. Science. 200;287(5453):637-640.

58 Krishnan A, Dujardin E, Ebbesen TW, Yianilos PN, Treacy MJ. Young’s modulus of single-walled nanotubes. Physics Review B. 1998;58(20):14013-14019.

59 Goze C, Vaccarini L, Henrard L, Bernier P, Herndandez E, Rubio A. Elastic and mechanical properties of carbon nanotubes. Synthetic Metals. 1999;103(1-3):2500-2501.

60 Wong EW, Sheehan PE, Liever CM. Nanobeam Mechanics: Elasticity, Strength, and Toughness of Nanorods and Nanotubes. Science. 1997;277(5334):1971-1975.

61 Treacy MMJ, Ebbesen TW, Gibson JM. Exceptionally high Young's modulus observed for individual carbon nanotubes. Nature. 1996;381:678-680.

62 Boccaleri E, Arrais A, Frache A, Gianelli W, Fino P, Caminoc G. Comprehensive spectral and instrumental approaches for the easy monitoring of features and purity of different carbon nanostructures for nanocomposite applications. Materials Science and Engineering: B. 2006;131(1-3):72-82.

63 Ogata S, Shibutani Y. Ideal tensile strength and band gap of single-walled carbon nanotubes. Physical Review B. 2003;68:165401, 1-4.

64 Troya D, Mielke SL, Schatz GC. Carbon nanotube fracture – differences between quantum mechanical mechanisms and those of empirical potentials. Chemical Physics Letters. 2003;382(1-2):133-141.

65 Xie S, Li W, Pan Z, Chang B, Sun L. Mechanical and physical properties of carbon nanotube. Journal of Physics and Chemistry of Solids. 2000;61:1153-1158.

66 Yu MF, Files BS, Arepalli S, Ruoff S. Tensile loading of ropes of single wall carbon nanotubes and their mechanical properties. Physical Review Letters. 2000;84:5552-5555.

67 Demczyk BG, Wang YM, Cumings J, Hetman M, Han W, Zettl A, Ritchie RO. Direct mechanical measurement of the tensile strength and,elastic modulus of multiwalled carbon nanotubes. Materials Science and Engineering A. 2002;334:173-178.

68 Wei BQ, Vajtai R, Ajayan PM. Reliability and current carrying capacity of carbon nanotubes. Applied Physics Letters. 2001;79:1172-1174.

69 Ebbesen TW, Lezec HJ, Hiura J, Bennett JW, Ghaemi HF, Thio T. Electrical conductivity of individual carbon nanotubes. Nature. 1996;382:54-56.

70 Berber S, Kwon YK, Tomanek D. Unusually high thermal conductivity of carbon nanotubes. Physical Review Letters. 2000;84:4613-4616.

71 Hone J, Whitney M, Piskoti C, Zettl A. Thermal conductivity of single walled nanotubes. Physical Review B. 1999;59:R2514-R2516.

72 Kim P, Shi L, Majumdar A, McEuen PL. Thermal transport measurements on individual multiwalled nanotubes. Physical review letters. 2001;87:2155021-2155024.

73 Zhang HL, Li JF, Yao KF, Chen LD. Spark plasma sintering and thermal conductivity of carbon nanotube bulk materials. Journal of Applied Physics. 2005;97:1143101–1143106.

74 Cho J, Boccaccini AR, Shaffer MSP. Ceramic matrix composites containing carbon nanotubes. Journal of Materials Science. 2009;44(8):1934-1951.

75 Harrison BS, Atala A. Carbon nanotube applications for tissue engineering. Biomaterials. 2007;28(2):344-353.

76 Baughman RH, Zakhidov AA, de Heer WA. Carbon Nanotubes--the Route Toward Applications. Science. 2002;297(5582):787-792.

77 Wardle BL, Saito DS, Enrique JG, Hart AJ, de Villoria RG, Verploegen EA. Fabrication and Characterization of Ultrahigh-Volume- Fraction Aligned Carbon Nanotube–Polymer Composites. Advanced Materials. 2008;20(14):2707-2714.

78 Tjong SC, Liang GD, Bao SP. Electrical behavior of polypropylene/multiwalled carbon nanotube nanocomposites with low percolation threshold. Scripta materialia. 2007;57(6):461-464.

79 Tjong SC, Liang GD, Bao SP. Effects of crystallization on dispersion of carbon nanofibers and electrical properties of polymer nanocomposites. Polymer Engineering and Science. 2008;48(1):177-183.

80 Otieno G, KimJ.Y. Conductive graphite/polyurethane composite films using amphiphilic reactive dispersant: Synthesis and characterization. Journal of Industrial and Engineering Chemistry. 2008;14(2):187-193.

81 Zhan GD, Kuntz JD, Wan J, Mukherjee AK. Single-wall carbon nanotubes as attractive toughening agents in alumina-based nanocomposites. Nature Materials. 2003;2:38-42.

82 Sun J, Gao L, Li W. Colloidal Processing of Carbon Nanotube/Alumina Composites. Chemistry of Materials. 2002;14(12):5169-5172.

83 Ning J, Zhang J, Pan Y, Guo J. Surfactants assisted processing of carbon nanotube-reinforced SiO2 matrix composites. Ceramics International. 2004;30(1):63-67.

84 Fan JP, Zhuang DM, Zhao DQ, Zhang G, Wu MS, Wei F, Fan ZJ. Toughening and reinforcing alumina matrix composite with single-wall carbon nanotubes. Applied Physics Letters. 2006;89(12):121910-121913.

85 Kim BM, Hiraga K, Morita K, Yoshida H. Spark plasma sintering of transparent alumina. Scripta Materialia. 2007;57(7):607-610.

86 Hiraga K, Kim BN. High-strain-rate superplasticity in oxide ceramics. Science and Technology of Advanced Materials. 2007;8(7-8):578-587.

87 Niihara K. New-design concept of structural ceramics-ceramic nanocomposites, the centennial issue of the ceramic society of Japan. Journal of the Ceramics Society of Japan. 1991;99(10):974-982.

88 Guldi DM, Martin N, editors. Carbon Nanotubes and Related Structures. Wiley-VCH; 2010.

89 Harris PJF. Carbon nanotube composites. International Materials Reviews. 2004;49(1):31-43.

90 Dai H. Carbon nanotubes: opportunities and challenges. Surface Science. 2002;500(1-2):218-241.

91 Mukhopadhyay A, Chu BTT, Green MLH, Todd RI. Understanding the mechanical reinforcement of uniformly dispersed multiwalled carbon nanotubes in alumino-borosilicate glass ceramic. Acta Materialia. 2010;58(7):2685-2697.

92 Cha SI, Kim K, Lee KH, Mo CB, Hong SH. Strengthening and toughening of carbon nanotube reinforced alumina nanocomposite fabricated by molecular level mixing process. Scripta Materialia. 2005;53(7):793-797.

93 Ning J, Zhang J, Pan Y, Guo J. Fabrication and mechanical properties of SiO2 matrix composites reinforced by carbon nanotube. Materials Science and Engineering: A. 2003;357(1-2):392-396.

94 Boccaccini AR, Acevedo DR, Brusatin PC. Borosilicate glass matrix composites containing multi-wall carbon nanotubes. Journal of European Ceramic Society. 2005;25:1515-1523.

95 Rul S, Lefevre-schlick F, Capria E, Laurent C, Peigney A. Percolation of single-walled carbon nanotubes in ceramic matrix nanocomposites. Acta Materialia. 2004;52(4):1061-1067.

96 Ahmad K, Pan W, Shi SL. Electrical conductivity and dielectric properties of multiwalled carbon nanotube and alumina composites. Applied Physics Letters. 2006;89(133122):1-3.

97 Mukhopadhyay A, Otieno G, Chu BTT, Wallwork A, Green MLH, Todd RI. Thermal and electrical properties of aluminoborosilicate glass–ceramics containing multiwalled carbon nanotubes. Scripta Materialia. 2011;65(5):408-411.

98 Zhan GD, Kuntz JD, Garay JE, Mukherjee AK. Electrical properties of nanoceramics reinforced with ropes of single-walled carbon nanotubes. Applied Physics Letters. 2003;83(6):1228-1230.

99 Wang J, Kou HM, Liu XJ, Pan YB, Guo JK. Reinforcement of mullite matrix with multi-walled carbon nanotubes. Ceramics International. 2007;33(5):719-722.

100 Poorteman M, Traianidis M, Bister G, Cambier F. Colloidal processing, hot pressing and characterisation of electroconductive MWCNT-alumina composites with compositions near the percolation threshold. Journal of the European Ceramic Society. 2009;29(4):669-675.

101 Sun J, Gao L, Jin X. Reinforcement of alumina matrix with multi-walled carbon nanotubes. Ceramics International. 2005;31(6):893-896.

102 Seeger T, Redlich P, Grobert N, Terrones M, Walton DRM, Kroto HW, Rhule M. SiOx-coating of carbon nanotubes at room temperature. Chemical Physics Letters. 2001;339(1-2):41-46.

103 Seeger T, Kohler T, Frauenheim T, Grobert N, Ruhle M, Terrones M, Seifert G. Nanotube composites: novel SiO2 coated carbon nanotubes. Chemical Communications. 2002 34-35.

104 Shaffer MSP, Sandler JKW. Carbon nanotube/nanofibre polymer composites. Singapore: World Scientific; 2006. p. 1-59.

105 Chu BTT, Tobias G, Salzmann CG, Ballesteros B, Grobert N, Todd RI, Green MLH. Fabrication of carbon-nanotube-reinforced glass–ceramic nanocomposites by ultrasonic in situ sol–gel processing. Journal of Materials Chemistry. 2008;18:5344-5349.

106 Hernadi K, Couteau E, Seo JW, Forro L. Al(OH)3/Multiwalled Carbon Nanotube Composite: Homogeneous Coverage of Al(OH)3 on Carbon Nanotube Surfaces. Langmuir. 2003;19(17):7026-7029.

107 Morisada Y, Miyamoto Y. SiC-coated carbon nanotubes and their application as reinforcements for cemented carbides. Materials Science and Engineering: A. 2004;381(1-2):57-61.

108 Guo Y, Cho H, Shi D, Lian J, Song Y, Abot J, Poudel B, Ren Z, Wang L, Ewing RC. Effects of plasma surface modification on interfacial behaviors and mechanical properties of carbon nanotube-Al2O3 nanocomposites. Applied Physics Letters. 2007;91(26):261903 1-3.

109 Hwang GL, Hwang KC. Carbon nanotube reinforced ceramics. Journal of Materials Chemistry. 2001;11:1722-1725.

110 Laurent C, Peigney A, Dumortier O, Rousset A. Carbon nanotubes–Fe–Alumina nanocomposites. Part II: microstructure and mechanical properties of the hot-Pressed composites. Journal of the European Ceramic Society. 1998;18(14):2005-2013.

111 Chicatún F, Cho J, Schaab S, Brusatin G, Colombo P, Roether JA, Boccaccini AR. Carbon nanotube deposits and CNT/SiO2 composite coatings by electrophoretic deposition. Advances in Applied Ceramics. 2007;106(4):186-195.

112 Chandrashekar A, Ramachandran S, Pollack G, Lee JS, Lee G, Overzet L. Forming carbon nanotube composites by directly coating forests with inorganic materials using low pressure chemical vapor deposition. Thin Solid Films. 2008;517(2):525-530.

113 Qian D, Dickey EC, Andrews R, Rantell T. Load transfer and deformation mechanisms in carbon nanotube-polystyrene composites. Applied Physics Letters. 2000;76(2068):126500 1-3.

114 Otieno G, Koos AA, Dillon F, Wallwork A, Grobert N, Todd RI. Processing and properties of aligned multi-walled carbon nanotube/aluminoborosilicate glass composites made by sol–gel processing. Carbon. 2010;48(8):2212-2217.

115 Peigney A, Flahaut E, Laurent C, Chastel F, Rousset A. Aligned carbon nanotubes in ceramic-matrix nanocomposites prepared by high-temperature extrusion. Chemical Physics Letters. 2002;352(1-2):20-25.

116 Ma RZ, Wu J, Wei BQ, Liang J, Wu DH. Processing and properties of carbon nanotubes–nano-SiC ceramic. Journal of Materials Science. 1998;33(21):5243-5246.

117 Chiou S, Hahn HT. Ultrasonic Sol/Gel Processing of Aluminoborosilicate Glass and Its Composite with Carbon Fiber Reinforcement. Journal of the American Ceramic Society. 1994;77(1):155-160.

118 Grobert N, Seeger T, Seifert G, Ruhle M. Processing, characterisation and theory of carbon nanotubes containing SiOx-based nanocomposites. Journal of Ceramic Processing and Research. 2003;4(1):1-5.

119 Zhang Y, Shen Y, Han D, Wang Z, Song J, Niu L. Reinforcement of silica with single-walled carbon nanotubes through covalent functionalization. Journal of Materials Chemistry. 2006;16:4592-4597.

120 Fan J, Zhao D, Wu M, Xu Z, Song J. Preparation and Microstructure of Multi-Wall Carbon Nanotubes-Toughened Al2O3 Composite. Journal of the American Ceramic Society. 2006;89(2):750-753.

121 Sun J, Iwasa M, Gao L, Zhang Q. Single-walled carbon nanotubes coated with titania nanoparticles. Carbon. 2004;42:885-901.

122 Hernadi K, Ljubovic E, Seo JW, Forro L. Synthesis of MWNT-based composite materials with inorganic coating. Acta Materialia. 2003;51(5):1447-1452.

123 Boccaccini AR, Thomas BJC, Brusatin G, Colombo P. Synthesis of MWNT-based composite materials with inorganic coating. Journal of Materials Science. 2007;42(6):2030-2036.

124 Shaffer MSP, Fan X, Windle AH. Dispersion and packing of carbon nanotubes. Carbon. 1998;36(11):1603-1612.

125 Poyato R, Vasiliev AL, Padture NP, Tanaka H, Nishimura T. Aqueous colloidal processing of single-wall carbon nanotubes and their composites with ceramics. Nanotechnology. 2006;17(6):1170-1777.

126 Du C, Ye J, Pan N. Carbon nanotube thin films with ordered structures. Journal of Materials Chemistry. 2005;15:548-550.

127 Ebbesen TW, Ajayan PM, Hiura H, Tanigaki K. Purification of nanotubes. Nature. 1994;367:319.

128 Zimmerman JL, Bradley RK, Huffman CB, Hague RH, Margrave JL. Gas-Phase Purification of Single-Wall Carbon Nanotubes. Chemistry of Materials. 2000;12(5):1361-1366.

129 Peigney A, Laurent C, Dumortier O, Rousset A. Carbon nanotubes–Fe–alumina nanocomposites. Part I: influence of the Fe content on the synthesis of powders. Journal of European Ceramic Society. 1998;18(14):1995-2004.

130 Flahaut E, Peigney ,A, Laurent C, Marliere C, Chastel F, Rousset A. Carbon nanotube–metal–oxide nanocomposites: microstructure, electrical conductivity and mechanical properties. Acta Materialia. 2000;48(14):3803-3812.

131 An JW, You DH, Lim DS. Tribological properties of hot-pressed alumina–CNT composites. Wear. 2003;255(1-6):677-681.

132 Kamalakaran R, Lupo F, Grobert N, Lozano-Castello D, Jin-Phillipp NY, Ruhle M. In-situ formation of carbon nanotubes in an alumina–nanotube composite by spray pyrolysis. Carbon. 2003;41(14):2737-2741.

133 Xia Z, Riester L, Curtin WA, Li H, Sheldon BW, Liang J, Chang B, Xu JM. Direct observation of toughening mechanisms in carbon nanotube ceramic matrix composites. Acta Materialia. 2004;52(4):931-944.

134 Xia Z, Curtin WA, Sheldon BW. Fracture Toughness of Highly Ordered Carbon Nanotube/Alumina Nanocomposites. Journal of Engineering Materials and Technology. 2004;126(3):238-244.

135 Jiang L, Gao L. Carbon nanotubes–metal nitride composites: a new class of nanocomposites. Journal of Materials Chemistry. 2005;15(2):260-266.

136 Jiang L, Gao L. Fabrication and Characterization of Carbon Nanotube–Titanium Nitride Composites with Enhanced Electrical and Electrochemical Properties. Journal of the American Ceramic Society. 2006;89(1):156-161.

137 Huang Q, Gao L. Multiwalled carbon nanotube/BaTiO3 nanocomposites: Electrical and rectification properties. Applied Physics Letters. 2005;86(123104):1884763 1-3.

138 Boccaccini AR, Zhitomirsky I. Application of electrophoretic and electrolytic deposition techniques in ceramics processing. Current Opinion in Solid State and Materials Science. 2002;6(3):251-260.

139 Boccaccini AR, Cho J, Roether JA, Thomas BJC, Minay EJ. Electrophoretic deposition of carbon nanotubes. Carbon. 2006;44(15):3149-3160.

140 Cho J, Schaab S, Roether JA, Boccaccini AR. Nanostructured carbon nanotube/TiO2 composite coatings using electrophoretic deposition (EPD). Journal of Nanoparticles Research. 2008;10(1):99-105.

141 Correa-Duarte MA, Wagner N, Rojas-Chapan J, Morsczeck C, Thie M, Giersig M. Fabrication and Biocompatibility of Carbon Nanotube-Based 3D Networks as Scaffolds for Cell Seeding and Growth. Nanoletters. 2004;4(11):2233-2236.

142 Aryala S, Bahadura KCR, Dharmaraj N, Kim KW, Kimb HY. Synthesis and characterization of hydroxyapatite using carbon nanotubes as a nano-matrix. Scripta Materialia. 2006;54(2):131-136.

143 Mahajan SV, Hasan SA, Cho J, Shaffer MSP, Boccaccini AR, Dickerson JH. Carbon nanotube–nanocrystal heterostructures fabricated by electrophoretic deposition. Nanotechnology. 2008;19:195301, 1-8.

144 Dobedoe RS, West GD, Lewis MH. Spark plasma sintering of ceramics: understanding temperature distribution enables more realistic comparison with conventional processing. Advances in Applied Ceramics. 2005;104(3):110-116.

145 Balazsi C, Shen Z, Konya Z, Kasztovszky Z, Webber F, Vertesy Z, Biro LP, Kiricsi I, Arato P. Processing of carbon nanotube reinforced silicon nitride composites by spark plasma sintering. Composites Science and Technology. 2005;65(5):727-733.

146 Tredway WK, Prewo KM. Fiber-matrix interfacial effects in carbon-fiber-reinforced glass matrix composites. Carbon. 1989;27(5):717-727.

147 Wang X, Padture NP, Tanaka H. Contact-damage-resistant ceramic/single-wall carbon nanotubes and ceramic/graphite composites. Nature Materials. 2004;3(8):539-544.

148 Berguiga L, Bellessa J, Vocanson F, Bernstein E, Plenet JC. Carbon nanotube silica glass composites in thin films by the sol–gel technique. Optical Materials. 2006;28(3):167-171.

149 Quinn DG, Bradt RC. On the Vickers Indentation Fracture Toughness Test. Journal of the American Ceramic Society. 2007;90(3):673-680.

150 Yamamoto G, Omori M, Hashida T, Kimura H. A novel structure for carbon nanotube reinforced alumina composites with improved mechanical properties. Nanotechnology. 2008;19:315708, 1-7.

151 Wei T, Fan Z, Luo G, Wei F. A new structure for multi-walled carbon nanotubes reinforced alumina nanocomposite with high strength and toughness. Materials Letters. 2008;62(4-5):641-644.

152 Katsuda Y, Gerstel P, Narayanan J, Bill J, Aldinger F. Reinforcement of precursor-derived Si–C–N ceramics with carbon nanotubes. Journal of the European Ceramic Society. 2006;26(15):3399-3405.

153 Ye F, Liu L, Wang Y, Zhou Y, Peng B, Meng Q. Preparation and mechanical properties of carbon nanotube reinforced barium aluminosilicate glass–ceramic composites. Scripta Materialia. 2006;55(10):911-914.

154 Guo S, Sivakumar R, Kagawa Y. Multiwall Carbon Nanotube-SiO2 Nanocomposites: Sintering, Elastic Properties, and Fracture Toughness. Advanced Engineering Materials. 2007;9(1-2):84-87.

155 Zheng C, Feng M, Zhen X, Huang J, Zhan H. Materials investigation of multi-walled carbon nanotubes doped silica gel glass composites. Journal of Non-Crystalline Solids. 2008;354(12-13):1327-1330.

156 Ahmad K, Pan W. Hybrid nanocomposites: A new route towards tougher alumina ceramics. Composite Science and Technology. 2008;68(6):1321-1327.

157 Balani K, Zhang T, Karakoti A, Li WZ, Seal S, Agarwal A. In situ carbon nanotube reinforcements in a plasma-sprayed aluminum oxide nanocomposite coating. Acta Materialia. 2008;56(3):571-579.

158 Xia ZH, Lou J, Curtin WA. A multiscale experiment on the tribological behavior of aligned carbon nanotube/ceramic composites. Scripta Materialia. 2008;58(3):223-226.

159 Mo CB, Cha SI, Kim KT, Lee KH, Hong SH. Fabrication of carbon nanotube reinforced alumina matrix nanocomposite by sol–gel process. Materials Science and Engineering: A. 2005;395(1-2):124-128.

160 de Andrade MJ, Lima DM, Bergmann CP, Ramminger GO, Malzaretti NM, Costa TMH, Gallas MR. Carbon nanotube/silica composites obtained by sol–gel and high-pressure techniques. Nanotechnology. 2008;19:265607, 1-7.

161 Lim DS, You DH, Choi HJ, Lim SH, Jang H. Effect of CNT distribution on tribological behavior of alumina–CNT composites. Wear. 2005;259(1-6):539-544.

162 Balani K, Chen Y, Harimkar SP, Dahotre NB, Agarwal A. Tribological behavior of plasma-sprayed carbon nanotube-reinforced hydroxyapatite coating in physiological solution. Acta Biomaterialia. 2007;3(6):944-951.

163 Chen Y, Zhang TH, Gan CH, Yu G. Wear studies of hydroxyapatite composite coating reinforced by carbon nanotubes. Carbon. 2007;45(5):998-1004.

164 Zapata-Solvas E, Poyato R, Gomez-Garcia D, Dominguez-Rodriguez A, Radmilovic V, Padture NP. Creep-resistant composites of alumina and single-wall carbon nanotubes. Applied Physics Letters. 2008;92(11):111912 - 111912-3.

165 Well JK, Beaumont PWR. Debonding and pull out processes in fibrous composites. Journal of Materials Science. 1985;20:1275-1284.

166 Cho J, Inam F, Reece MJ, Chlup Z, Dlouhy I, Shaffer MSP, Boccaccini AR. Carbon nanotubes: do they toughen brittle matrices? Journal of Materials Science. 2011;46(14):4770-4779.

167 Shi SL, Liang J. Effect of Multiwall Carbon Nanotubes on Electrical and Dielectric Properties of Yttria-Stabilized Zirconia Ceramic. Journal of the American Ceramic Society. 2006;89(11):3533-3535.

168 Song Y, Noh TW, Lee SI, Gaines JR. Experimental study of the three-dimensional ac conductivity and dielectric constant of a conductor-insulator composite near the percolation threshold. Physical Review B. 1986;33(2):904-909.

169 Yang Y, Gupta MC, Dudley KL, Lawrence RW. A Comparative Study of EMI Shielding Properties of Carbon Nanofiber and Multi-Walled Carbon Nanotube Filled Polymer Composites. Journal of Nanoscience and Nanotechnology. 2005;5(6):927-931.

170 Li N, Huang Y, Du F, He X, Lin X, Gao H, Ma Y, Li F, Chen Y, Eklund PC. Electromagnetic Interference (EMI) Shielding of Single-Walled Carbon Nanotube Epoxy Composites. Nanoletters. 2006;6(6):1141-1145.

171 Xiang C, Pan Y, Gao G. Electromagnetic interference shielding effectiveness of multiwalled carbon nanotube reinforced fused silica composites. Ceramics International. 2007;33(7):1293-1297.

172 Sivakumar R, Guo S, Nishimura T, Kagawa Y. Thermal conductivity in multi-wall carbon nanotube/silica-based nanocomposites. Scripta Materialia. 2007;56(4):265-268.

173 Jiang L, Gao L. Densified multiwalled carbon nanotubes–titanium nitride composites with enhanced thermal properties. Ceramics International. 2008;34(1):231-235.

174 Shenogina N, Shenogin S, Xue L, Keblinski P. On the lack of thermal percolation in carbon nanotube composites. Applied Physics Letters. 2005;87(133106):2056591, 1-3.

175 Biercuk MJ, Llaguno MC, Radosavljevic M, Hyun JK, Johnson AT, Fischer JE. Carbon nanotube composites for thermal management. Applied Physics Letters. 2002;80(2767):1469696, 1-3.

176 Huxtable ST, Cahill DG, Shenogin S, Xue L, Ozisik R, Barone P, Usrey M, Strano MS, Siddons G, Shim M, et al. Interfacial heat flow in carbon nanotube suspensions. Nature Materials. 2003;2:731-734.

177 Koo's AA, Dillon F, Obraztsova EA, Crossley A, Grobert N. Comparison of structural changes in nitrogen and boron-doped multi-walled carbon nanotubes. Carbon. 2010;48(11):3033-3041.

178 Chu BTT. Carbon nanotube reinforced inorganic matrix. Department of Materials; 2008.

179 Egerton RF. Physical Principles of Electron Microscopy. Springer; 2005.

180 Dresselhaus MS, Jorio A, Hofmann M, Dresselhaus G, Saito R. Perspectives on Carbon Nanotubes and Graphene Raman Spectroscopy. Nanoletters. 2010;10(3):751-758.

181 Wood JR, Zhao Q, Wagner HD. Orientation of carbon nanotubes in polymers and its detection by Raman spectroscopy. Composites Part A. 2001;32(3-4):391-399.

182 Dresselhaus MS, Dresselhaus G, Jorio A, Souza Filho AG, Saito R. Raman spectroscopy on isolated single wall carbon nanotubes. Carbon. 2002;40(12):2043-2061.

183 Egerton RF. Electron energy-loss spectroscopy in the TEM. Reports on Progress in Physics. 2009;72:016502, 1-25.

184 Oliver WC, Pharr GM. Measurement of hardness and elastic modulus by instrumented indentation: Advances in understanding and refinements to methodology. Journal of Materials Research. 2004;19(1):3-20.

185 Tabor D. The hardness of metals. Oxford university press; 2002.

186 Young W. Roark’s Formulas for Stress and Strain. 6th ed. McGraw-Hill; 1989.

187 Rosing R, Reichenback R, Richardson A. Generation of component level fault models for MEMS. Microelectronics Journal. 2002 861-868.

188 Santos WN, Baldo JB, Taylor R. Effect of SiC on the thermal diffusivity of silica-based materials. Materials Research Bulletin. 2000;35(13):2091-2100.

189 Lourie O, Cox DM, Wagner HD. Buckling and Collapse of Embedded Carbon Nanotubes. Physical Review Letters. 81(8):1638-1641.

190 Lu Q, Keskar G, Ciocan R, Rao R, Mathur RB, Rao AM, Larcom LL. Determination of Carbon Nanotube Density by Gradient Sedimentation. American Chemical Society. 2006;110(48):24371-24376.

191 Barber AS, Andrews R, Wagner LS. On the tensile strength distribution of multiwalled carbon nanotubes. Applied Physics Letters. 2005;87(203106):1-4.

192 Miyata Y, Mizuno K, Kataura H. Purity and Defect Characterization of Single-Wall Carbon. Journal of Nanomaterials. 2011;2011:786763,1-7.

193 Huang W, Wang Y, Luo G, Wei F. 99.9% purity multi-walled carbon nanotubes by vacuum high-temperature annealing. Carbon. 2003;41(13):2585-2590.

194 Verma ARB, Murthy VSR, Murty GS. Microstructure and Compressive Strength of SiC-Platelet-Reinforced Borosilicate Composites. Journal of American Ceramic Society. 1995;78(10):2732-2736.

195 Bourhis E. Glass Mechanics and Technology. Wiley VCH; 2007.

196 Lawn BR, Wilshaw TR. Fracture of brittle solids. Cambridge University Press; 1975.

197 Gailard J, Skove M, Rao AP. Mechanical properties of chemical vapor deposition grown multiwalled carbon nanotubes. Applied Physics Letters. 2005;86(233109):1946186,1-3.

198 Salvetat JP, Kulik AJ, Bonard JM, Briggs GAD, Stockli T, Metenier K, Bonnamy S, Beguin F, Burnham NA, Forro L. Elastic modulus of ordered and disoriented multiwalled carbon nanotubes. Advanced Materials. 1999;11(2):161-165.

199 Pathak S, Cambaz ZG, Kalidindi SR, Swadener JG, Gogotsi Y. Viscoelastic and high buckling stress of dense carbon nanotube brushes. Carbon. 2009;47(8):1969-1976.

200 Hull D, Clyne TW. Introduction to Composite Materials. Second Edition ed. Cambridge University Press; 1996.

201 Green DJ. An introduction to mechanical properties of ceramics. Cambridge University Press; 1998.

202 Derby B, Hills D, Ruiz C. Materials for engineering: a fundamental design approach. Longman Scientific and Technical; 1992.

203 Callister WD. Materials Science and Engineering, An Introduction. 7th ed. John Wiley and Sons; 2007.

204 Newnham RE. Properties of Materials. Oxford University Press; 2005.

205 Kreith F,MRMaBMS. Principles of Heat Transfer. Cengage Learning; 2011.

206 Ivanov I, Puretzky A, Eres G, Wang H, Pan Z, Cui H, Jin R, Howe J, Geohegan DB. Fast and highly anisotropic thermal transport through vertically aligned carbon nanotube arrays. Applied Physics Letters. 2006;89:223110,1-3.

207 Borca-Tasciuc T, Vafaei S, Borca-Tasciuc AA, Wei BQ, Vajtai R, P.M. A. Anisotropic thermal diffusivity of aligned multiwall carbon nanotube arrays. Applied Physics. 2005;98(5):054309, 1-6.

208 Hou J, Wang X, Liu C, Cheng H. Development of photothermal-resistance technique and its application to thermal diffusivity measurement of single-wall carbon nanotube bundles. Applied Physics Letters. 2006;88:181910.

209 Xie H, Cai A, Wang X. Thermal diffusivity and conductivity of multiwalled carbon nanotube arrays. Physics Letters A. 2007;369(1-2):120-123.

210 Lian G, Jiang L, Sun J. Carbon nanotube-ceramic composites. Journal of Electroceramics. 2006;17:51-55.

211 Seeger T, Fuente G, Maser WK, Benito AM, Callejas AM, Martinez MT. Evolution of multiwalled carbon-nanotube/SiO2 composites via laser treatment. Nanotechnology. 2003;14(2):184-187.

212 Hata K, Futaba DN, Mizuno K, Namai T, Yumura M, and Iijima S. Water-assisted highly efficient synthesis of impurity-free single-walled carbon nanotubes. Science. 2004;306(5700):1362-1364.

213 Suhr J, Victor P, Ci L, Sreekala S, Zhang X, Nalamasu O, Ajayan PM. Fatigue resistance of aligned carbon nanotube arrays under cyclic compression. Nature Nanotechnology. 2007;2:417-421.

214 Maschmann MR, Zhang Q, Du F, Dai L, Baur J. Length dependent foam-like mechanical response of axially indented vertically oriented carbon nanotube arrays. Carbon. 2011;49(2):386-397.

215 Deck CP, Flowers J, McKee GSB, Vecchio K. Mechanical behavior of ultralong multiwalled carbon nanotube mats. Journal of Applied Physics. 2007;101(023512):1-6.

216 Vagaggini E, Domergue JM, Evans AG. Relationships between Hysteresis Measurements and the Constituent Properties of Ceramic Matrix Composites: I,

Theory. Jouranal of the American Ceramic Society. 1995;78(10):2709-2720.

217 Levi CG, Yang JY, Dalgleish BJ, Zok FW, Evans AG. Processing and Performance of an All-Oxide Ceramic Composite. Journal of the American Ceramic Society. 1998;81(8):2077-2086.

218 Griffith AA. The phenomena of rapture and flow in solids. Philosophical Transactions of the Royal Society of London, Series A. 1921;221:163-198.

219 Klug T, Bruckner R. Preparation of C-fibre borosilicate glass composites: Influence of the fibre type on mechanical properties. Journal of Materials Science. 1994;29(15):4013-4021.

220 Blanco J, Garcia EJ, Villoria RG, Wardle BL. Limiting Mechanisms of Mode I Interlaminar Toughening of Composites Reinforced with Aligned Carbon Nanotubes. Journal of Composite Materials. 2009;43(8):825-841.

221 Ayatollahi MR, Shadlou S, Shokrieh MM, Chitsazzadeh M. Effect of multi-walled carbon nanotube aspect ratio on mechanical and electrical properties of epoxy-based nanocomposites. Polymer Testing. 2011;30(5):548-556.

APPENDICES

APPENDIX A1: Energy Consumed by Bridging During the Debonding Process.

An estimation of the strain energy absorbed during bridging and frictional sliding by the GCNTs during debonding can be estimated using equation below assuming a solid glass fibre,

$$G_{bridging} = \frac{\sigma_{glass}^{2} V_{GCNT} l_{d}}{3E_{glass}}$$

where σ_{glass} is the strength of glass in the microcantilever bend tests (1.3 GPa), V_{GCNT} is 0.45, l_d is the debonded length (200 nm) and E_{glass} is the elastic modulus of glass (65 GPa). For the 50% of CNTs that show matrix pull-out, the energy consumed in bridging during debond is ca. 0.39 Jm^{-2}.

APPENDIX A2: Cross-sectional Fracture Energy

Contribution of fracture of glass in the cross-sectional area during the debonding process can be obtained using the following equation

$$W_{fracture} = \pi(R^2 - r^2)G_c \times N$$

where G_c is the fracture energy of glass (7.5 Jm^{-2}) and the cross-sectional area is obtained from the schematic a2 below. The number of GCNTs, $N = V_{GCNT}/\pi r^2$ while the V_{GCNT} is obtained from the know area fraction of CNTs (0.2 %) in the composite as 0.45 vol.%. The fracture energy for 50% of the CNTs that showed matrix pull-out is estimated to be ~ 1 Jm^{-2}.

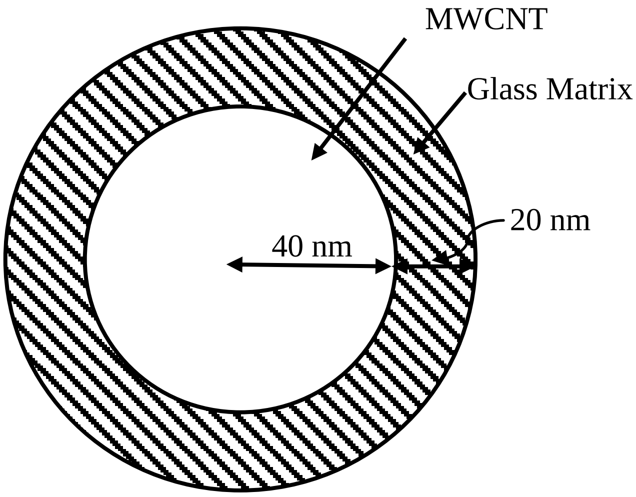

Schematic representation of a cross-section of a matrix pull-out.